Wind Tunnel Investigations of an Inclined Stay Cable with a Helical Fillet

U.S. Department of Transportation
Federal Highway Administration

FOREWORD

Cable-stayed bridges have become the form of choice over the past several decades for bridges in the medium-to-long-span range. In some cases, serviceability problems involving large amplitude vibrations of stay cables under certain wind and wind-rain conditions have been observed. This study was conducted in response to State transportation departments' requests to develop improved design guidance for mitigation of excessive cable vibrations on cable-stayed bridges. The study included wind tunnel testing of a full-scale cable model to evaluate the influence of damping, turbulence, and aerodynamic surface treatment on cable stability. The results of this study will be made available to the Post-Tensioning Institute's DC-45 Cable-Stayed Bridge Committee for consideration during their periodic updates of the Guide Specification, *Recommendations for Stay Cable Design, Testing, and Installation*.[1]

This report will be of interest to bridge engineers, wind engineers, and consultants involved in the design of cable-stayed bridges. It is the third in a series of reports addressing the subject of aerodynamic stability of bridge stay cables that will be published in the coming months.

Jorge E. Pagán-Ortiz
Director, Office of Infrastructure
Research and Development

TECHNICAL DOCUMENTATION PAGE

1. Report No. FHWA-HRT-14-070	2. Government Accession No.	3. Recipient's Catalog No.
4. Title and Subtitle Wind Tunnel Investigations of an Inclined Stay Cable with a Helical Fillet		5. Report Date September 2014
		6. Performing Organization Code
7. Author(s) Guy L. Larose and Annick D'Auteuil		8. Performing Organization Report No. LTR-AL-2011-0093
9. Performing Organization Name and Address National Research Council of Canada Institute for Aerospace Research 1200 Montreal Road Ottawa, Ontario Canada K1A OR6 Genex Systems, LLC 2 Eaton Street, Suite 603 Hampton, VA 23669		10. Work Unit No. (TRAIS)
		11. Contract or Grant No. DTFH61-07-D-00034
12. Sponsoring Agency Name and Address Office of Infrastructure R&D Federal Highway Administration 6300 Georgetown Pike McLean, VA 22101-2296		13. Type of Report and Period Covered Laboratory Report March 2011–March 2012
		14. Sponsoring Agency Code HRDI-50
15. Supplementary Notes The Contracting Officer's Technical Representative (COTR) was Harold R. Bosch, (HRDI-50).		

16. Abstract

Cable-stayed bridges have been recognized as the most efficient and cost effective structural form for medium-to-long-span bridges over the past several decades. With their widespread use, cases of serviceability problems associated with large amplitude vibration of stay cables have been reported. Stay cables are laterally flexible structural members with very low inherent damping and thus are highly susceptible to environmental conditions such as wind and rain/wind combination.

Recognition of these problems has led to the incorporation of different types of mitigation measures on many cable-stayed bridges around the world. These measures include surface modifications, cable crossties, and external dampers. Modification of cable surfaces has been widely accepted as a means to mitigate rain/wind vibrations. Recent studies have firmly established the formation of a water rivulet along the upper side of the stay and its interaction with wind flow as the main cause of rain/wind vibrations. Appropriate modifications to exterior cable surfaces effectively disrupts the formation of a water rivulet.

The objective of this study is to supplement the existing knowledge base on some of the outstanding issues of stay cable vibrations and to develop technical recommendations that may be incorporated into design guidelines. Specifically, this project focused on the wind-cable interaction, with particular interest in details of the air flow and flow field close to the cable as well as forces on the cable surface. A helical fillet was attached to an existing cable model to evaluate the influence of this common mitigation feature on dynamic behavior. The cable inclination angle was varied during testing to represent field orientations, and the model was rotated on its longitudinal axis to assess the influence of high-density polyethylene roundness. Tests were conducted at various levels of damping, with and without the fillet, and in turbulent as well as smooth flow conditions.

17. Key Words Cable-stayed bridges, Cables, Vibrations, Wind, Rain, Wind tunnel testing, Wind turbulence, Galloping, Vortex shedding, Aerodynamic surface treatment, Helical fillet	18. Distribution Statement No restrictions. This document is available to the public through the National Technical Information Service, Springfield, VA 22161. http://www.ntis.gov		
19. Security Classif. (of this report) Unclassified	20. Security Classif. (of this page) Unclassified	21. No. of Pages 222	22. Price

Form DOT F 1700.7 (8-72)   Reproduction of completed page authorized

SI* (MODERN METRIC) CONVERSION FACTORS

APPROXIMATE CONVERSIONS TO SI UNITS

Symbol	When You Know	Multiply By	To Find	Symbol
LENGTH				
in	inches	25.4	millimeters	mm
ft	feet	0.305	meters	m
yd	yards	0.914	meters	m
mi	miles	1.61	kilometers	km
AREA				
in^2	square inches	645.2	square millimeters	mm^2
ft^2	square feet	0.093	square meters	m^2
yd^2	square yard	0.836	square meters	m^2
ac	acres	0.405	hectares	ha
mi^2	square miles	2.59	square kilometers	km^2
VOLUME				
fl oz	fluid ounces	29.57	milliliters	mL
gal	gallons	3.785	liters	L
ft^3	cubic feet	0.028	cubic meters	m^3
yd^3	cubic yards	0.765	cubic meters	m^3
NOTE: volumes greater than 1000 L shall be shown in m^3				
MASS				
oz	ounces	28.35	grams	g
lb	pounds	0.454	kilograms	kg
T	short tons (2000 lb)	0.907	megagrams (or "metric ton")	Mg (or "t")
TEMPERATURE (exact degrees)				
^oF	Fahrenheit	5 (F-32)/9 or (F-32)/1.8	Celsius	^oC
ILLUMINATION				
fc	foot-candles	10.76	lux	lx
fl	foot-Lamberts	3.426	candela/m^2	cd/m^2
FORCE and PRESSURE or STRESS				
lbf	poundforce	4.45	newtons	N
lbf/in^2	poundforce per square inch	6.89	kilopascals	kPa

APPROXIMATE CONVERSIONS FROM SI UNITS

Symbol	When You Know	Multiply By	To Find	Symbol
LENGTH				
mm	millimeters	0.039	inches	in
m	meters	3.28	feet	ft
m	meters	1.09	yards	yd
km	kilometers	0.621	miles	mi
AREA				
mm^2	square millimeters	0.0016	square inches	in^2
m^2	square meters	10.764	square feet	ft^2
m^2	square meters	1.195	square yards	yd^2
ha	hectares	2.47	acres	ac
km^2	square kilometers	0.386	square miles	mi^2
VOLUME				
mL	milliliters	0.034	fluid ounces	fl oz
L	liters	0.264	gallons	gal
m^3	cubic meters	35.314	cubic feet	ft^3
m^3	cubic meters	1.307	cubic yards	yd^3
MASS				
g	grams	0.035	ounces	oz
kg	kilograms	2.202	pounds	lb
Mg (or "t")	megagrams (or "metric ton")	1.103	short tons (2000 lb)	T
TEMPERATURE (exact degrees)				
^oC	Celsius	1.8C+32	Fahrenheit	^oF
ILLUMINATION				
lx	lux	0.0929	foot-candles	fc
cd/m^2	candela/m^2	0.2919	foot-Lamberts	fl
FORCE and PRESSURE or STRESS				
N	newtons	0.225	poundforce	lbf
kPa	kilopascals	0.145	poundforce per square inch	lbf/in^2

*SI is the symbol for the International System of Units. Appropriate rounding should be made to comply with Section 4 of ASTM E380.
(Revised March 2003)

TABLE OF CONTENTS

LIST OF FIGURES

LIST OF TABLES

LIST OF SYMBOLS

Symbols

C_d Drag coefficient.

C_x Along-wind force coefficient.

C_y Across-wind force coefficient

d, D Cable diameter.

f Frequency.

I Turbulence intensity.

L Wind exposed length of cable model.

^xL Integral length scale of turbulence.

m Mass per unit exposed length of cable model.

q Dynamic pressure.

Re Reynolds number.

Sc Scruton number.

U Mean wind speed.

U/fB Reduced velocity.

α Spring rotation.

β Flow yaw angle.

ζ Damping ratio as a fraction of critical.

θ Stay cable inclination.

μ Air viscosity.

ρ Air density.

ϕ Model inclination.

Subscripts

h Heave, along-wind.

s Sway, across-wind.

u, v, w Longitudinal, lateral, and vertical components of the flow fluctuations.

EXECUTIVE SUMMARY

Experiments on a 1:1 scale sectional model of a stay cable were conducted in the 3-by-6-m Propulsion and Icing Wind Tunnel at the Institute for Aerospace Research, National Research Council Canada (NRC-IAR). The purpose of the experiments was to study the effect of adding a helical fillet to the surface of a stay cable and monitor the response of the cable during wind-induced excitation.

The experiments were carried out on a 6.7-m-long sectional model with a diameter of 0.162 m composed of a central steel core covered with a high-density polyethylene (HDPE) tube obtained from a bridge construction site. A double parallel helical fillet with a rectangular cross section of 2.3 by 2.4 mm and a right-handed helix angle of 45 degrees was glued to the surface of the model. The geometry of the helical fillet was selected to represent what is currently used on stay cables of long-span cable-stayed bridges to mitigate rain/wind-induced oscillations.

The sectional model was mounted in an eight-spring suspension rig allowing along-wind and across-wind vibrations of the model at a frequency of 1.4 Hz in both directions. The total sprung mass was 406 kg, and the inherent structural damping of the suspension rig was low, between 0.07 and 0.15 percent of critical damping for vibration amplitudes observed during the tests. Simultaneous measurements of fluctuating surface pressures on the circumference of the model and response at its extremities were carried out for wind speeds ranging from 4 to 36 m/s covering the entire critical number regime and beyond ($43,000 < Re < 391,000$), where Re represents Reynolds number.

The wind-tunnel investigation included experiments with the cable model at 60- and 45-degree inclinations in smooth flow with the helical fillet, at a 60-degree inclination in turbulent flow with and without the helical fillet, and at a 60-degree inclination in smooth flow without the helical fillet. The tests were conducted for several rotations of the cable model on its longitudinal axis.

The experiments revealed that a stay cable with a helical fillet inclined at 60 degrees to the flow can experience wind-induced vibrations with large amplitudes in smooth or turbulent flow for a low level of structural damping. The oscillations observed appeared to be self-limited in amplitude and could be mitigated with an increase of structural damping. The cable model with the helical fillet experienced a drag crisis almost as pronounced as for the smooth cable. The experiments also revealed that the aerodynamic forces at the source of the vibrations were highly sensitive to a rotation of the cable model on its axis. Measurements of the external diameter of the smooth cable model have shown a maximum eccentricity equivalent to 1 percent of the mean diameter, which appeared to be sufficient to influence the aerodynamics of the cable model, even with the helical fillet in place.

CHAPTER 1: INTRODUCTION

In response to concerns expressed in the wind engineering community with regards to the aerodynamics of inclined stay cables with helical fillets, NRC-IAR, in collaboration with the University of Bristol and the University of Stavanger, was mandated to conduct an experimental study in its 3-by-6-m Propulsion and Icing Wind Tunnel. This project was initiated by the Federal Highway Administration (FHWA), which has undertaken the task to fill the knowledge gap on aerodynamics of stay cables with helical fillets. The main objective of the investigation was to define the sensitivity of stay cables with helical fillets (such as those commonly used on cable-stayed bridges in the United States and Europe) to galloping. For this purpose, a small helical fillet was affixed to an existing stay cable model composed of a steel core covered with a HDPE tube, typical of actual bridge stay cables. The aeroelastic stability of the cable as well as the nature of underlying aerodynamic forces were investigated.

The investigation was divided in two phases. In phase I, the aerodynamic stability of a cable with helical fillets was studied with a spring-supported cable model in smooth flow for a cable inclined at 60 degrees from the horizontal. The dynamic response of the model and the cross-sectional wind-induced surface pressures were monitored as a function of Reynolds number.

In phase II, different cable orientations were studied (45 and 60 degrees). For the cases where important cable vibrations were observed in smooth flow, tests in turbulent flow for conditions representative of field conditions were carried out.

This report documents the work undertaken by NRC-IAR and presents the results of the investigation. The approach adopted was to carry out the test in a 3-by-6-m wind tunnel on a 6.7-m-long sectional model built at a geometrical scale of 1:1 and free to respond on an eight-spring suspension system. The tests took place from May 2, 2011, to June 24, 2011.

The main findings of the investigation for both rounds of tests are presented in this report. The documentation of the tests also includes video recordings, still images, and all the experimental data in electronic form.

CHAPTER 2: EXPERIMENTAL CONDITIONS

PROTOTYPE STAY CABLES

Over the last 20 years, structural engineers and architects have proposed the use of cable-stayed bridges for increasingly diverse situations. Either for long main spans where only suspension bridges would have been traditionally considered or wide roadways with medium spans where cantilever or arch bridges would have been selected, cable-stayed bridges are now being built as the more economical and practical solution. This has promoted the development of innovative structural design and fabrication techniques. For example, the majority of the modern cable-stayed bridges now use stay cables that are fabricated directly on the construction site as opposed to being pre-fabricated in a factory and shipped to the site in large coils, providing substantial cost and time savings.

Typical in-situ fabricated stay cables are each made of a bundle of parallel steel cables that are fed through an HDPE tube one by one and are anchored to the towers and deck at a prescribed tension. Each cable is made of five to seven steel strands and is covered by a polyethylene sheath. A 16-cm external diameter stay cable would be made of approximately 40 to 55 steel cables and would have a mass per unit length of 60 to 80 kg/m. Approximately 50 to 60 percent of the surface area of the stay is steel, and the other 40 to 50 percent is polyethylene, air, grease, wax, or concrete grout. Figure 1 and figure 2 show stay cables of the Millau Viaduct in France and the Clark Bridge that spans from Alton, IL, to West Alton MO, respectively.

Figure 1. Photo. Modern stay cables with HDPE tube cover on the Millau Viaduct.

Figure 2. Photo. Modern stay cables with HDPE tube cover on the Clark Bridge.

The HDPE tube serves three main purposes: (1) aerodynamic drag reduction, (2) corrosion protection, and (3) aesthetics. However, it has some drawbacks, in particular when it comes to the effects of wind. Stay cables generally have low structural damping ($\approx$ 0.1 to 0.2 percent of critical damping) and are exposed to wind and are thus prone to wind-induced vibrations. The HPDE tube helps by reducing the drag coefficient of the stays, therefore reducing vibrations due to buffeting from turbulence. However, the smooth surface of the tube combined with light rain and light winds can translate to severe rain/wind-induced vibrations of the stay cables. Also, the smooth surface of the tube in combination with its attitude (inclination and yaw angles) to the wind can induce undesirable dry-inclined cable galloping for a specific range of mean wind speeds corresponding to the critical Reynolds number regime.

To mitigate the increased sensitivity to wind-induced vibrations of the stay cable covered with a smooth HDPE tube, three approaches are being used:

- Increase the structural damping of the stays.

- Alter the surface of the HDPE tubes to prevent the formation of water rivulets and prevent rain/wind-induced vibrations.

- Install ropes or crossties between the stays.

Since the construction of the Pont de Normandie in France in the early 1990s, the majority of cable-stayed bridges built in Europe and North America have stay cables fitted with a helical fillet to prevent rain/wind vibrations. This countermeasure has proven to be highly effective against this phenomenon, in particular when combined with an increase of structural damping.

Wind tunnel tests have been conducted to verify that the helical fillet worked.[2,3] However, no official design guidelines or specifications exist on what the geometry of the helical fillet should be for it to be effective. The industry has adopted what experience has shown as a viable solution based on its first use for Pont de Normandie, and nowadays, stay cable manufacturers are each proposing their own solutions. Table 1 presents a short list of helical fillet geometry that has been installed on bridges. The pitch and helix angle of the helical fillet are defined in figure 3. For this study, a double, parallel, and right-handed helical fillet was used.

Table 1. Typical prototype helical fillet geometries (all double helix).

Bridge and Location	Cable Diameter (mm)	Pitch (mm)	Helix Angle (degrees)	Pitch to Diameter Ratio	Helical Fillet (mm)	Description Helical Fillet
Normandie; France	170	600	41.7	3.5	1.3 diameter	Round
Oresund; Sweden to Denmark	250	550	55.0	2.2	2.1 high × 3.0 wide	Rectangular
Charles River; Boston, MA	178	610	42.5	3.4	1.5 high × 3.3 wide	Rectangular
Generic 1	200	600	46.3	3.0	2.0 diameter	Round
Generic 2	160	490	45.7	3.1	4.0 diameter	Round
Generic 3	200	620	45.4	3.1	2.0 diameter × 4.0 wide	Round
Generic 4	200	630	45.0	3.1	2.0 diameter × 4.0 wide	Round
Present study	162	520	44.4	3.2	2.3 high × 2.4 wide	Rectangular

Note: Generic refers to HDPE pipe specimens with helical fillet.
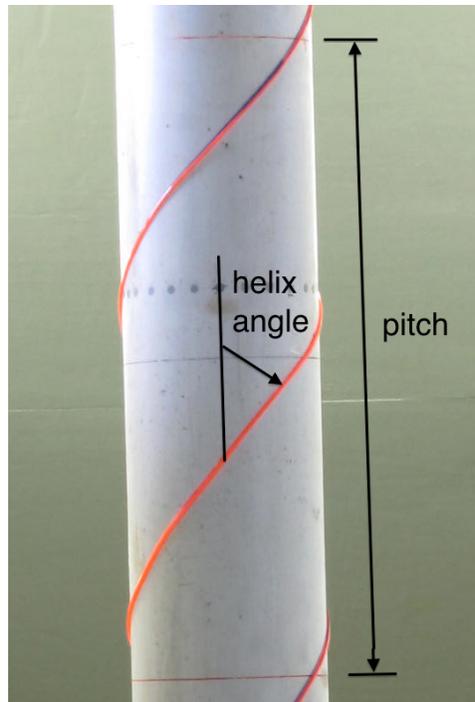
Figure 3. Photo. Pitch and helix angle.

Without official specifications for the helical fillet geometry, it is understandable that the aerodynamics of the stay cable with a helical fillet is not generally well defined. It is hard to find in literature the mean force coefficients of stay cables with helical fillets and, in particular, the across-wind coefficients. The rule of thumb is that the helical fillet increases the drag coefficient of the stay cables to around 0.7 to 0.8. For stay cables inclined and yawed to the wind with a helical fillet (i.e., for the majority of stay cables built in the last 15 years), the aerodynamic force coefficients are not available.

Whether such alteration to the smooth HDPE tube covering the stays could cause inclined cable galloping is not known, and to the authors' knowledge, this issue has not been addressed. The purpose of the present study is to fill this gap.

MODEL PROPERTIES

The cable model used for two previous 1:1 scale studies in 2001 and 2008 at NRC-IAR in the same wind tunnel facility was reused for the present study. (See references 4–7.) No modifications of the model itself were necessary with the exception of a thorough cleaning of the surface to make it as uniform as possible, a verification of each of the surface pressure taps and pneumatic tubing installed for the 2008 measurement campaign and the installation of removable helical fillets.

The model was composed of a rigid steel tube 6,687 mm long with an outer diameter of 139.7 mm and a wall thickness of 15.9 mm. The steel tube was covered with a white HDPE tube 6,198 mm long with an inner diameter of 141 mm and a mean outer diameter of 161.7 mm. Two hatches were cut in the steel pipe and HDPE tube to allow for the installation of the surface pressure taps, pneumatic tubing, and electronic pressure transducers.

The main characteristics of the model were as follows:

- **Mean diameter**: 161.7 mm.

- **Length-to-diameter ratio**: 38.5.

- **Surface roughness**: Sanded HDPE surface with repaired scratches and roughness depth-to-diameter ratio of $\approx 6.5 \times 10^{-6}$.

Visual inspection of the model revealed that the outside geometry of the HDPE tube was not perfectly round. To characterize its relative eccentricity, the outside diameter of the model was measured at every 10 degrees of azimuth at four span-wise locations, which correspond to the location of the four rings of surface pressure taps. The results are presented in figure 4. The largest observed deviation was equivalent to 1 percent of the mean diameter with four distinct regions alternating from peak to valley. Flamand and Boujard have reported a similar profile for a HDPE tube and suggest that the method of production of the tube using extrusion results in a shape that differs systematically from a circle.[8]
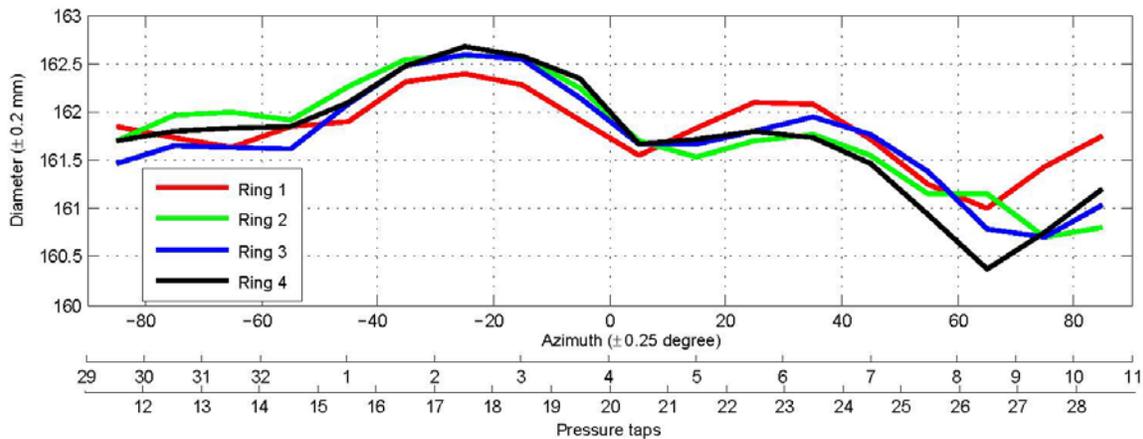
Figure 4. Graph. Variations of the cable model diameter with azimuth at four span-wise locations.

A helical fillet with a rectangular cross section 2.3 mm high and 2.4 mm wide was fixed in a right-handed direction to the surface of the model with double-sided tape that was 0.1 mm thick. The geometry was selected to represent as close as possible what is used in practice as presented in table 1. A double parallel helix with a pitch of 520 mm was used with a helix angle of 44.5 degrees (See figure 5 and figure 6). The method of installation of the helical fillet was selected so that it could be removed without marking the external surface of the HDPE tube.
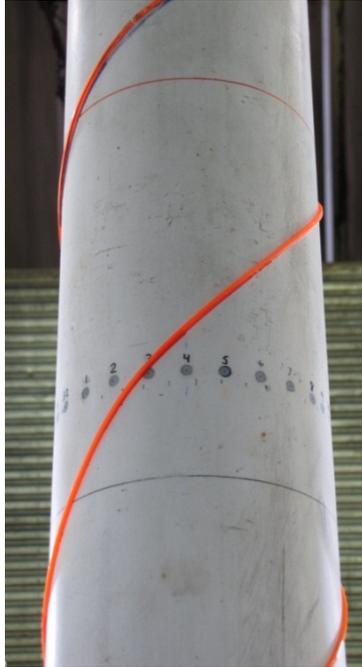
Figure 5. Photo. Close-up view of double helical right-handed fillet.

Figure 6. Photo. Overview of double helical right-handed fillet.

SUSPENSION SYSTEM

The sectional model rig used for the two previous experiments with an inclined cable in the same test facility was also used for the present study.[7] The only modification that was made to the rig was to allow rotation of the cable model on its axis without a rotation of the spring plane. In the previous experiments, it was possible to rotate the cable on its axis by rotating the spring plane, therefore changing two parameters at the same time. In light of the variations of diameter shown in figure 4, it was considered important to keep the rotation of the model on its axis as an independent parameter.

The suspension system was composed of eight springs and one axial suspension cable. The rig allowed for motion of the cable in two orthogonal planes, with four springs per plane, which is described as sway for a nominally across-wind motion and heave for a nominally along-wind motion. The springs were set on two large drums and tensioning frames, one for each extremity of the model, known as the lower and upper rigs (see figure 7 and figure 8). The stiffness of each spring could be adjusted by changing the number of active coils. The tension in each spring could also be adjusted using a threaded rod pulling system. The orientation of the spring planes with the flow could be changed by rotating the large drums of the lower and upper rig on their axes. Finally, by changing the position of the upper rig in relation to the lower rig, the inclination of the model could be changed.

Figure 7. Photo. Lower rig with spring rotation at 0 degrees.

Figure 8. Photo. Upper rig with spring rotation at 45 degrees.

The axial suspension cable linked the top end of the model to a cross beam at the ceiling of the wind tunnel building. Its role was to take a large part of the weight of the model, preventing it from sliding downwards. The length and the angle of the axial cable in relation to the model

were fully adjustable. Figure 9 and figure 10 show overall views of the experimental setup. In figure 9, the red arrow above the wind tunnel roof points to the axial cable supporting the model.

Figure 9. Photo. Cable model at an inclination of 60 degrees from outside the test section of the 3-by-6-m Propulsion and Icing Wind Tunnel.

Figure 10. Photo. Cable model at an inclination of 60 degrees from inside the test section of the 3-by-6-m Propulsion and Icing Wind Tunnel.

To allow for rotation of the model on its axis, two small turntables were added to the flanges that link the extremities of the model to the springs (see figure 11). The model was set free to rotate on its axis by simply loosening two set screws at its extremities. Any rotation was possible.

Figure 11. Photo. Turntable that allowed rotation of the cable model on its axis.

Because all springs were identical, it was possible to adjust their axial stiffness by carefully controlling the number of active coils. For each spring, a steel perch could be threaded in and out

of the springs, therefore freeing or locking out a set number of coils. From the 2001 inclined cable study, it was established that 28 active coils corresponded to an axial stiffness of 4.78 kN/m.[4,5] From the 2008 study, it was observed that the axial cable contributed to a non-negligible part of the stiffness of the upper rig.[6,7] At an inclination angle of 60 degrees, the tension in the axial cable contributed to a stiffness of approximately 1.0 kN/m.

To maintain the previous oscillation frequencies ($\approx$ 1.41Hz) and frequency ratio ($\approx$ 1.02 sway-to-heave) as well as the upper and lower rig stiffness, the springs were adjusted to the number of active coils as shown in table 2.

Table 2. Number of active coils per spring.

Springs	Sway (Two Springs)	Heave (Two Springs)
Upper rig	28.00	26.75
Lower rig	24.38	25.38

Each spring was pre-tensioned independently to ensure a linear motion for the entire range of vibrations expected during the tests. The level of tension in the springs in one plane affected the frequencies of oscillations in the other plane, so care was taken to adjust the tension through a control of the spring extension when the model was at rest.

Taking into account the masses of the steel core of the model, the HDPE tube, the instrumentation, the links between the model and the springs, and one-third of the mass of the active part of the springs, the suspended mass was established at 407 kg for this study in accordance with the 2001 and 2008 mass estimates. (See references 4–7.) The distance between the two spring planes was fixed at 6,858 mm. As stated earlier, the length of the steel core of the model was 6,687 mm. However, the length of the model exposed to the flow was slightly shorter at 6,100 mm for the 60-degree inclination case. The mass per unit exposed length of the cable model was therefore equivalent to 66.7 kg/m. Table 3 summarizes the dimensions of the cable related to its length or to the distance between lasers used at both extremities of the cable.

Table 3. Cable length or distance for instrumentation at both extremities of the cable.

Measurement	Length (mm)
Cable length (polyethylene part)	6,198
Cable length (steel part)	6,687
Distance between spring planes	6,858
Distance between displacement transducers for sway	7,116
Distance between displacement transducers for heave	7,285
Representative exposed cable length at 60-degree inclination	6,100
Representative exposed cable length at 45-degree inclination	6,000

The upper end of the model pierced through the roof of the wind tunnel. The lower end of the model and the lower rig were fully immersed in the flow. For the majority of the tests, the circular hole at the interface between the roof and the model was kept open and allowed model displacement of approximately 120 mm. For one case, the hole was sealed to identify the influence of the end conditions on the mean aerodynamic characteristics of the cable model. Figure 12 and figure 13 show the top end of the model.

Figure 12. Photo. Top of the open interface between the cable model and the roof of the wind tunnel.

Figure 13. Photo. Underside of the sealed interface between the cable model and the roof of the wind tunnel.

FLOW CONDITIONS

Smooth Flow

All tests were carried out in the NRC-IAR 3-by-6-m Propulsion and Icing Wind Tunnel in Ottawa, Canada. This test facility is an open circuit wind tunnel of the blowing type. A 7.9-m-diameter 16-blade fan draws outdoor air and pushes it through a large settling chamber followed by a 6:1 ratio contraction before entering the 12.2-m-long test section. The fan is fitted with a set of anti-swirl stators, and the settling chamber has a set of fine mesh screens to keep flow turbulence to a minimum. The test section is followed by a diffuser with a 90-degree bend and exhausts directly outdoors. The test section is 3.05 m wide and 6.1 m high. It is equipped with removable fillets reducing in size in the direction of the flow to mitigate stream-wise pressure gradients associated with growth of the wall boundary layers. The entire floor of the test section is mounted on jacks and can be raised by 2 m.

The fan is powered by a 750-kW direct current motor, providing a maximum wind speed of 39 m/s for the empty test section. The wind speed is controlled by increasing the fan revolutions per minute, which can be done in small increments, allowing a fine adjustment of the mean wind

speed when outdoor conditions are calm. In gusty conditions, the wind speed inside the test section can experience low frequency modulation for wind speed below about 14 m/s.

For the present study, only the fillets of the test section roof where installed. Prior to the installation of the cable model, a calibration of the test section dynamic pressure in relation to the pressure difference between the settling chamber and the test section inlet was carried out. The latter was measured during the entire investigation to provide the test section dynamic pressure and wind speed. Figure 14 shows a downstream view of the configuration of the test section during calibration.

Figure 14. Photo. Downstream view of the test section during dynamic pressure calibration prior to the installation of the cable model.

The turbulence intensity of the flow was measured throughout the tests at the entrance of the test section, 4 m above the floor, using a Turbulent Flow Instrumentation (TFI) Cobra Probe, which provides, with a high sampling frequency, the three unsteady components of the wind speed and the turbulence characteristics of the wind. For mean wind speeds above 14 m/s, the turbulence intensity varied between 0.35 and 0.5 percent. For lower wind speeds (8 to 12 m/s) in calm days outdoors, similar turbulence levels were observed. On windy days, the turbulence level below 14 m/s generally increased and was typically in the 0.7 to 1.2 percent range. Figure 15 compares the variations of longitudinal turbulence intensity (I_u) with wind speed for the smooth flow case on a calm day versus a windy day.
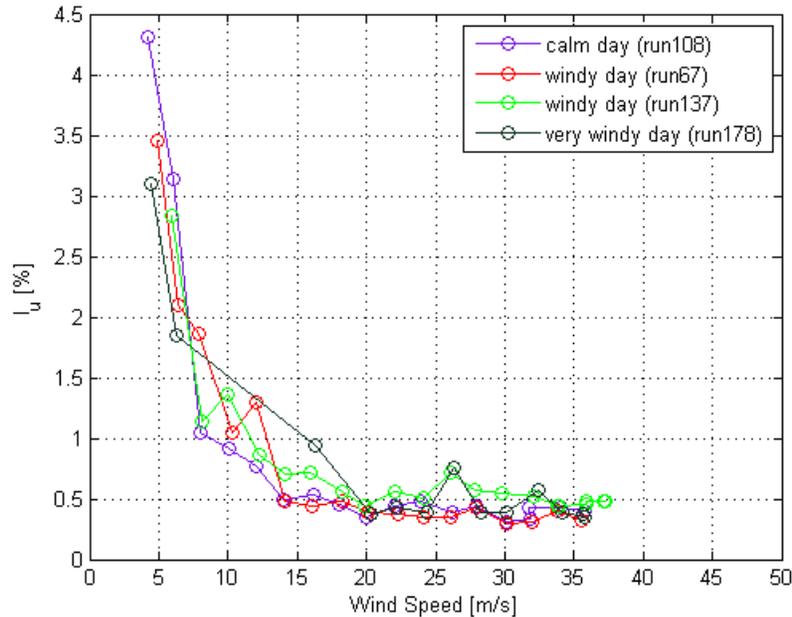
Figure 15. Graph. Variations of I_u with wind speed measured at the entrance of the test section for different external conditions for the smooth flow case.

Turbulent Flow

The test program included experiments in turbulent flow for the cable model with a 60-degree inclination. The objective was to study the aerodynamics of the cable with and without the helical fillet in a uniform flow field with turbulence characteristics representative of conditions found in the field.

The following characteristics were deemed important to consider in the definition of the turbulence field to use:

1. Turbulence level between 3 and 6 percent.

2. Turbulence integral scales larger than the expected boundary layer thickness at the surface of the model and larger than the thickness of the helical fillet.

3. Relatively uniform turbulence along the length of the model.

4. Turbulence spectrum with a representative level of energy at high frequency (i.e., with a representative energy level for the small scale turbulence).

Given the limited length of the test section in relation to the length of the model, it was not possible to use large vortex generators such as large bar lattice structures, spires, or panels far ahead of the model and let this turbulence stretch in the test section before reaching the model. It was also not possible to use a rope net or mesh with a small bar size and mesh size to fulfill characteristics 2 and 4.

To obtain a uniform turbulence level, a grid had to be used. However, since the turbulence level decayed rapidly as the vortices traveled downstream, the grid could not be installed vertically at the entrance of the test section like it is commonly done. The turbulence level at the top of the model (closer to the grid) would have been larger than the turbulence level at the bottom of the model, which was approximately 3 m downstream of the top of the model. To fulfill characteristic 3, the grid had to be installed parallel to the cable (i.e., inclined at 60 degrees from the floor). The bar size of the grid had to be large enough to produce eddies bigger than the helical fillet cross section, and the mesh size had to be small enough to promote flow mixing downstream. The logistics of installing a turbulence grid inclined at 60 degrees and with enough strength to sustain 39 m/s winds for a long period suggested the use of a light metallic structure.

Five aluminum ladders 6.4 m long were fastened together and lifted in place in parallel to the model. The ladders spanned the entire height of the test section and 80 percent of the width. They formed a quasi-uniform grid with a bar size of 35 mm and mesh size of 305 mm. Two positions upstream of the model were investigated. The first position was 3.3 m upstream and had a turbulence level above the limit defined in characteristic 1. The second position was 5.1 m upstream of the model and had a mean turbulence level of 3.5 to 4.5 percent and was retained as the solution for the tests. Figure 16 and figure 17 show downstream views of the ladder grid for the two investigated positions.

Figure 16. Photo. Grid of ladders used to generate the turbulent flow field for position 1.

Figure 17. Photo. Grid of ladders used to generate the turbulent flow field for position 2.

A TFI Cobra Probe was used to document the turbulent flow field behind the ladder grid. The cable model was used to support the probe at several heights above the floor (see figure 18). The probe was mounted 430 mm in front of the model.

Figure 18. Photo. TFI Cobra Probe attached to the cable model to measure the turbulence level behind the grid of ladders.

Figure 19 and figure 20 present the results of the measurements of the oncoming turbulent flow field for the turbulent flow test cases. The integral scales of the turbulence, calculated using the autocorrelation function approach, were as follows: longitudinal, $^{x}L_u = 90$ mm, lateral, $^{x}L_v = 47$ mm, and vertical, $^{x}L_w = 46$ mm. The turbulence length scales were 40 times larger than the

size of the helical fillet for the longitudinal components of the flow and 20 times for the other directions.

I_u = Longitudinal turbulence intensity.
I_v = Lateral turbulence intensity.
I_w = Vertical turbulence intensity.
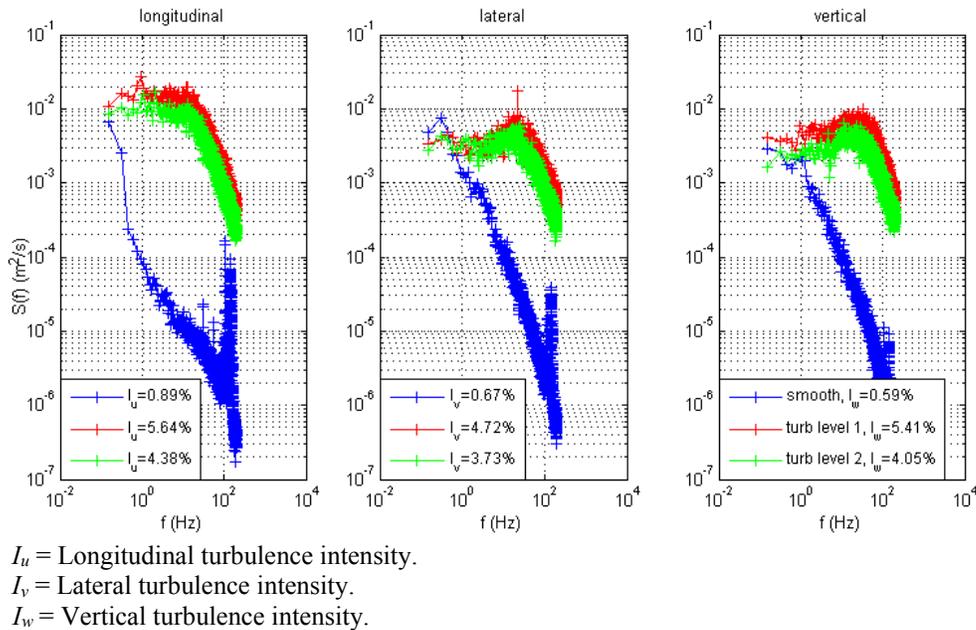
Figure 19. Graph. Variations of the normalized spectral densities of the wind velocity fluctuations with frequencies for the smooth and turbulent flow cases.
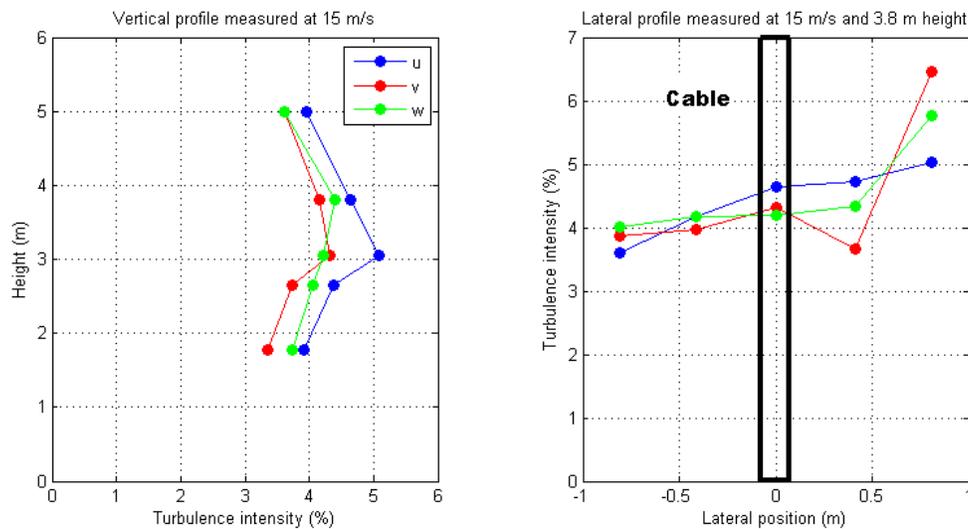
Figure 20. Graph. Vertical and lateral profiles of the intensity of turbulence for the three wind components for the turbulent flow for position 2.

The left graph in figure 20 presents the variations of the turbulence intensity with height at the model location. The turbulence intensity was uniform along the length of the model with the exception of a slight increase at the wind tunnel mid-height corresponding to a region where the grid of ladders had a higher density. The ladders forming the upper part of the grid overlapped with the ladders forming the lower part of the grid over a 1.5-m section at the center of the wind

tunnel. The lateral uniformity of the turbulence (right graph of figure 20) was also acceptable with the exception of an increase in turbulence level near the starboard wall. Within a region of ±4 cable diameters from the model centerline, the flow turbulence can be considered uniform laterally.

CHAPTER 3: EXPERIMENTAL PROCEDURES AND ANALYSIS

TEST PROGRAM

The experiments were carried out in two distinct phases. The focus of the first phase was to identify any potential divergent vibrations for the cable model with a helical fillet at an inclination of 60 degrees for various rotations of the model on its longitudinal axis and spring rotations. In the event that vibrations would be identified in the first phase, the focus of the second phase would be to define the level of structural damping necessary to mitigate the vibrations and to define the effect of adding turbulence to the oncoming flow on the vibrations. In addition, tests in the second phase were to be carried out to look for other divergent vibrations at other inclination angles and spring rotations with the helical fillet in place.

The exploratory nature of the experiments resulted in the original test program evolving over time. The findings of the day were used to define the tests for the next day as well as for the entire duration of the investigation. The original main objective, which was to define the aerodynamics of the cable model fitted with a helical fillet as a function of wind speed and model attitude to the flow, was reached. Tests were added to link the present study with the two previous studies at NRC-IAR on a smooth cable in 2001 and 2008. (See references 4–7.) For this, the helical fillet was removed for the last 4 days of the investigation, and tests on the smooth model in smooth and turbulent flow at 60 degrees were carried out.

Two inclination angles were investigated, 60 and 45 degrees. The former was selected as the prime inclination to study since it was identified in previous experiments as having aerodynamic characteristics in the critical Reynolds number range most likely to lead to instability for a smooth stay cable. The latter was selected since the flow on one side of the model is fully perpendicular to the helical fillet. A large asymmetry in the pressure field was thus anticipated, resulting in a steady across-wind force that could possibly vary within the critical regime.

The test program is outlined in table 4, and a detailed run log is presented in appendix A.

Table 4. Summary of test program for phases I and II.

Day	Run	Inclination (degree)	Spring Rotation (degree)	Cable Rotation (degree)	Case	Comments
Phase I						
1	27, 28	60	0	0	Dynamic	Increasing and decreasing wind speed
2	32, 35, 37	60	0	0, 0, 27.7	Static	Increasing and decreasing wind speed
3	39, 41	60	0	-13.8, 13.8	Static	
	44, 46	60	0	-13.8	Dynamic	46 is a repeat of 44
4	49, 52	60	0	-30, -40	Dynamic	
	56, 60	60	0	-50, -60	Dynamic	
5	63, 66, 67	60	0	-75, -90, -90	Dynamic	67 has decreasing wind speed
	69, 71	60	0	5, 65	Dynamic	
6	73, 75	60	0	50, -90	Dynamic	75 is a repeat of 66
	81, 85	60	0	-90, -86	Static	
7	88, 90	60	0	-88, -92	Static	
	92, 94	60	0	-94, -90	Static	94 is a repeat of 81
8	108	60	0	-90	Dynamic	Medium damping
	118, 122, 123	60	0	-90	Dynamic	High and low damping
	123	60	0	-90	Dynamic	Decreasing wind speed
Phase II						
10	125, 131	60	0, -54.7	-88, -90	Dynamic	
12	136	60	0	-90	Dynamic	
13	137, 140	45	0	0, 90	Dynamic	
	142, 144	45	0	27, -25	Dynamic	
15	149, 152	45	-54.7	-25, 0	Dynamic	
	155	45	-45	-25	Dynamic	
16	159	45	-12.5	-25	Dynamic	
18	163	60	-12.5	-90	Dynamic	Windy
22	167	60	-12.5	-90	Dynamic	167 is repeat of 163
23	176, 178	60	0	-92, -90	Dynamic	
27	197, 199	60	0	-90, -92	Dynamic	Turbulent flow
28	203, 205, 208	60	0	-88, 0, 50	Dynamic	Turbulent flow
30	211, 214	60	0	50, 0	Dynamic	Turbulent, no helical fillet
31	216, 219, 222	60	0	-90, -88, -92	Dynamic	Turbulent, no helical fillet
	225, 226	60	0	-54.7	Dynamic	Turbulent, no helical fillet
32	230, 233	60	0	-57.7, 0	Dynamic	Smooth, no helical fillet
	237, 239	60	0	-2, 2	Dynamic	Smooth, no helical fillet
33	244	60	0	2	Dynamic	Smooth, no helical fillet

248, 250	60	0	-93	Static	Top gap open and sealed
253, 255	60	0	-93, -90	Dynamic	Smooth, no helical fillet
257, 260	60	0	-88	Dynamic	10–90 s sampling
262, 263	60	0	-88	Dynamic	12-22 m/s, ramp up

The spring rotation angles were selected to represent common field conditions based on the relationships defined in 2001.[9] The model inclination (ϕ) and spring rotation (α) relate to stay cable inclination (θ) and the flow yaw angle (β) through the following equations:

$$\cos \phi = \cos \beta \cdot \cos \theta$$

Figure 21. Equation. Model inclination.

$$\tan \alpha = \frac{\tan \beta}{\sin \theta}$$

Figure 22. Equation. Spring rotation.

Using these relationships, a model inclination angle of 60 degree and a spring rotation of -54.7 degrees correspond to a stay cable inclination of 45 degrees and yaw angle of 45 degrees. Table 5 presents the relationships for the other cases where a rotation of the spring plane was carried out during the tests. A negative sign for the spring and cable rotation was related with a clockwise rotation when looking down along the cable axis.

Table 5. Relationship between model wind-angle planes and field conditions.

	Model Experiments		Field Conditions	
Run	Inclination ϕ (degree)	Spring Rotation α (degree)	Inclination θ (degree)	Yaw β (degree)
131	60	-54.7	45	45
149, 152	45	-54.7	30	35
155	45	-45	35	30
159	45	-12.5	44	8
163, 167	60	-12.5	59	11

INSTRUMENTATION

All electronic equipment used for the tests was specifically calibrated for this project or verified by the expert technical staff in conformity with NRC-IAR's quality assurance procedures which are compliant with ISO 9001-2008.

The dynamic pressure in the test section was obtained from two independent pressure measurements using two differential pressure transducers. Two parallel measurements were made for redundancy. The temperature of the flow in the settling chamber and the barometric pressure at the inlet of the test section were also recorded for each run. As described in the section on smooth flow in chapter 2, a test section calibration was carried out to relate the recorded flow characteristics to the wind speed at the model location in the center of the test section.

The sway and heave motion at the extremities of the cable model were measured with laser displacement transducers. Four transducers were used, one pair per each end of the model. The laser sensing heads were placed approximately 250 mm away from the targets fastened to the spring restraining rods. The distance between the sway sensors was 7,116 mm, and the distance between the heave sensors was 7,285 mm. Four accelerometers were also used in parallel with the displacement transducers to provide a redundant monitoring of the motion. The heave and sway motion were calculated by directly averaging the two time histories of displacements per mode. The end-to-end motion in both directions was calculated by subtracting the time histories of the displacement signals at the extremity of the models.

All analogue outputs from the laser transducers and accelerometers were low-pass filtered prior to being sampled simultaneously at frequencies of 500 or 2,500 Hz with a National Instruments® VXI 1629 data acquisition system and LabVIEW® custom-made software. The sampling time was typically 90 s and was increased to 300 s for the damping tests.

Two TFI Cobra Probes were used for the tests in smooth flow to monitor the flow fluctuations. A sampling frequency of 2,500 Hz was used when the signal from the TFI Cobra Probes were recorded and 500 Hz when the probes were not in use. Each probe monitored three components of the flow fluctuations: longitudinal, lateral, and vertical. Both probes had sturdy probe holders cantilevered from the south wall of the test section. One probe was installed at the inlet plane of the test section to monitor the fluctuations of the oncoming flow. The second probe was installed behind the model at the center of the test section to monitor the flow fluctuations in the wake at the same height as the ring 3 pressure sensors. The tip of the probe in the model wake was located 403 mm behind the cable model and 5 mm inboard of the model edge on the port side. The probes had an acceptable frequency response in excess of 1,500 Hz and were capable of capturing low- and high-frequency fluctuations of the flow.

As was done for the 2008 experiments, the cable model was instrumented with 160 pressure taps. The pressure taps were arranged in 4 cross-sectional rings of 32 taps and 2 longitudinal lines of 16 taps as shown in figure 23.[6,7] Four electronic pressure scanners (Scanivalve Inc.® ZOC 33 and ZOC 23b) were embedded directly in the model to keep the length of the pneumatic tubing to a minimum. Lengths of tubing of 1.2 m were used systematically for all taps. The frequency response of each pressure tap and tubing system was measured prior to the 2008 experiments and was reused for this study to correct for the distortion of the pressure signals due to the tubing. A detailed description of the pressure measurements of the 2008 experiments is given in Andersen et al., Andersen, Nikitas et al., and Jakobsen et al. (See references 6, 7, 10, and 11.)
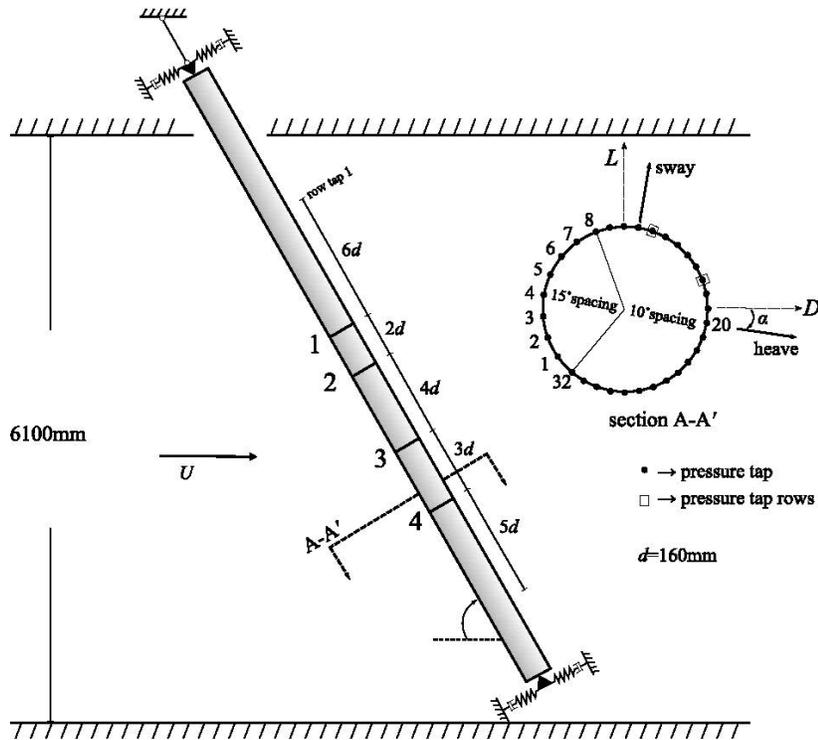
d = Nominal cable diameter of 160 mm.
U = Flow direction.
L = Lift direction.
D = Drag direction.

Figure 23. Illustration. Sketch of the pressure tap arrangement.

The pressure signals from the scanners were monitored using a Scanivalve Inc.® RAD system and a dedicated data acquisition system independent of the National Instruments® VXI 1629 system described previously. The pressure signals were sampled at a rate of 312.5 Hz for 90 s. The analog signals from the laser displacement transducers and the accelerometers were also monitored by the surface pressure data acquisition system to provide synchronous recordings of pressure field fluctuations and corresponding motion of the cable model. In addition, a square wave analog signal was monitored by both the National Instruments® VXI 1629 and the surface pressure data acquisition system to allow a precise synchronization of both systems. This way, the fluctuations of the flow in the wake of the model captured with the TFI Cobra Probe could be associated with the pressure fluctuations at the surface of the cable model.

TEST PROCEDURES

Two types of experiments were carried out during this study: dynamic and static tests. Prior to any testing, a thorough inspection of the cable model was carried out to ensure that dirt, small bugs, or small leaves had not been left on the model from the previous test series. If any were found, the model was systematically cleaned. Inspection of the helical fillet was also carried out to ensure that it remained affixed to the model surface during the experiments. The fillet had a tendency to lift from the surface during cold weather conditions. Figure 24 shows a typical model inspection.

27

Figure 24. Photo. Model inspection in the test section.

For the dynamic tests, a wind-off value of all transducer signals was first recorded with the doors of the wind tunnel test section closed. With the doors open, flow is generally present in the test section given the open circuit of the wind tunnel. Subsequently, the wind speed was increased to a desired value displayed continuously from the data acquisition system, and the model displacements and acceleration were graphically displayed on a screen in the control room. Once a steady state wind speed and model response were reached, the operator started the data acquisition process. Once the 90-s data acquisition was completed, the wind tunnel operator increased the wind speed to the next set point. Small increments of wind speed were used, generally 1 or 2 m/s depending on the observed behavior of the cable model. The wind speed sweeps generally covered the entire range of wind speed possible in the facility, from 4 to 36 m/s in 16 to 18 points. Unless otherwise specified, the wind speed sweeps were carried out with positive increments of wind velocity.

In the event that the wind tunnel operator observed a growth of the vibration after 90 s of data acquisition, a second recording was initiated at the same wind speed. For selected cases at high wind speeds, the motion of the model was manually stopped and released to identify the rate of growth of the oscillations. For some of the same cases, the model was excited manually to a high amplitude, and the decay or growth of the vibrations was monitored for 90 s.

The growth of the motion was first captured by manually preventing the cable model to move, starting the acquisition of the data, and finally letting the model move freely. The decay traces were captured by first manually imposing cable motion with large amplitude in the first sway mode, starting the data acquisition, and finally letting the model move freely. In both cases,

28

traces of the displacement of the cable with time could be analyzed, and aerodynamic damping characteristics could be extracted.

An example of a trace measured for the sway mode for the cable with the helical fillet inclined at 60 degrees and rotated at -88 degrees is presented in figure 25. It only took a few seconds for the cable to start building energy and to vibrate with high amplitude even if the effective sprung mass was as high as 407 kg, and the oscillation frequency was 1.4 Hz. It has been reported that for previous tests done with the same cable model in 2001 and 2008, the aerodynamic response of the cable took much longer to build up. (See references 4–7.) In this present case, the cable was prompt to respond, inferring strong negative aerodynamic damping. The presence of the helical fillet, the wind speed at which the motion took place and the frequency ratio of 1.0 between the sway and heave modes could have had a role to play with this observation.
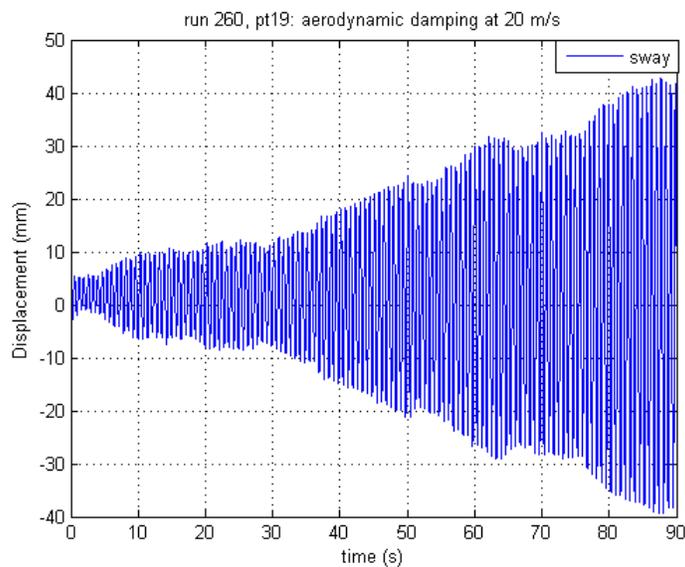
Figure 25. Graph. Growth of the cable model vibration as a function of time inclined at 60 degrees and rotated at -88 degrees.

Another example of an increase of vibrations is shown in figure 26. It corresponds to vibrations in the sway mode for the cable with helical fillet inclined at 60 degrees and rotated at -90 degrees with no spring plane rotation. In this case, the growth of the vibration in the sway end-to-end mode was rapid and appeared to dominate the motion.
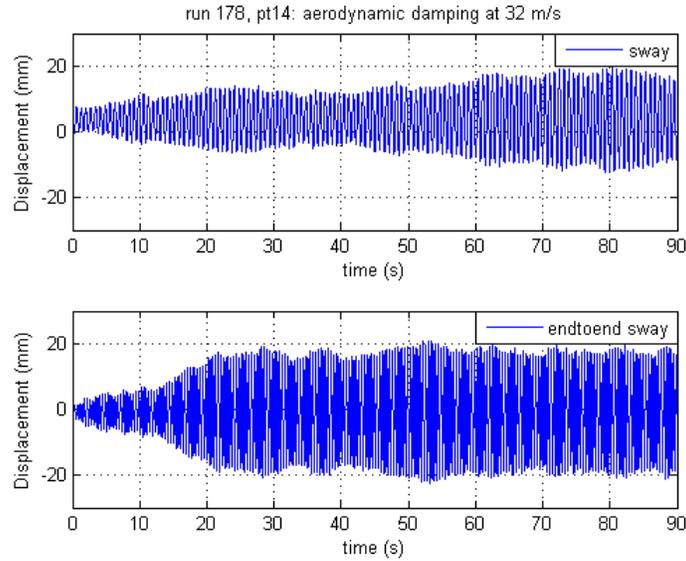
Figure 26. Graph. Growth of the cable model vibration as a function of time inclined at 60 degrees and rotated at -90 degrees.

Each dynamic test took between 1.5 and 2 h. Prior of the dynamic tests, the structural damping of the suspension rig was established through 300-s decay tests in still air. The structural damping of the cable model and suspension system was evaluated in situ by analysis of decay traces. The model was manually excited at its natural frequency in each mode. When the desired amplitude was reached, the model was released to obtain a smooth decay trace using optical displacement transducers at the model extremities. Piece-wise linear fit of the Hilbert transform of the decay signal in blocks of 10 s produced the amplitude of vibration versus damping curve as presented in figure 27.
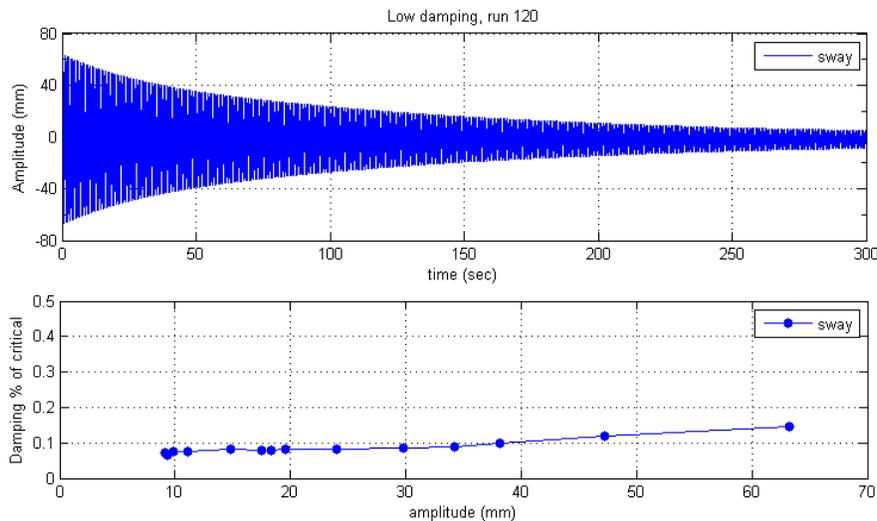
Figure 27. Graph. Example of decay trace for the sway mode of vibration and corresponding variation of damping with amplitude of vibrations.

For the static tests, steel locking pins were inserted at the extremities of the cable model to restrain oscillations. A tare of the surface pressure transducers was carried out with the doors of the test section closed. The wind speed was then increased to a desired value. Once a steady state wind speed was reached, the operator started the data acquisition process. The tests were repeated for 13 to 15 mean wind speeds.

The test program included several rotations of the cable model on its longitudinal axis (see table 4). The following procedures were used to adjust the angle to a prescribed value as illustrated by figure 28:

1. The prescribed angle was marked on the cable model.

2. The locking pins were inserted at the bottom end of the model to prevent sway or heave motion.

3. A self-leveling laser beam was projected along the length of the model to mark its center.

4. The turn-table at each end of the model was unlocked.

5. The model was manually rotated until the mark of the prescribed angle intersected with the laser beam.

6. The turn-table at each end of the model was locked, and the locking pins were released.
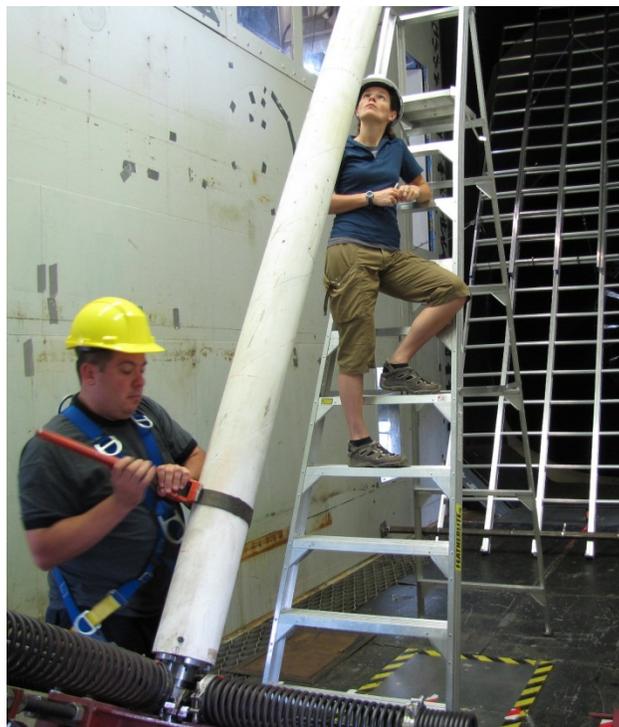
Figure 28. Photo. Procedures followed to set the azimuth angle of the cable model.

DATA ANALYSIS AND REPORTING

Preliminary data reduction was performed at the end of each run using a dedicated MATLAB$^®$ program as follows:

- The tare values were subtracted from the wind-on data.

- The signal was converted to engineering units.

- Wind speed was calculated based on the measured dynamic pressure including corrections for temperature and atmospheric pressure.

- Combination of channels were made (addition or subtraction) to provide sway and heave responses from the displacement and acceleration measurements.

- Statistics (mean, root mean square, maximum, and minimum) were calculated.

- The surface pressure signals were corrected for the distortion caused by the pneumatic tubing, and pressure coefficients were calculated.

- The surface pressure distributions were integrated to calculate mean and fluctuation force coefficients.

- Graphs of response and load coefficients were produced to allow a fine diagnostic of the acquired data as the tests proceeded.

- All time histories were stored in a binary file in MATLAB$^®$ format for each point.

- Natural frequencies and structural damping were extracted from the decay traces.

Post processing of the data using MATLAB$^®$ was carried out. The following additional data reduction was carried out:

- Spectral analysis of all time histories was carried out.

- The modal frequency and structural damping were extracted from each decay test.

- The stiffness of the suspension rig was calculated for each mode, and the cross sectional static mean load coefficients as a function of wind speed were calculated based on the mean displacements of the entire model.

- All processed data were added to the output binary files for further analysis.

- A detailed run summary including frequency and damping estimates was made (presented in appendix A).

CHAPTER 4: RESULTS AND DISCUSSION OF EXPERIMENTS

GENERAL

A two-page graphical summary of the results collected is presented in appendix B for each test run defined in table 4 (see figure 59 through figure 183). For the dynamic tests, the graphs present the variation of the response of the model for four modes of oscillations as a function of wind speed and Reynolds number. The four modes of oscillations are: (1) the sway (across-wind), (2) heave (along-wind), (3) first modes where both ends of the cable model moved in a synchronous manner, and (4) end-to-end modes (sway and heave) where the model extremities were out of phase with each other. The Reynolds number in the graphs is based on the mean wind speed as measured in the frame of reference of the wind tunnel and the cable model mean diameter, $D = 161.7$ mm.

The response given in the graphs corresponds to the maximum amplitude of motion of the cable model both from the displacement transducers and from the accelerometers during a 90-s period at the mean wind speeds indicated in the graphs. For the same period of time and experimental conditions, the graphs in appendix B show the following parameters as a function of Reynolds number as follows:

- The variations of the mean force coefficients, along-wind (C_x) and across-wind (C_y), calculated from integration of the surface pressure for each of the four cross-sectional rings of taps.

- The average of the four sets of mean force coefficients for both directions.

- The static force coefficients calculated from a conversion of the mean cable displacement during a run for each direction to an equivalent mean force based on the dynamic stiffness of the suspension system and normalized by the dynamic pressure and the frontal area of the entire cable model.

- The variations of the mean displacements of the cable model with wind speed.

- The peak factor of the response defined as the maximum amplitude divided by the standard deviation (root-mean-square) of the measured signal.

- The along wind and across wind trajectories of the cable model at a strategically selected wind speed.

- The variations of the longitudinal turbulence level of the oncoming flow as measured at the inlet of the wind tunnel for each of the wind speeds in smooth flow.

When specific test conditions did not apply (e.g., when the cable model was locked for the static tests), the appropriate graphs were left blank.

The two main findings of the first phase of the investigation were: (1) a stay cable with a typical helical fillet and inclined at 60 degrees to the flow can sustain wind-induced vibrations in smooth

flow, and (2) the amplitude of the cable vibrations observed were greatly influenced by the geometry of the HDPE tube, whereby a rotation of the cable model on its longitudinal axis could translate into vibrations with unacceptable amplitudes or vibrations with small amplitude. The first finding is new (i.e., it has not been reported elsewhere). It was not expected since the general belief was that the helical fillet would reduce the sensitivity of the aerodynamics of the model to Reynolds number effects in the critical regime, which is believed to be a primary cause of inclined cable galloping. It might explain observations of stay cable vibrations of cables with a helical fillet in dry conditions as reported in field measurement campaigns. The oscillations were not caused by buffeting due to turbulence and were similar to high reduced velocity vortex shedding.[4] The oscillations occurred in some cases at higher wind speeds than what were reported earlier for a smooth cable, in a Reynolds number range above what is generally considered the critical range for which the static coefficients do not vary significantly with wind speed.

The second finding is also unique and strongly affected the course of the tests. However, it was anticipated based on the observations reported by Flamand and Boujard who pointed out the systematic deviation of general HDPE tubes from a circular shape and its possible corresponding consequences on the mean aerodynamic force coefficients.[8] The test cable cross sectional shape exhibited the same type of asymmetry as measured at four longitudinal positions (see figure 4). The measurements showed deviations of up to 1 percent of the mean cable diameter. The location of the deviations around the circumference appeared to be consistent along the length of the model, suggesting that they were formed during the extruding process of the HDPE tube or during its long-term storage. If an asymmetric pressure distribution can be observed on a smooth round model in the critical regime due to the formation of a small laminar separation bubble on one side of the model and not on the other, as reported in Larose et al., it is understandable that a mildly asymmetric cable shape will have complex aerodynamic properties in the same critical Reynolds number regime.[12]

Based on the second finding, it was concluded that each time the cable was rotated on its axis, a new shape was exposed to the flow, and a different behavior could be expected. This affected the test program greatly since originally it was planned to rotate the cable model on its axis at four azimuths, 0, 13.8, -13.8, and 27.7 degrees, to obtain a clear understanding of the mean force coefficients based on the integration of the surface pressures at four rings. These four azimuths were selected so that three of the four rings of pressure taps for each azimuth would be located at three different cross-sectional locations in relation to the helical fillet.

In four cable rotations, 12 different cross sections of the model with helical fillets would have been covered. Assuming that the model was symmetric, it was believed that a reliable representation of the quasi-steady aerodynamics of cable model would come from the average of cross-sectional coefficients of the four rings for four azimuths (i.e., the average of 16 measurements). However, since the cable model was not symmetric, this averaging across the four azimuths was not sufficient to represent the aerodynamics of the entire model. Several of the static tests, designed to provide the quasi-steady aerodynamics of the cable model, were replaced by dynamic tests at various additional model rotations.

INFLUENCE OF THE ATTITUDE OF THE CABLE TO THE MAIN WIND FLOW

Influence of the Cable Rotation

As described in the "Suspension System" section in chapter 2, a new feature of the mechanical setup of the cable allowed for the rotation of the cable along its main axis without changing the spring plane angle, therefore not affecting the wind-angle plane and the main direction of motion of the cable. An evaluation of the response of the cable for different angles of rotation was carried out. While the original plan was to perform only a few angles to identify the azimuth for which the largest response of the cable was observed, the differences in the results led to a reconsideration of the number of azimuth angles to be selected for performing the measurements.

In fact, for the cable with the helical fillet and inclined at 60 degrees, in smooth flow 13 rotations of the cable were carried out from -92 to 65 degrees. Significant vibration of the model in the sway mode was observed for the cable rotated at angular positions of -92, -90, and -88 degrees. The angular position was defined as being 0 degrees when pressure tap 4 was the stagnation point, and a negative angle was associated with a clockwise rotation of the cable from a top view perspective. The 0-degree azimuth defined in this manner corresponded to the same 0 degrees of the 2001 and 2008 studies. (See references 4–7.) Large amplitude displacements in the first sway mode (across-wind) on the order of 30 to 75 mm were observed in the vicinity of -90 degrees but did not occur for the other rotations examined. Figure 29 shows the amplitude of motion in sway obtained for four different angles of rotation of the cable.
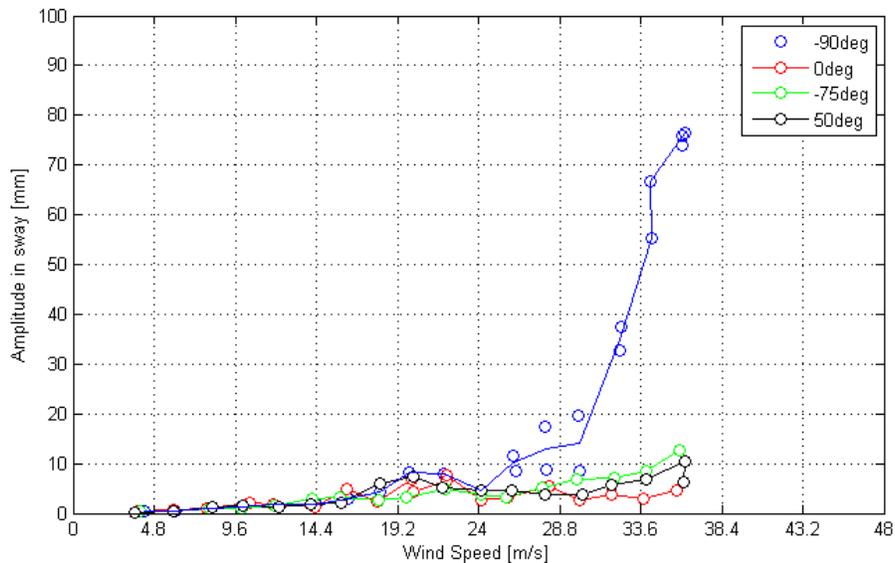
Figure 29. Graph. Amplitude of motion in sway for four different rotations of the cable along its main axis for the cable inclined at 60 degrees with helical fillet and in smooth flow.

The azimuth angles were picked through inspection of the cross-sectional profiles of the cable model shown in figure 4. It was theorized that a point of inflection in the cross-sectional profile that would be located in the vicinity of the point of separation of the boundary layer at the surface of the model could have an influence on the response, especially if this point of inflection was not symmetric between the two sides of the model. With figure 4 as a reference, when the

azimuth of the model was set at -90 degrees, the point of inflection in the profiles centered at azimuth 4 degrees was at 94 degrees from the stagnation point and therefore likely near the area on the cable model where separation of the boundary layer could be expected. This surface deformation could have caused the boundary layer to separate earlier or later on one side of the cable or the other, creating fluctuating across-wind forces due to the motion of the model and undefined possible instabilities.

It is difficult to attribute the variation in the response of the cable model solely on its orientation or attitude to the flow as other factors might have contributed to affect the response. However, there is evidence that around a certain range of cable rotations, the model appeared to be more lively, inferring stronger wind excitation, stronger buildup of energy, and larger vibrations.

A similar verification of the influence of the model orientation on the wind induced response was carried out for the other configurations of the cable (i.e., in turbulent flow or for the cable without the helical fillet). Fewer angles of rotation were tested to evaluate the response of the cable under these other conditions and surprisingly, it was not only around -90 degrees that the cable moved considerably but also around 0, 50, and -54.7 degrees. Under the circumstances of this study, it is therefore difficult to predict the worst response of a stay cable without performing systematic measurements at multiple azimuth angles (over the 360-degree range) as the cable and its HDPE tube are not perfectly round and its behavior appeared to be strongly dependent on its attitude to the main direction of the wind. This conclusion also applies to a stay cable in turbulent flow or without a helical fillet since all those configurations have shown that the cable can give a different response depending on its angle of rotation. It is possible that larger sway vibrations could have occurred for the cable model of this study with rotation beyond the -94 to +65 degrees that was covered. It was out of the scope of work to look for the extreme response in relation to this parameter.

Influence of Cable-Wind Angle Plane

The baseline position of the upper and lower four-spring planes was 0 degrees, with four springs allowing mostly across-wind motion and four springs allowing mostly along-wind motion. The system of spring-planes could be rotated equally at the top and bottom of the cable model to modify the trajectory that the model would take in relation to the main flow direction, referred to here as the "cable-wind plane." As for the 2001 and 2008 studies, it was possible to adjust the cable-wind plane to any desired values. (See references 4–7.) However, thanks to the new cable model turntables, it was possible to modify the cable-wind plane without affecting the attitude of the cable model to the flow. Both parameters (cable-wind plane and rotation of cable on its axis) could be changed independently, allowing the evaluation the effect of the cable-wind plane only on the response of the cable.

Tests were performed with the cable inclined at 60 degrees in smooth flow with the cable rotated at -90 degrees where strong vibrations were observed for a cable-wind plane of 0 degrees. The cable-wind angle plane was changed to -54.7 and -12.5 degrees. The angle of rotation of the spring plane was negative for a clockwise rotation of the system from a top-down point of view. The first angle of the spring plane of -54.7 degrees was chosen because it represents, in combination with a 60-degree inclination of the cable, a configuration identical to a 45-degree inclination and 45-degree yaw of the cable, which is of interest for cable stay bridges as defined

in table 5. This cable-wind plane was also studied in 2001 and 2008. (See references 4–7.) The second spring angle of -12.5 degrees was selected based on the motion path of the cable observed when the spring angle was at 0 degrees; the cable was not moving perfectly in the across-wind direction but rather at -12.5 degrees from the across-wind axis (see figure 107 in appendix B).

Tests were performed for both additional cable-wind planes, keeping the angle of rotation of the model on its axis at -90 degrees. The tests indicated that the response of the cable was different depending on the spring plane angle. At 0 degrees, the cable was moving strongly with displacement around 75 mm at 36 m/s, while for the spring angle of -54.7 degrees (run 131), the cable was not oscillating significantly. This clearly demonstrated the importance of the relative angle between the motion of the cable and the wind, as anticipated by Macdonald and Larose.[13]

For a spring angle of -12.5 degrees, two runs were performed. The first one (run 163) did not result in significant vibration of the cable, while the second run (run 167) had large amplitude displacements of 50 mm in the sway mode for the wind speed range of 22 to 36 m/s (see figure 30). The difference between the responses of the cable for those two runs is believed to be associated with the flow disturbance coming from outside of the test section. The first run was carried out during a very windy day, which affected the turbulence intensity of the oncoming flow on the cable, especially for wind speeds lower than 20 m/s. The longitudinal turbulence intensity was above 1 percent for speeds below 20 m/s. The variations of the mean wind speed due to this turbulence can affect not only the response of the cable for the low mean wind speeds but also the susceptibility of the cable motion to build and to undergo larger vibration at higher wind speed. The second run (run 167) was performed during a relatively calm day, with a longitudinal turbulence intensity measured at the entrance of the test section lower than 1 percent for wind speeds higher than 5 m/s. Large displacements were observed, but the amplitudes did not exceed the amplitudes observed for a cable-wind plane of 0 degrees.
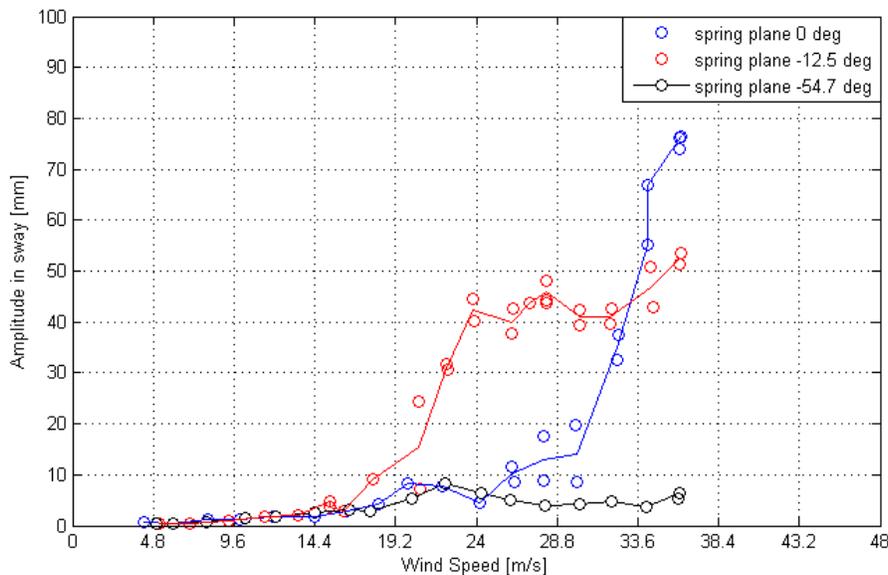
Figure 30. Graph. Amplitude of motion in sway for three different spring plane rotations for the cable inclined at 60 degrees with helical fillet and in smooth flow.

Additional analysis of the turbulence characteristics and its potential influence on the cable vibrations, which is beyond the scope of the present study, is recommended for these cases.

Influence of Cable Inclination

As part of the second phase of the investigation, the inclination of the model was changed from 60 to 45 degrees (see figure 31). Comparison of the results obtained for both cable inclinations with the same cable rotation (-90 and 0 degrees) and cable-wind plane (0 degrees) was performed. It can be observed in figure 59, figure 106, figure 114, and figure 116 in appendix B that the inclination of the cable did affect the response of the cable for a rotated angle of -90 degrees. At a 45-degree inclination, the cable did not oscillate significantly as it did for the cable inclined at 60 degrees where 75 mm amplitude displacement were observed at 36 m/s. At a 0-degree rotation of the model, no significant vibrations were observed for both cable inclinations.

Figure 31. Photo. Cable model at 45-degree inclination and 0-degree spring rotation with smooth flow.

The mean force coefficients calculated from each ring of surface pressures revealed that the cable inclined at 45 degrees showed much less variation of the mean C_y as a function of Reynolds number compared to the cable inclined at 60 degrees (see figure 32). This observation was consistent with the mean C_y, which presented large variations for wind speeds lower than 19 m/s, showing negative and positive values for the case of the cable at 60 degrees inclination. At 45 degrees, C_y was stable with a more-or-less constant value between 0.2 and 0.5.
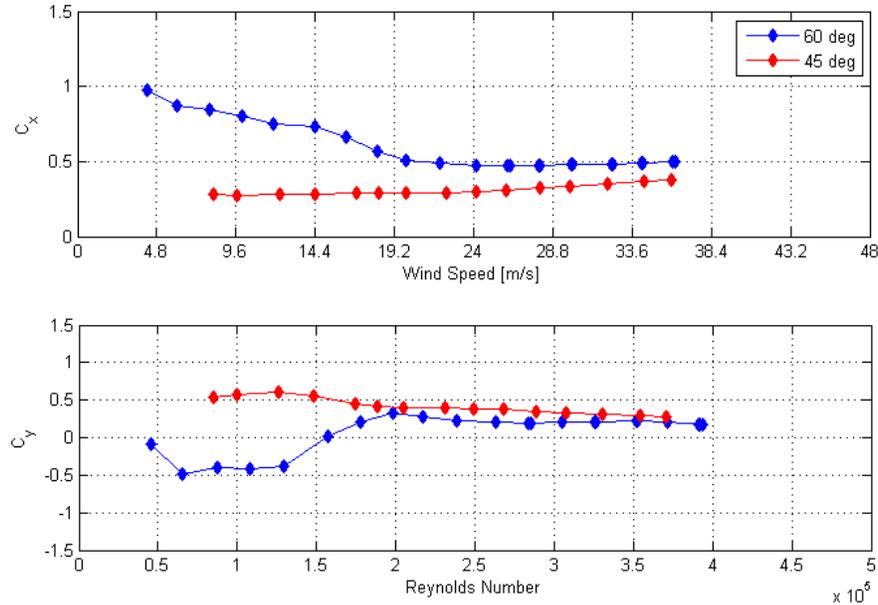
Figure 32. Graph. Mean force coefficients calculated from the integration of surface pressure measurements for the cable inclined at 60 and 45 degrees and rotated at -90 degrees along its main axis in smooth flow and with a helical fillet.

Several other tests were carried out for a cable inclination of 45 degrees with the helical fillet in place to look for galloping or other wind-induced vibrations. The model was rotated on its axis (-90, 0, 23, and -25 degrees) and the spring plane was also rotated (-54.7, -45, and -12.5 degrees). No significant wind-induced vibrations were observed for a wind speed range of 4 to 36 m/s for these cases. Since the cable model experienced more variations of its cross-sectional force coefficients and larger amplitude of motion at 60-degree inclination, the focus of the second phase of the study was defined to investigate the factors that affect the behavior of the cable only for a 60-degree inclination.

INFLUENCE OF STRUCTURAL DAMPING

As reported earlier, tests at an inclination of 60 degrees with the helical fillet in smooth flow revealed large oscillations of the cable model in the sway modes at several wind speeds. Experiments were subsequently carried out to define the level of damping necessary to mitigate the vibrations. As per the 2001 tests, the structural damping of the suspension system was first increased by wrapping viscoelastic material (rubber bands) around the active coils of the springs (see figure 33).[4,5] Several rubber bands had to be used to increase by 66 percent the damping level. To obtain a larger increase of the damping level, adding rubber bands was not sufficient to reach a damping level corresponding to a Scruton number (*Sc*) of 5.0 or more. Scruton number is defined in figure 34.

Figure 33. Photo. Elastic bands used to increase the structural damping of the suspension system.

$$Sc = \frac{m\zeta}{\rho d^2}$$

Figure 34. Equation. Scruton number.

Where:

m = Mass per unit length of the model.
ζ = Damping ratio (fraction of critical damping).
ρ = Air density.
d = Mean diameter of the model.

A Scruton number of 5.0 is used as a reference value by the Post-Tensioning Institute guidelines as the mass damping parameter level necessary to mitigate rain/wind-induced vibrations of stay cables with a helical fillet.[1] To reach a Scruton number greater than 5.0, washers covered with a visco-elastic material were inserted between the suspension rig frame and the locking nuts of the threaded rods that were used to control the tension in the springs (see figure 35). It was observed that the damping level of the suspension system was sensitive to the level of contact between the locking nuts and the frame, with a larger contact lowering the damping. By reducing the contact pressure through the compression of a viscoelastic material, the level of damping was increased to the desired value in a repeatable way.

Figure 35. Photo. Viscoelastic washer used to increase the structural damping of the suspension system.

Figure 36 and figure 37 show the variations of structural damping with amplitude for the three levels of damping examined for both the sway and heave modes respectively. The damping level were referred as follows:

- **Low**: 0.08 percent at an amplitude of 30 mm ($Sc = 1.6$).

- **Medium**: 0.15 percent at an amplitude of 30 mm ($Sc = 3.0$).

- **High**: 0.25 percent at an amplitude of 20 mm ($Sc = 5.1$) for the sway mode, and 0.10 and 0.15 percent for the heave mode at amplitudes of 10 mm.

The graphs showing the actual decay traces for each case are presented in appendix B (see figure 184 through figure 186).
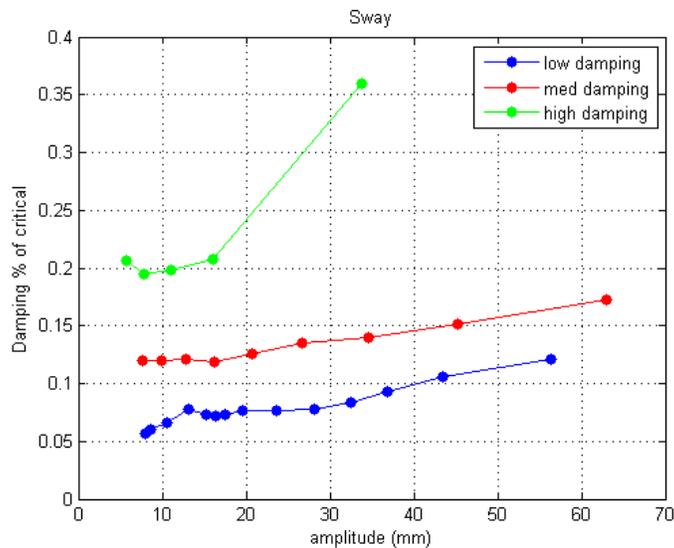
Figure 36. Graph. Structural damping level as a function of amplitude of motion of the cable for the sway mode.

41
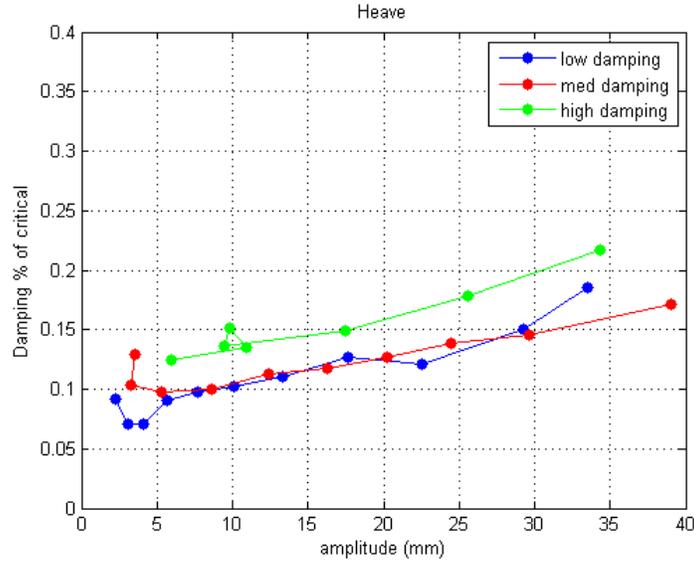
Figure 37. Graph. Structural damping level as a function of amplitude of motion of the cable for the heave mode.

Figure 38 shows the response of the cable for three different levels of damping. The cable was oriented at 60 degrees from the horizontal with a wind-angle plane of 0 degrees. The cable was rotated along its main axis to -90 degrees with the helical fillet and in smooth flow.

The graphs on the left side of figure 38 indicate the amplitude of motion as detected by the laser displacement and by the accelerometers. The amplitudes were obtained by averaging the maximum and minimum displacement or acceleration. Results indicate that a structural damping level of 0.25 percent (Sc = 5.1) in sway allowed a reduction the amplitude of displacement from 75 to 25 mm or from 7 to 2 m/s^2 at the maximum wind speed of 36 m/s. The graphs on the right side of figure 38 show that the mean forces acting on the cable (drag and lift force in the cable axis reference) were not significantly affected by the variation of damping level.

Figure 38 also presents results associated with a repetition of the same configuration at the low damping level case. It can be observed that the maximum amplitude of displacement was not repeated for both low damping level cases. One of the reasons could be linked with the variation of the turbulence intensity of the oncoming flow due to the wind conditions outdoors. The first test where large amplitude was observed was done on a calm day (run 122) with longitudinal turbulence intensity generally low (0.5 percent from 19 to 36 m/s), while the repeat test where low amplitude was observed (run 178) was done on a windy day with more variation of the turbulence intensity as measured at the entrance of the test section and presented in figure 107 for run 122 and in figure 139 for run 178 (see appendix B).
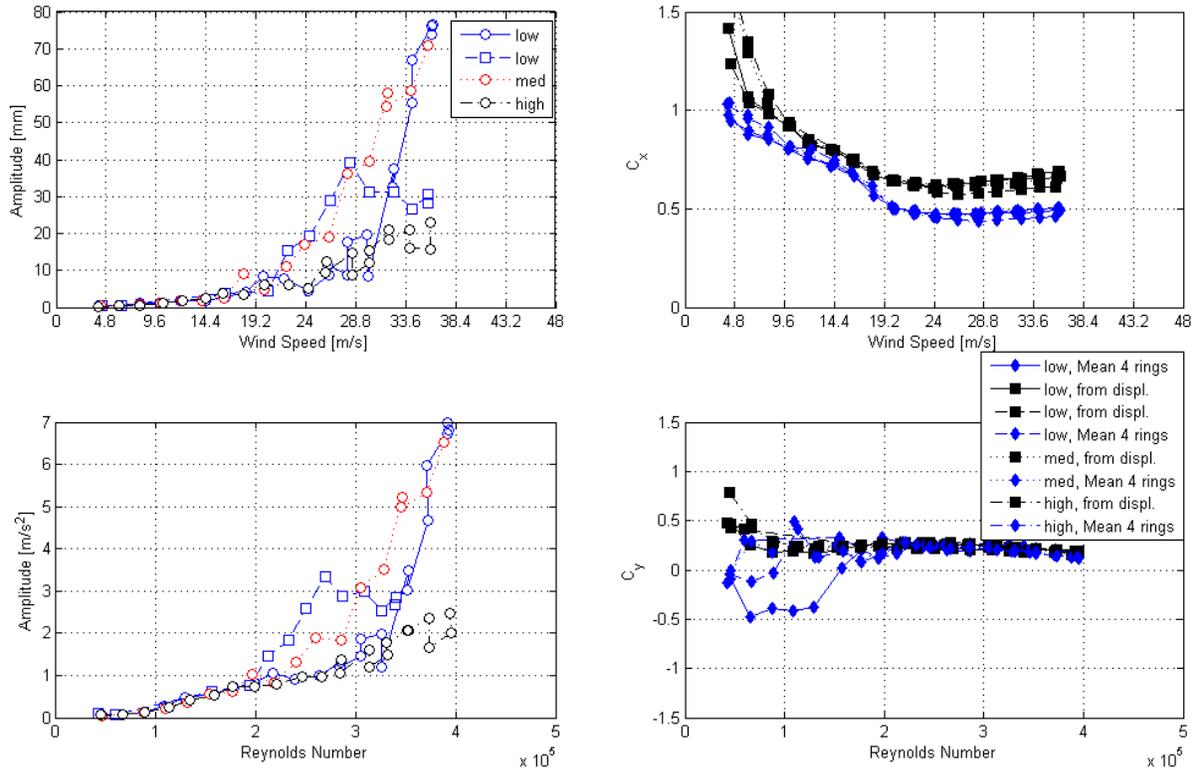
Figure 38. Graph. Response of the cable model as a function of wind speed or Reynolds number for three damping levels as measured by lasers, accelerometers, and surface pressures for different levels of damping.

No other tests were carried out during the present investigation to evaluate the level of damping needed to mitigate the observed vibrations.

INFLUENCE OF TURBULENCE

Several tests were conducted in turbulent flow for the test section configuration described in the "Turbulent Flow" section in chapter 2 and shown in figure 39. The effect of wind turbulence on the response of the cable rotated at -90 degrees is presented in figure 40 through figure 43 for the cable with and without the helical fillet, respectively. The results indicate that a 4 to 5 percent intensity of turbulence was not sufficient to mitigate the large vibration of the cable in the sway mode that was observed in smooth flow condition for a cable rotation on its axis between -88 and -92 degrees for the cable with or without a helical fillet. The turbulence seemed to reduce the amplitude of motion, and the vibrations took place at a lower wind speed compared to the smooth flow condition when the helical fillet was present.

However, large vibrations were observed in turbulent flow at higher wind speeds in the end-to-end sway mode that were not present in smooth flow. The same observations were made for the cable without the helical fillet; end-to-end sway motion was strong and present for many of the configurations investigated in turbulent flow. It was accompanied by oscillations in the first sway mode, which were strong not only for cable rotations of -90 and -88 degrees but also at -54.7, 0, -2, and 2 degrees for the cable model without the helical fillet and at an inclination of 60 degrees.

43

The turbulence had a pronounced effect on the cross-sectional force coefficients, both for the cable model with the helical fillet and for the smooth cable. The effect was similar for the two cases, as illustrated in figure 41 and figure 43, for a cable inclination of 60 degrees and model rotation of -90 degrees.

For the case with the helical fillet, the turbulence reduced the velocity at which C_x reached its minimum by approximately 10 m/s. The rate of change of C_x with Reynolds number appeared to be slightly larger in turbulent flow than in smooth flow for parts of the drag crisis. Note that the larger the rate of change of the coefficients with Reynolds number, the higher the possibility of wind excitation from a quasi-steady aerodynamics point of view.

The turbulence appeared to have eliminated or at least greatly reduced the strong asymmetric pressure distributions in the wind speed range from 5 to 15 m/s that were causing the mean C_y to reach values around -0.45 in smooth flow. This can be considered as a stabilizing influence.

For the case of the smooth cable, the turbulence reduced (with even a larger margin) the velocity at which C_x reached its minimum. The lowest C_x was reached at a velocity 16 m/s lower in turbulent flow than in smooth flow. As for the case with the helical fillet, the rate of change of C_x with Reynolds number appeared to be slightly larger in turbulent flow than in smooth flow. For C_y, the smooth cable had a positive C_y of 0.5 at a velocity of 19 m/s in smooth flow. This positive value was eliminated almost completely by the turbulence with the exception of a small region with $C_y \approx 0.2$ at 8 m/s.

Figure 39. Photo. Cable model at 60-degree inclination and 0-degree spring rotation in turbulent flow.

44
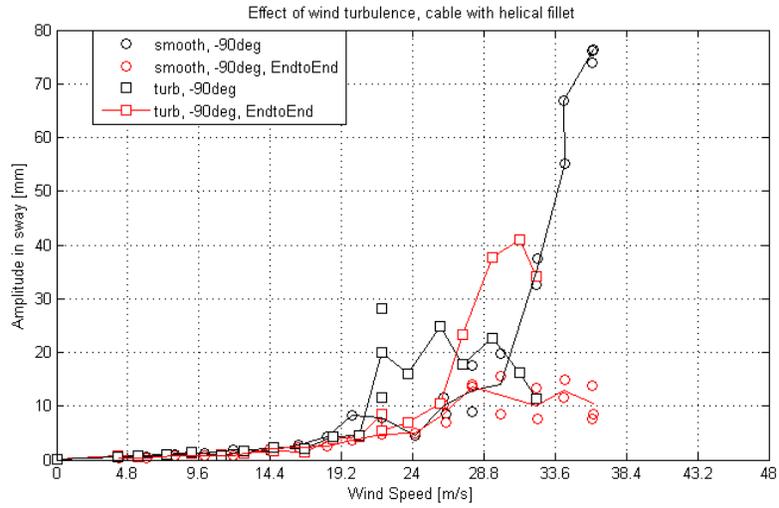
Figure 40. Graph. Amplitude of motion in sway and end-to-end sway at cable rotation of -90 degrees and inclined at 60 degrees with a helical fillet in smooth and turbulent flow.
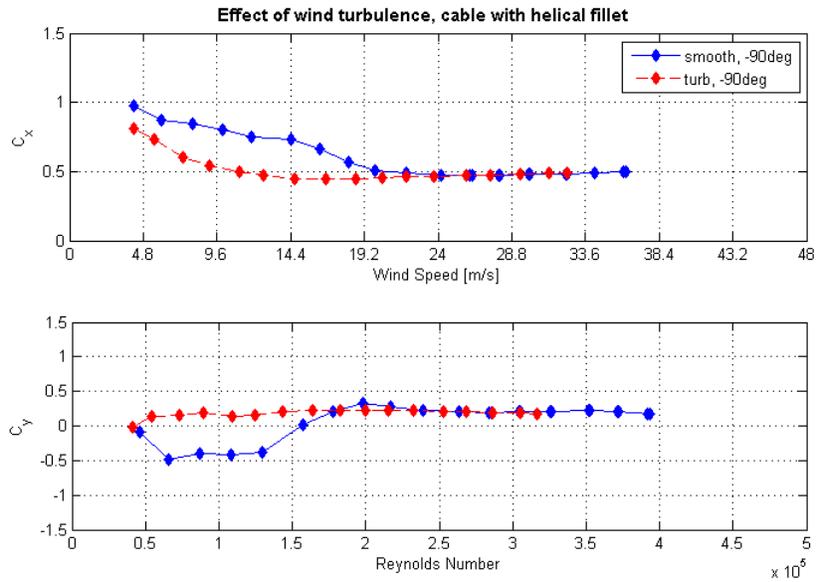
Figure 41. Graph. Mean force coefficients at cable rotation of -90 degrees and inclined at 60 degrees with a helical fillet in smooth and turbulent flow.

45
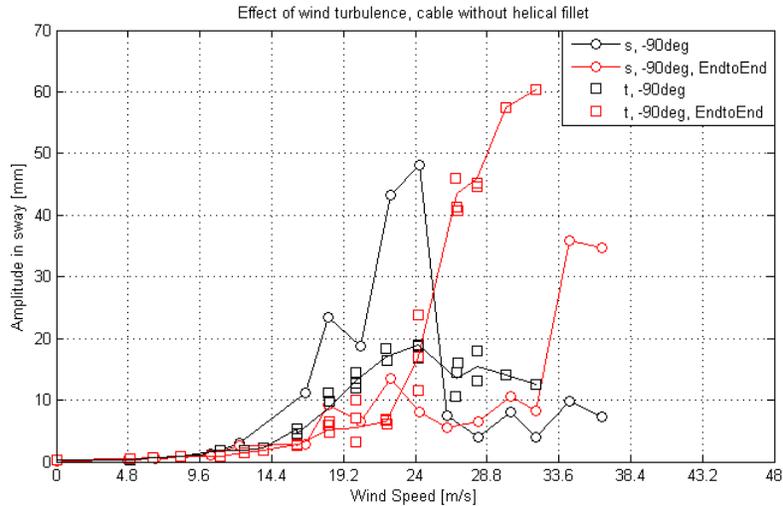
Figure 42. Graph. Amplitude of motion in sway and end-to-end sway at cable rotation of -90 degrees and inclined at 60 degrees without a helical fillet in smooth and turbulent flow.
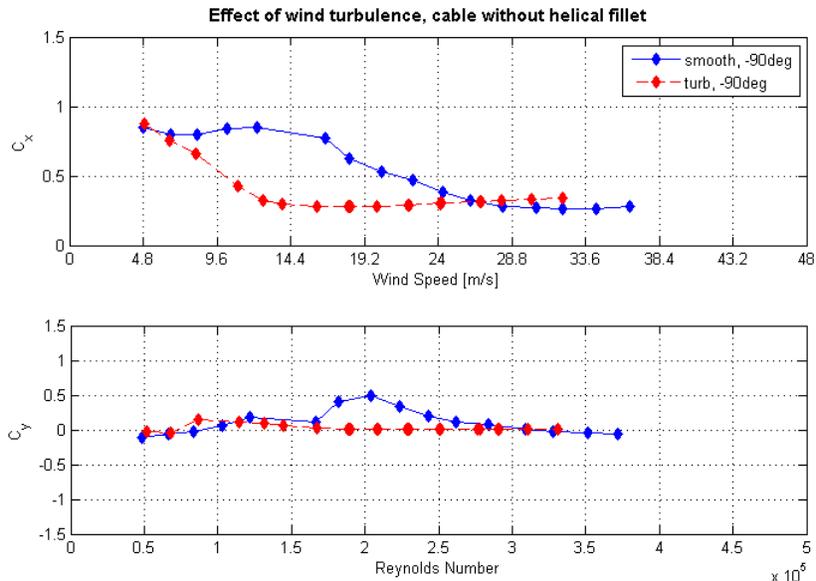
Figure 43. Graph. Mean force coefficients at cable rotation of -90 degrees and inclined at 60 degrees without a helical fillet in smooth and turbulent flow.

INFLUENCE OF THE HELICAL FILLET

The helical fillet did not mitigate the vibration of the cable. Figure 40 and figure 42 show examples of the response of the cable for different conditions with and without the presence of the helical fillet, respectively. Figure 44 and figure 45 present the results associated with the effect of the presence of the helical fillet for cable rotated at -90 and 0 degrees in smooth flow and the effect of the helical fillet on the mean force coefficients observed for the case at 0 degrees. Sinusoidal wind-induced vibrations were observed independent of the helical fillet. However, the amplitude of vibrations was in general lower when the fillet was in place, and the vibrations occurred at a higher wind speeds.

46
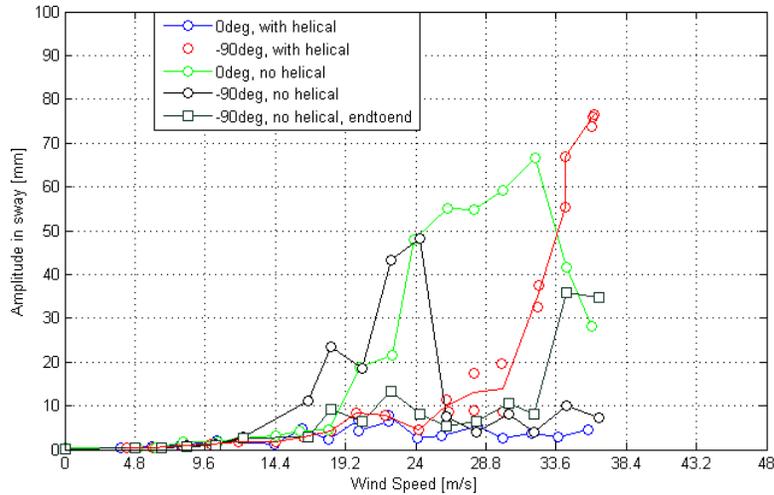
Figure 44. Graph. Amplitude of motion in sway and end-to-end sway for cable rotated at -90 and 0 degrees and inclined at 60 degrees in smooth flow with and without a helical fillet.
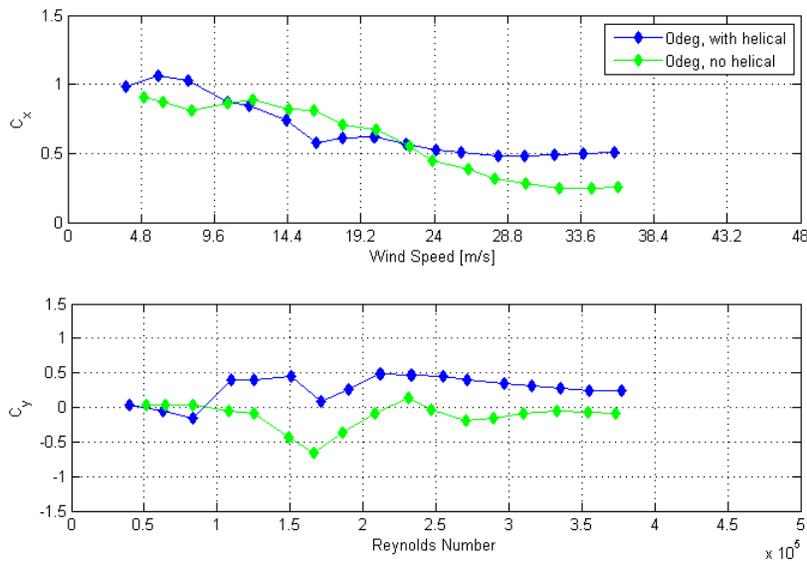
Figure 45. Graph. Mean force coefficients for cable rotated at 0 degrees and inclined at 60 degrees in smooth flow with and without helical fillet.

The helical fillet shifted the critical Reynolds number regime to lower wind speeds similar to the effect associated with an increase of surface roughness. The rate of change of both the along-wind and across-wind mean force coefficients with Reynolds number was found to be lower with the helical fillet in place. Nevertheless, large vibrations were observed for the cable model inclined at 60 degrees with the helical fillet in smooth flow over a range of Reynolds number where the coefficients did not change rapidly with wind speed. This is opposite to observations made during previous studies on the same model, where the change of the coefficients with Reynolds number was identified as the primary cause of the cable vibrations, in particular when the static coefficient curves reached a point of inflection as a function of Reynolds number, as clearly demonstrated by Andersen.[7] It can thus be inferred that the local increase of surface

47

roughness of the cable model due to the presence of the helical fillet had an influence on the excitation mechanism.

INFLUENCE OF MOTION ON THE MEAN AERODYNAMIC FORCE COEFFICIENTS

For selected configurations, it was possible to compare the mean force coefficients for the model locked in a static position to the coefficients when the model was free to respond to wind excitation using the spring suspension system. In general, for cable rotation angles of -92, -90, and -88 degrees, the mean C_y proved to be similar between the stationary model case and the moving model case for the model with a helical fillet in smooth flow at 60 degrees inclination. However, locally, the four different rings did not show similar distributions of surface pressures for the two cases. Figure 46 and figure 47 show the mean surface pressure distribution at approximately 11.5 m/s for the cable rotated at -90 degrees and in a static position and for the cable in motion (dynamic). The pressure around the four rings was not evenly distributed and that more surface pressure taps would be required to accurately predict the mean forces acting on the entire cable length. For the static cable, the negative lobe of pressure due to the laminar separation bubbles was active over a larger surface of the cable, and the magnitude was larger than for the case when the cable was in motion.
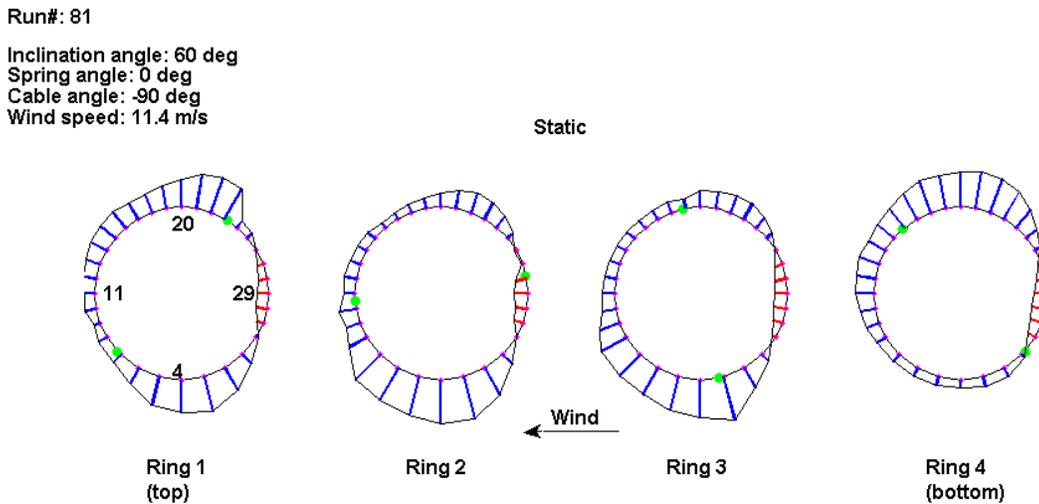
Figure 46. Illustration. Distribution of surface pressure coefficient for the four rings with the cable in a static position (run 81).
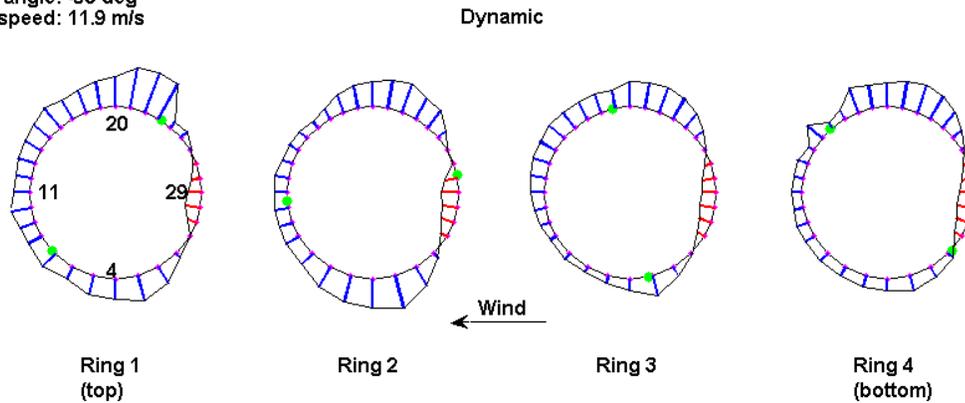
Figure 47. Illustration. Distribution of surface pressure coefficient for the four rings with the cable in motion (run 122).

Tests with the cable in a static position were also conducted to identify possible galloping using the Den Hartog criterion. Figure 48 shows the mean C_x and C_y calculated from the surface pressure distribution on the four rings as a function of wind angle for the cable in static position and as a function of wind speed for the cable in motion. A negative slope of C_y with cable rotation was depicted between -94 and -92 degrees. However, this slope was not large enough to satisfy the Den Hartog criterion.
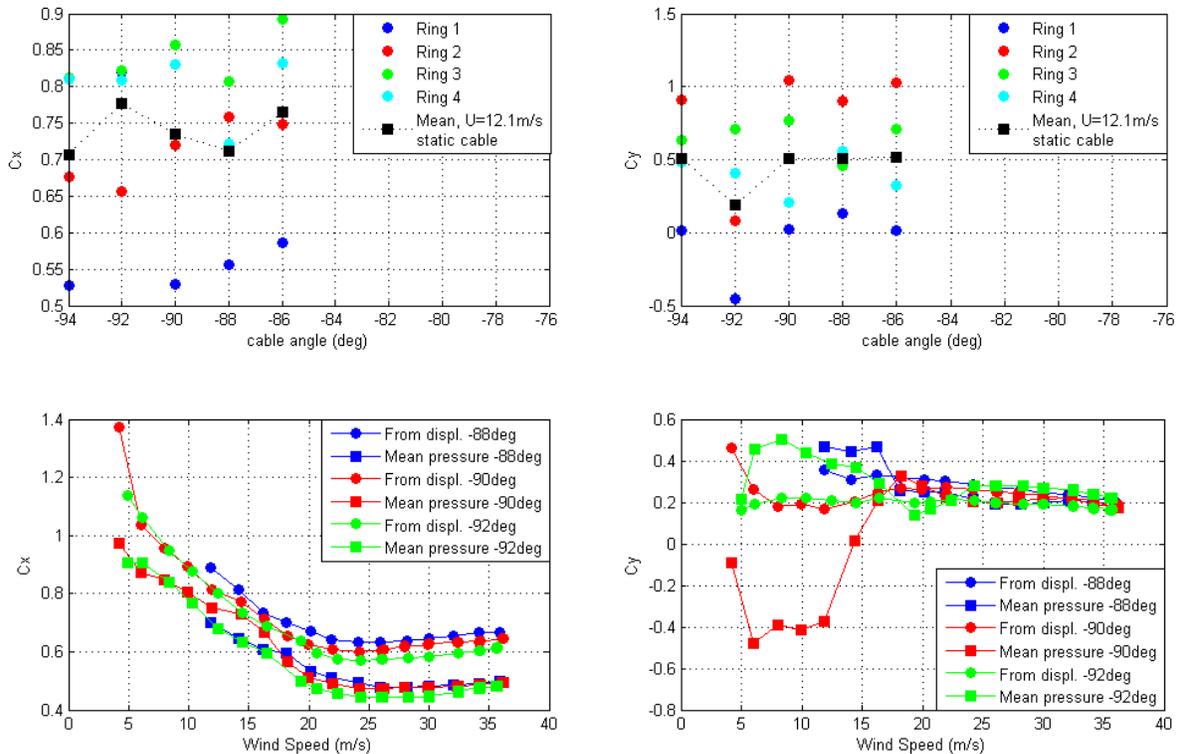
Figure 48. Graph. Mean force coefficients as a function of cable rotation for the static cable and as a function of wind speed for cable in motion.

INFLUENCE OF THE END CONDITIONS AT THE TOP OF THE CABLE MODEL

Tests were conducted with the cable in a static position with the gap at the top of the cable open and sealed. The gap is necessary to allow the cable to move freely during dynamic test. The size of the opening was selected based on the amplitude of vibration expected. However, this opening has an impact on the flow around the cable near the roof of the test section. To evaluate the effect of this opening on the mean force coefficients as calculated from the surface pressure distributions, the gap was left opened and then sealed, as illustrated in figure 12 and figure 13. Results presented in figure 174 and figure 175 in appendix B indicate that C_x and C_y were not affected by the end conditions of the model, at least not for the region of the cable where the pressure rings were located.

It should be noted that the four rings of pressure taps are far (11 to 17 cable diameters) from the top of the cable where the opening is located. Therefore, the surface pressure distribution at those four locations might not have captured the difference in the flow field that is locally affected at the top of the cable. Adding rings of pressure taps along the main axis of the cable would have helped to better estimate the mean force coefficient acting on the entire cable length. The verification of the influence of the end conditions was carried out in smooth flow for the cable model without helical fillet at an inclination of 60 degrees corresponding to the test conditions of the 2001 and 2008 experiments. (See references 4–7.)

50

RELATIONSHIP BETWEEN THE SURFACE PRESSURES AND THE WAKE SIGNATURE

A TFI Cobra Probe was installed directly downwind of pressure ring 3 to look for any correlation between the surface pressure and the wake characteristics. The position of the TFI Cobra Probe in relation to the model is crucial to capture wake characteristics associated with flow phenomena of the separated shear layers. The appropriate position would be a function of Reynolds number, the trajectory of the motion, and the cable rotation. In light of all the possible ideal probe positions and time limitations, it was decided to set the probe at a fixed position during the entire test. The position was considered appropriate to capture the flow shed in the wake: wake of ring 3, on the tip of the probe 403 mm (2.5 cable diameters) behind the cable model, and 5 mm inboard of the model edge on the port side (south side). Figure 49 shows the TFI Cobra Probe as positioned relative to the model.

Figure 49. Photo. TFI Cobra Probe placed in the wake of the cable model directly behind ring 3 of pressure taps.

Spectral analysis of selected pressure ports located on the port side of the cable along with a spectral analysis of the signal captured by the probe in the wake have indicated that a relationship can be established for some cases. Figure 50 presents the spectrum of the longitudinal wind speed measured with the TFI Cobra Probe and the spectrum of pressure port 30 on ring 3 for a wind speed of approximately 24 m/s (run 178). These spectrums were obtained from a dynamic test featuring the model with a helical fillet in smooth flow. Both spectrums showed a peak of energy at about 1.5 and 2.1 Hz, corresponding to the frequencies of oscillation of the cable model. A detailed study of the relationships between unsteady pressure fluctuations, the cable motion, and fluctuations in the wake is beyond the scope of the present report.
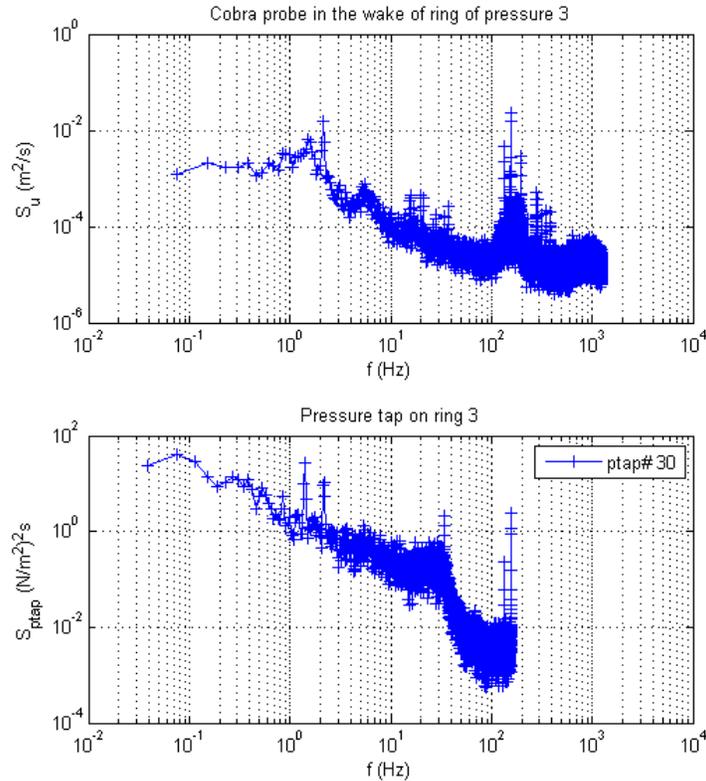
Figure 50. Graph. Spectrum of the longitudinal flow velocity fluctuations located in the wake of the model and spectrum of the surface pressure signal of port 30 on ring 3 with a wind speed of 24 m/s.

GENERAL CHARACTERISTICS OF MEAN FORCE COEFFICIENTS WITH REYNOLDS NUMBER

The mean C_y was calculated for each configuration of the cable using two methods. The first method is based on the overall mean displacement of the cable measured with the lasers, which was converted into the aerodynamic force necessary to obtain the measured mean displacement using the stiffness of the dynamic rig in the direction of the motion. The force was then divided by the mean dynamic pressure in the test section and by the diameter and length of the cable corresponding to the frontal area of the model. This method is identical to the method put in place by Andersen et al. and Andersen for analysis of the data from the 2001 and 2008 experiments.[6,7] The second method is based directly on the surface pressure measurements at four locations along the main axis of the cable with a total of 32 pressure ports for each of the four rings of taps. Integration of the mean surface pressure measurements provided the local aerodynamic forces perpendicular to the main axis of the cable and normalized by the dynamic pressure, the cable diameter and a cable length of 1 m to provide C_y and C_x. The force coefficients at the four locations along the main axis of the cable were then averaged to provide the mean C_y and C_x.

It could be argued that both techniques used to calculate the mean force coefficient for the entire cable are not fully representative of the mean aerodynamic forces. The first method assumes that the cable is moving only in one mode with one given frequency and that the mean force acts at

52

mid-length of the cable with the wind speed being constant along the entire length of the cable. Observations of the cable motion have indicated that these assumptions were not fully true. The second method assumes that the pressure distributions at other locations along the main axis of the cable are similar to the pressure distribution obtained from the four measurement locations along the cable axis and that the mean wind speed is constant along the entire length of the cable. Given the measured deviations from the mean diameter reported earlier (See "General" section in chapter 4) and the presence of the helical fillet, it is clear that these assumptions are also not true. However, it is believed that a more representative prediction of mean aerodynamic force coefficients on the cable model could be given by the average of the force coefficients obtained from both sets of measurements. The results from surface pressure measurements have the tendency to underestimate the aerodynamic forces since the part related to friction is not considered, while the forces calculated from the measured overall displacements and the frequency of oscillations can represent an overestimation of the forces.

The force coefficients were calculated using both methods for each configuration of the cable model. It was assumed at first that a rotation of the cable along its main axis should not be a factor that affected the mean aerodynamic force coefficients. However, during the wind-tunnel tests, it was observed that the response of the cable for different cable rotations along its main axis differed greatly from angle to angle. Variations in terms of amplitude of motion of the cable, wind speed at which vibration occurred, and modes of vibration that were excited were observed for the different cable rotations tested. Variations of the mean force coefficients were also observed.

Figure 51 shows C_x and C_y calculated from measured displacements (top), from surface pressure measurements (center), and from the average of both methods (bottom) for the 17 different cable rotation angles tested for the cable inclined at 60 degrees in smooth flow and with the helical fillet. The red line on the bottom graphs represents a least-square fit of the mean force coefficient versus Reynolds number for the 17 configurations combined together. The red lines should be taken as the best representation of the cross-sectional force coefficients of the cable for the configuration mentioned previously. The same analysis was carried out and is presented in figure 52 through figure 55, where coefficients are calculated from mean displacement (top), integration of surface pressure (center), and mean of both methods (bottom).

Cable at 60 degree inclination, with helical fillet, in smooth flow
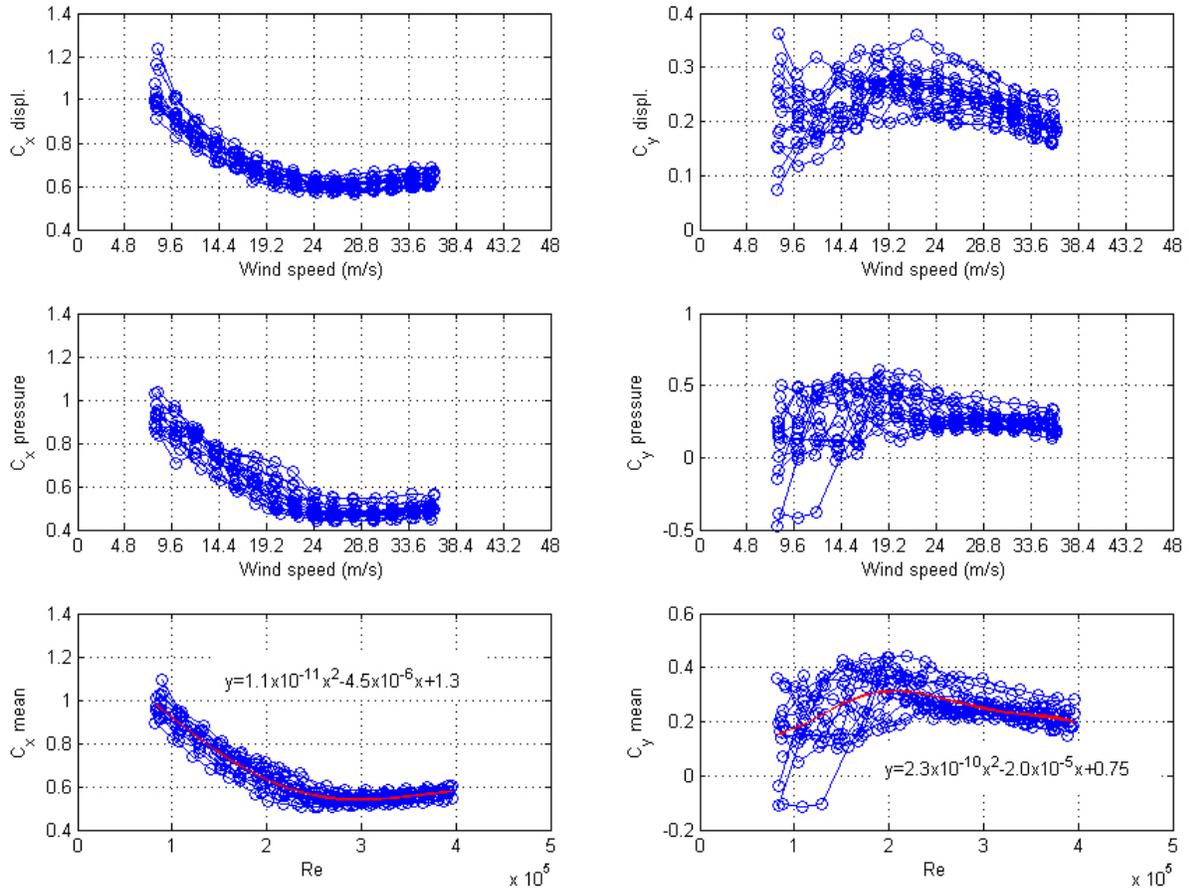
Note: Coefficients are calculated from mean displacement in the top row, from integration of surface pressure in the center row, and from mean of both methods in the bottom row.

Figure 51. Graph. Variations of C_x and C_y with wind speed for 17 cable rotations with cable inclined at 60 degrees in smooth flow and with the helical fillet.

Cable at 60 degree inclination, with helical fillet, in turbulent flow
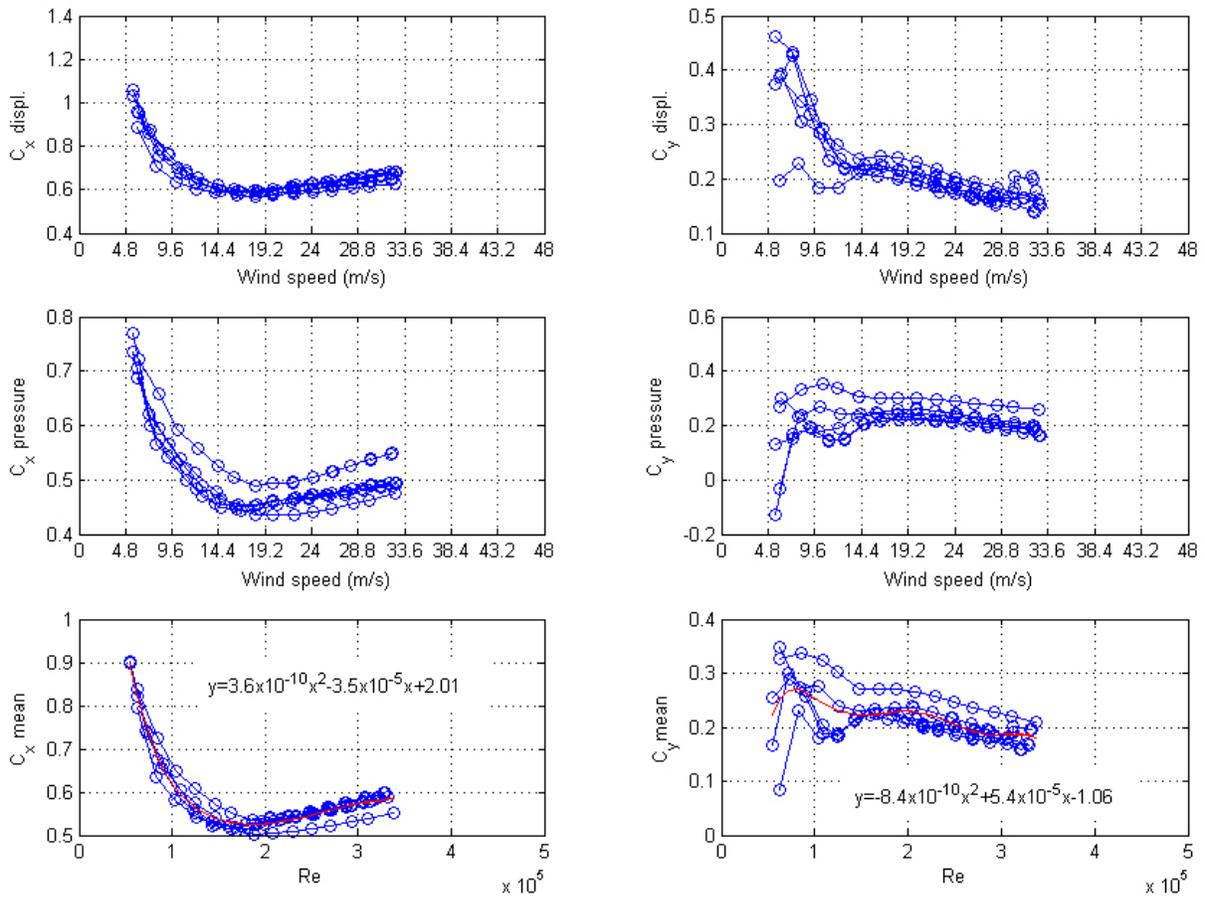
Note: Coefficients are calculated from mean displacement in the top row, from integration of surface pressure in the center row, and from mean of both methods in the bottom row.

Figure 52. Graph. Variations of C_x and C_y with wind speed for five cable rotations with cable inclined at 60 degrees in turbulent flow and with the helical fillet.

Cable at 60 degree inclination, without helical fillet, in turbulent flow

$y = -1.2 \times 10^{-9} x^2 + 7.0 \times 10^{-5} x - 0.54$

$y = -2.6 \times 10^{-10} x^2 + 1.7 \times 10^{-5} x - 0.41$
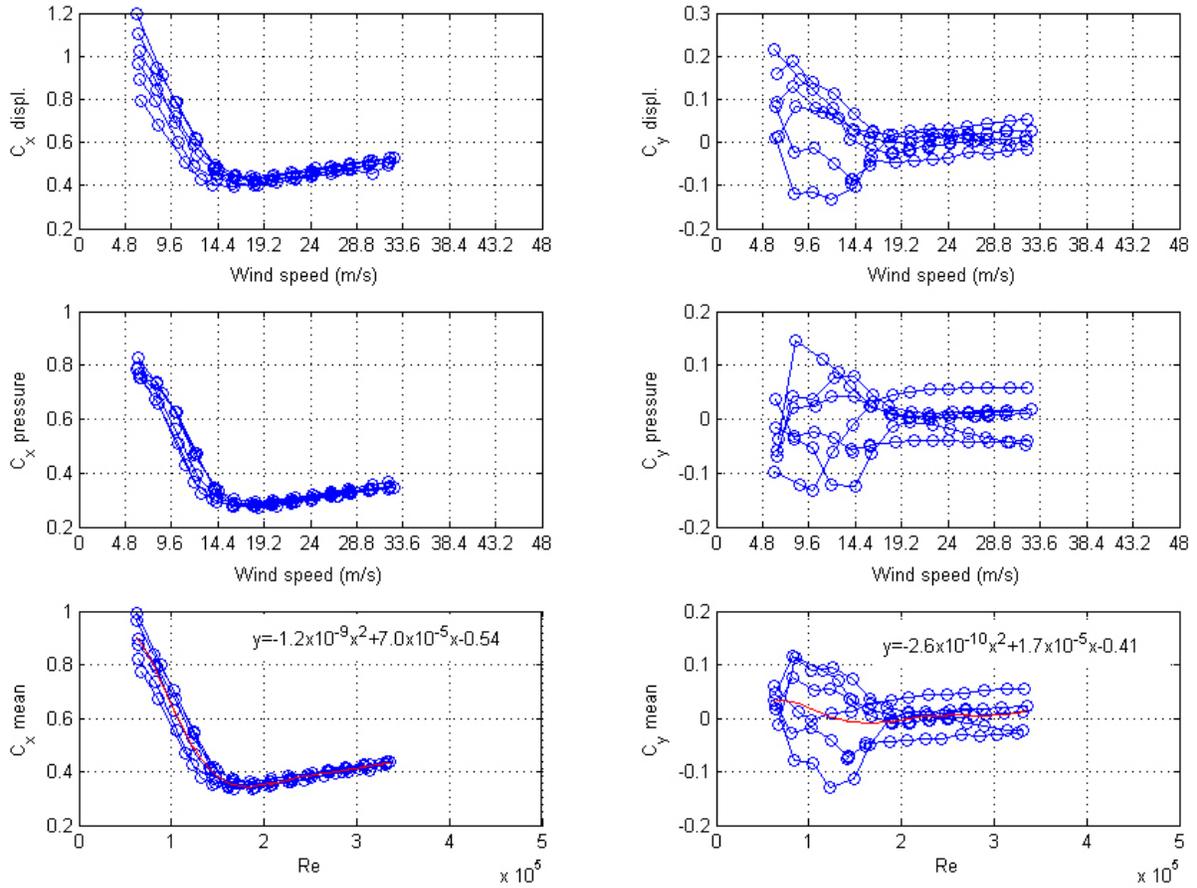
Note: Coefficients are calculated from mean displacement in the top row, from integration of surface pressure in the center row, and from mean of both methods in the bottom row.

Figure 53. Graph. Variations of C_x and C_y with wind speed for six cable rotations with cable inclined at 60 degrees in turbulent flow and without the helical fillet.

56

Cable at 60 degree inclination, without helical fillet, in smooth flow
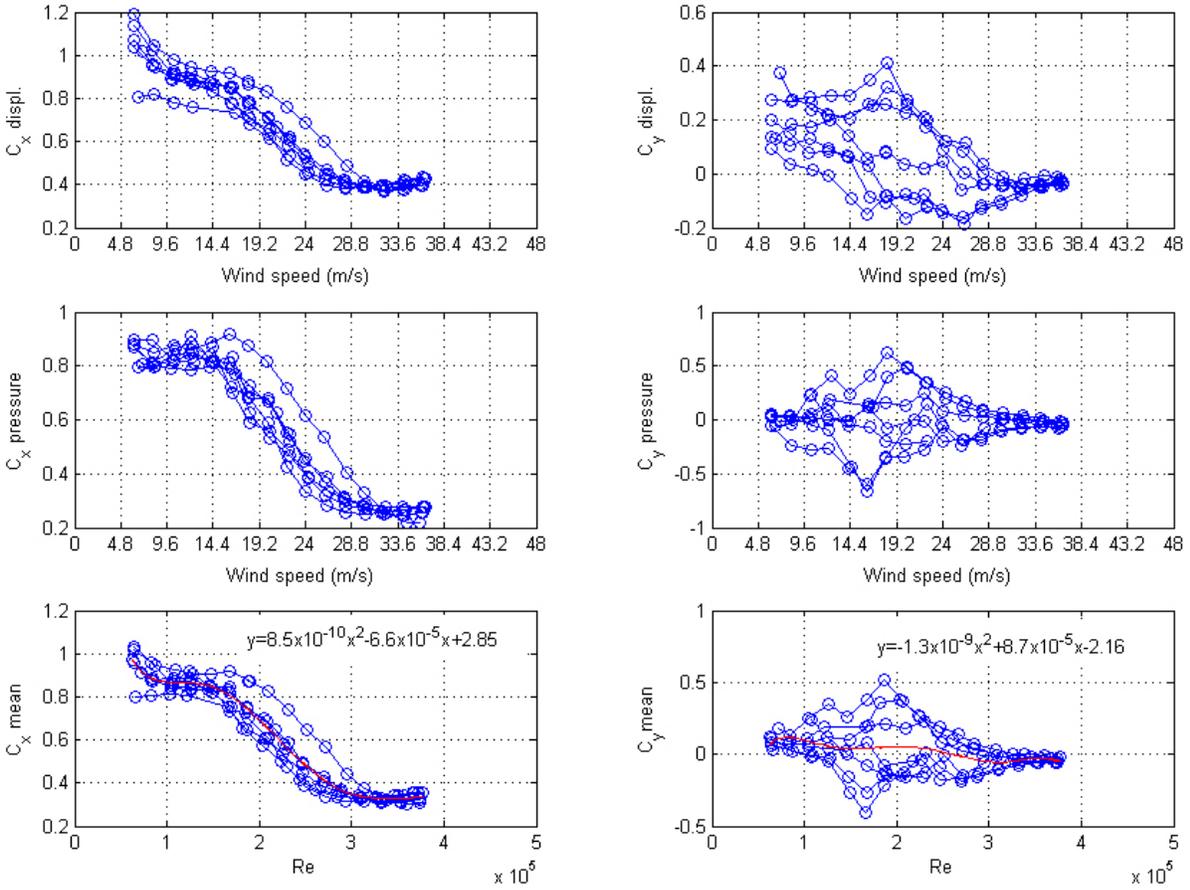
Note: Coefficients are calculated from mean displacement in the top row, from integration of surface pressure in the center row, and from mean of both methods in the bottom row.

Figure 54. Graph. Variations of C_x and C_y with wind speed for seven cable rotations with cable inclined at 60 degrees in smooth flow and without the helical fillet.

Cable at 45 degree inclination, with helical fillet, in smooth flow
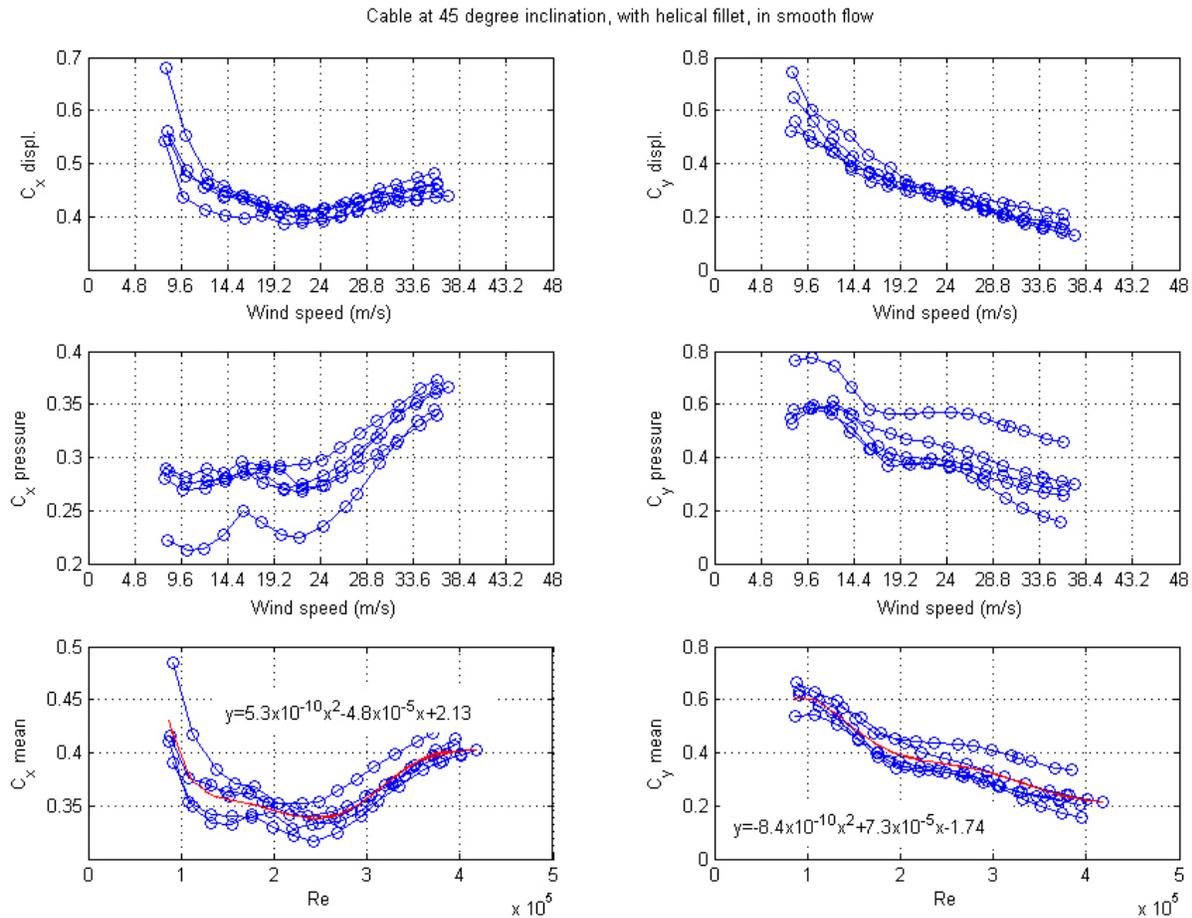
Note: Coefficients are calculated from mean displacement in the top row, from integration of surface pressure in the center row, and from mean of both methods in the bottom row.

Figure 55. Graph. Variations of C_x and C_y with wind speed for five cable rotations with cable inclined at 45 degrees in smooth flow and with the helical fillet.

REPEATABILITY OF THE TESTS

The test program included verifications of the degree of repeatability that could be achieved during the experimental investigation. Selected static and dynamic tests were systematically repeated for conditions as close as possible to the original conditions.

For the static tests, comparisons of the mean cross-sectional force coefficients for the four rings of pressure taps between two identical runs showed excellent repeatability. The differences between the curves of C_x and C_y with Reynolds number were found to be negligible for the cable in smooth flow with helical fillet. Note that each coefficient was based on the integration of 90-s time histories of 32 pressure taps composed of 28,000 points that were time averaged to obtain a single value.

For the dynamic tests, the following four factors had a significant influence on repeatability:

- The wind conditions outdoors.

- The level of structural damping.

- The procedure used by the operator to increment the wind speed of the wind tunnel.

- The surface conditions of the model.

As illustrated in the "Influence of Structural Damping" section earlier in this chapter, the wind conditions outside the wind tunnel were a significant factor to consider when tests were repeated. On windy days, the turbulence of the flow in the test section increased, and low frequency modulation of the wind speed were observed. The wind tunnel operator had to be vigilant in setting up the mean wind speed, deviating in some cases with the standard procedure and the desired increments.

It was observed early in the test program that during long tests with large amplitude of vibration, elements of the dynamic rig had a tendency to loosen up, increasing the friction between moving parts and therefore the structural damping. These elements were identified and systematically verified afterwards to keep the structural damping to a constant level.

Given the dependency of the mean wind speed inside the test section to the outdoor conditions, the wind tunnel operator had to set the wind speed manually based on a live display of the wind velocity in the test section. Once the speed was set, data were collected for 90 s, and the operator increased the speed to the next desired wind speed and repeated the process for 16–17 increments. Care was taken never to reduce the wind speed if the desired wind speed was overshot. It was observed in some occasions that the model had a tendency to behave differently if the wind speed was increased rapidly or slowly. Given the important inertia of the model (407 kg) and the low frequency of oscillations (1.4 Hz), it is possible that oscillations present at low wind speed would carry to higher wind speeds. The excitation of the end-to-end modes in some instances complicated things as well. Therefore, the difficulty for the operator to adjust the mean wind speed in windy days could have combined with the increase of turbulence in the test section to affect the repeatability of the experiments.

In the 2001 and 2008 experiments, carried out in early spring, bugs (e.g., mosquitos, black flies, etc.) were found at several occasions on the windward surface of the model, significantly affecting the surface roughness. (See references 4–7.) The present investigation was carried out later in the spring than the previous experiments. As a result, bugs were observed only occasionally and were systematically removed from the surface of the model during model inspection.

When all four factors were controlled and the dynamic tests were repeated back to back, the variation of the model response with wind speed is repeatable. If a particular test that had large vibration amplitude needed to be repeated for further analysis, it was possible to reproduce the same amplitude of vibrations in the majority of the cases.

Figure 56 and figure 57 compare results of two sets of tests that were repeated. The first case involved static tests where mean force coefficients were compared (runs 81 and 94) and the second case involved dynamic tests where a run that was aborted midway was reran shortly after (runs 239 and 244). The agreement for both cases was excellent, as seen by the overlapping data in the figures.
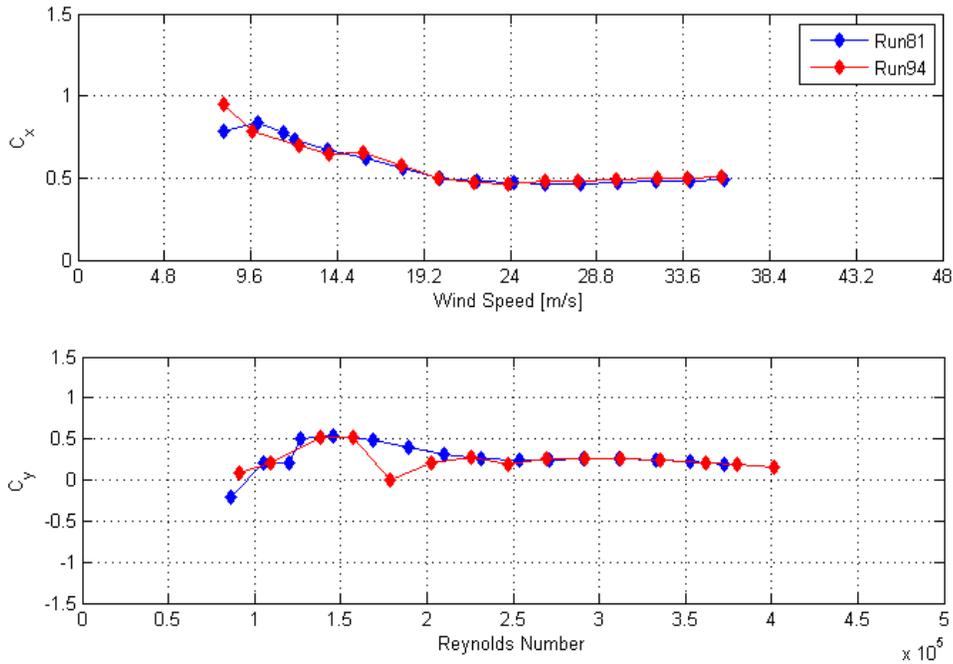
Figure 56. Graph. Mean C_x and C_y calculated from the integration of surface pressure measurements for two runs with cable inclined at 60 degrees and rotated at -90 degrees in smooth flow and with helical fillet.
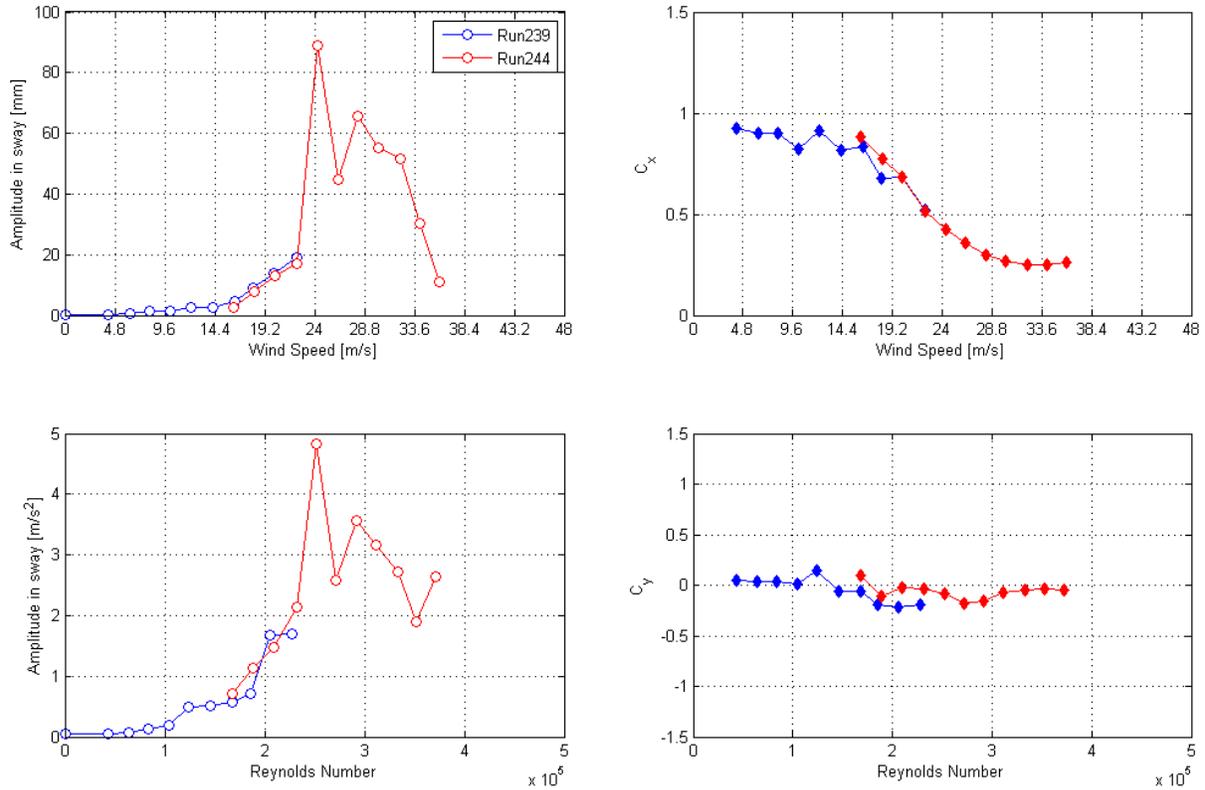
Figure 57. Graph. Response of the cable for two consecutive runs for the cable inclined at 60 degrees and rotated at 2 degrees in smooth flow and without the helical fillet.

Figure 58 shows the results of four runs carried out for the exact same conditions without manipulation of the model. The first run was carried out rapidly with a sampling time of 10 s, the second run was carried out slowly with a sampling time of 90 s, the third run was done for only the low speed range up to 22 m/s, and the fourth run focused only on a peak in the amplitude around 22 m/s. The large peak observed in the first run had a lower amplitude during the second run. The peak was reproduced during the fourth run where the operator rapidly increased or decreased the wind speed to the desired value.

61
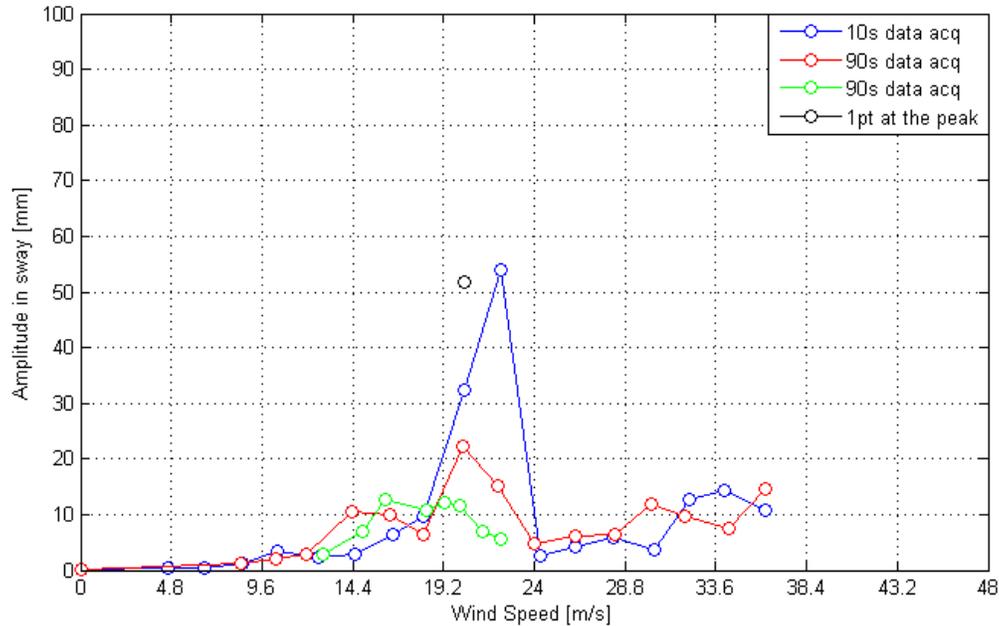
Figure 58. Graph. Amplitude of motion in sway for four consecutive runs for the cable inclined at 60 degrees and rotated at -88 degrees without the helical fillet and in smooth flow.

MECHANISMS CAUSING THE VIBRATIONS

At the time of the initiation of this experimental investigation, the phenomenon referred to as *dry-inclined cable galloping* could be defined as follows: wind-induced vibrations of stay cables for wind speed ranging from 4 to 40 m/s in dry conditions; sustained vibrations, mostly sinusoidal, mostly across-wind; self-limited in amplitude or divergent; and sensitive to fluctuations of the mean wind speed. It is different than buffeting due to turbulence; galloping due to the impinging wake of another structural element; parametric excitation; and galloping due to ice-accretion or other surface contamination.

The mechanisms involved for dry-inclined cable galloping include the following:

- **Quasi-steady aerodynamic instability**: The excitation of the cable is linked with the observation that the combination of the cable diameter and the wind speed range coincide with the critical Reynolds number regime for bi-dimensional circular cylinders. In this regime, several sub-regimes exist, associated with the state of the boundary layers at the surface of the stay cables. The different sub-regimes have different aerodynamic characteristics such as different along-wind and across-wind static force coefficients. The passage from one sub-regime to another due to a small change of apparent wind speed or direction can induce a sudden change of static force coefficients. The rate of change of the static coefficients with Reynolds number and cable wind angle could make it so that the Den Hartog instability criterion is satisfied, and the stay cable experiences galloping. It could also be that the aerodynamics of the stay cable fluctuate from one sub-regime to the next due to motion, fluctuating mean wind speed, and/or change of direction, generating fluctuating forces and causing vibrations. Finally, the rate of change of the

62

static coefficients with Reynolds number could make it so that the aerodynamic damping in one of the modes of vibration becomes negative causing a growth of the vibrations.

- **High-reduced velocity vortex shedding***:* The excitation of the cable is linked with the axial flow and axial vortices that develop along the leeward surface of the inclined stay cable. The low-reduced velocity vortex shedding process known as von Kármán vortex shedding interferes with the axial flow and axial vortices that are travelling slightly downward along the length of the cable, moving farther away from the cable in the process until they are finally released. Vortex cells are formed, and the low-reduced velocity vortex shedding process gets synchronized with the axial vortex shedding process, creating the shedding of entire vortex cells. The process is influenced by many factors and is not necessarily regular and not necessarily coherent along the length of the cable. The excitation occurs at low frequency, 20–30 times lower than the regular vortex-shedding frequency, hence the name "high-reduced velocity vortex shedding."

These two instability mechanisms are intertwined for inclined stay cables. For example, the variations of the state of the boundary layer due to Reynolds number effects will affect the generation of the axial vortices, affecting the shedding frequency and the wind speed at which the vibration occurs. The vortex shedding and associated motion will affect the apparent wind speed and direction, defining the critical Reynolds number sub-regime experienced by the stay cable and affecting the cross-sectional force coefficients.

In light of the experiments carried out in the framework of this investigation, it can be concluded that the vibrations observed for the cable model with a helical fillet in smooth and turbulent flow generally matched the earlier definition of dry-inclined cable galloping with some exceptions. The vibrations were mostly sinusoidal, across-wind, self-limited in amplitude, influenced by slow fluctuations of the mean wind speed, and affected by the level of structural damping. Peaks at lower wind speeds were observed and disappeared with an increase of speed similar to a typical vortex shedding process or due to a change of Reynolds number sub-regime.

For the tests in smooth flow with the helical fillet for several cable angle rotations, the maximum amplitude occurred at the highest wind speed attainable in the wind tunnel—36 m/s. At this Reynolds number, the cable model had cross-sectional force coefficients varying slowly with wind speed in contrast to what would be expected from dry-inclined cable galloping. Tests were carried out to define if the Den Hartog criterion was met due to variations of the static coefficients with cable angle rotation. This was not the case even though a negative slope of the across-wind coefficients with cable rotation was depicted. It was not possible to verify if it was a high-reduced vortex shedding peak given that the maximum speed of the wind tunnel was reached.

Tests in turbulent flow for the same conditions have shown that the peak occurred at lower wind speed (i.e., at a lower Reynolds number) and that the vibrations switched to a higher frequency mode with end-to-end sway when wind speed was increased. It is possible that a similar behavior would have been observed in smooth flow if it had been possible to increase the wind speed past the observed peak.

For other cases, sinusoidal vibrations with constant amplitude were observed, and the amplitude increased when wind speed was increased. This was the case for a large number of wind speed increments corresponding to a range of 10 to 12 m/s. At higher speeds, the vibrations in the sway mode subsided, and vibrations in the end-to-end sway mode occurred. Given the large range of wind speeds covered, this behavior does not match 100 percent with the expected general behavior of dry-inclined cable galloping.

Nevertheless, the fact that stay cables operate in the critical Reynolds number regime with or without the helical fillet and in smooth or turbulent flow makes the description of the phenomenon more complex. In this regime, the boundary layers near the surface of the stay cable experience a transition from laminar to turbulent flow where separation and sometimes reattachment followed by separation occur. These processes are known to be unstable and can lead to unstable behavior. Boundary layer transition from laminar to turbulent at the surface of a circular cylinder is an instability phenomenon that is sensitive to components such as the micro-structure of the surface, geometric asymmetry, flow turbulence, noise, and small motion. It amplifies the effects of these external factors. A deviation of 1 percent of the mean diameter that normally might have been negligible in different conditions becomes a dominating factor in the critical Reynolds number regime. Adding this to the complexity of the aerodynamics of circular cylinders inclined to the flow has proved to be a challenging instability problem to describe and control.

CHAPTER 5: CONCLUSIONS

The aerodynamics of a stay cable model fitted with a helical fillet and inclined to the oncoming flow were studied to evaluate the effect of adding a helical fillet at the surface of a stay cable in relation to its response to strong winds. A helical fillet with a double helix representative of what can be found on stay cables in Europe and North America was affixed to the surface of the HDPE tube of an existing cable model. The helical fillet had a rectangular cross section 2.3 mm high and 2.4 mm wide, a pitch equivalent to 3.2 cable diameters, and a helix angle of 45 degrees.

The experiments revealed that a stay cable with a representative surface roughness, cross-sectional shape, and helical fillet inclined at 60 degrees to the flow can experience wind-induced vibrations with large amplitudes in smooth or turbulent flow for a low level of structural damping. The oscillations observed appeared to be self-limited in amplitude and could be mitigated with an increase of structural damping equivalent to a Scruton number of 5.1. The cable model with the helical fillet experienced a drag crisis almost as pronounced as for the smooth cable but at a lower Reynolds number range.

The experiments revealed also that the aerodynamic forces at the source of the vibrations were highly sensitive to a rotation of the cable model on its axis. Measurements of the external diameter of the smooth cable model have shown a maximum eccentricity equivalent to 1 percent of the mean diameter, which appeared to be sufficient to influence the aerodynamics of the cable model even with the helical fillet in place. Such deviation from the mean cable diameter was deemed representative of field conditions. The trajectory of the cable motion in relation to the prevailing wind direction was also found to be a parameter of importance in the study of cable behavior and stability. During the previous studies on inclined cable galloping, it had not been possible to reach any conclusions on this aspect since the cable-wind plane and rotation of the cable on its axis could not be evaluated separately.

For a stay cable inclined at 45 degrees with a helical fillet, no large vibrations were observed for the range of wind speed investigated, 4 to 36 m/s, for several experimental conditions including spring-plane rotation and rotation of the cable on its axis. The rate of change of the mean aerodynamic force coefficients with wind speeds for a model inclination of 45 degrees were found to be lower than for the 60-degree inclination cases.

Complementary tests on the cable model without the helical fillet in smooth and turbulent flow at an inclination of 60 degrees revealed large vibrations in accordance with the results of previous studies on the same cable model. The vibrations were equivalent and sometimes larger in amplitude than what was previously reported and did not happen at the same wind speeds. This emphasized the importance of the shape of the polyethylene tube covering the stay cable, a local 1 percent deviation from the mean diameter, which was sufficient to amplify the wind excitation.

APPENDIX A. DETAILED LIST OF RUNS AND EXPERIMENTAL CONDITIONS

Table 6. Description of all the runs completed during the 2011 wind tunnel test.

Day	Tare	Run No.	No. of Pts	Inclin-ation (Degree)	Spring Rotation (Degree[a])	Cable Rotation (Degree[a])	Case	Description	Freq. Sway (Hz)	Freq. Heave (Hz)	Freq. Ratio	Damping Sway (Percent)	Damping Heave (Percent)	Sc Sway	Sc Heave	Comments
5/6		24	4	60	0	0	Dynamic	Damping trace	1.39	1.39	1.0	0.08	0.10	1.6	2.1	pt1: sway; pt2: heave; pt3: end-to-end sway; pt4: end-to-end heave
5/6	25	27	19	60	0	0	Dynamic	Increasing speed sweep								pt1–19: speed sweep
5/6	25	28	20	60	0	0	Dynamic	Decreasing speed sweep								pt1–20: speed sweep
5/9	31	32	15	60	0	0	Static	Increasing speed sweep								pt1–15: speed sweep
5/9	34	35	15	60	0	0	Static	Decreasing speed sweep								pt1–15: speed sweep
5/9	36	37	12	60	0	27.7	Static	Increasing speed sweep								pt1–12: speed sweep
5/10	38	39	15	60	0	-13.8	Static	Increasing speed sweep								pt1–15: speed sweep
5/10	40	41	15	60	0	13.8	Static	Increasing speed sweep								pt1–15: speed sweep
5/10		42	2	60	0	-13.8	Dynamic	Damping trace	1.39	1.39	1.00	0.08	0.10	1.6	2.1	pt1: sway; pt2: heave
5/10	43	44	17	60	0	-13.8	Dynamic	Increasing speed sweep								pt1–17: speed sweep
5/10	45	46	17	60	0	-13.8	Dynamic	Increasing speed sweep								pt1–17: speed sweep; repeat of run 44
5/10	45	47	5	60	0	-13.8	Dynamic	Forced oscillations								pt1: 12m/s; pt2: 18m/s; pt3: 24m/s; pt4: 30m/s; pt5: 34m/s
5/11	48	49	17	60	0	-30	Dynamic	Increasing speed sweep								pt1–17: speed sweep
5/11	48	50	4	60	0	-30	Dynamic	Forced oscillations								pt1: 24m/s; pt2: 26m/s; pt3: 28m/s; pt4: 34m/s
5/11	51	52	17	60	0	-40	Dynamic	Increasing speed sweep								pt1–17: speed sweep
5/11	51	53	3	60	0	-40	Dynamic	Forced oscillations								pt1: 24m/s; pt2: 28m/s; pt3: 34m/s
5/11	55	56	17	60	0	-50	Dynamic	Increasing speed sweep								pt1–7: speed sweep
5/11	55	58	2	60	0	-50	Dynamic	Forced oscillations								pt1: 24m/s; pt2: 28m/s
5/11	59	60	17	60	0	-60	Dynamic	Increasing speed sweep								pt1–17: speed sweep
5/11	59	61	6	60	0	-60	Dynamic	Forced oscillations								pt1: 14m/s; pt2: 22m/s; pt3: 22m/s; pt4: 30m/s; pt5/6: 36m/s
5/12	62	63	17	60	0	-75	Dynamic	Increasing speed sweep								pt1–17: speed sweep
5/12	62	64	3	60	0	-75	Dynamic	Forced oscillations								pt1: 16m/s; pt2: 22m/s; pt3: 36m/s
5/12	65	66	19	60	0	-90	Dynamic	Increasing speed sweep								pt1–19: speed sweep
5/12	65	67	17	60	0	-90	Dynamic	Decreasing speed sweep								pt1–17: speed sweep

Day	Tare	Run No.	No. of Pts	Inclination (Degree)	Spring Rotation (Degree[a])	Cable Rotation (Degree[a])	Case	Description	Freq. Sway (Hz)	Freq. Heave (Hz)	Freq. Ratio	Damping Sway (Percent)	Damping Heave (Percent)	Sc Sway	Sc Heave	Comments
5/12	68	69	17	60	0	5	Dynamic	Increasing speed sweep								pt1–17: speed sweep
5/12	70	71	17	60	0	65	Dynamic	Increasing speed sweep								pt1–17: speed sweep
5/13	72	73	18	60	0	50	Dynamic	Increasing speed sweep								pt1–18: speed sweep
5/13	74	75	20	60	0	-90	Dynamic	Increasing speed sweep								pt1–20: speed sweep, repeat run 66
5/13	74	76	2	60	0	-90	Dynamic	Aerodynamic damping test								pt1–2: aerodynamic damping at 32m/s
5/13	74	79	5	60	0	-90	Dynamic	Aerodynamic damping test								pt1: 20m/s; pt2:data taken from 20–22m/s; pt3: data taken while increasing speed from 20 to 22m/s; pt4: aero damping at 32m/s
5/13	80	81	16	60	0	-90	Static	Increasing speed sweep								pt1–16: speed sweep
5/13	84	85	15	60	0	-86	Static	Increasing speed sweep								pt1–15: speed sweep
5/16	87	88	15	60	0	-88	Static	Increasing speed sweep								pt1–15: speed sweep
5/16	89	90	15	60	0	-92	Static	Increasing speed sweep								pt1–15: speed sweep
5/16	91	92	15	60	0	-94	Static	Increasing speed sweep								pt1–15: speed sweep
5/16	93	94	15	60	0	-90	Static	Increasing speed sweep								pt1–15: speed sweep, repeat run 81 (helical fillet lifted because of cold weather)
5/16		96	2	60	0	-90	Dynamic	Damping trace	1.39	1.39	1.00					pt1: sway; pt2: heave
5/16		97	1	60	0	-90	Dynamic	Damping trace	1.39							pt1: sway
5/16		98	1	60	0	-90	Dynamic	Damping trace	1.4							pt1: sway
5/16		99	1	60	0	-90	Dynamic	Damping trace	1.4							pt1: sway
5/16		100	3	60	0	-90	Dynamic	Damping trace	1.4	1.4	1.00	0.15	0.40	3.0	8.1	pt1: sway; pt2: heave
5/17	100	101	20	60	0	-90	Dynamic	Increasing speed sweep								pt1–20: speed sweep, two elastic bands broke during pt8
5/17	100	102	2	60	0	-90	Dynamic	Aerodynamic damping test								pt1–2: aerodynamic damping at 36m/s
5/17		103	2	60	0	-90	Dynamic	Damping trace	1.4	1.4	1.00					pt1: sway; pt2: heave
5/17		104	1	60	0	-90	Dynamic	Damping trace	1.4							pt1: sway
5/17		105	1	60	0	-90	Dynamic	Damping trace		1.4						pt1: heave
5/17		106	4	60	0	-90	Dynamic	Damping trace	1.4	1.4	1.00	0.15	0.15	3.0	3.0	pt3: sway; pt4: heave, medium damping
5/17	107	108	18	60	0	-90	Dynamic	Increasing speed sweep								pt1–18: speed sweep
5/17		109	2	60	0	-90	Dynamic	Damping trace	1.4	1.4	1.00					pt1: sway; pt2: heave
5/17		110	2	60	0	-90	Dynamic	Damping trace	1.4	1.4	1.00					pt1: sway; pt2: heave

Day	Tare	Run No.	No. of Pts	Inclin-ation (Degree)	Spring Rotation (Degree[a])	Cable Rotation (Degree[a])	Case	Description	Freq. Sway (Hz)	Freq. Heave (Hz)	Freq. Ratio	Damping Sway (Percent)	Damping Heave (Percent)	Sc Sway	Sc Heave	Comments
5/17		111	1	60	0	-90	Dynamic	Damping trace	1.39							pt1: sway
5/17		112	1	60	0	-90	Dynamic	Damping trace	1.39							pt1: sway
5/17		113	1	60	0	-90	Dynamic	Damping trace		1.4						pt1: heave
5/17		114	2	60	0	-90	Dynamic	Damping trace		1.42						pt1: heave
5/17		115	1	60	0	-90	Dynamic	Damping trace	1.4							pt1: sway
5/18		116	2	60	0	-90	Dynamic	Damping trace	1.4	1.42	0.99	0.25	0.25	5.1	5.1	pt1: sway; pt2: heave, high damping
5/18	117	118	23	60	0	-90	Dynamic	Increasing speed sweep								pt1–23: speed sweep
5/18		119	2	60	0	-90	Dynamic	Damping trace	1.4	1.42	0.99					pt1: sway; pt2: heave
5/18		120	2	60	0	-90	Dynamic	Damping trace	1.39	1.4	0.99	0.08	0.15	1.0	3.1	pt1: sway; pt2: heave, low damping
5/18	121	122	24	60	0	-90	Dynamic	Increasing speed sweep								pt1–24: speed sweep
5/18	121	123	12	60	0	-90	Dynamic	Decreasing speed sweep								pt1–12: speed sweep
End of Phase I and Start of Phase II																
5/19	124	125	13	60	0	-88	Dynamic	Increasing speed sweep								pt1–13: speed sweep
5/19		126	2	60	0	-88	Dynamic	Damping trace	1.39	1.39	1.00					pt1: sway; pt2: heave
5/19		128	8	60	-54.7	-90	Dynamic	Damping trace	1.4			0.12		2.5		pt1: sway
5/19		129	1	60	-54.7	-90	Dynamic	Damping trace		1.42			0.20		4.2	pt1: heave
5/19	130	131	18	60	-54.7	-90	Dynamic	Increasing speed sweep								pt1–18: speed sweep
Change to 45-Degree Inclination																
5/24		133	3	45	0	-90	Dynamic	Damping trace	1.42	1.37	1.04	0.12	0.10	2.4	2.1	pt2: sway; pt3: heave
5/24	135	136	15	45	0	-90	Dynamic	Increasing speed sweep								pt1–15: speed sweep
5/25	137	137	21	45	0	0	Dynamic	Increasing speed sweep								pt1–21: speed sweep
5/25		138	2	45	0	90	Dynamic	Damping trace	1.42	1.39	1.02	0.12	0.08	2.4	1.6	pt1: sway; pt2: heave
5/25	139	140	17	45	0	90	Dynamic	Increasing speed sweep								pt1–17: speed sweep
5/25	141	142	17	45	0	23	Dynamic	Increasing speed sweep								pt1–17: speed sweep
5/25	143	144	18	45	0	-25	Dynamic	Increasing speed sweep								pt1–18: speed sweep
5/27		147	2	45	-54.7	-25	Dynamic	Damping trace	1.42	1.43	0.99	0.09	0.07	1.8	1.4	pt1: heave; pt2: sway
5/27	148	149	24	45	-54.7	-25	Dynamic	Increasing speed sweep								pt1–24: speed sweep, beating
5/27		150	1	45	-54.7	0	Dynamic	Damping trace		1.43			0.05		1.0	pt1: heave
5/27	151	152	18	45	-54.7	0	Dynamic	Increasing speed sweep								pt1–18: speed sweep, beating
5/27		153	2	45	-45	-25	Dynamic	Damping trace	1.42	1.43	0.99	0.16	0.06	3.3	1.2	pt1: heave; pt2:sway
5/27	154	155	24	45	-45	-25	Dynamic	Increasing speed sweep								pt1–23: speed sweep; pt24: deceleration, beating
5/30		157	3	45	-12.5	-25	Dynamic	Damping trace	1.45	1.39	1.04	0.14	0.10	3.0	2.1	pt2: heave; pt3: sway

Day	Tare	Run No.	No. of Pts	Inclination (Degree)	Spring Rotation (Degree[a])	Cable Rotation (Degree[a])	Case	Description	Freq. Sway (Hz)	Freq. Heave (Hz)	Freq. Ratio	Damping Sway (Percent)	Damping Heave (Percent)	Sc Sway	Sc Heave	Comments
5/30	158	159	21	45	-12.5	-25	Dynamic	Increasing speed sweep								pt1–23: speed sweep; pt24: deceleration, beating
Change Back to 60-Degree Inclination																
6/1		161	4	60	-12.5	-90	Dynamic	Damping trace	1.43	1.39	1.01	0.10	0.14	2.2	3.0	pt3: sway; pt4: heave
6/1	162	163	24	60	-12.5	-90	Dynamic	Increasing speed sweep								pt1–23: speed sweep; pt24: deceleration run, very windy
6/1		164	2	60				Damping trace								pt1: sway; pt2: heave
6/7		165	2	60				Damping trace	1.43	1.39	1.03	0.09	0.10	2.0	2.2	pt1: sway; pt2: heave
6/7	166	167	31	60	-12.5	-90	Dynamic	Increasing speed sweep								pt1–29: speed sweep; pt30–31: aerodynamic damping
6/7																Repeat of run 163
6/7	166	168	1	60	-12.5	-90	Dynamic	Ramp down from max speed to 0 m/s								pt1: deceleration run
6/7		171	2	60				Damping trace								pt1: sway
6/8		173	5	60				Damping trace	1.4	1.39	1.01	0.08	0.15	1.7	3.3	pt3: sway; pt4: heave
6/8	174	176	25	60	0	-92	Dynamic	Increasing speed sweep								pt1–22: speed sweep; pt23–24: aerodynamic damping; pt25: deceleration
6/8	177	178	16	60	0	-90	Dynamic	Increasing speed sweep								pt1–13: speed sweep; pt14–15: aerodynamic damping
6/15	179	180	4	60					Turbulent flow characteristic								Position 1 of the ladders upstream of the cable
6/15	181	182	5	60					Turbulent flow characteristic								Position 2 of the ladders (167.64 cm further away from the cable)
6/15	183	184	4	60					Turbulent flow characteristic								Position 2 of the ladders, first vertical measurement
6/15	185	186	4	60					Turbulent flow characteristic								Position 2 of the ladders, second vertical measurement
6/15	187	188	4	60					Turbulent flow characteristic								Position 2 of the ladders, third vertical measurement
6/16	189	190	4	60					Turbulent flow characteristic								Position 2 of the ladders, fourth vertical measurement
6/16	191	192	12	60					Turbulent flow characteristic								Calibration of the test section in turbulent flow, speed sweep
6/16	193	194	5	60					Turbulent flow characteristic								Position 2 of the ladders, measure of flow for different lateral positions

Day	Tare	Run No.	No. of Pts	Inclin-ation (Degree)	Spring Rotation (Degree[a])	Cable Rotation (Degree[a])	Case	Description	Freq. Sway (Hz)	Freq. Heave (Hz)	Freq. Ratio	Damping Sway (Percent)	Damping Heave (Percent)	Sc Sway	Sc Heave	Comments
6/16		195	2	60	0	-90	Dynamic	Damping trace	1.4	1.39	1.01	0.08	0.15	1.7	3.3	pt1: sway; pt2: heave
6/16	196	197	22	60	0	-90	Dynamic	Increasing speed sweep, turbulent flow								pt1–19: speed sweep; pt20–21: aerodynamic damping; pt22: deceleration
6/16	198	199	24	60	0	-92	Dynamic	Increasing speed sweep, turbulent flow								pt1–23: speed sweep; pt24: aerodynamic damping, one threaded rod broke after pt24
6/17		201	3	60	0	-88	Dynamic	Damping trace	1.4	1.39	1.01	0.07	0.13	1.5	2.7	pt1: sway, pt2:heave
6/17	202	203	24	60	0	-88	Dynamic	Increasing speed sweep, turbulent flow								pt1–21: speed sweep; pt22–23: aerodynamic damping; pt24: deceleration, new threaded rod
6/17	204	205	2	60	0	0	Dynamic	Increasing speed sweep, turbulent flow								pt1: 0m/s; pt2: 4m/s
6/17	204	206	19	60	0	0	Dynamic	Increasing speed sweep, turbulent flow								pt1–16: speed sweep; pt17–18: aerodynamic damping; pt19: deceleration
6/17	207	208	27	60	0	50	Dynamic	Increasing speed sweep, turbulent flow								pt1–24: speed sweep; pt25–26: aerodynamic damping; pt27: deceleration
Removal of Helical Fillet																
6/20		209	3	60	0	50	Dynamic	Damping trace	1.4	1.39	1.01	0.07	0.15	1.5	3.2	pt1: sway; pt2: heave
6/20	210	211	20	60	0	50	Dynamic	Increasing speed sweep, turbulent flow, no helical								pt1–17: speed sweep; pt16: lost laser heave top; pt18–19: aerodynamic damping; pt17–20: not good, the cable was touching the top opening of the wind tunnel and damped motion; pt20: deceleration
6/20		212	2	60	0	0	Dynamic	Damping trace	1.4	1.39	1.01	0.08	0.12			pt1: sway; pt2: heave
6/20	213	214	23	60	0	0	Dynamic	Increasing speed sweep, turbulent flow, no helical								pt1–19: speed sweep; pt20–21: aerodynamic damping; pt22: deceleration; pt23: tare
6/22	215	216	31	60	0	-90	Dynamic	Increasing speed sweep, turbulent flow, no helical								pt1–28: speed sweep; pt29–30: aerodynamic damping; pt31: deceleration
6/22	218	219	19	60	0	-88	Dynamic	Increasing speed sweep, turbulent flow, no helical								pt1–16: speed sweep; pt17–18: aerodynamic damping; pt19: deceleration
6/22		220	2	60	0	-92	Dynamic	Damping trace	1.4	1.39	1.01	0.09	0.11	1.9	2.3	pt1: sway; pt2: heave

Day	Tare	Run No.	No. of Pts	Inclination (Degree)	Spring Rotation (Degree[a])	Cable Rotation (Degree[a])	Case	Description	Freq. Sway (Hz)	Freq. Heave (Hz)	Freq. Ratio	Damping Sway (Percent)	Damping Heave (Percent)	Sc Sway	Sc Heave	Comments
6/22	221	222	16	60	0	-92	Dynamic	Increasing speed sweep, turbulent flow, no helical								pt1–15: speed sweep; pt16: data at 32m/s but one threaded rod broke after 38 s of data
6/22		223	2	60	0	-54.7	Dynamic	Damping trace	1.4	1.39	1.01	0.08	0.13	1.7	2.8	pt1: sway; pt2: heave
6/22	224	225	19	60	0	-54.7	Dynamic	Increasing speed sweep, turbulent flow, no helical								pt1–16: speed sweep; pt17–18: aerodynamic damping; pt19: deceleration
6/22	227	226	9	60	0	-54.7	Dynamic	Increasing speed sweep, turbulent flow, no helical								pt1–8: speed sweep (from 6 to 9.5 m/s); pt9: 0 m/s
Removal of Turbulent Flow Exposure																
6/23		228	2	60	0	-54.7	Dynamic	Damping trace	1.4	1.39	1.01	0.07	0.11	1.5	2.3	pt1: sway, pt2: heave
6/23	229	230	22	60	0	-54.7	Dynamic	Increasing speed sweep, turbulent flow, no helical								pt1–19: speed sweep; pt20–21: aerodynamic damping; pt22: deceleration
6/23	232	234	20	60	0	0	Dynamic	Increasing speed sweep, turbulent flow, no helical								pt1–18: speed sweep; pt19–20: aerodynamic damping, one threaded rod broke during the run
6/23		235	2	60	0	-2	Dynamic	Damping trace	1.4	1.39	1.01	0.07	0.13	1.5	2.7	pt1: sway; pt2: heave
6/23	236	237	21	60	0	-2	Dynamic	Increasing speed sweep, turbulent flow, no helical								pt1–18: speed sweep; pt19–20: aerodynamic damping; pt21: deceleration
6/23	238	239	12	60	0	2	Dynamic	Increasing speed sweep, turbulent flow, no helical								pt1–11: speed sweep; pt12: one threaded rod broke during the run
6/23		240	3	60	0	2	Dynamic	Damping trace	1.42	1.39	1.02	0.07	0.13	1.5	2.8	pt1: sway; pt2: heave
6/24	241	244	14	60	0	2	Dynamic	Increasing speed sweep, turbulent flow, no helical								pt1–11: speed sweep (run 239 with a new rod); pt12–13: aerodynamic damping; pt14: deceleration
6/24	247	248	15	60	0	-93	Static	Increasing speed sweep, turbulent flow, no helical								pt1–15: speed sweep
6/24	249	250	16	60	0	-93	Static	Increasing speed sweep, turbulent flow, no helical								pt1–16: speed sweep, top gap sealed
6/24	252	253	22	60	0	-93	Dynamic	Increasing speed sweep, turbulent flow, no helical								pt1–19: speed sweep; pt20–21: aerodynamic damping; pt22: deceleration
6/24		254	2	60	0	-90	Dynamic	Damping trace	1.4	1.39	1.01	0.07	0.12	1.5	2.6	pt1: sway; pt2: heave

Day	Tare	Run No.	No. of Pts	Inclin- ation (Degree)	Spring Rotation (Degree[a])	Cable Rotation (Degree[a])	Case	Description	Freq. Sway (Hz)	Freq. Heave (Hz)	Freq. Ratio	Damping Sway (Percent)	Damping Heave (Percent)	Sc Sway	Sc Heave	Comments
6/24	254	255	23	60	0	-90	Dynamic	Increasing speed sweep, turbulent flow, no helical								pt2–18: speed sweep; pt19–22: aerodynamic damping; pt23: deceleration (no data for pt1)
6/24	256	257	19	60	0	-88	Dynamic	Increasing speed sweep, turbulent flow, no helical								pt1–18:speed sweep; pt19: aerodynamic damping, only 10-s sampling time at 500 Hz
6/24	256	258	1	60	0	-88	Dynamic	Aerodynamic damping								pt1: aerodynamic damping
6/24	259	260	22	60	0	-88	Dynamic	Speed sweep, increasing, turbulent flow, no helical								pt1–16: speed sweep; pt17–21: aerodynamic damping; pt22: deceleration, repeat run 257 with 90-s sampling time at 2500 Hz
6/24	261	262	8	60	0	-88	Dynamic	Increasing speed sweep, turbulent flow, no helical								pt1–8: speed sweep, 12 to 22 m/s increase by 2 m/s
6/24	261	263	7	60	0	-88	Dynamic	Increasing speed sweep, turbulent flow, no helical								pt1: ramp up to 20 m/s; pt2: 20 m/s; pt3: down to 8 m/s and back to 20 m/s; pt4–21: 7 m/s; pt5: 20 m/s; pt6: up to 36 m/s and back to 20 m/s and take data

[a] Negative degrees indicate clockwise direction.
Note: Blank cells indicate that no information is available.

73
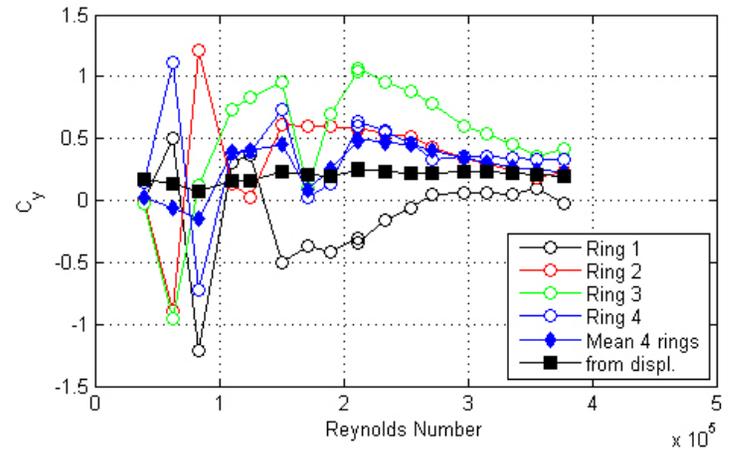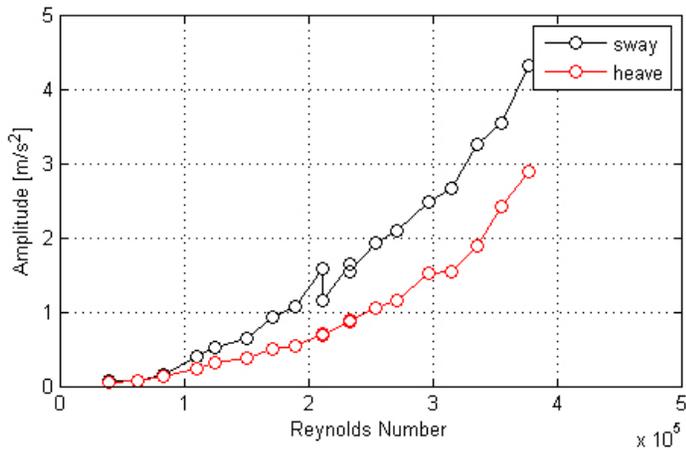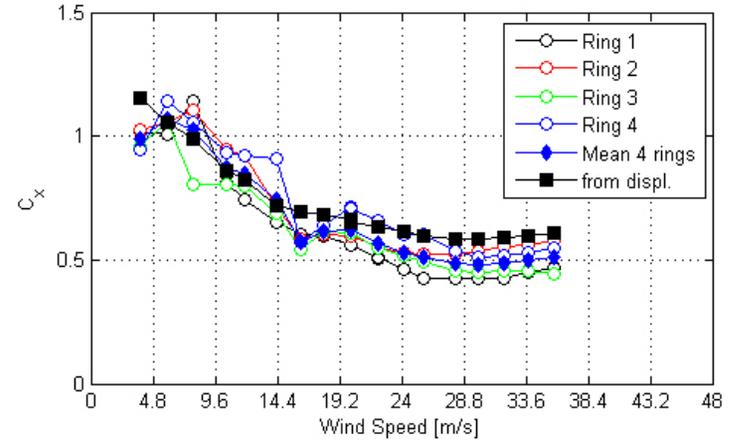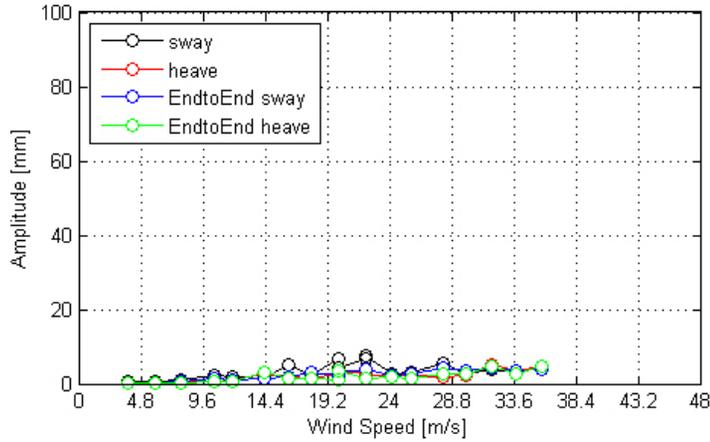
Figure 59. Graph. Response of the cable as a function of wind speed or Reynolds number as measured by the lasers, accelerometers, and surface pressures for run 27.
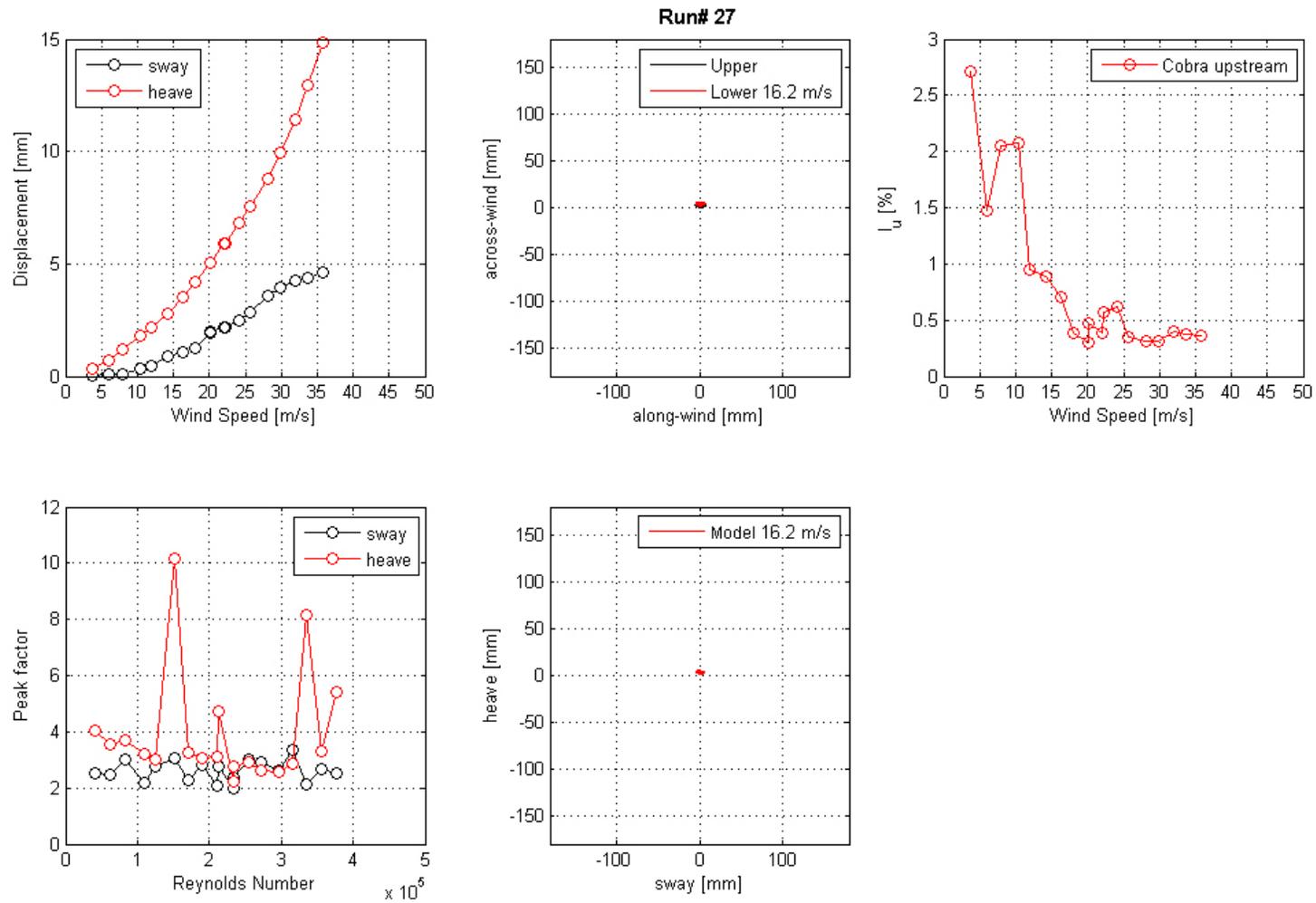
Figure 60. Graph. Mean displacement and peak factor from the laser, motion path at one wind speed, and intensity of turbulence measured at the entrance of the test section for run 27.
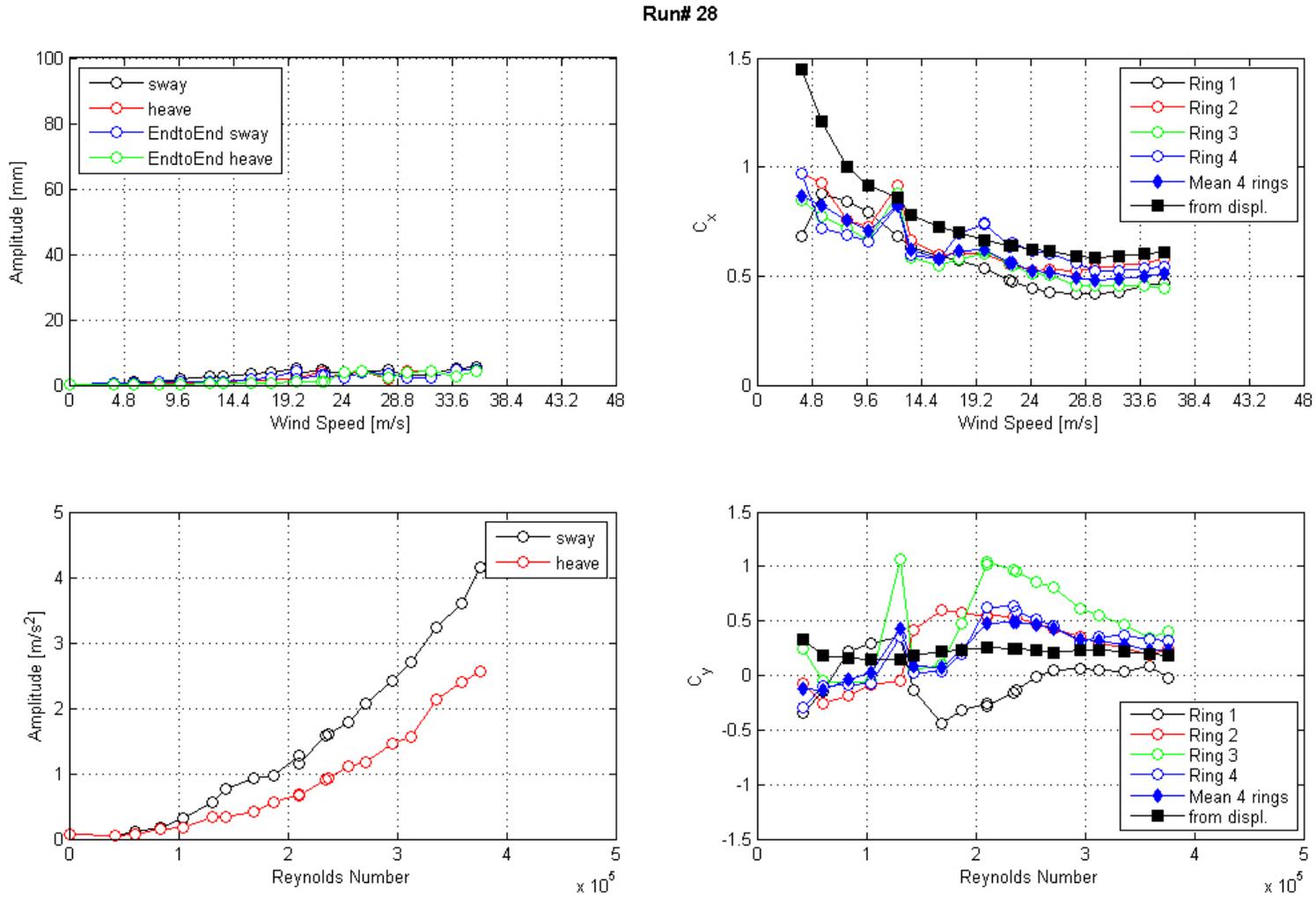
Figure 61. Graph. Response of the cable as a function of wind speed or Reynolds number as measured by the lasers, accelerometers, and surface pressures for run 28.
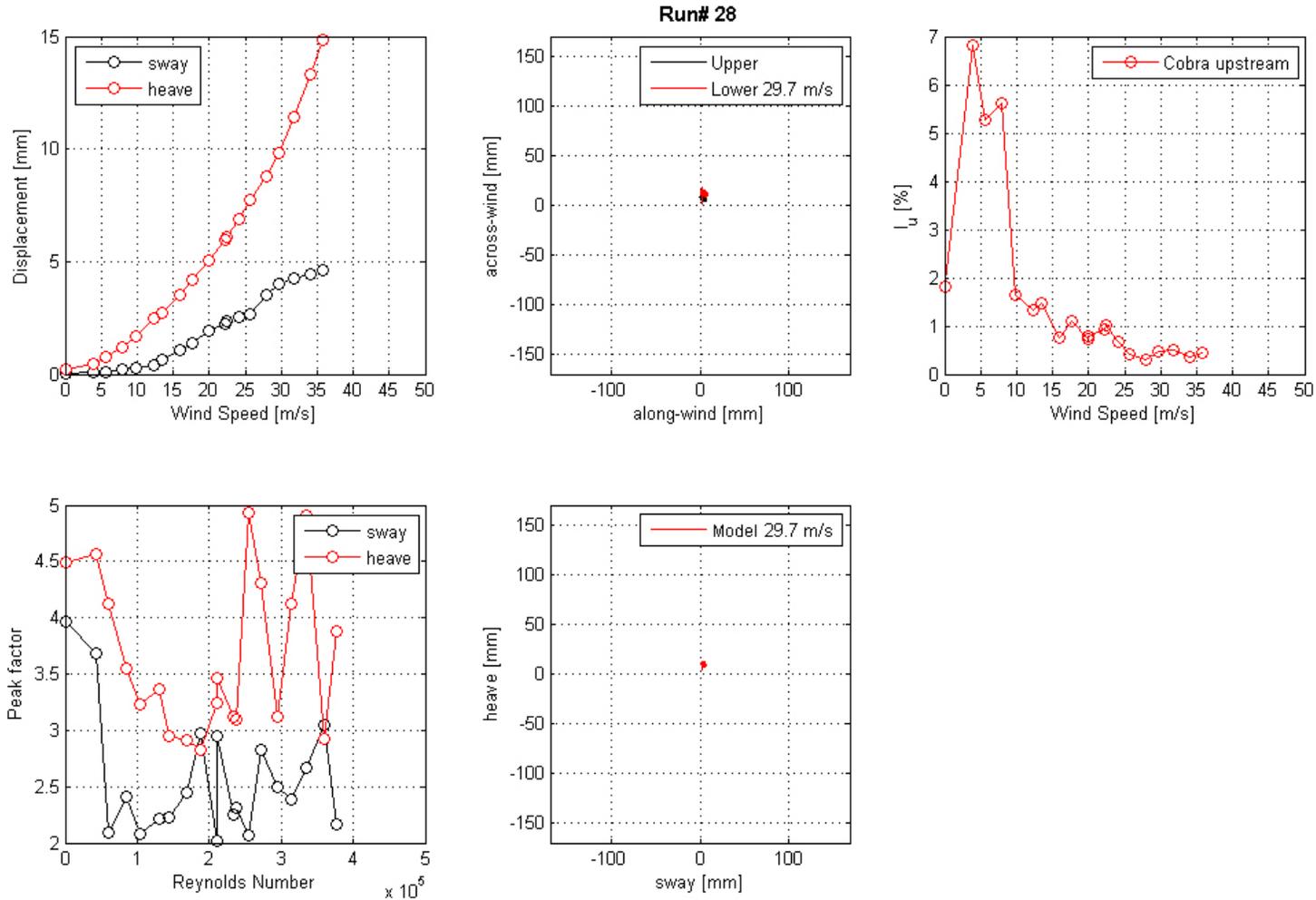
Figure 62. Graph. Mean displacement and peak factor from the laser, motion path at one wind speed, and intensity of turbulence measured at the entrance of the test section for run 28.
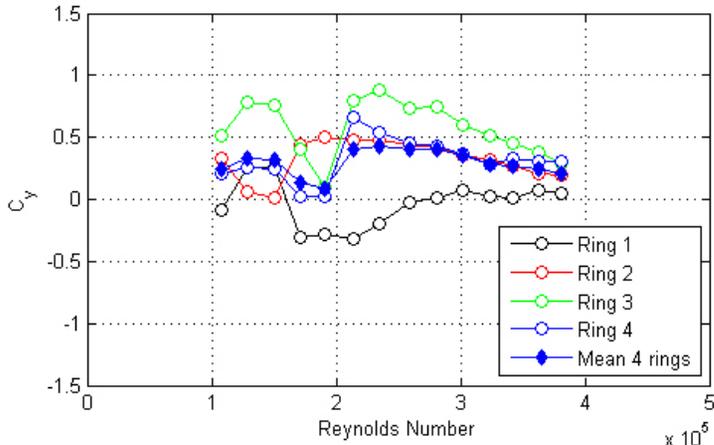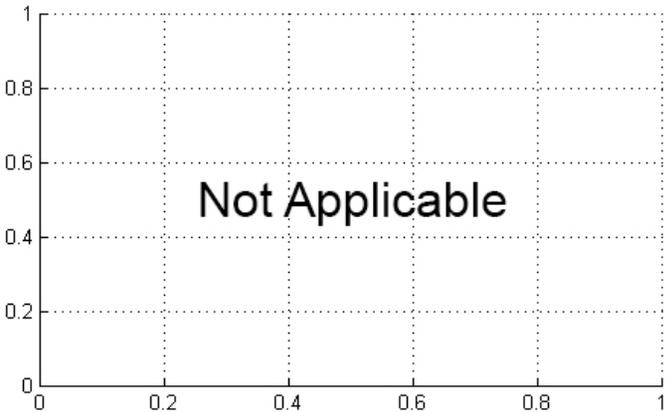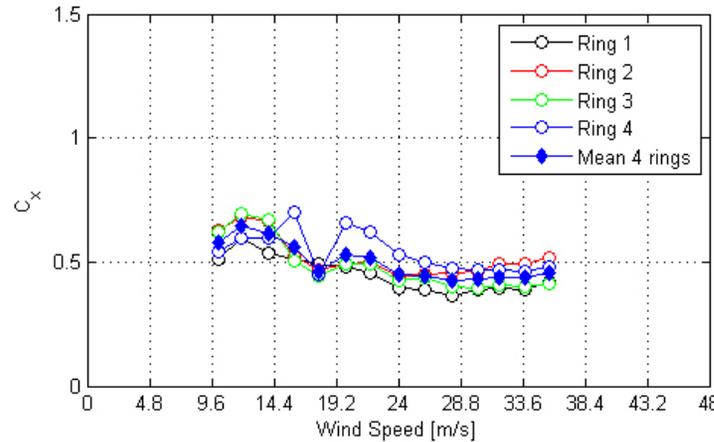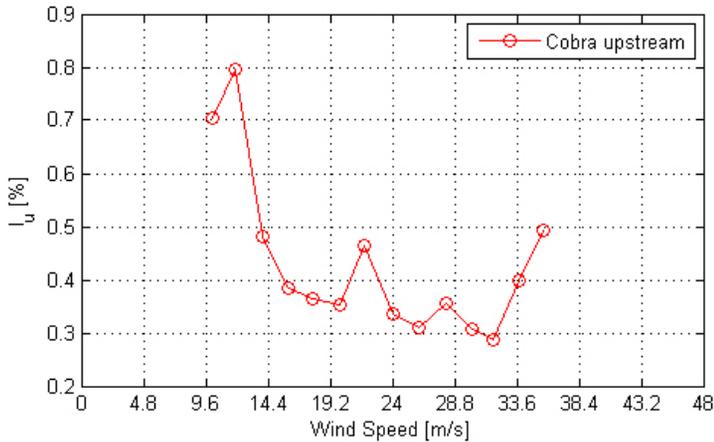
Figure 63. Graph. Intensity of turbulence measured at the entrance of the test section and C_x and C_y calculated from surface pressure measurements as a function of Reynolds number and wind speed for run 32.
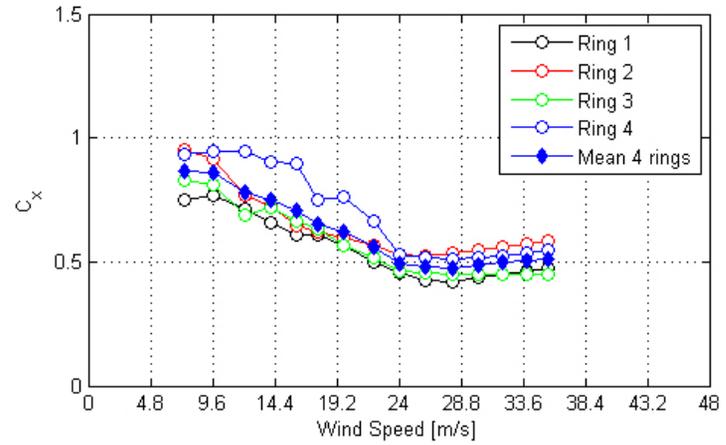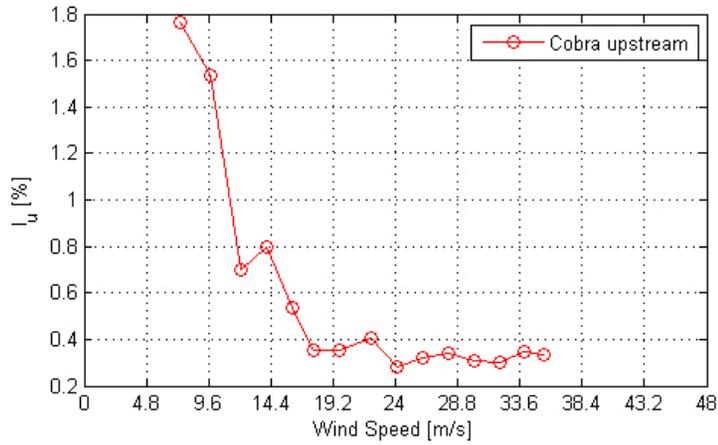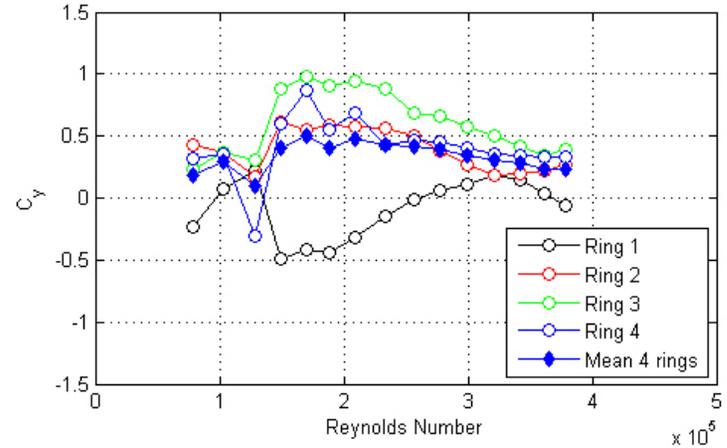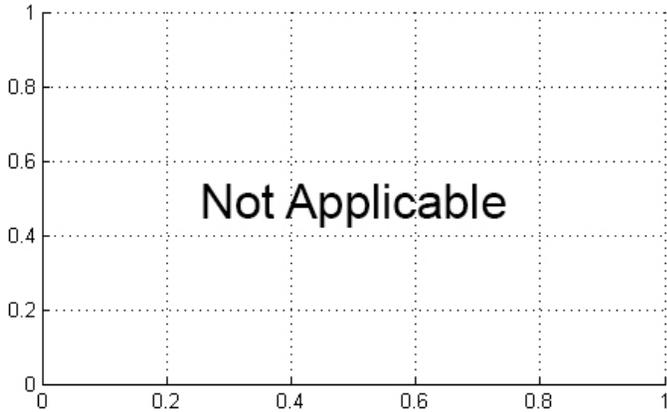
Figure 64. Graph. Intensity of turbulence measured at the entrance of the test section and C_x and C_y calculated from surface pressure measurements as a function of Reynolds number and wind speed for run 35.
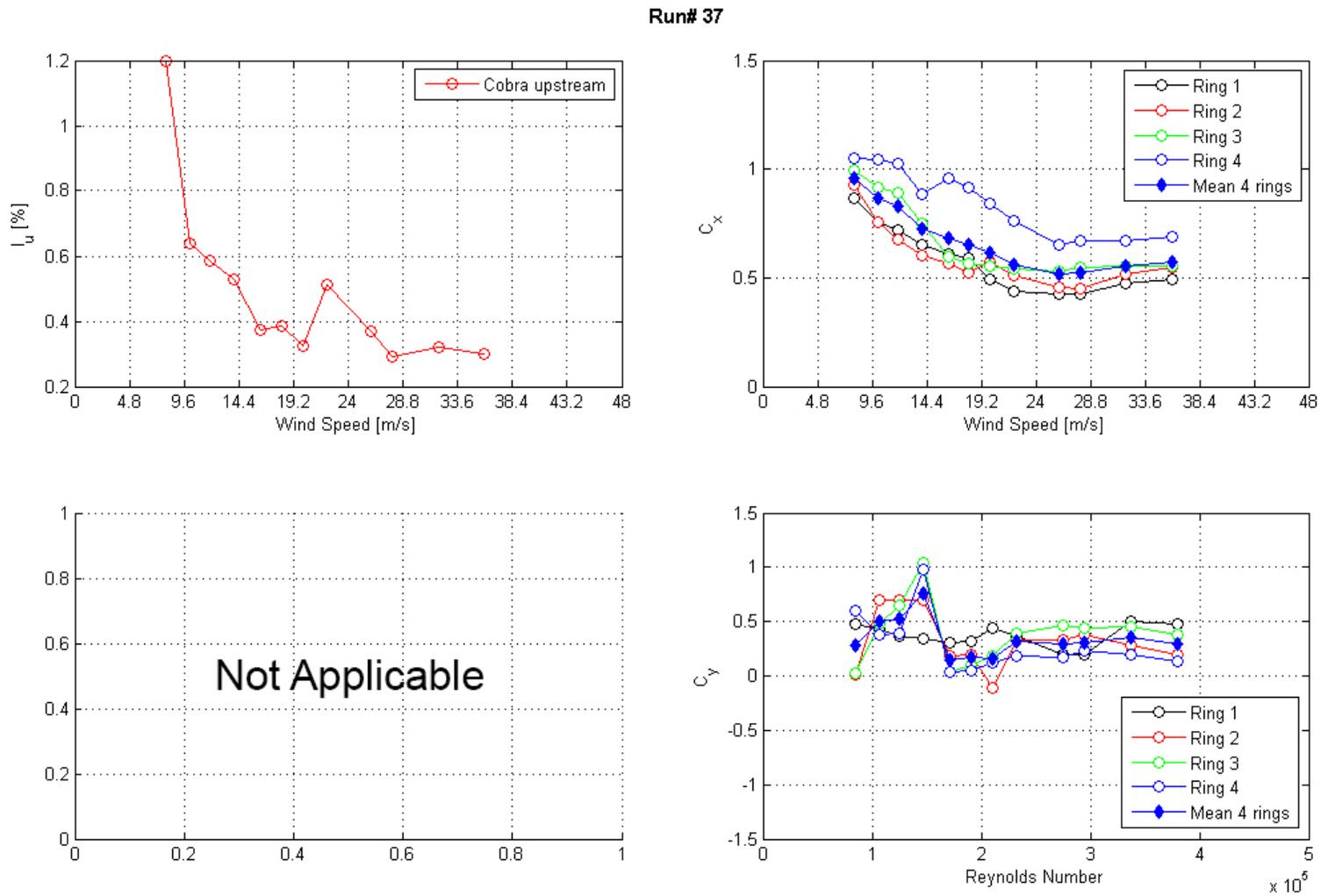
Figure 65. Graph. Intensity of turbulence measured at the entrance of the test section and C_x and C_y calculated from surface pressure measurements as a function of Reynolds number and wind speed for run 37.
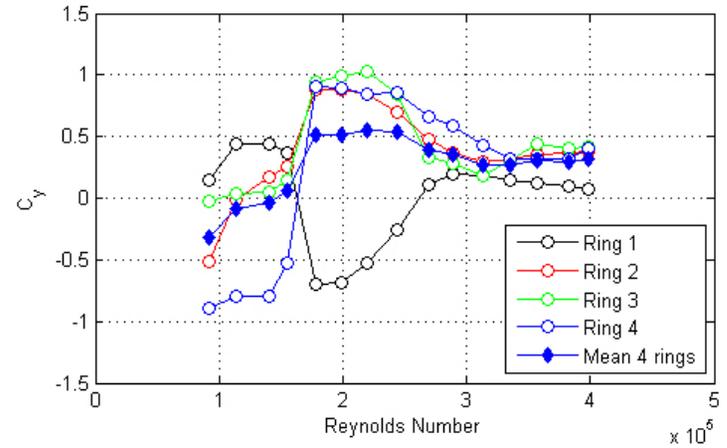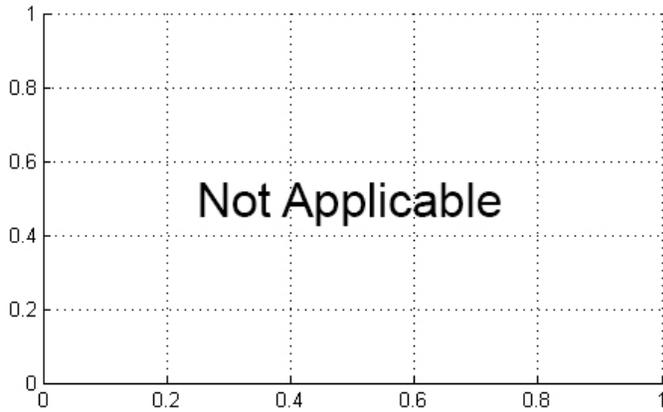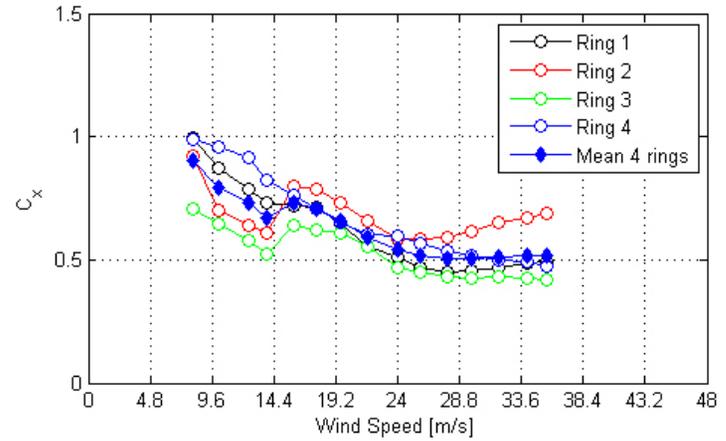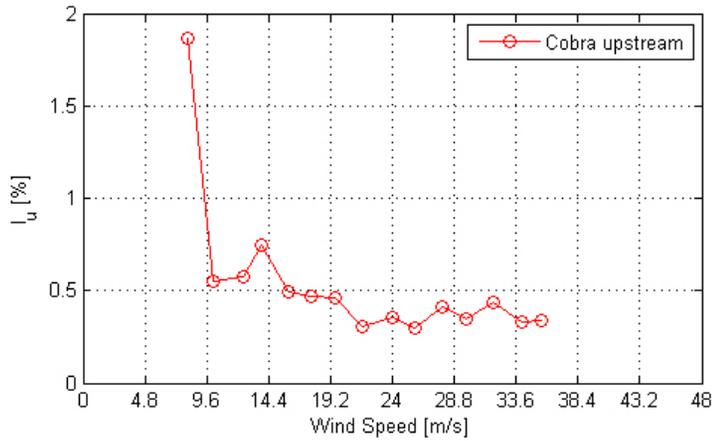
Figure 66. Graph. Intensity of turbulence measured at the entrance of the test section and *C_x* and *C_y* calculated from surface pressure measurements as a function of Reynolds number and wind speed for run 39.

Run# 41
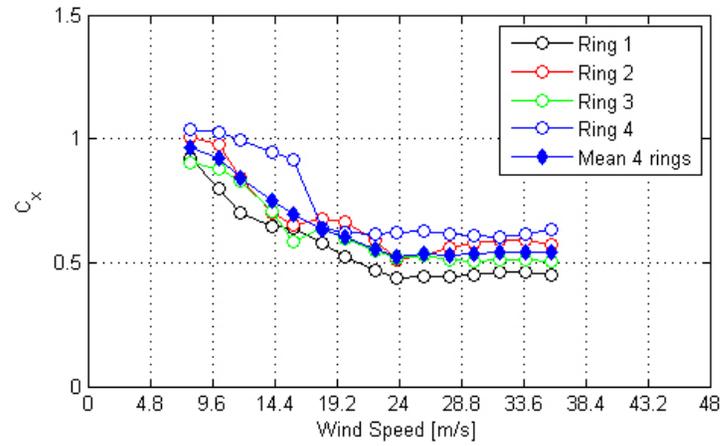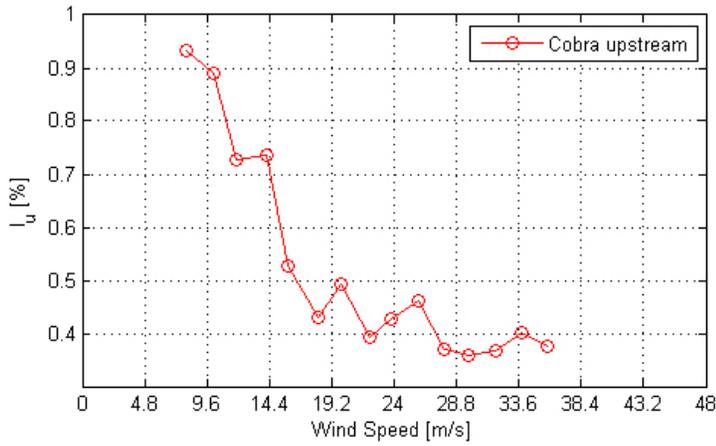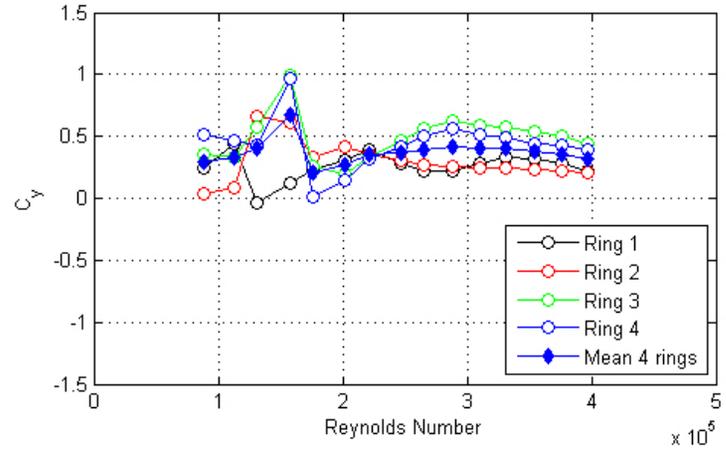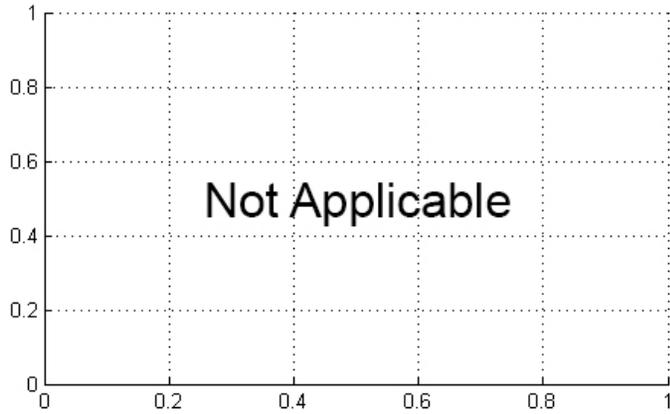
Figure 67. Graph. Intensity of turbulence measured at the entrance of the test section and C_x and C_y calculated from surface pressure measurements as a function of Reynolds number and wind speed for run 41.
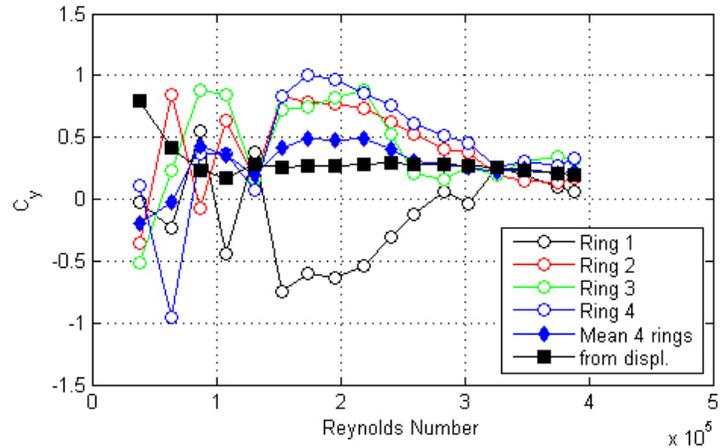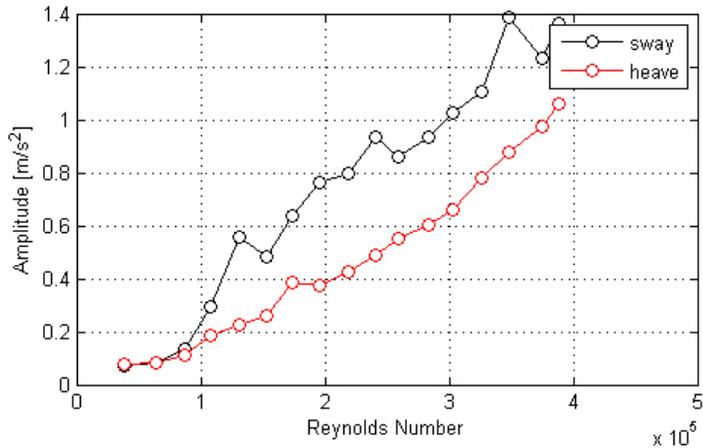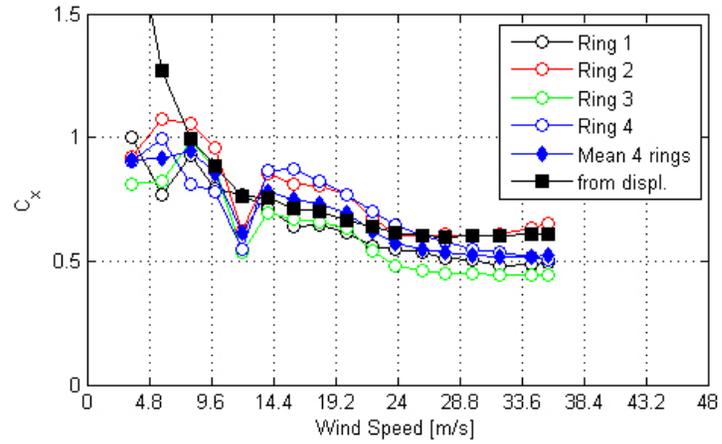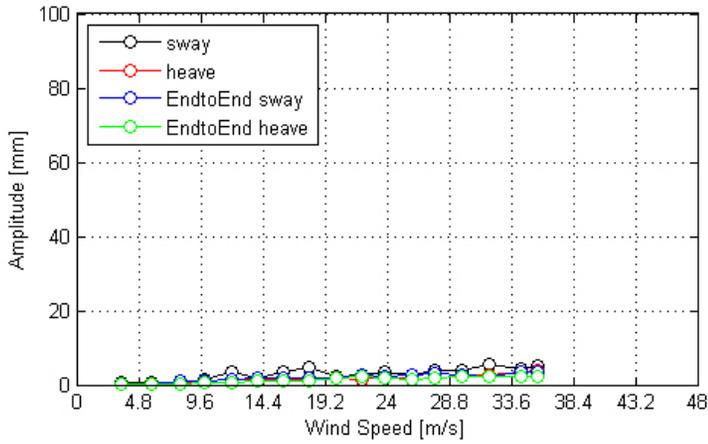
Figure 68. Graph. Response of the cable as a function of wind speed or Reynolds number as measured by the lasers, accelerometers, and surface pressures for run 44.
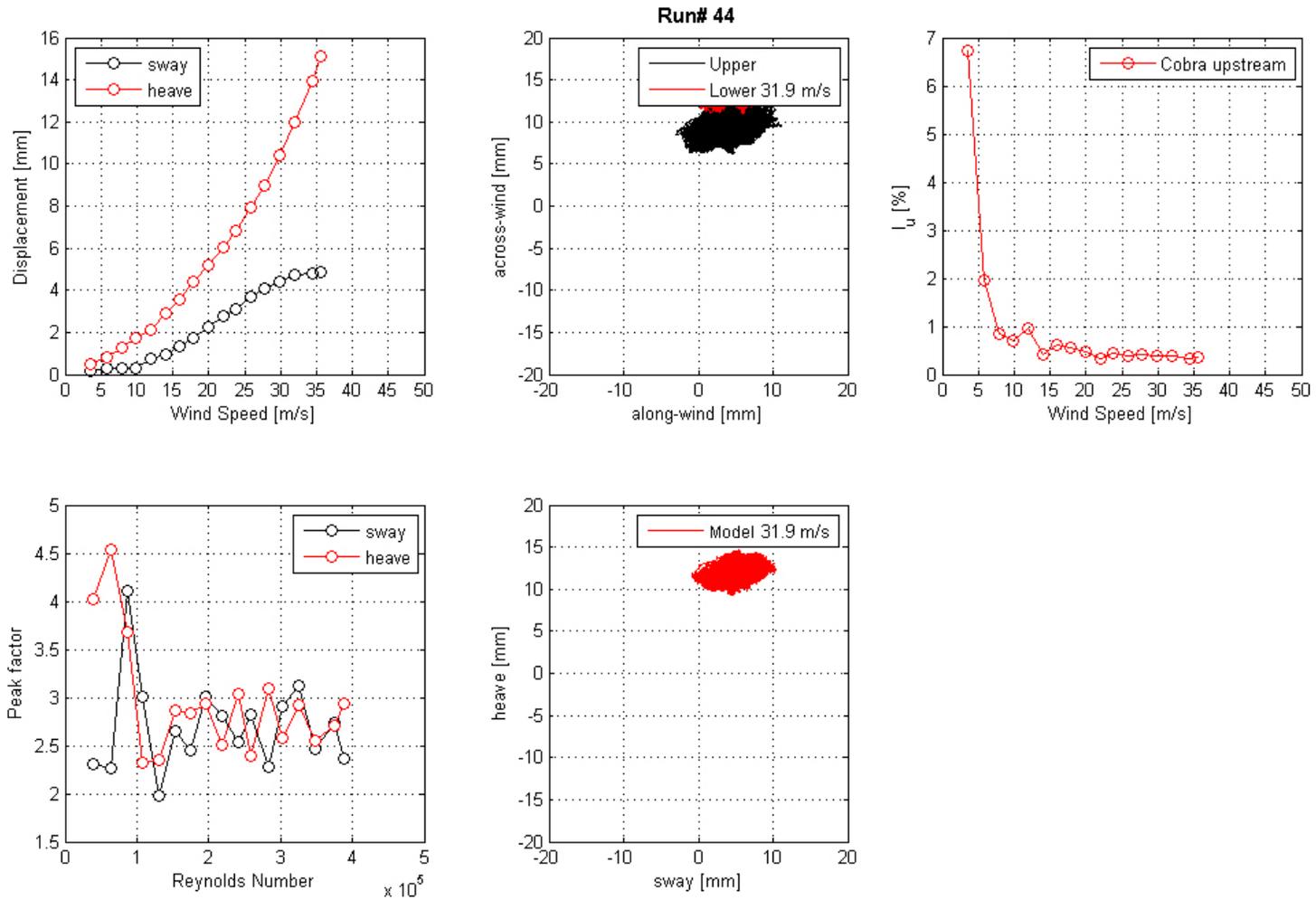
Figure 69. Graph. Mean displacement and peak factor from the laser, motion path at one wind speed, and intensity of turbulence measured at the entrance of the test section for run 44.
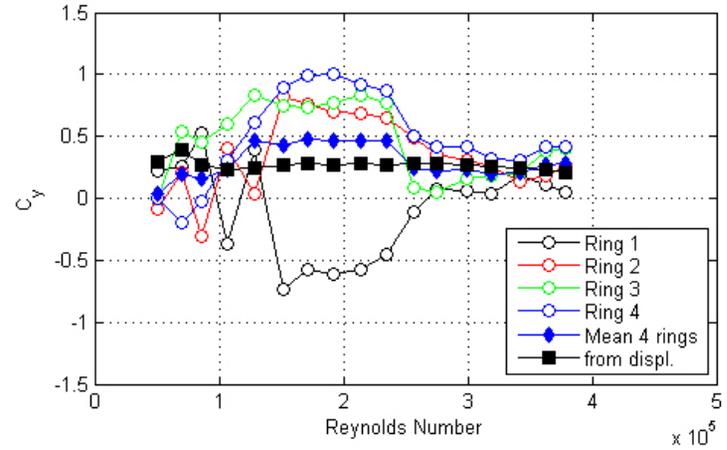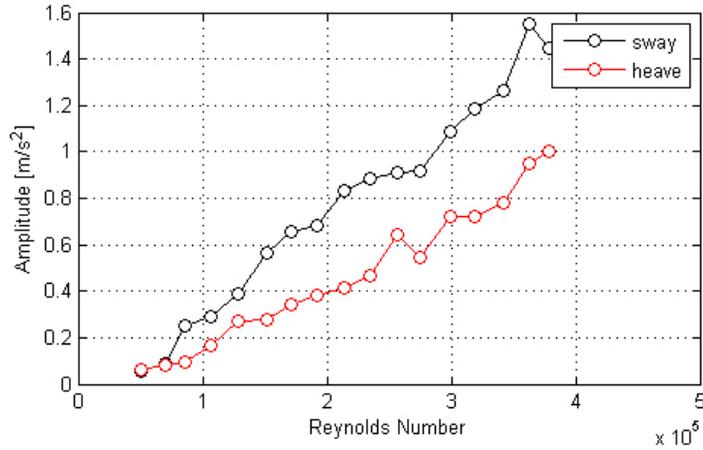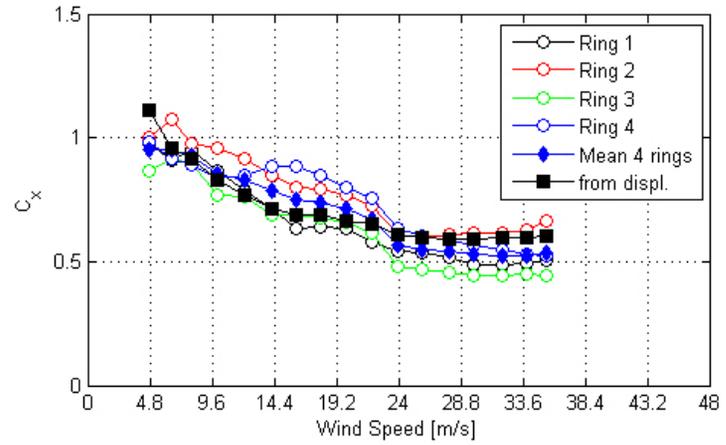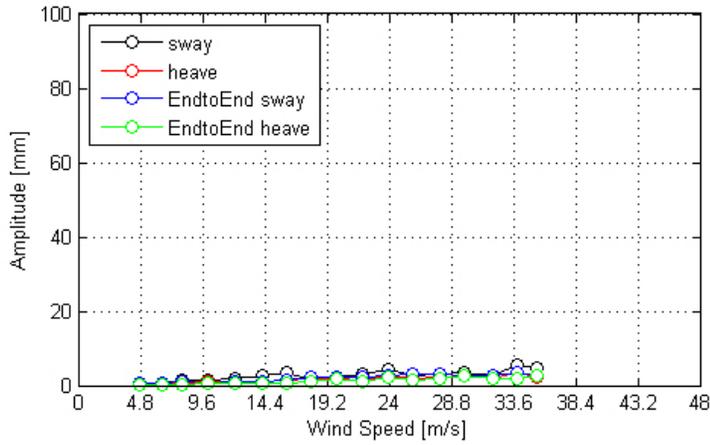
Figure 70. Graph. Response of the cable as a function of wind speed or Reynolds number as measured by the lasers, accelerometers, and surface pressures for run 46.
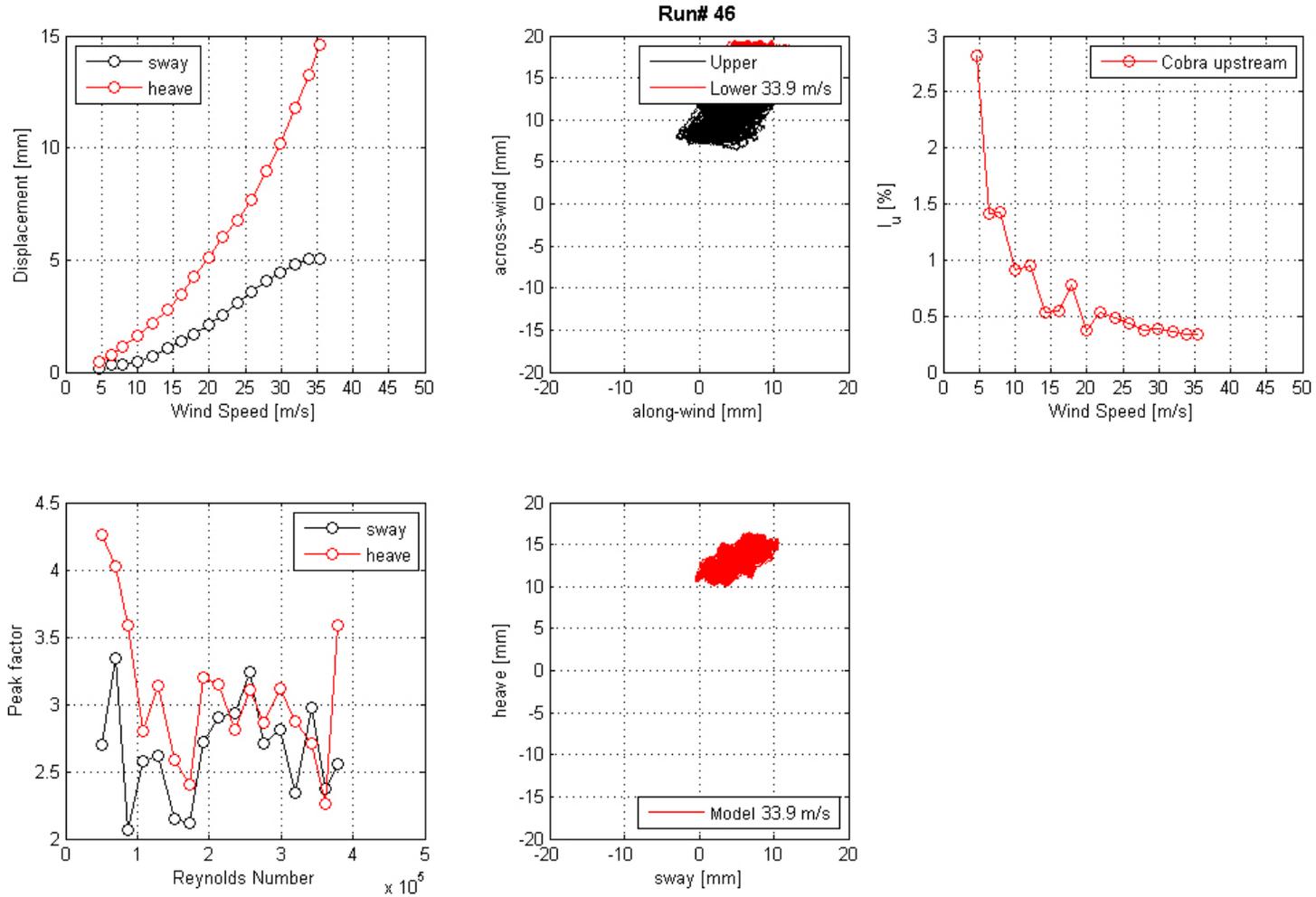
Figure 71. Graph. Mean displacement and peak factor from the laser, motion path at one wind speed, and intensity of turbulence measured at the entrance of the test section for run 46.
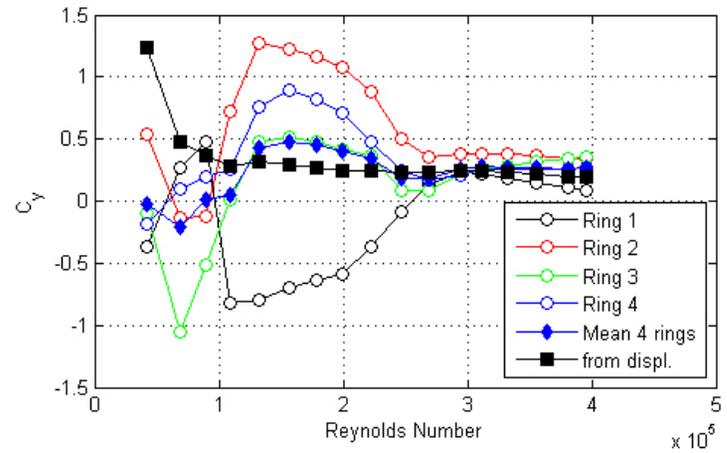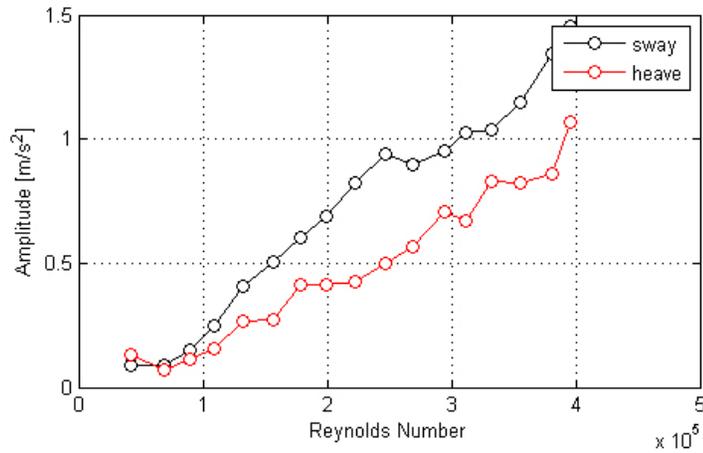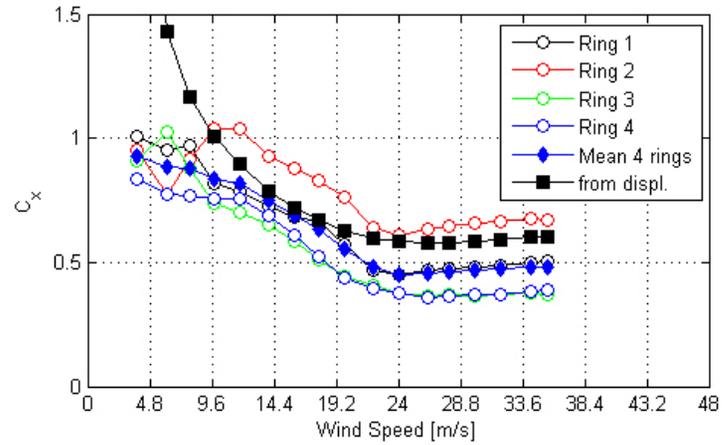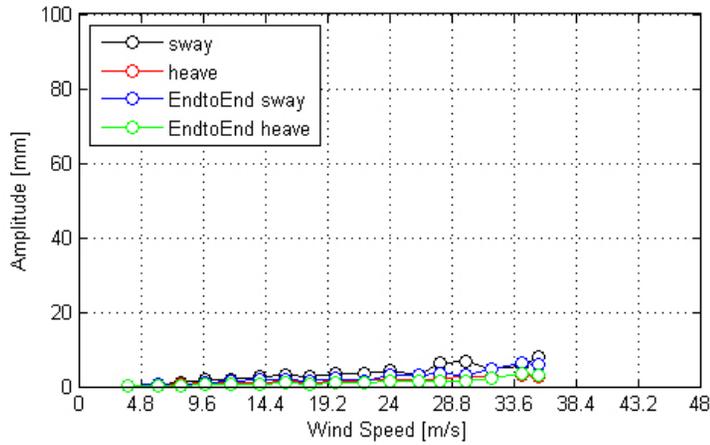
Figure 72. Graph. Response of the cable as a function of wind speed or Reynolds number as measured by the lasers, accelerometers, and surface pressures for run 49.
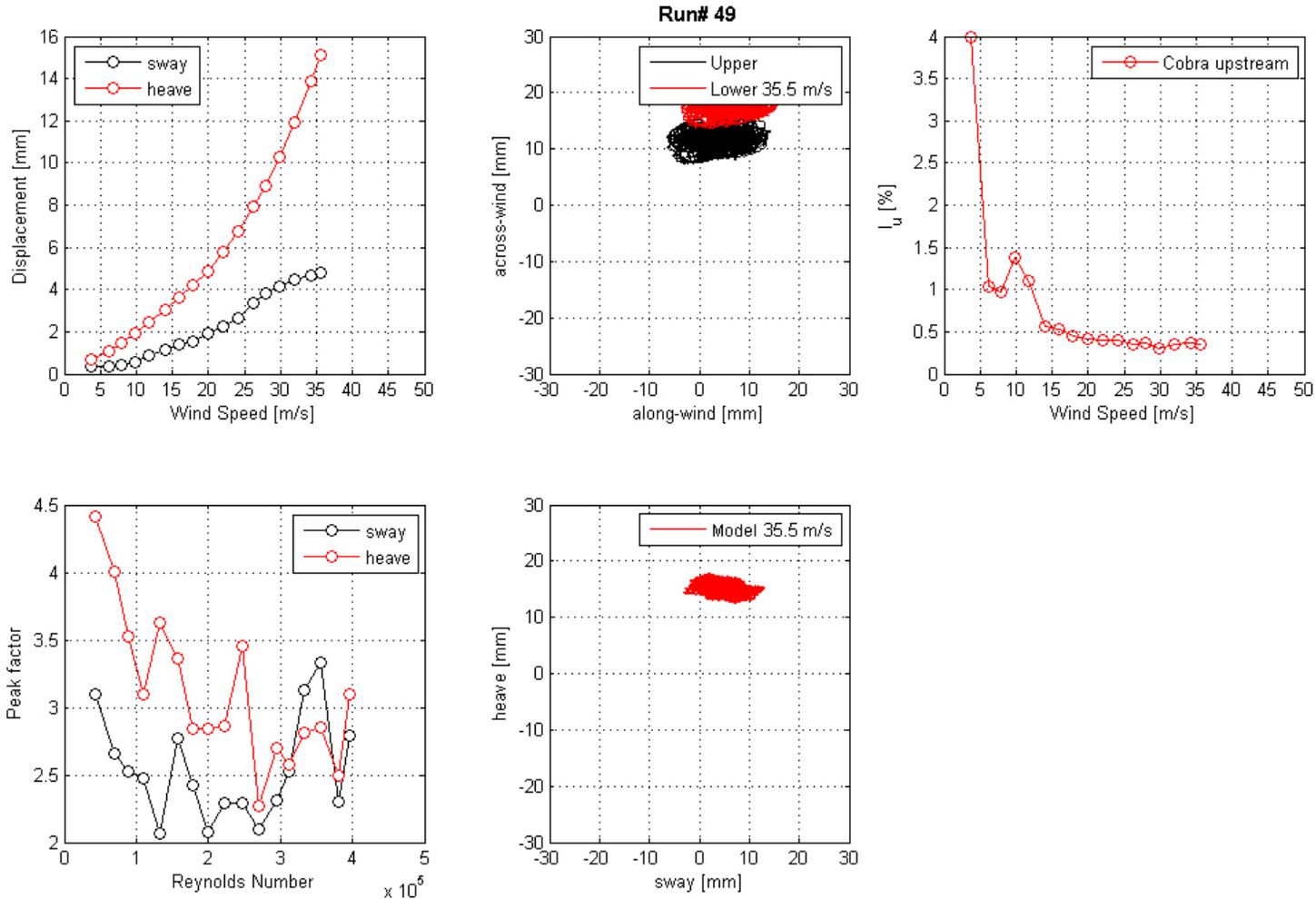
Figure 73. Graph. Mean displacement and peak factor from the laser, motion path at one wind speed, and intensity of turbulence measured at the entrance of the test section for run 49.
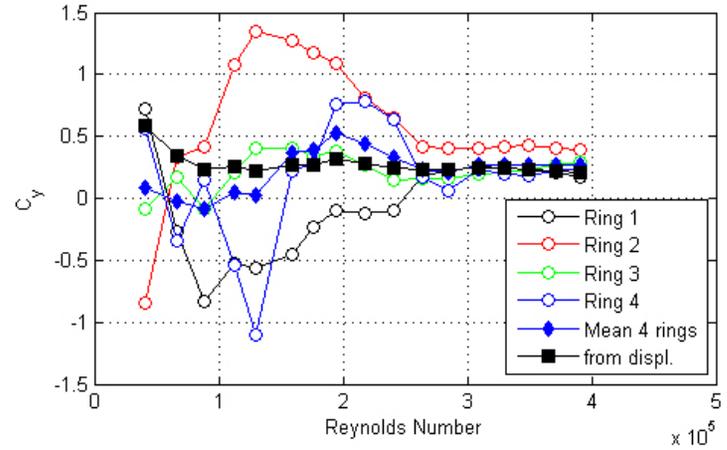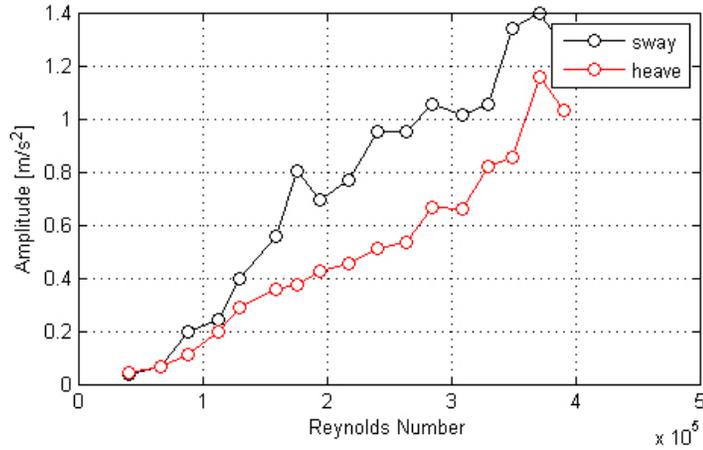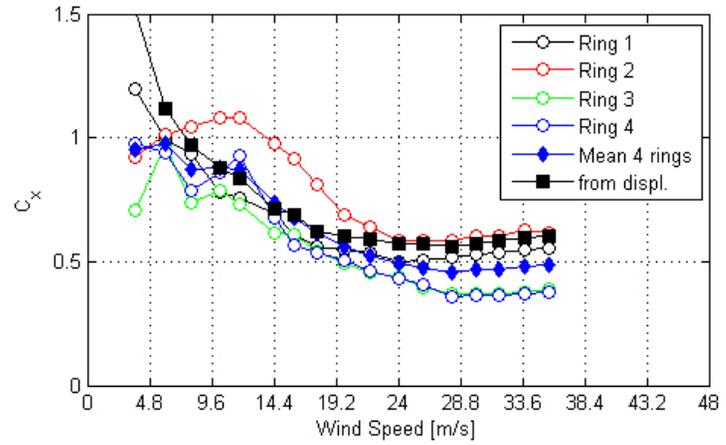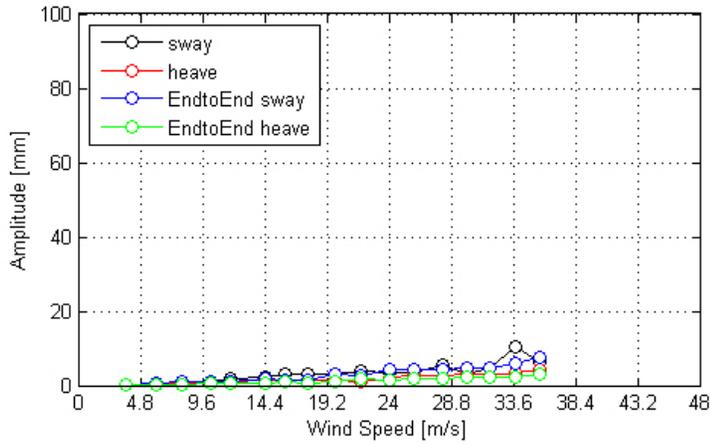
Figure 74. Graph. Response of the cable as a function of wind speed or Reynolds number as measured by the lasers, accelerometers, and surface pressures for run 52.
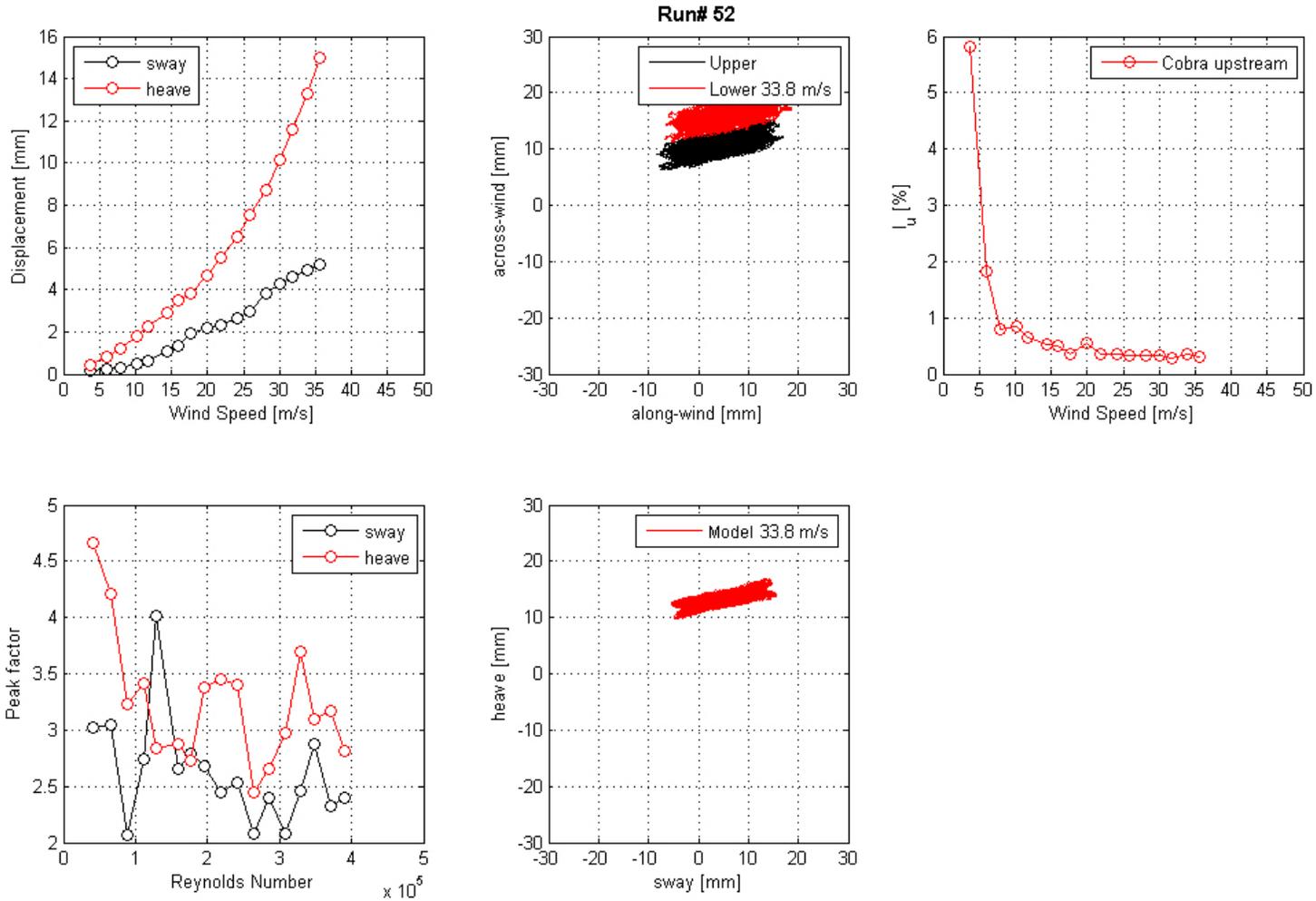
Figure 75. Graph. Mean displacement and peak factor from the laser, motion path at one wind speed, and intensity of turbulence measured at the entrance of the test section for run 52.
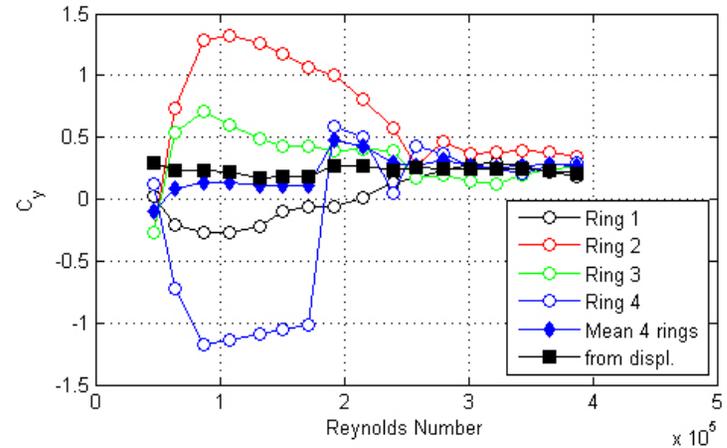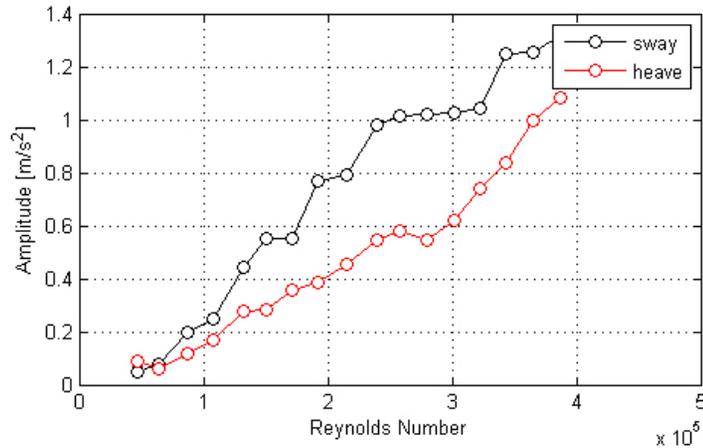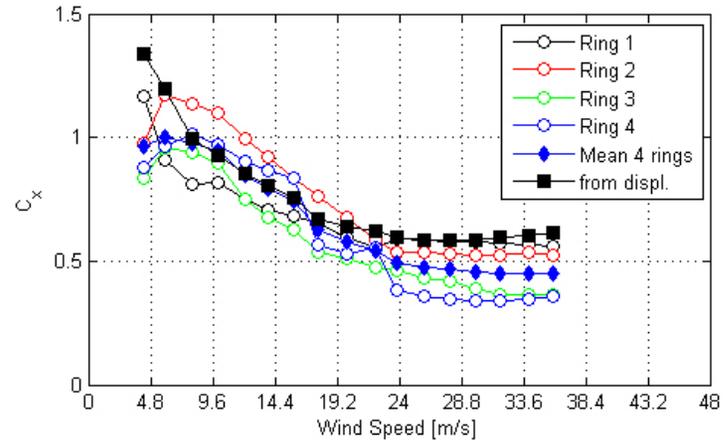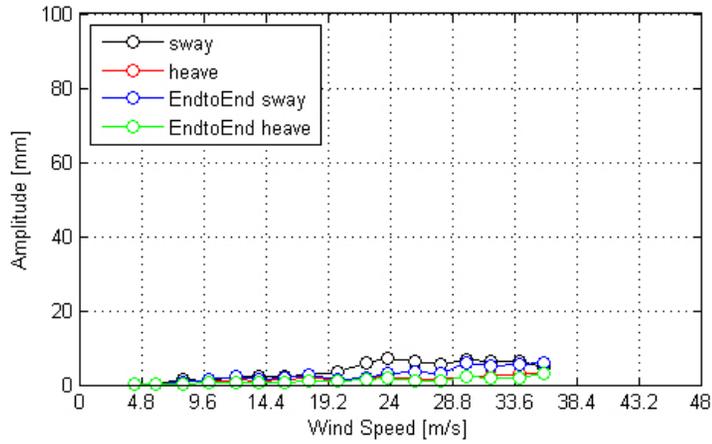
Figure 76. Graph. Response of the cable as a function of wind speed or Reynolds number as measured by the lasers, accelerometers, and surface pressures for run 56.
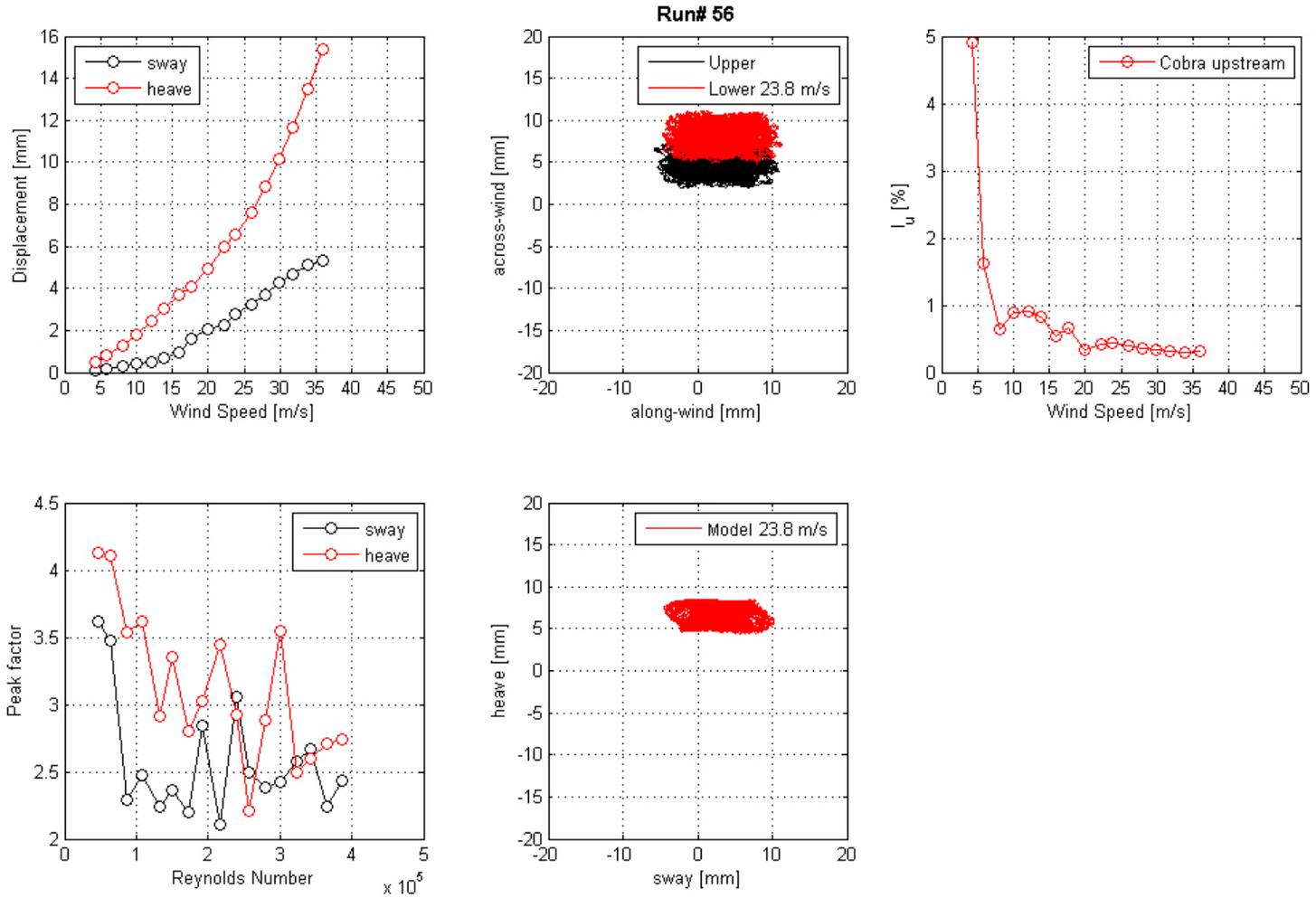
Figure 77. Graph. Mean displacement and peak factor from the laser, motion path at one wind speed, and intensity of turbulence measured at the entrance of the test section for run 56.
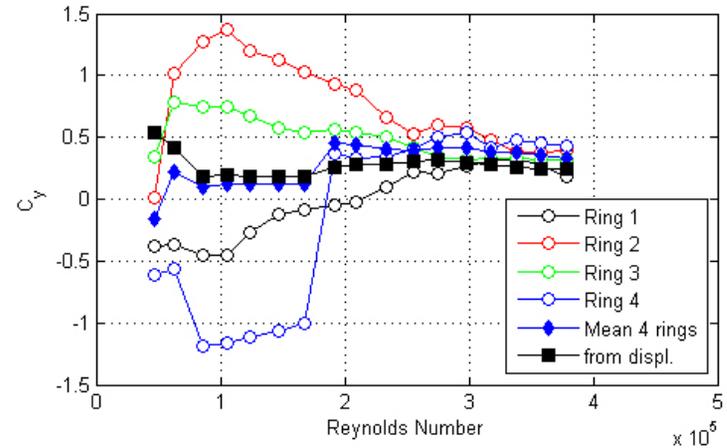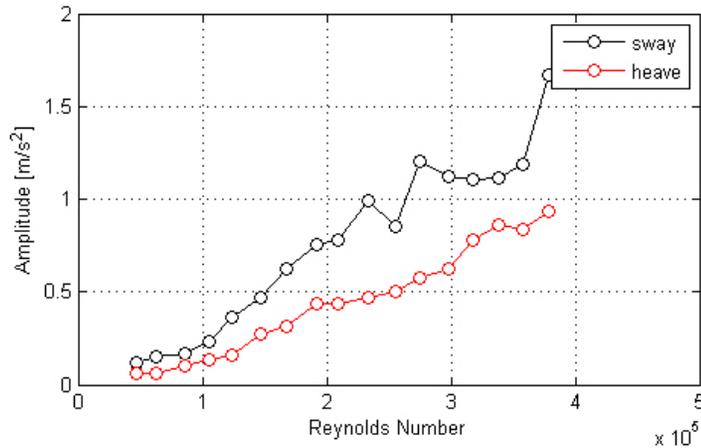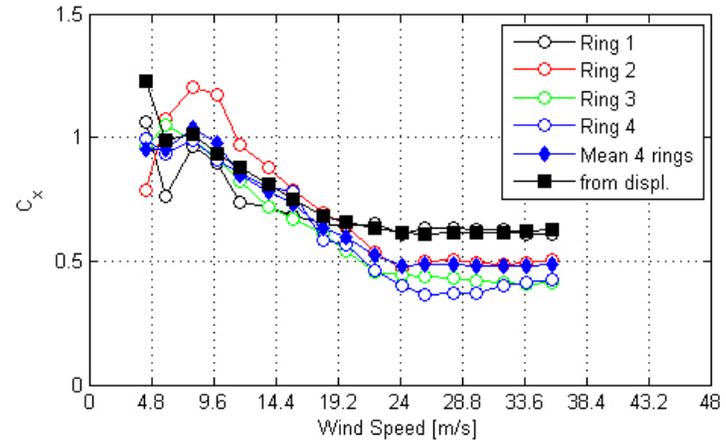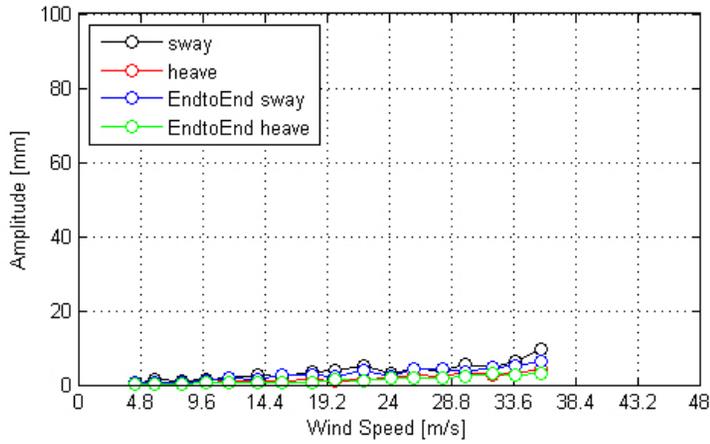
Figure 78. Graph. Response of the cable as a function of wind speed or Reynolds number as measured by the lasers, accelerometers, and surface pressures for run 60.
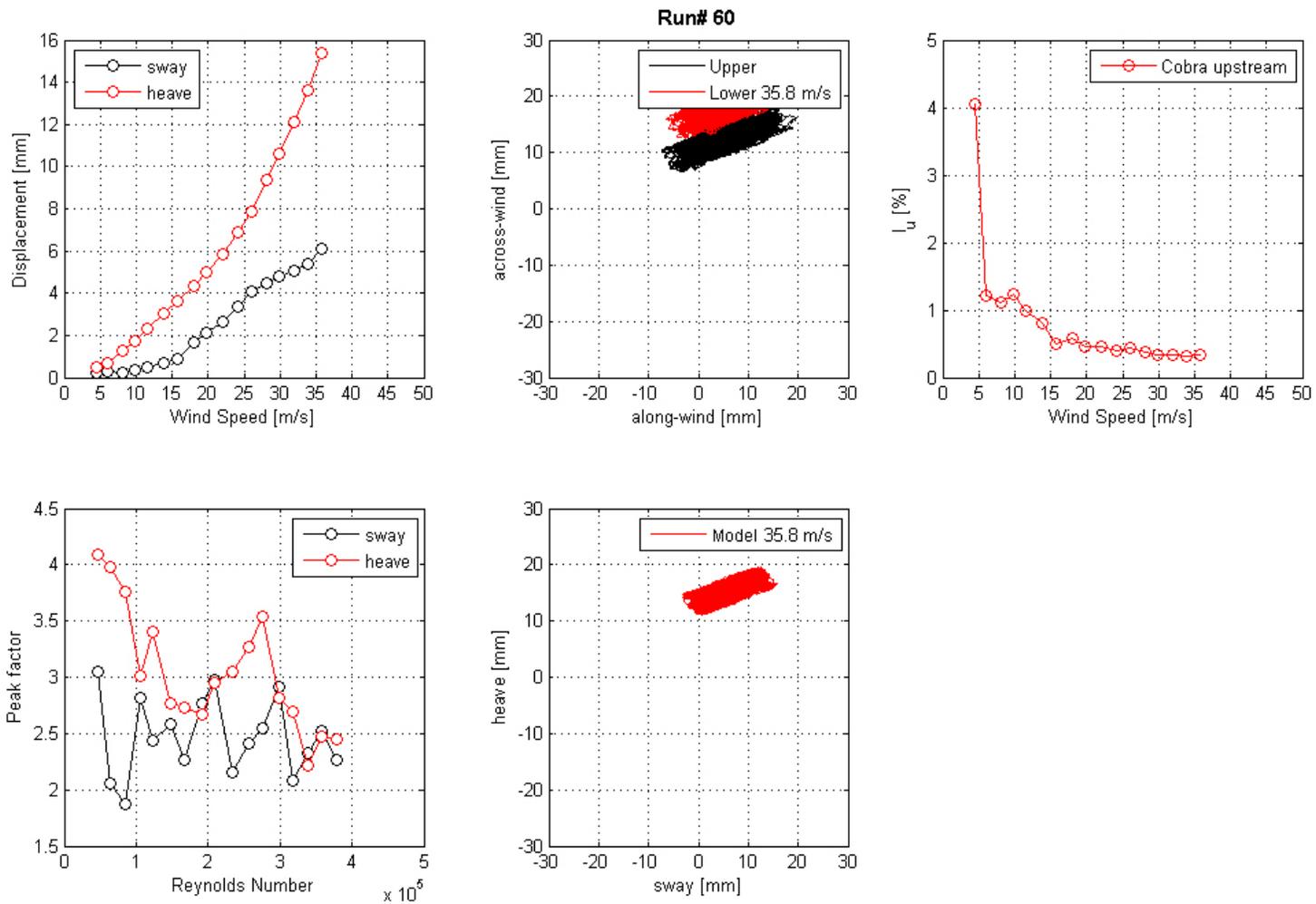
Figure 79. Graph. Mean displacement and peak factor from the laser, motion path at one wind speed, and intensity of turbulence measured at the entrance of the test section for run 60.
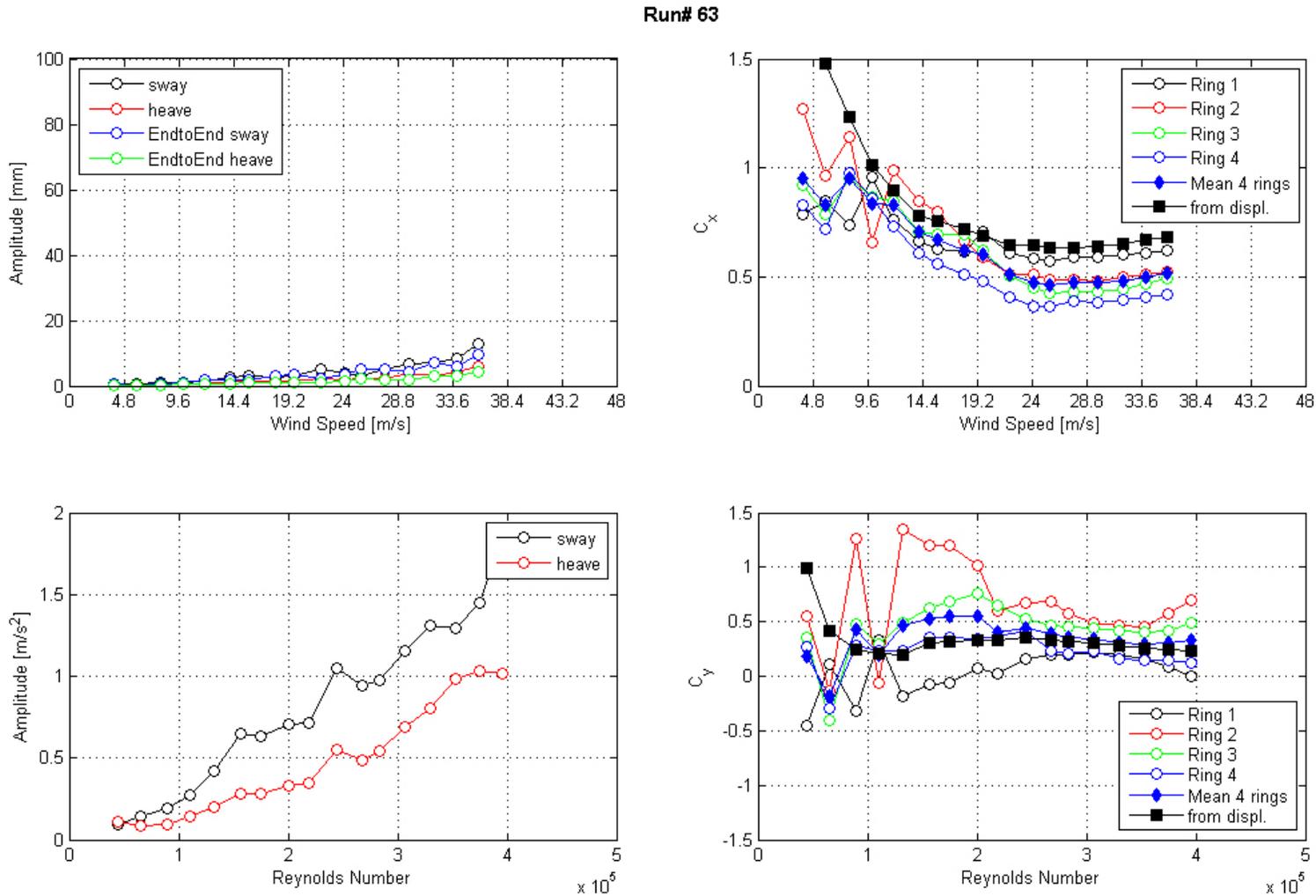
Figure 80. Graph. Response of the cable as a function of wind speed or Reynolds number as measured by the lasers, accelerometers, and surface pressures for run 63.
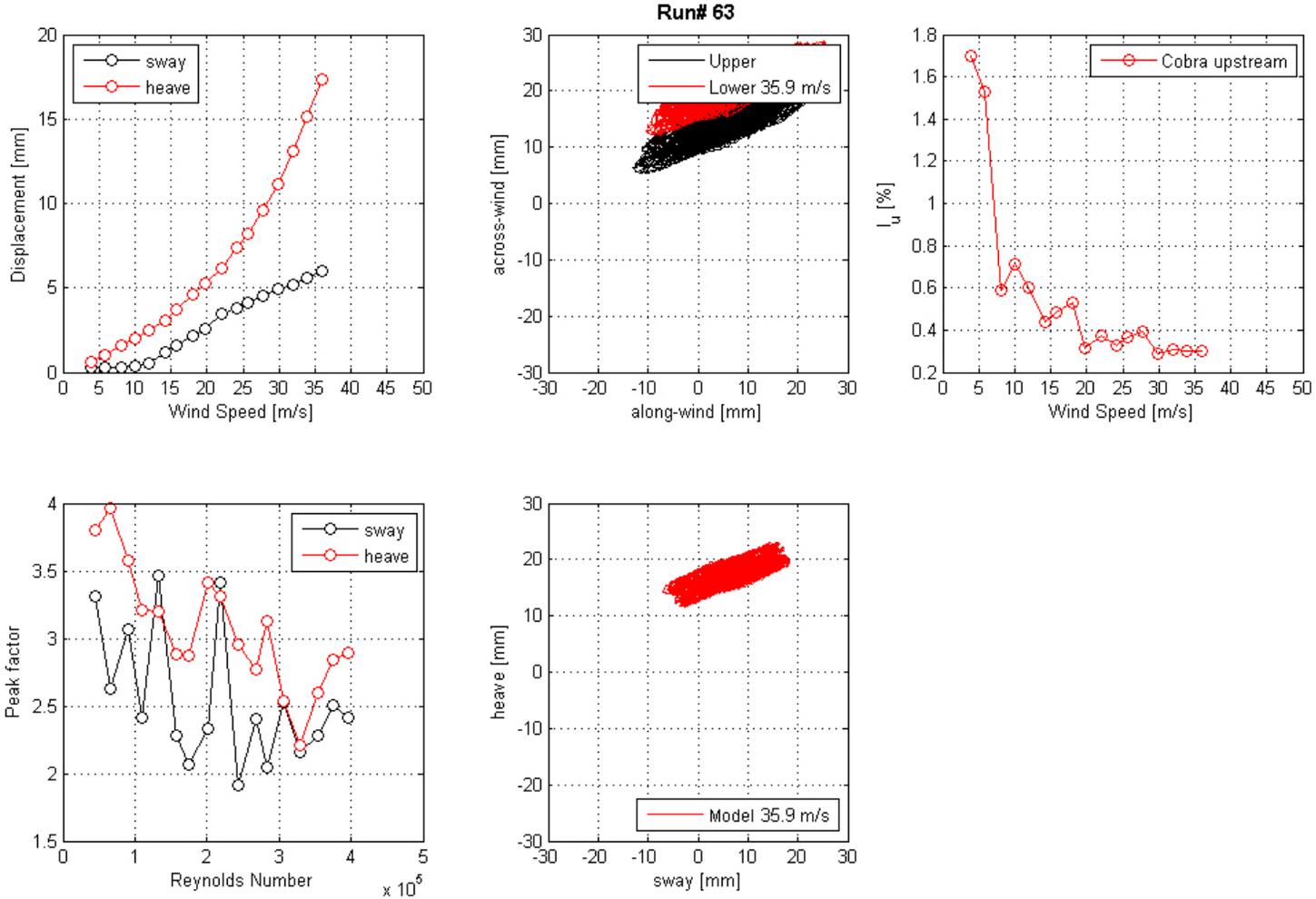
Figure 81. Graph. Mean displacement and peak factor from the laser, motion path at one wind speed, and intensity of turbulence measured at the entrance of the test section for run 63.
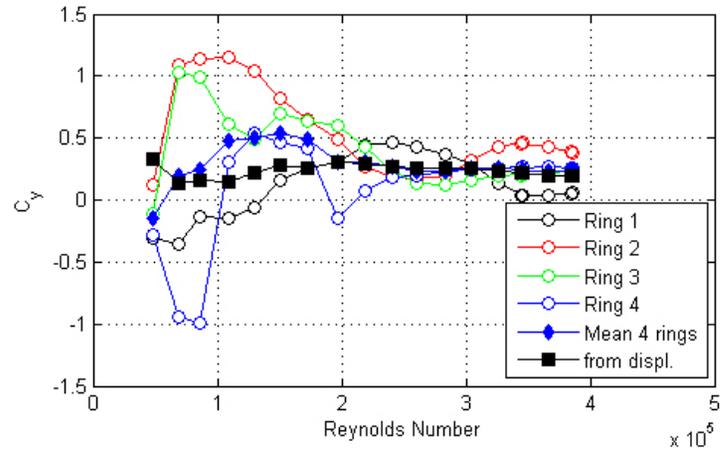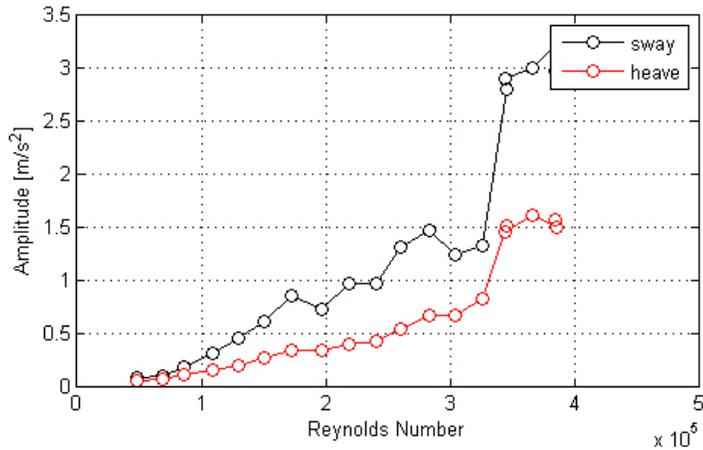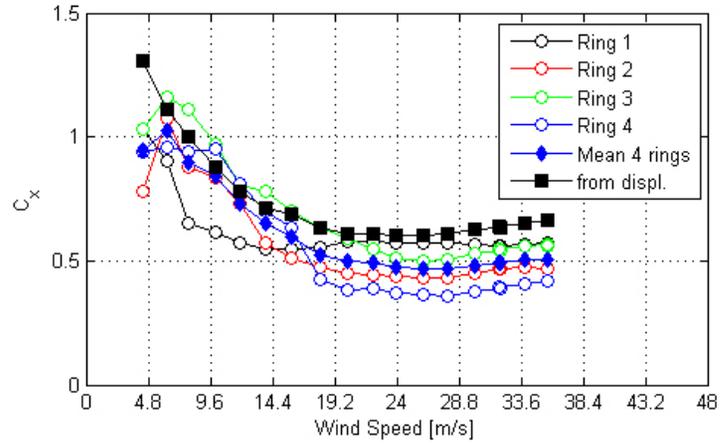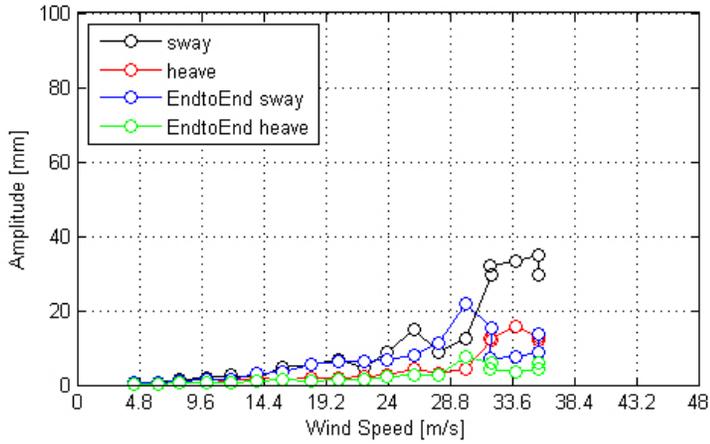
Figure 82. Graph. Response of the cable as a function of wind speed or Reynolds number as measured by the lasers, accelerometers, and surface pressures for run 66.
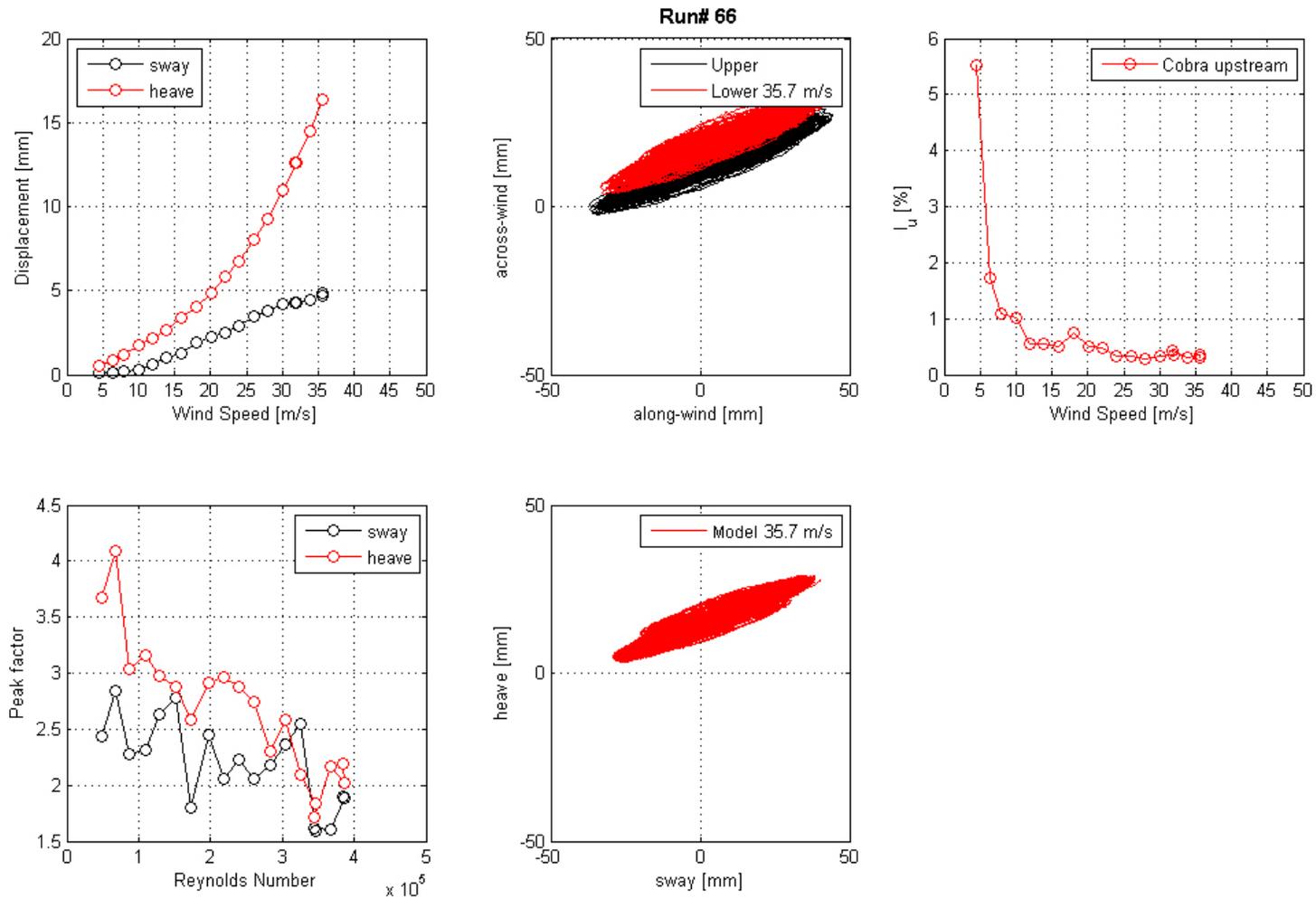
Figure 83. Graph. Mean displacement and peak factor from the laser, motion path at one wind speed, and intensity of turbulence measured at the entrance of the test section for run 66.
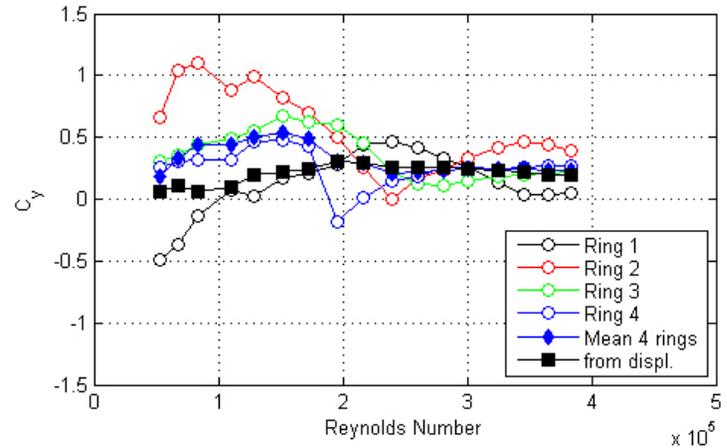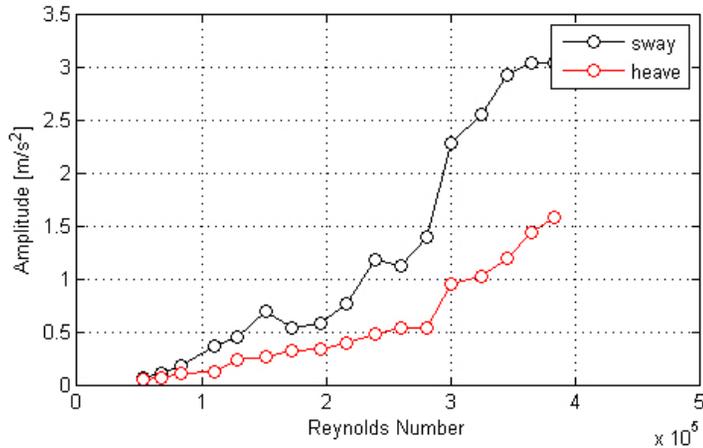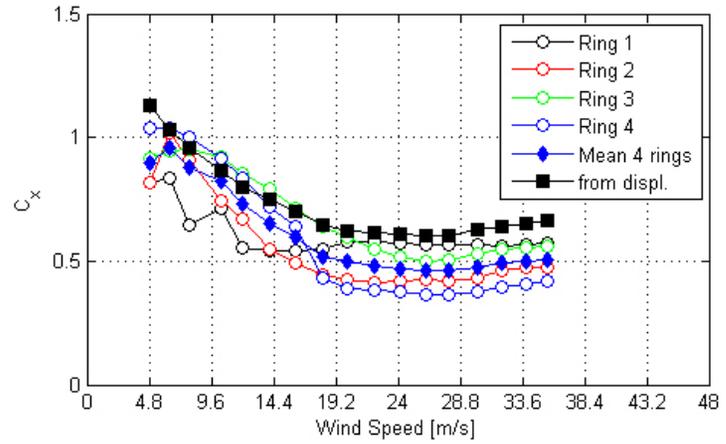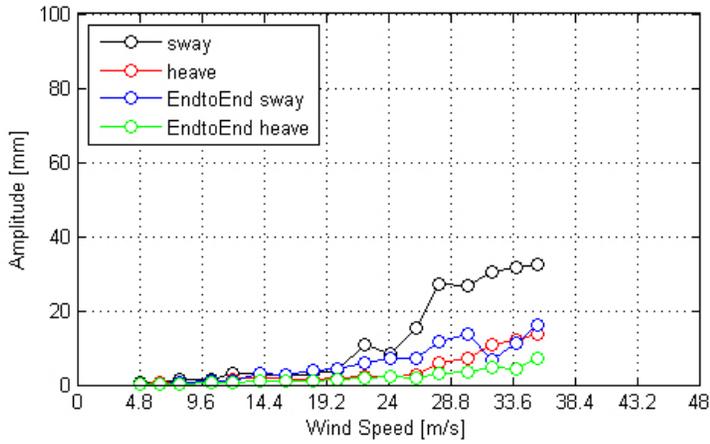
Figure 84. Graph. Response of the cable as a function of wind speed or Reynolds number as measured by the lasers, accelerometers, and surface pressures for run 67.
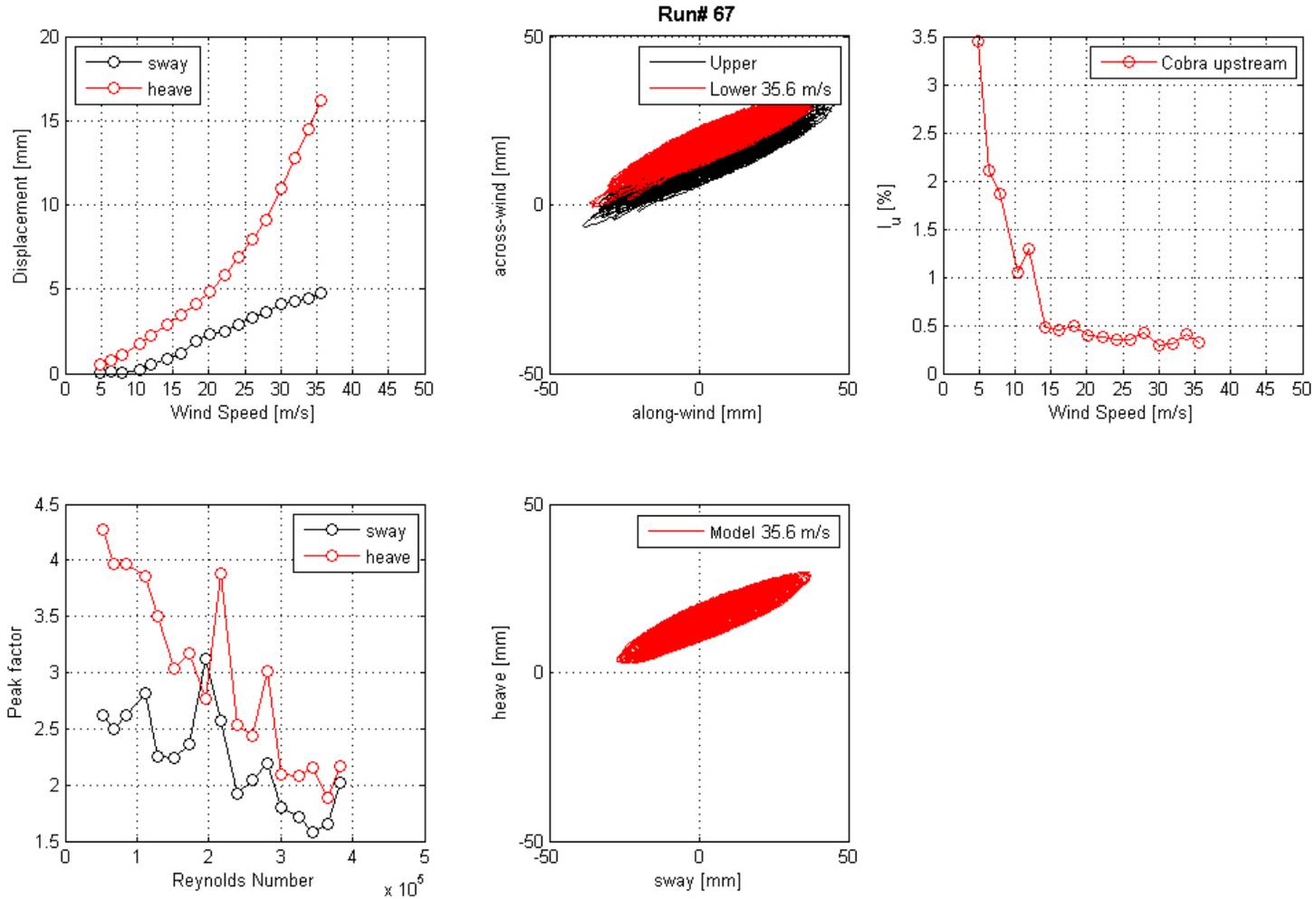
Figure 85. Graph. Mean displacement and peak factor from the laser, motion path at one wind speed, and intensity of turbulence measured at the entrance of the test section for run 67.
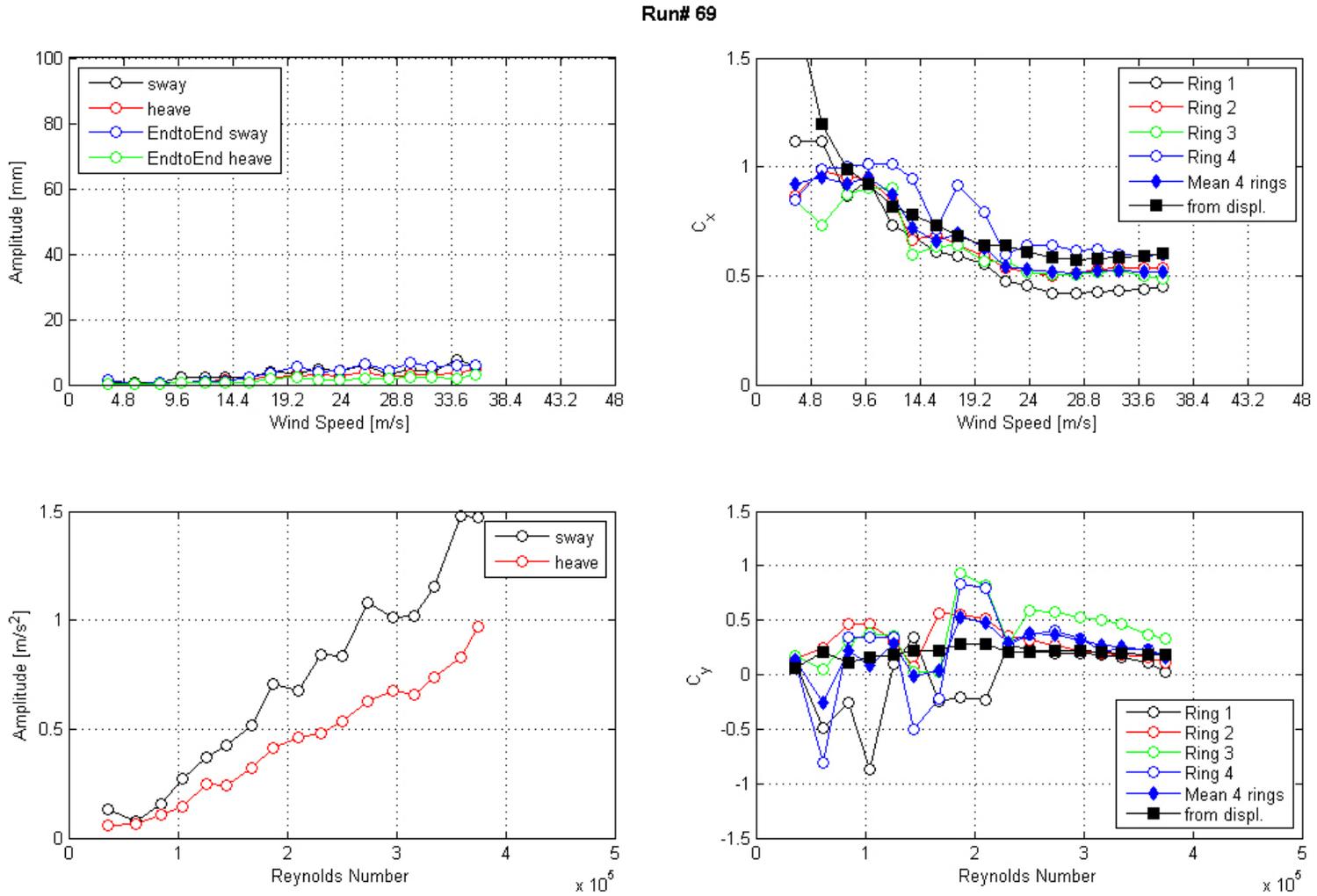
Figure 86. Graph. Response of the cable as a function of wind speed or Reynolds number as measured by the lasers, accelerometers, and surface pressures for run 69.
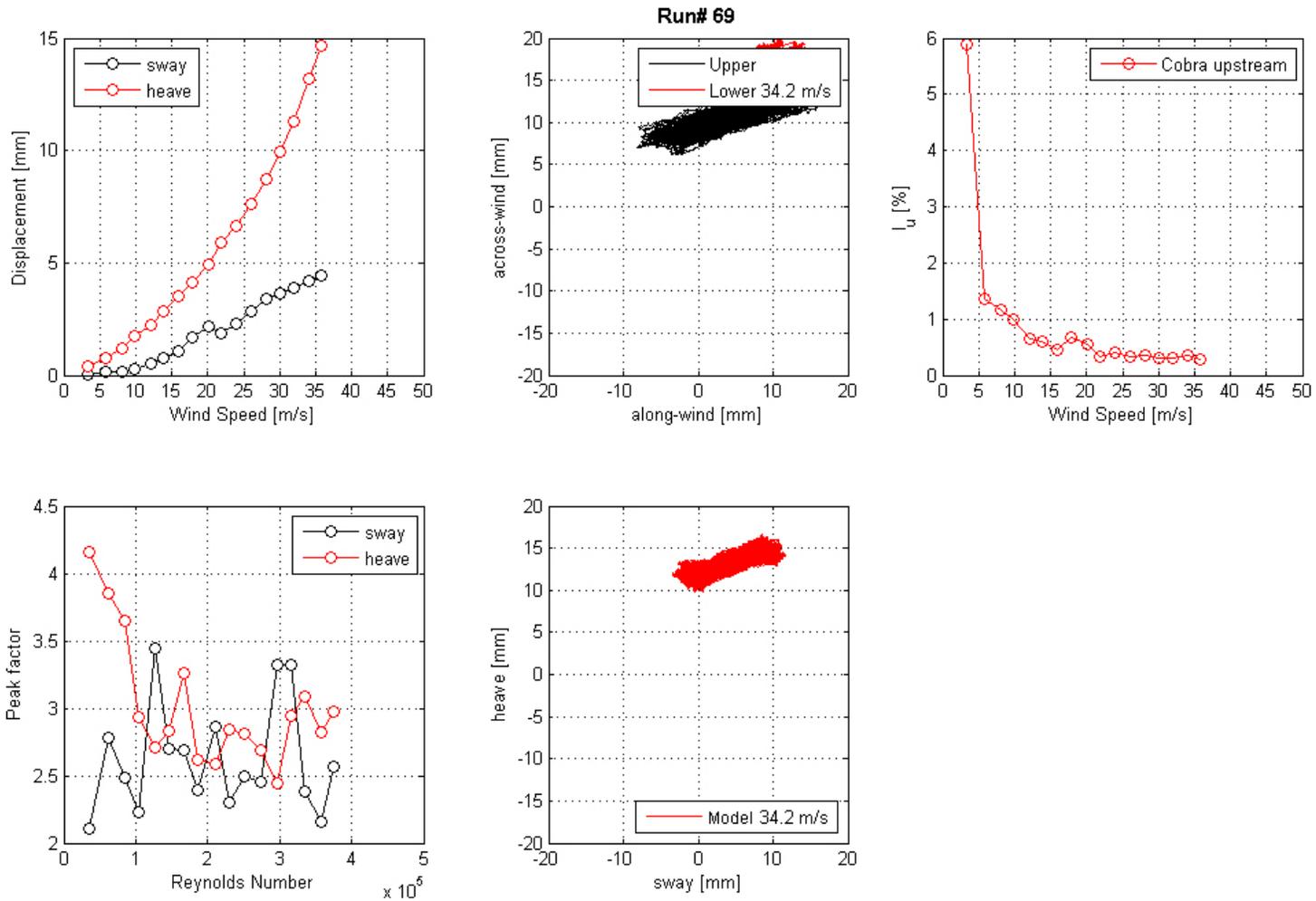
Figure 87. Graph. Mean displacement and peak factor from the laser, motion path at one wind speed, and intensity of turbulence measured at the entrance of the test section for run 69.
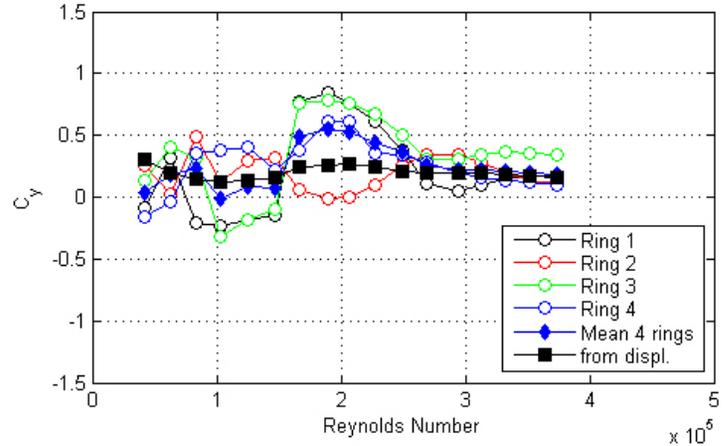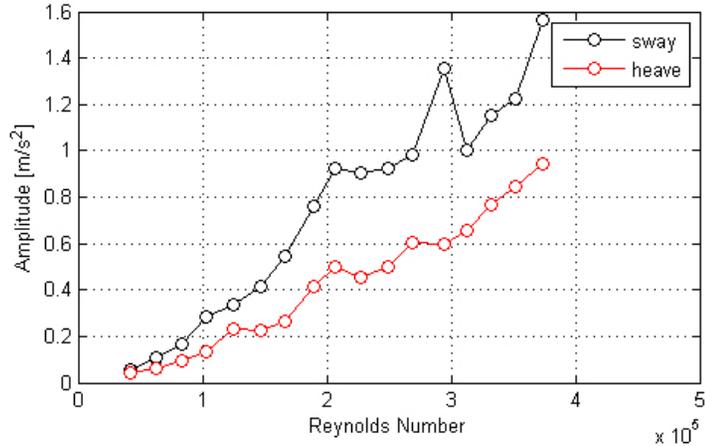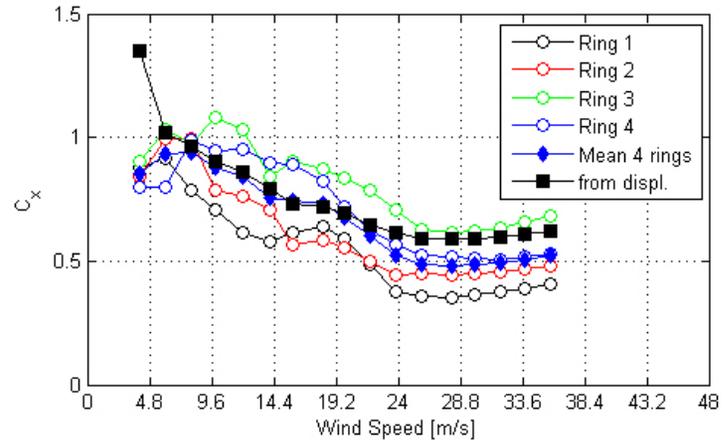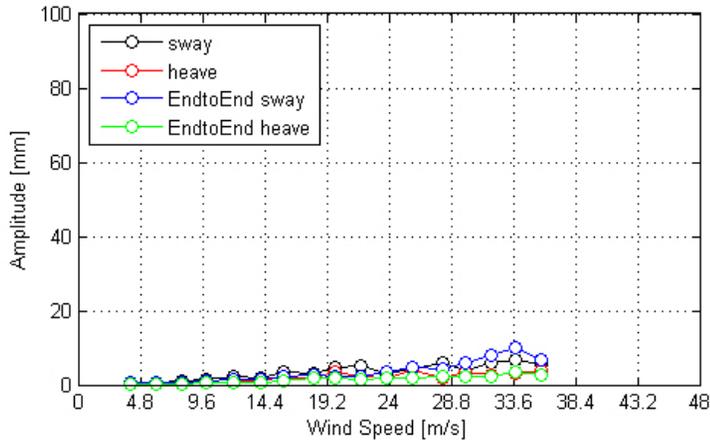
Figure 88. Graph. Response of the cable as a function of wind speed or Reynolds number as measured by the lasers, accelerometers, and surface pressures for run 71.
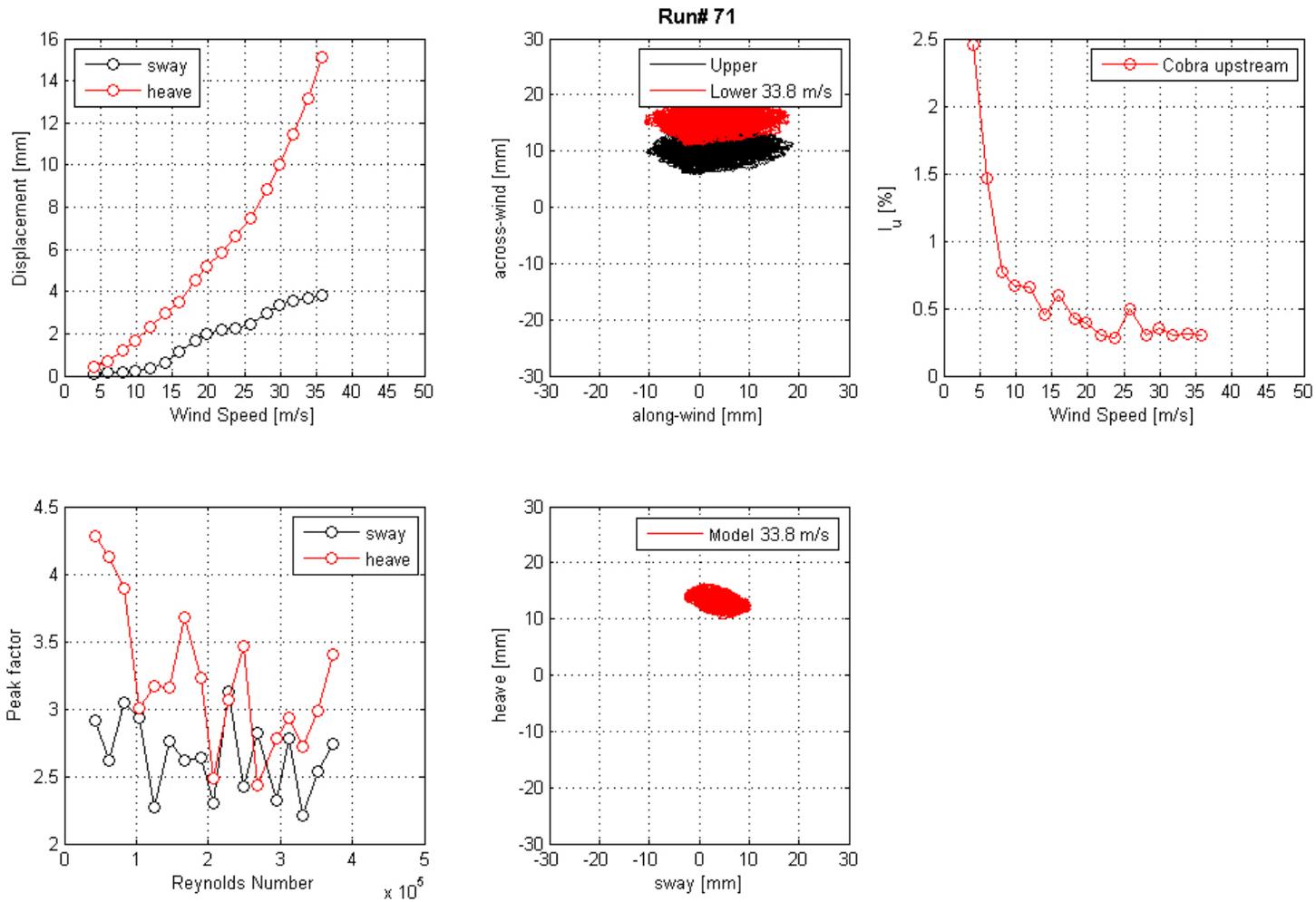
Figure 89. Graph. Mean displacement and peak factor from the laser, motion path at one wind speed, and intensity of turbulence measured at the entrance of the test section for run 71.
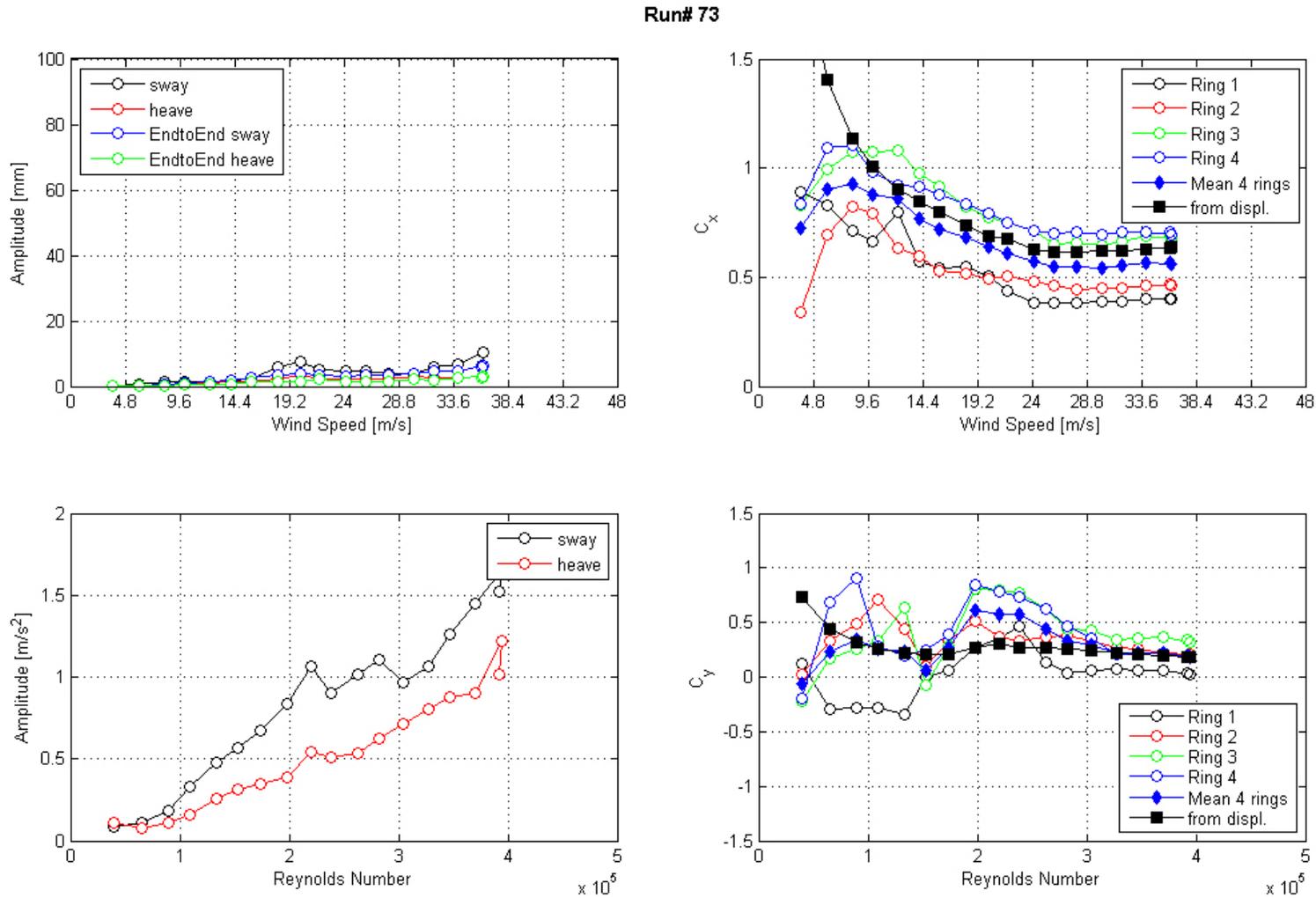
Figure 90. Graph. Response of the cable as a function of wind speed or Reynolds number as measured by the lasers, accelerometers, and surface pressures for run 73.
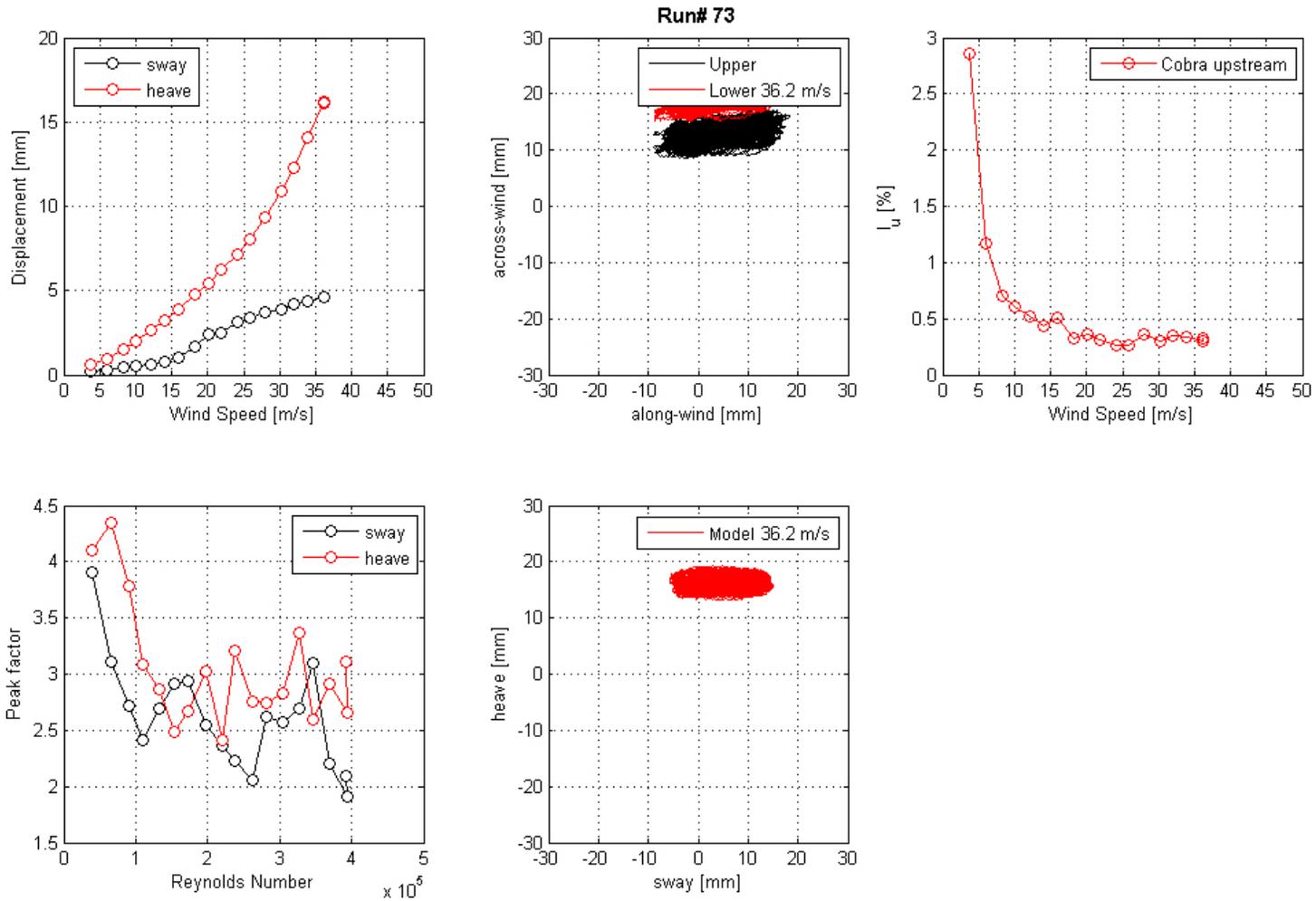
Figure 91. Graph. Mean displacement and peak factor from the laser, motion path at one wind speed, and intensity of turbulence measured at the entrance of the test section for run 73.
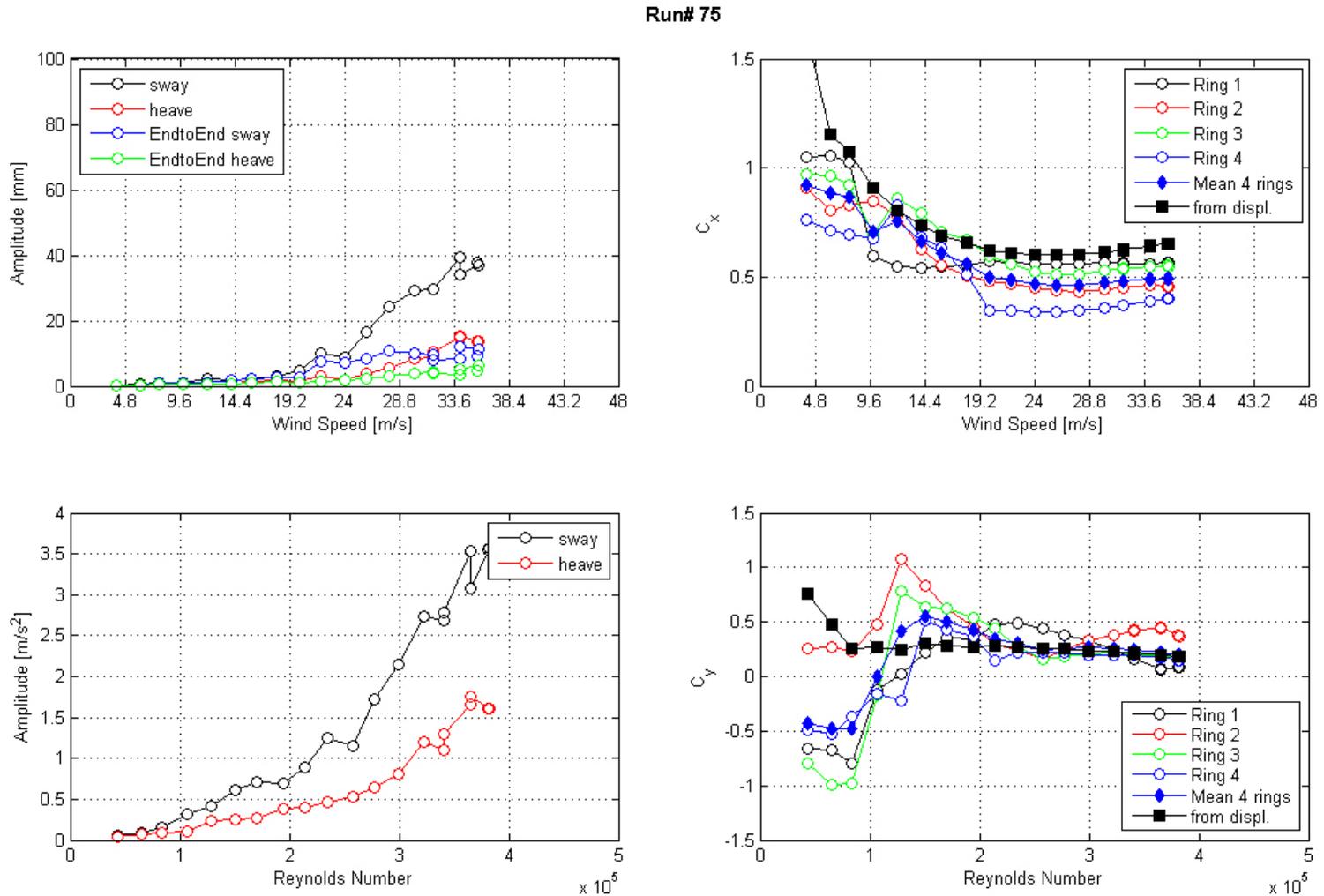
Figure 92. Graph. Response of the cable as a function of wind speed or Reynolds number as measured by the lasers, accelerometers, and surface pressures for run 75.
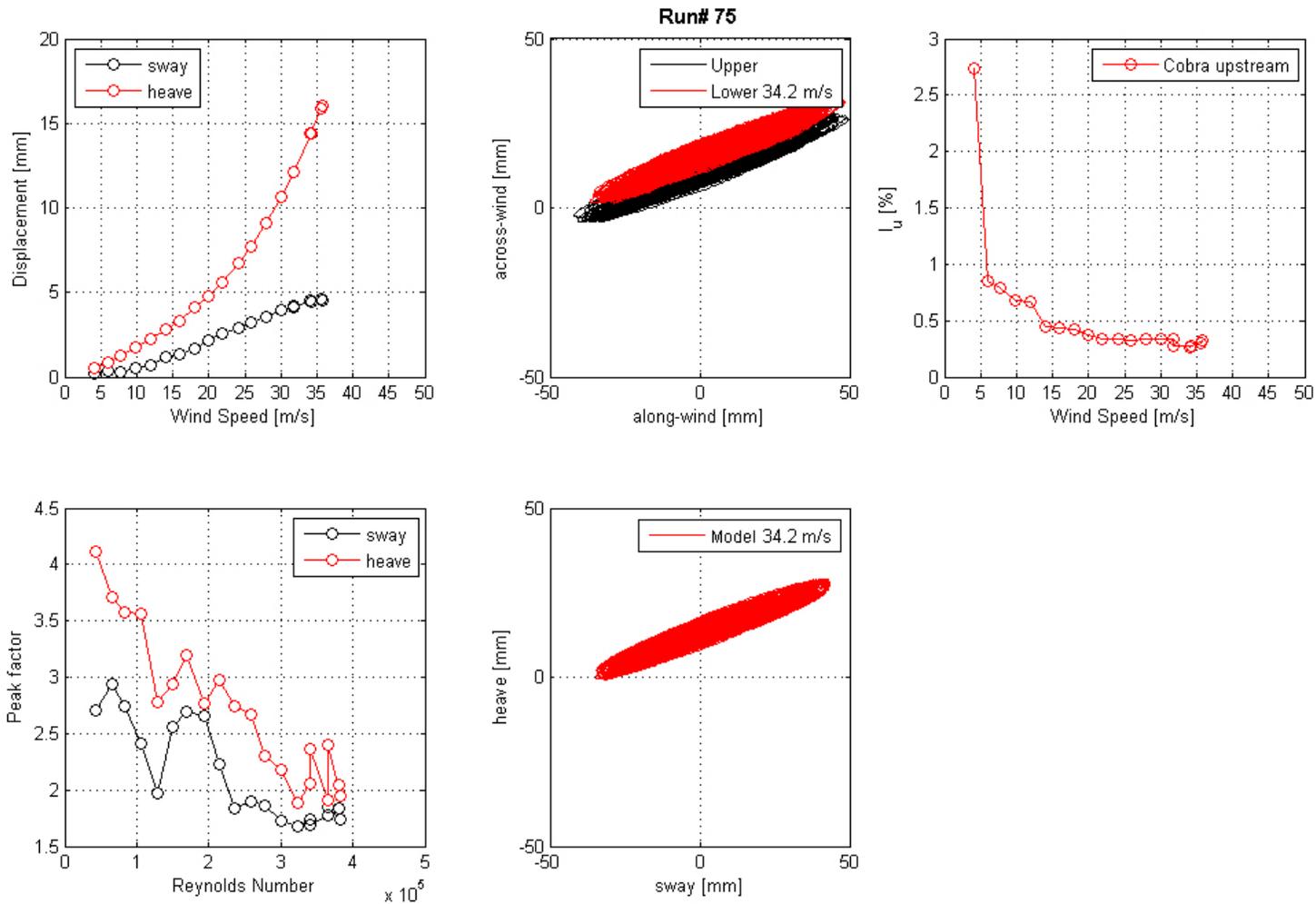
Figure 93. Graph. Mean displacement and peak factor from the laser, motion path at one wind speed, and intensity of turbulence measured at the entrance of the test section for run 75.
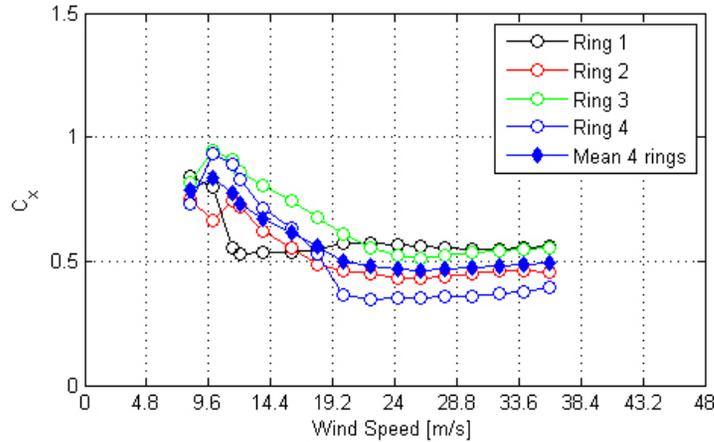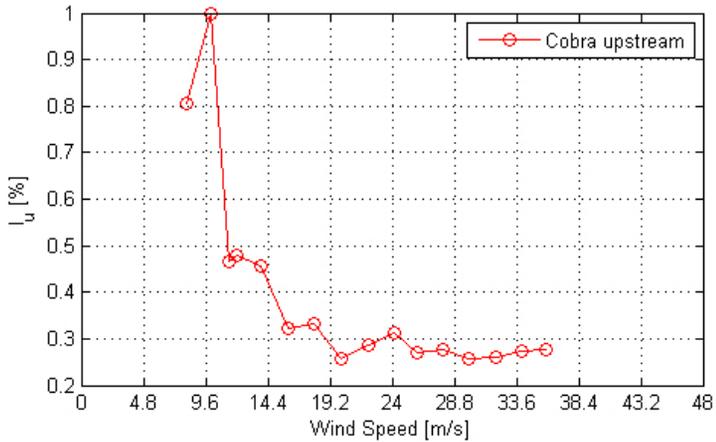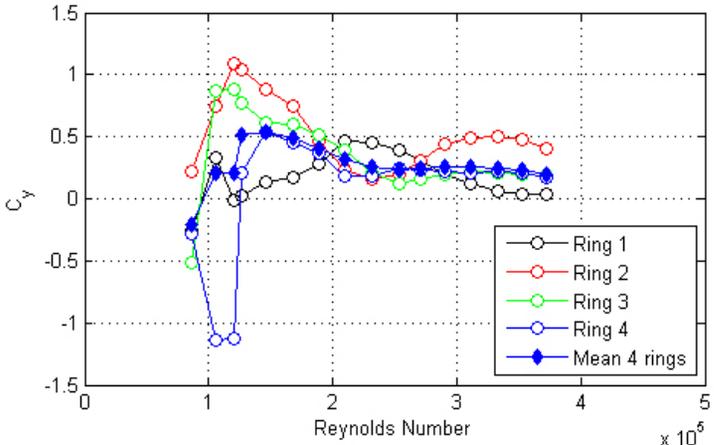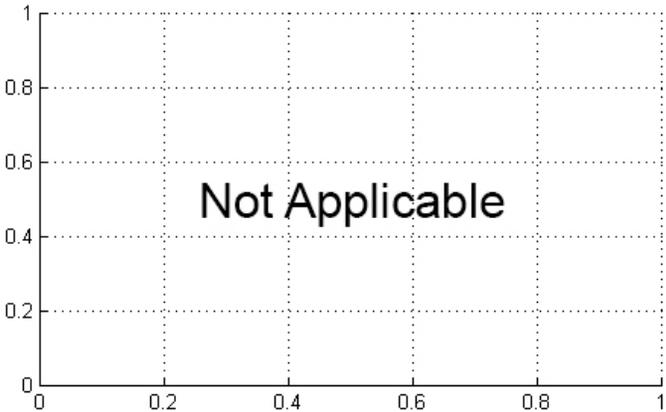
Figure 94. Graph. Intensity of turbulence measured at the entrance of the test section and C_x and C_y calculated from surface pressure measurements as a function of Reynolds number and wind speed for run 81.
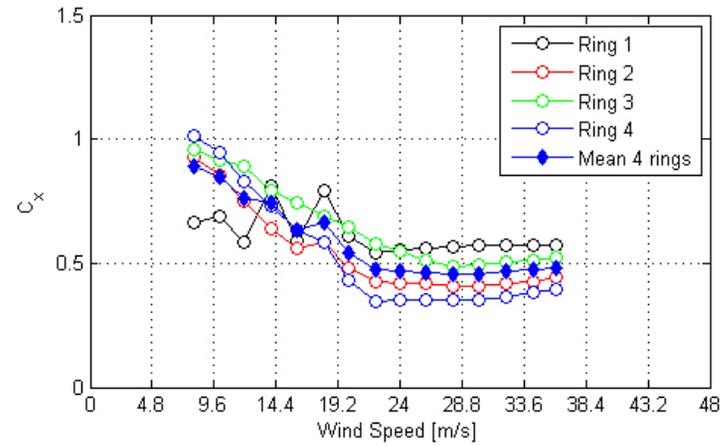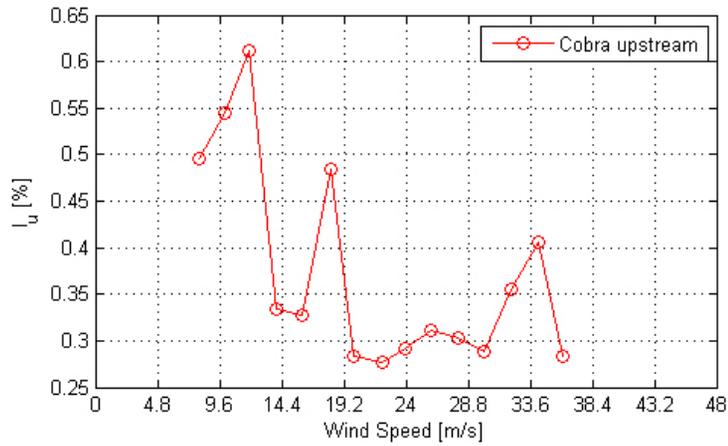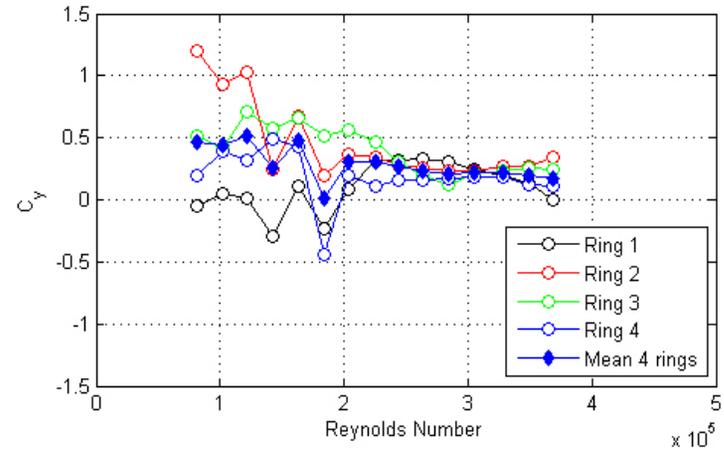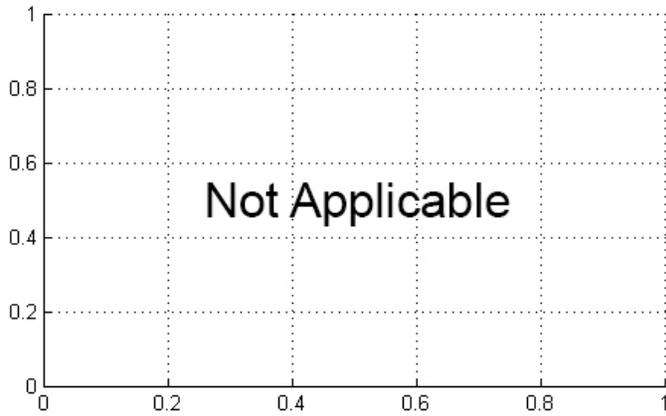
Figure 95. Graph. Intensity of turbulence measured at the entrance of the test section and C_x and C_y calculated from surface pressure measurements as a function of Reynolds number and wind speed for run 85.
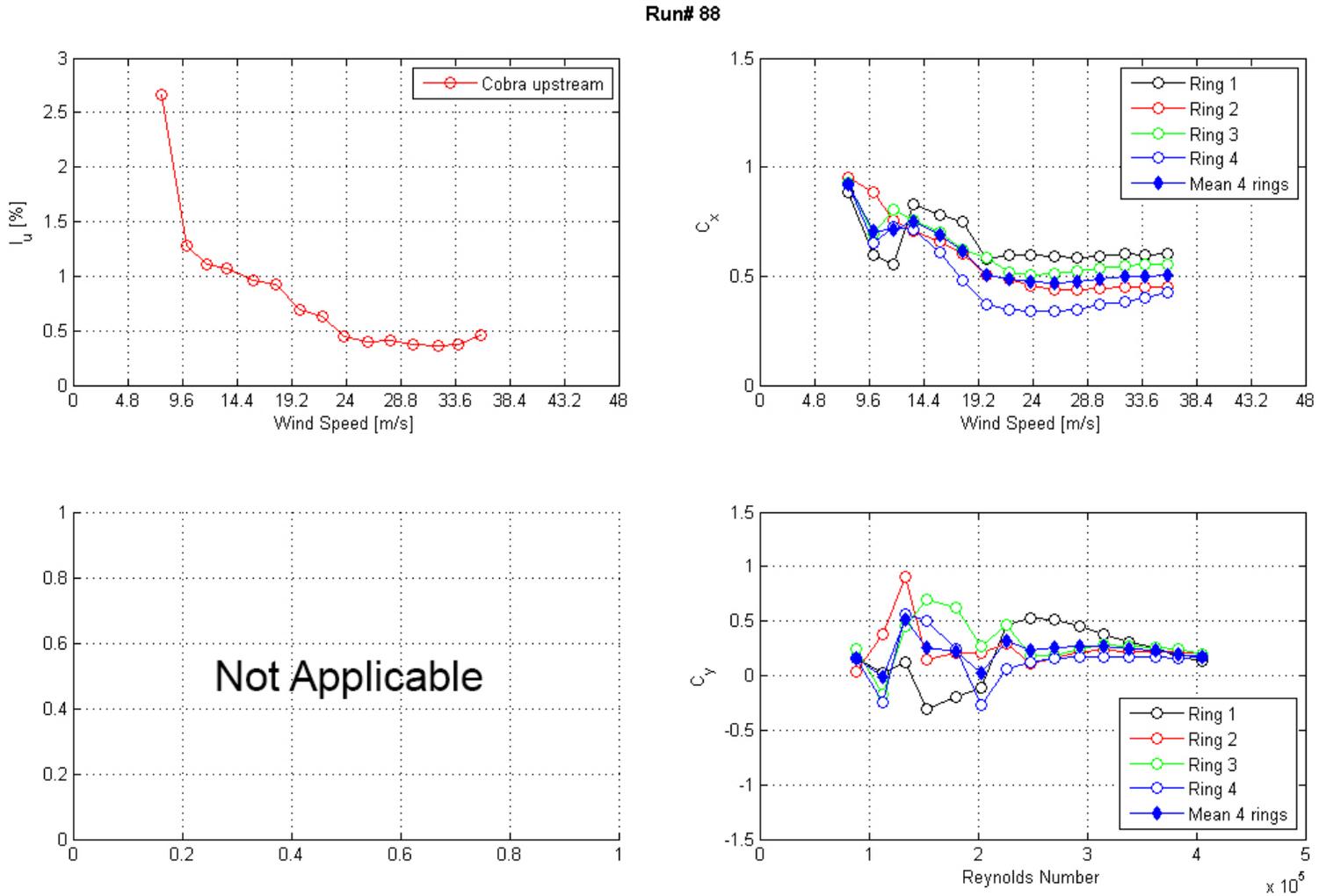
Figure 96. Graph. Intensity of turbulence measured at the entrance of the test section and C_x and C_y calculated from surface pressure measurements as a function of Reynolds number and wind speed for run 88.
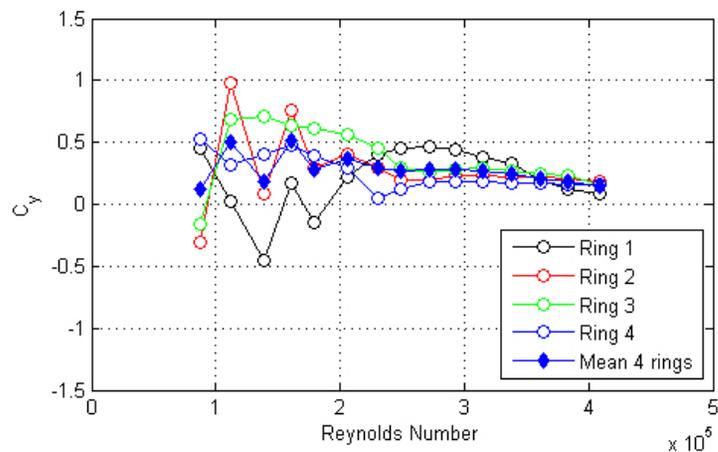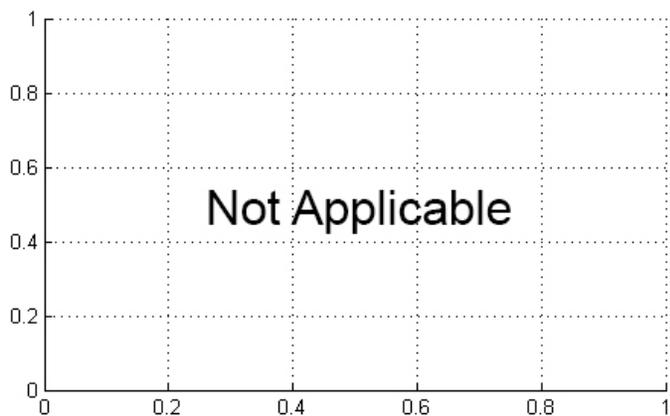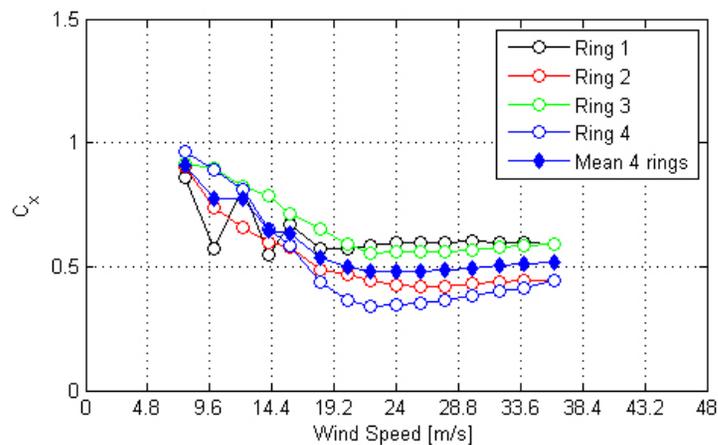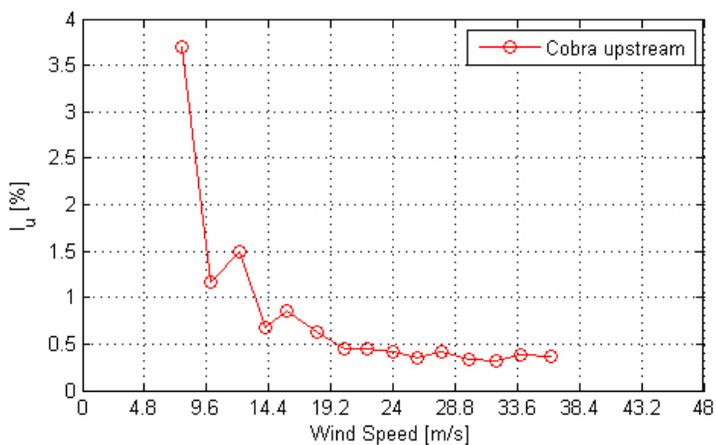
Figure 97. Graph. Intensity of turbulence measured at the entrance of the test section and C_x and C_y calculated from surface pressure measurements as a function of Reynolds number and wind speed for run 90.
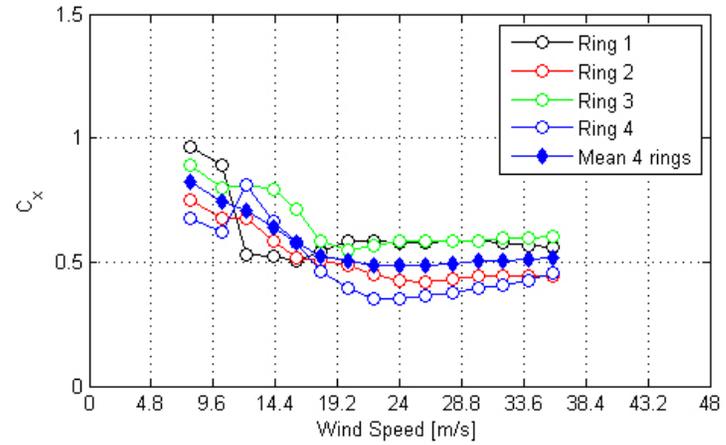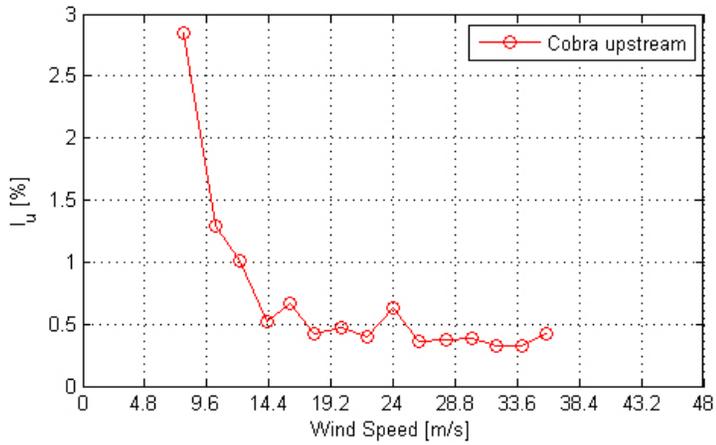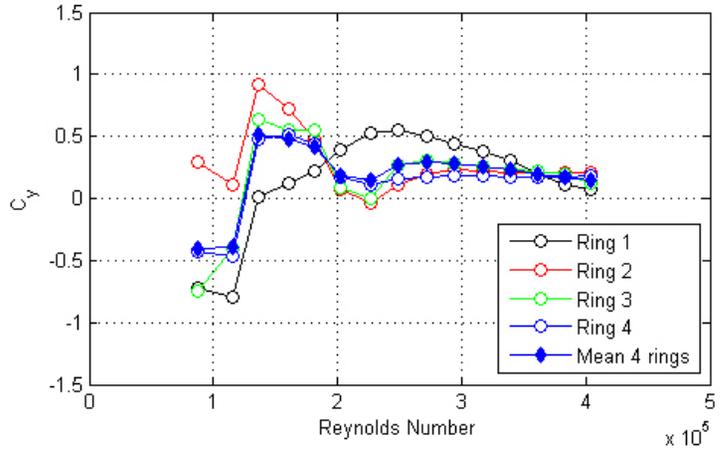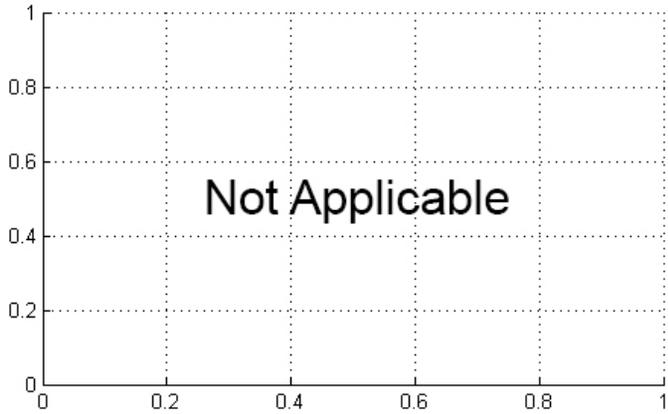
Figure 98. Graph. Intensity of turbulence measured at the entrance of the test section and C_x and C_y calculated from surface pressure measurements as a function of Reynolds number and wind speed for run 92.
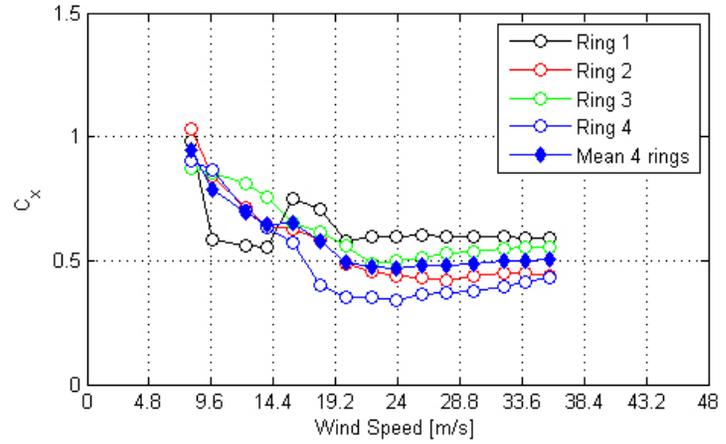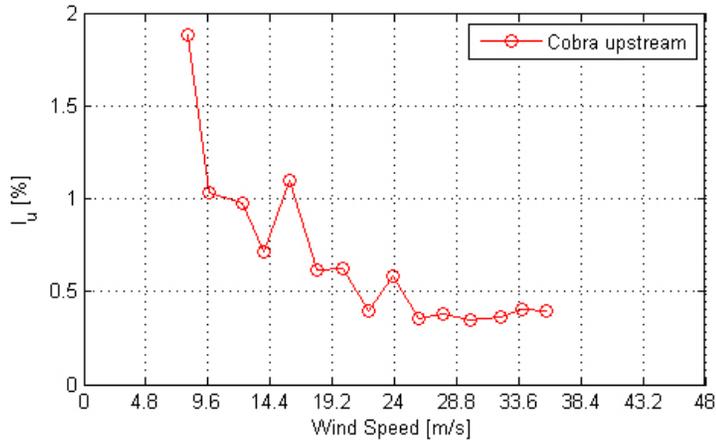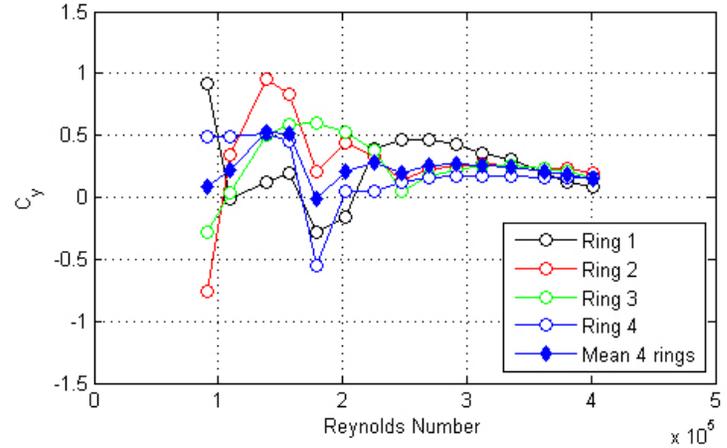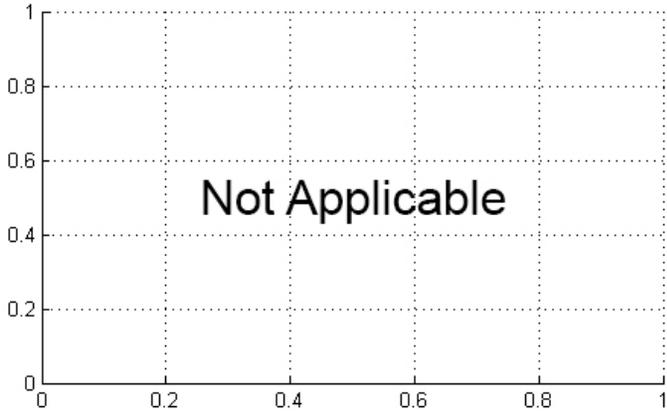
Figure 99. Graph. Intensity of turbulence measured at the entrance of the test section and *C_x* and *C_y* calculated from surface pressure measurements as a function of Reynolds number and wind speed for run 94.
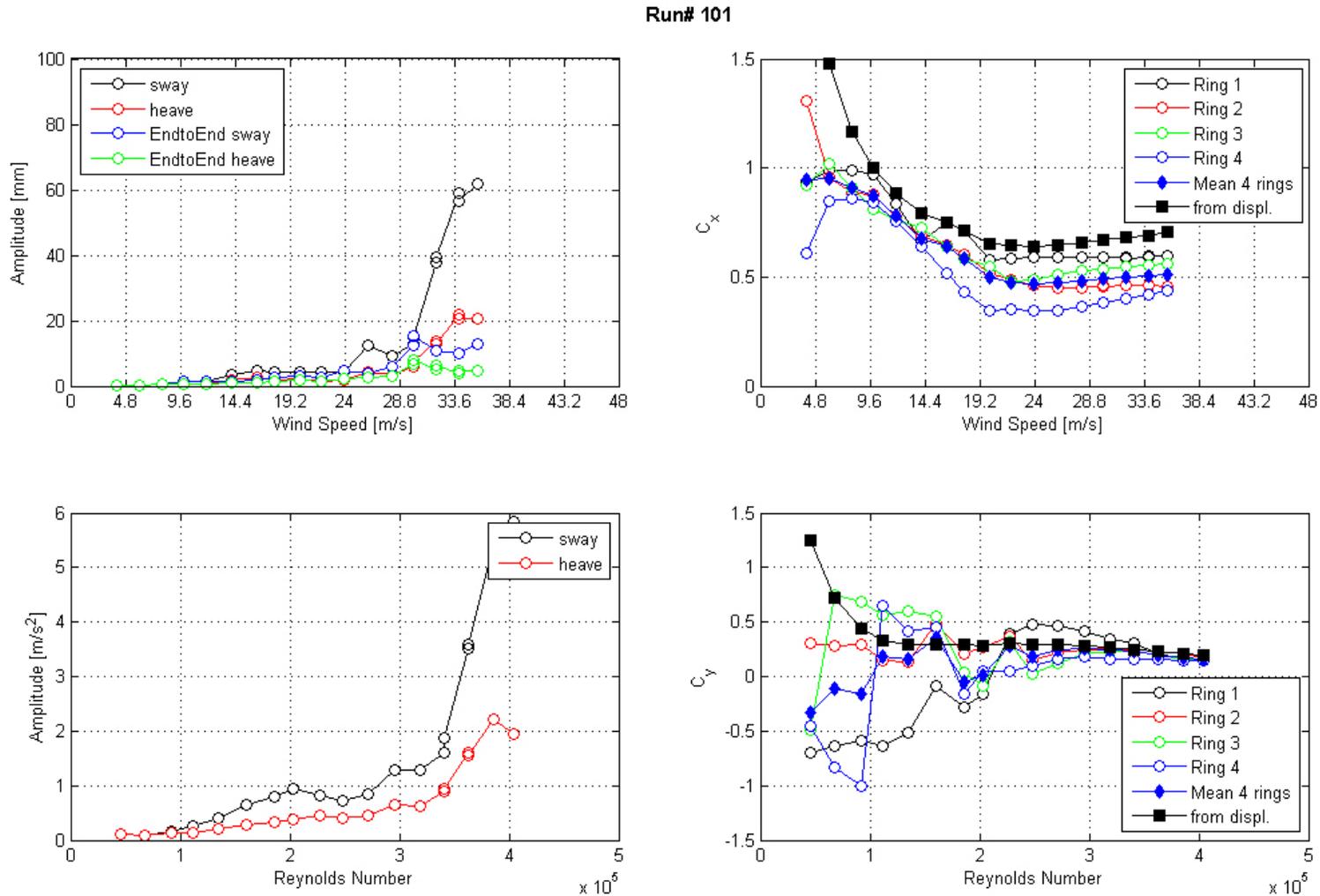
Figure 100. Graph. Response of the cable as a function of wind speed or Reynolds number as measured by the lasers, accelerometers, and surface pressures for run 101.
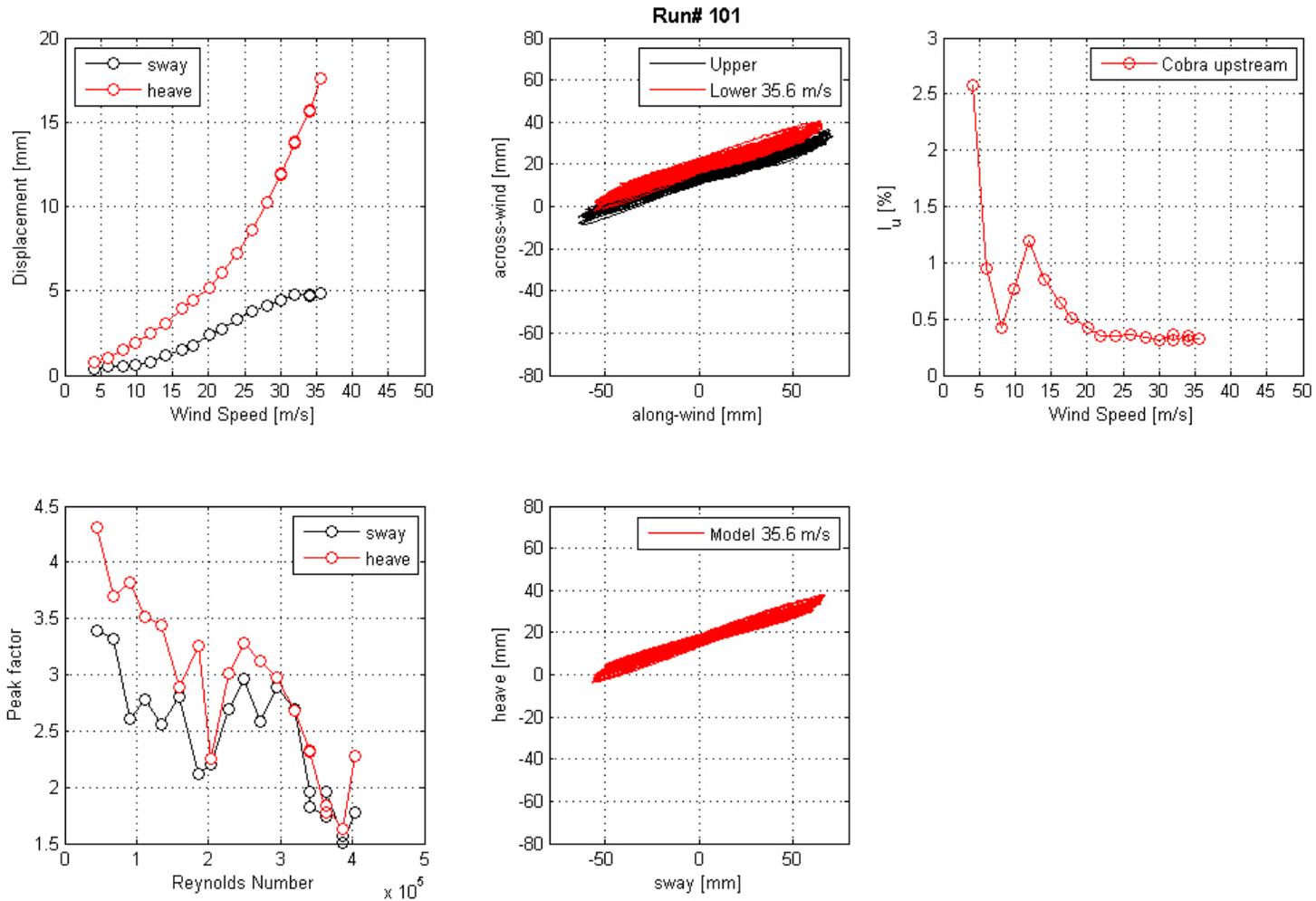
Figure 101. Graph. Mean displacement and peak factor from the laser, motion path at one wind speed, and intensity of turbulence measured at the entrance of the test section for run 101.
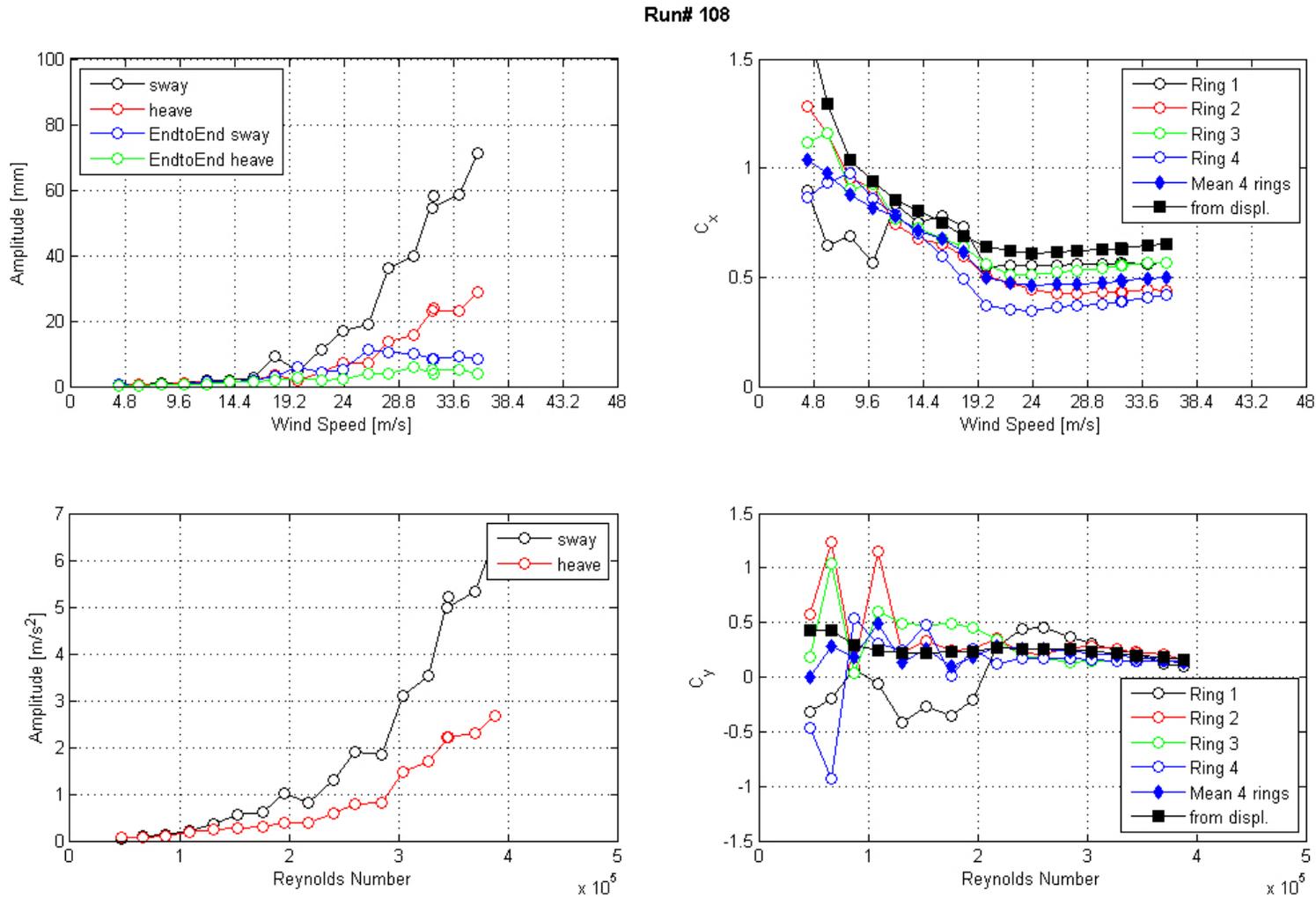
Figure 102. Graph. Response of the cable as a function of wind speed or Reynolds number as measured by the lasers, accelerometers, and surface pressures for run 108.
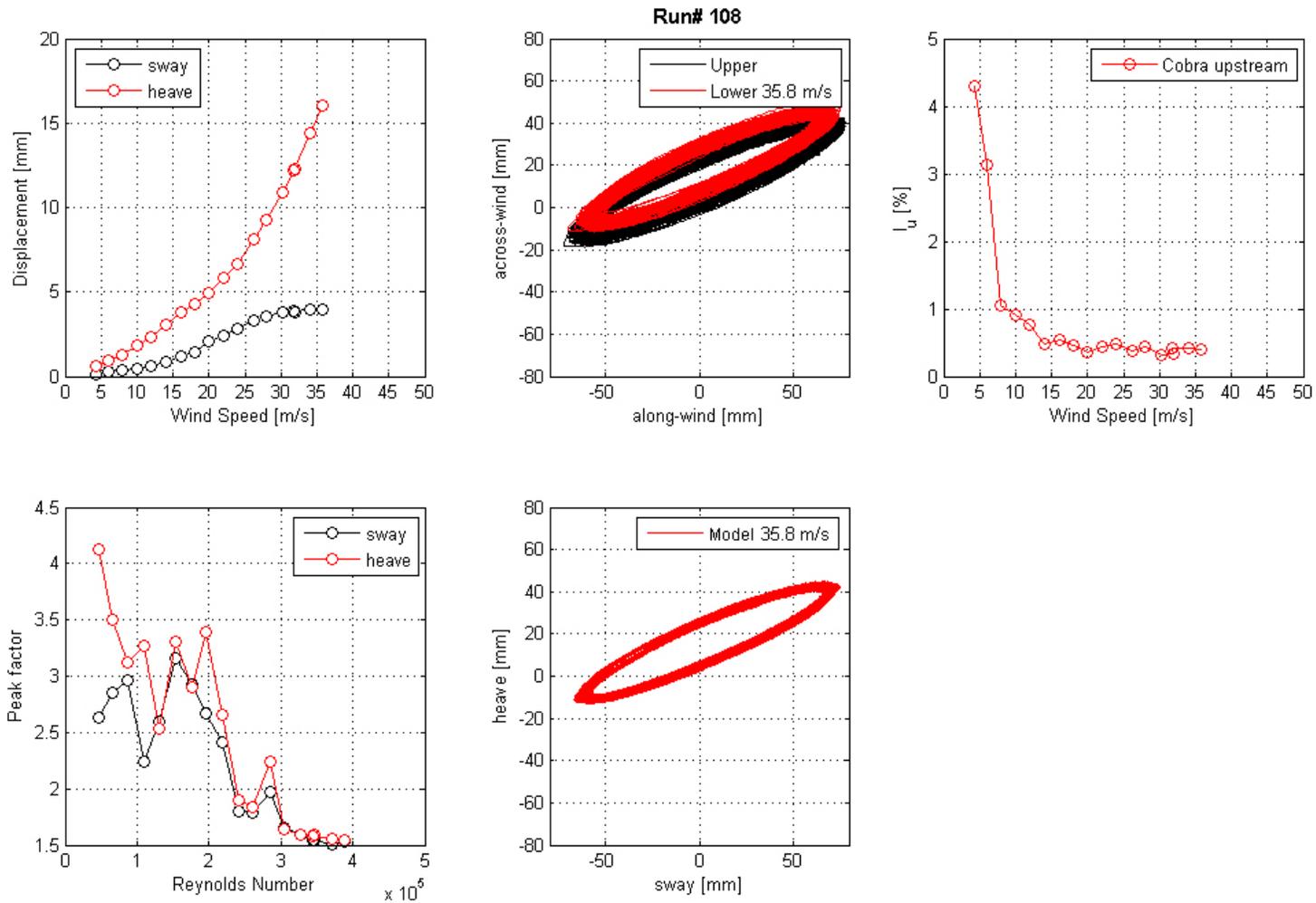
Figure 103. Graph. Mean displacement and peak factor from the laser, motion path at one wind speed, and intensity of turbulence measured at the entrance of the test section for run 108.
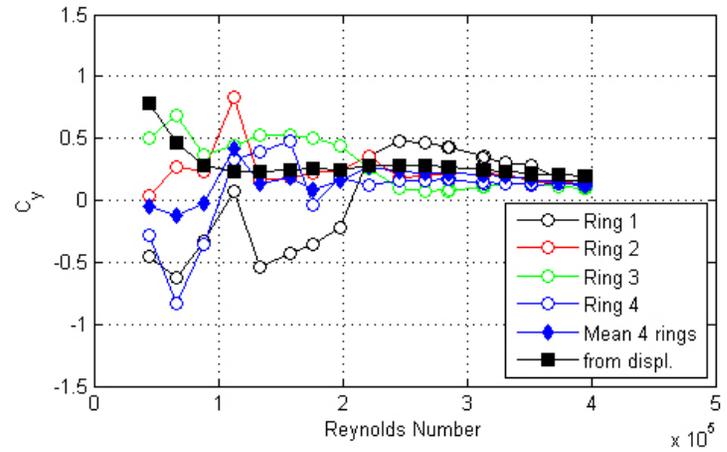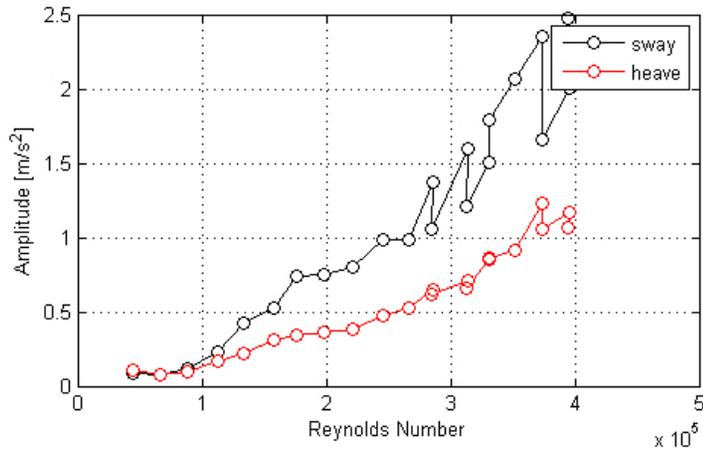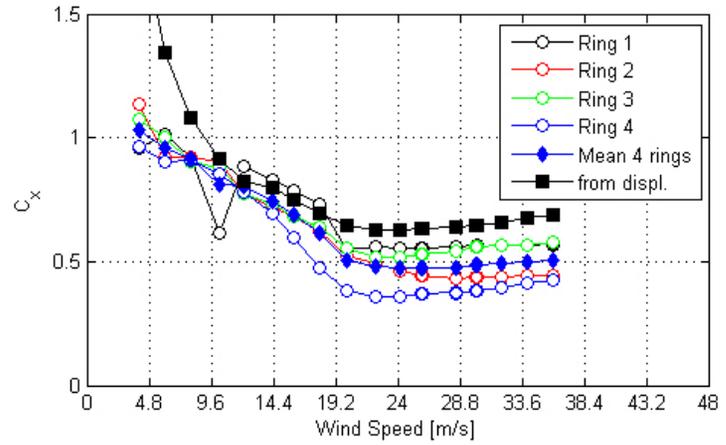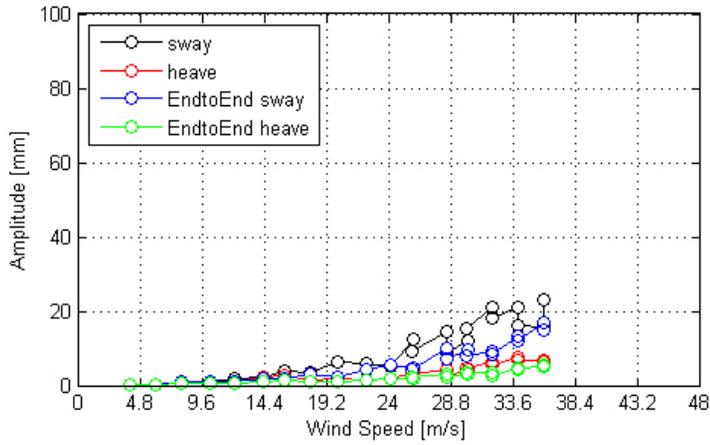
Figure 104. Graph. Response of the cable as a function of wind speed or Reynolds number as measured by the lasers, accelerometers, and surface pressures for run 118.
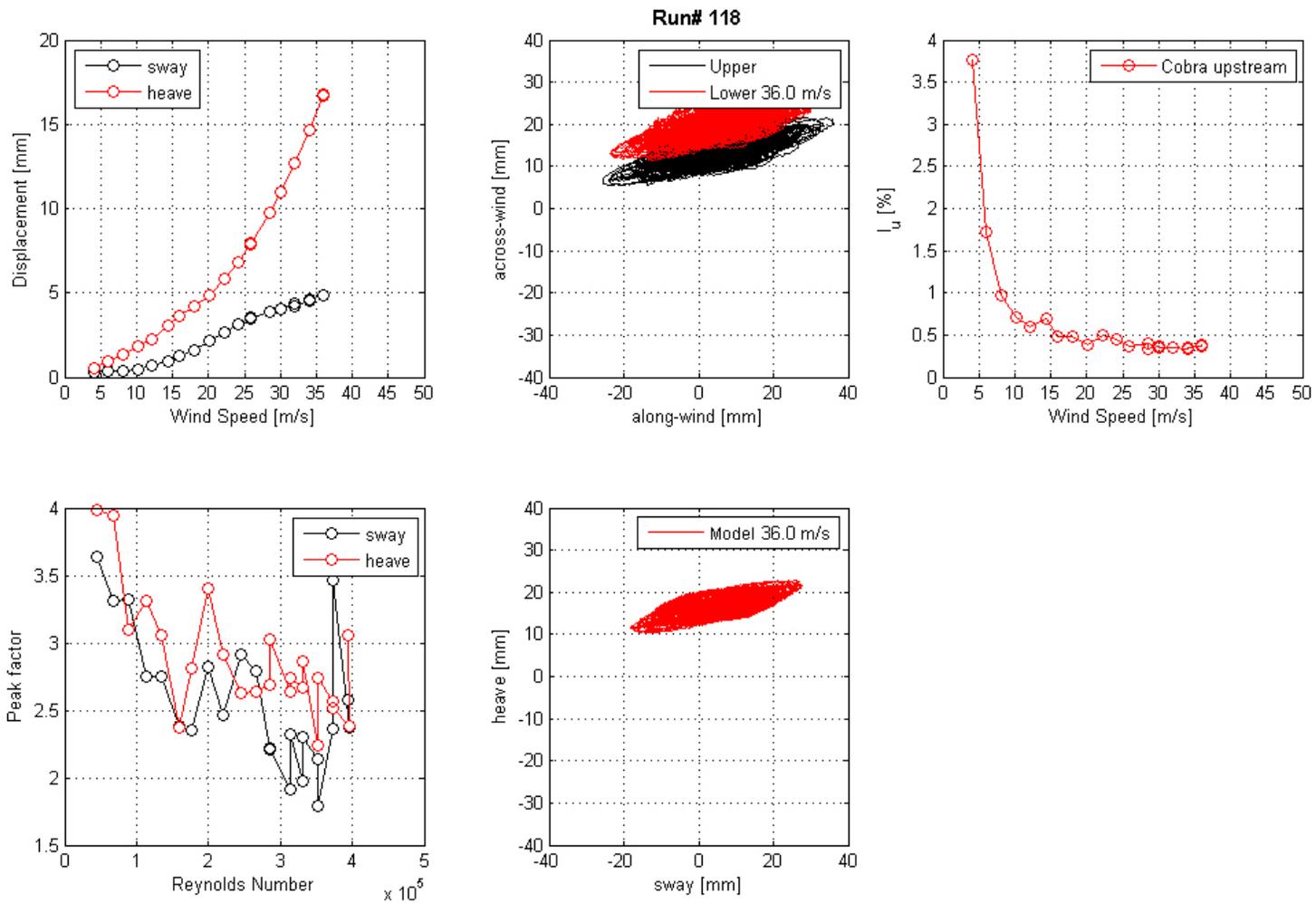
Figure 105. Graph. Mean displacement and peak factor from the laser, motion path at one wind speed, and intensity of turbulence measured at the entrance of the test section for run 118.

Run# 122
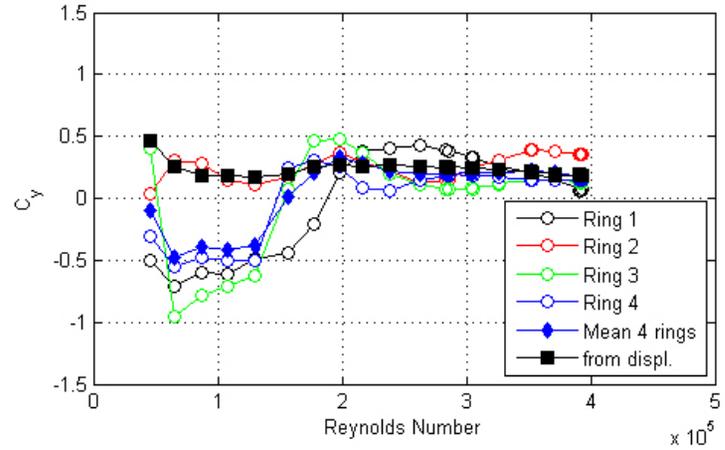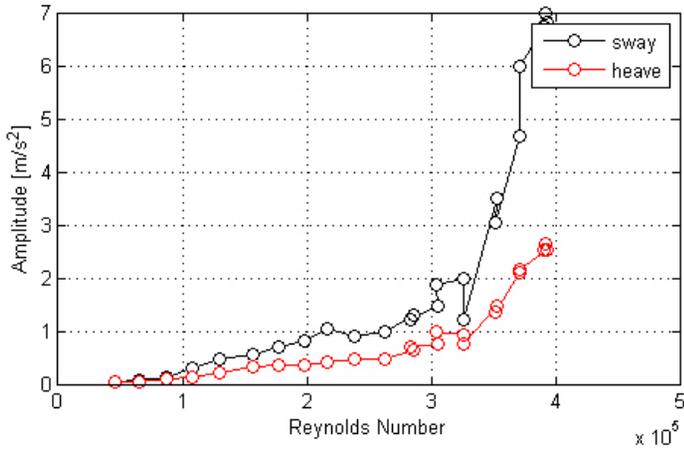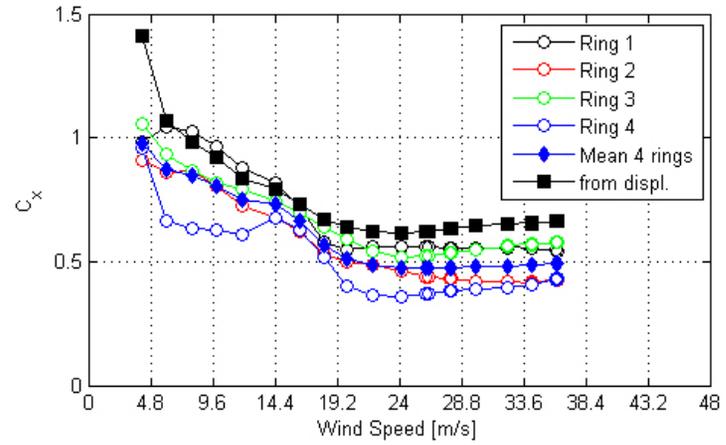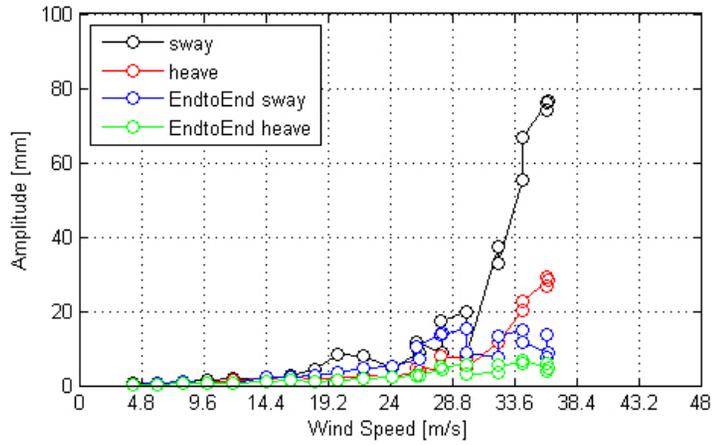
Figure 106. Graph. Response of the cable as a function of wind speed or Reynolds number as measured by the lasers, accelerometers, and surface pressures for run 122.
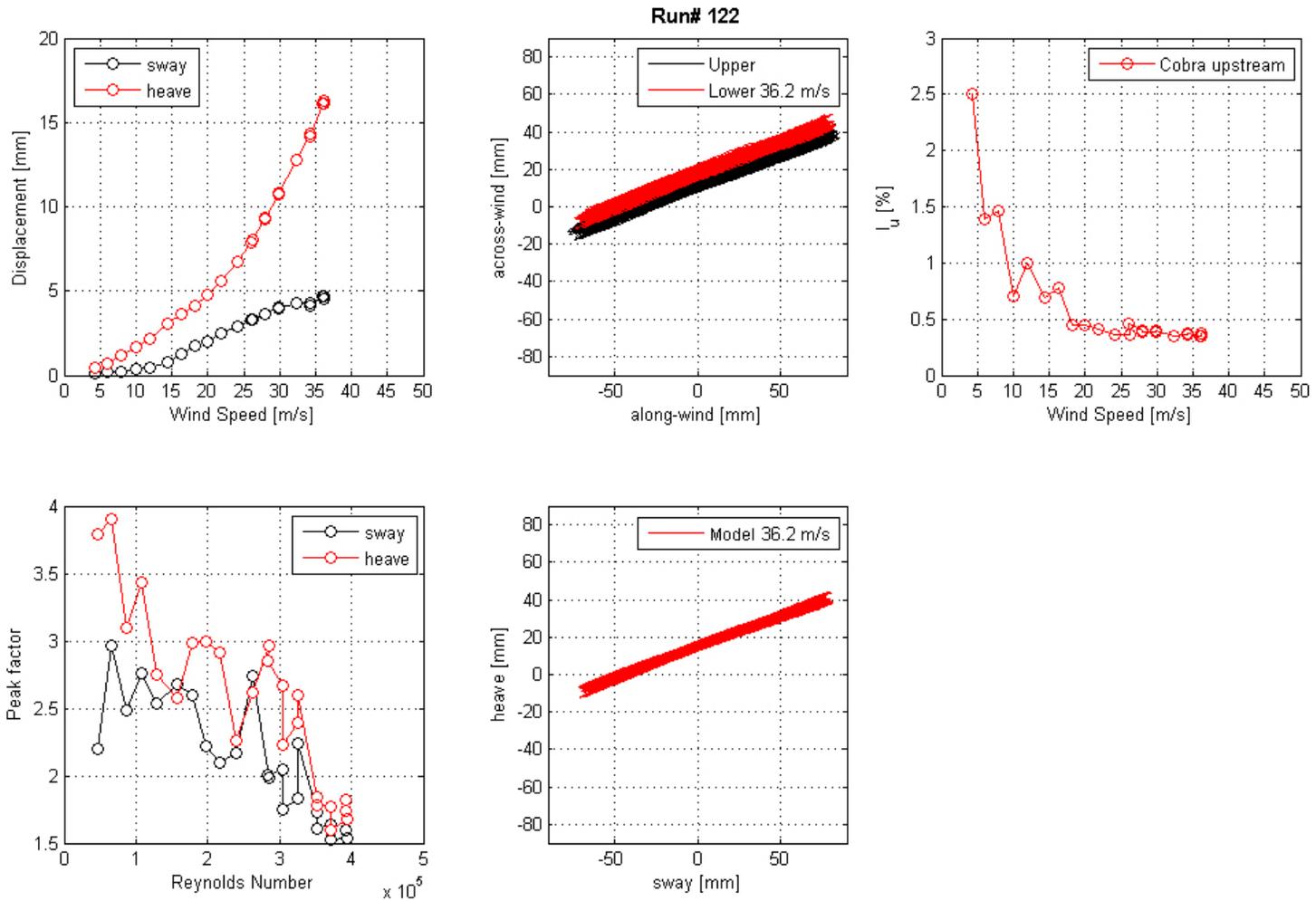
Figure 107. Graph. Mean displacement and peak factor from the laser, motion path at one wind speed, and intensity of turbulence measured at the entrance of the test section for run 122.
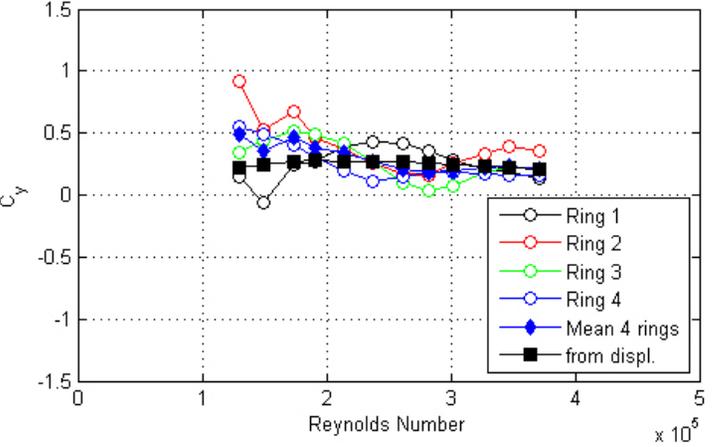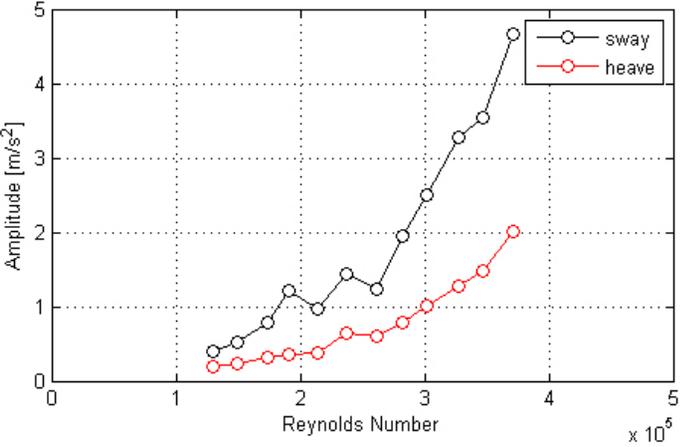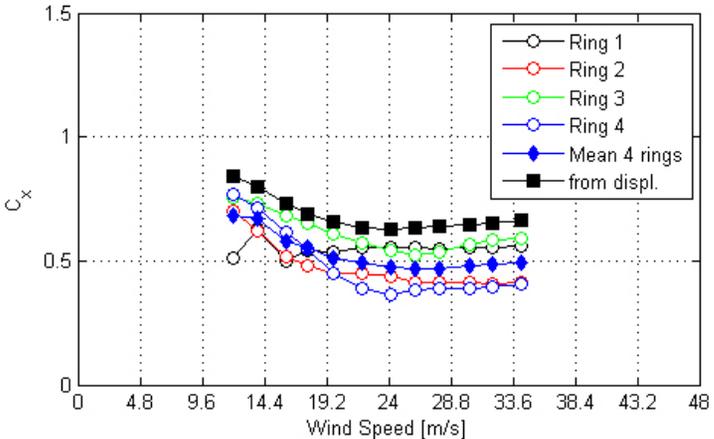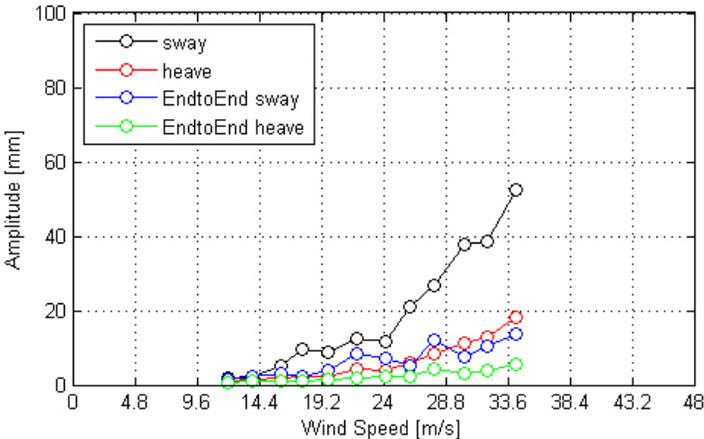
Figure 108. Graph. Response of the cable as a function of wind speed or Reynolds number as measured by the lasers, accelerometers, and surface pressures for run 123.
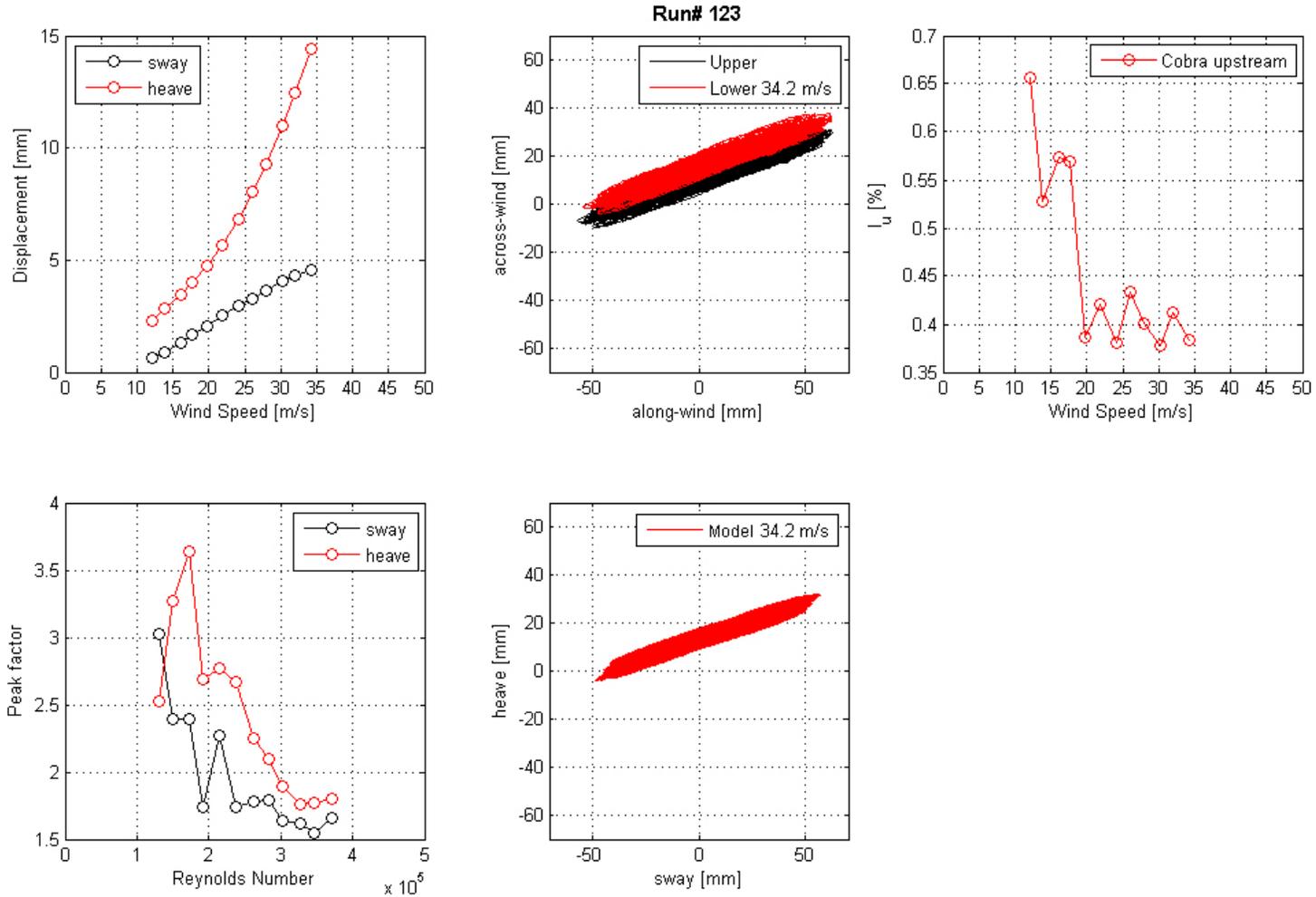
Figure 109. Graph. Mean displacement and peak factor from the laser, motion path at one wind speed, and intensity of turbulence measured at the entrance of the test section for run 123.
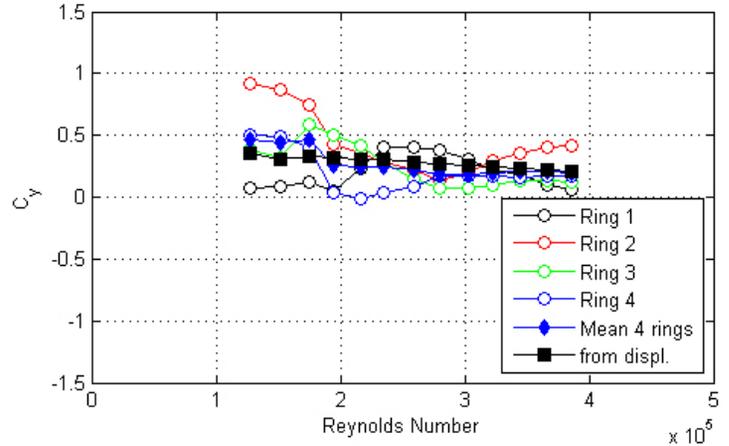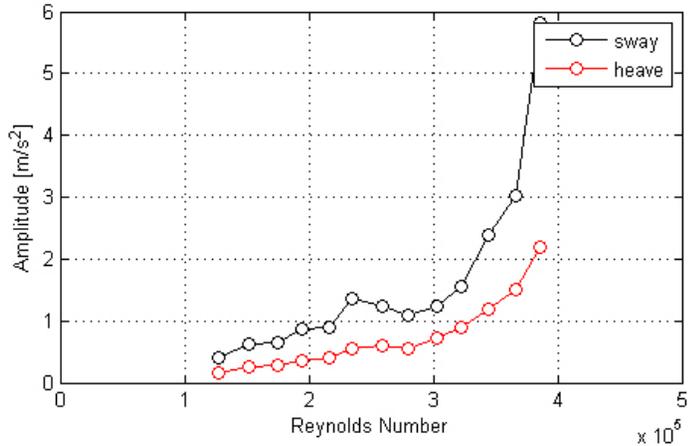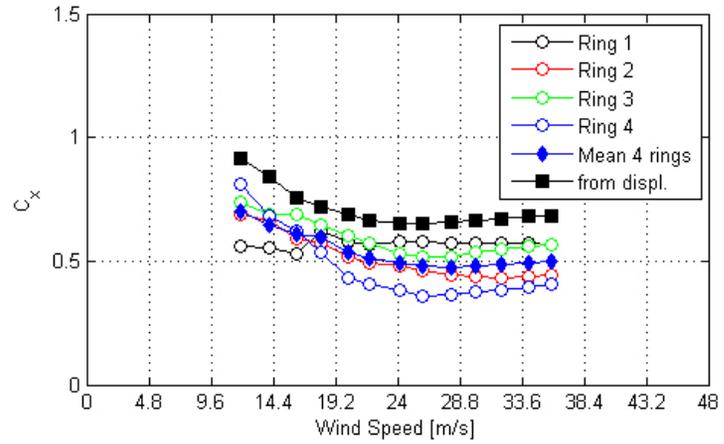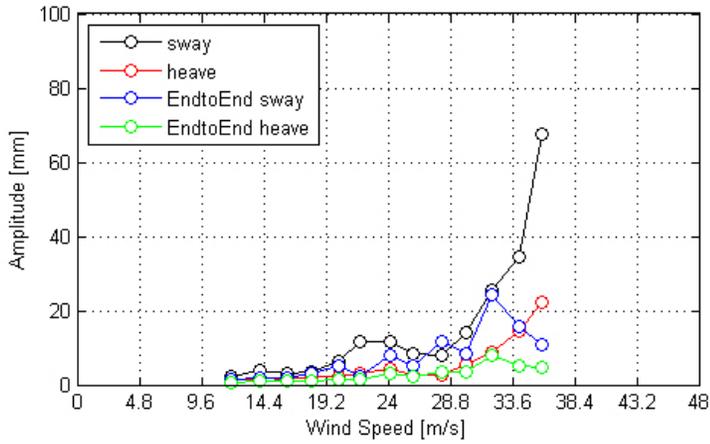
Figure 110. Graph. Response of the cable as a function of wind speed or Reynolds number as measured by the lasers, accelerometers, and surface pressures for run 125.
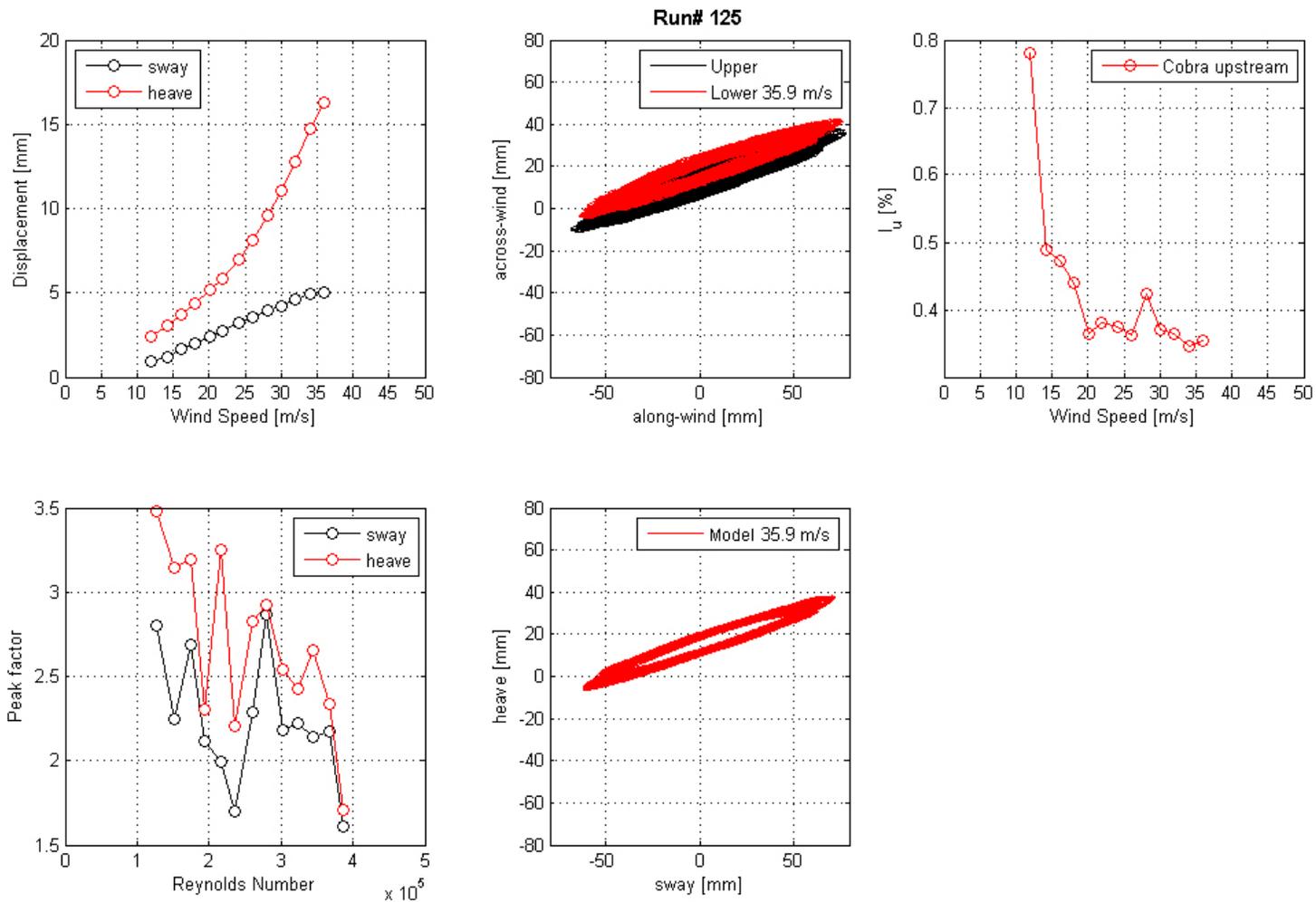
Figure 111. Graph. Mean displacement and peak factor from the laser, motion path at one wind speed, and intensity of turbulence measured at the entrance of the test section for run 125.
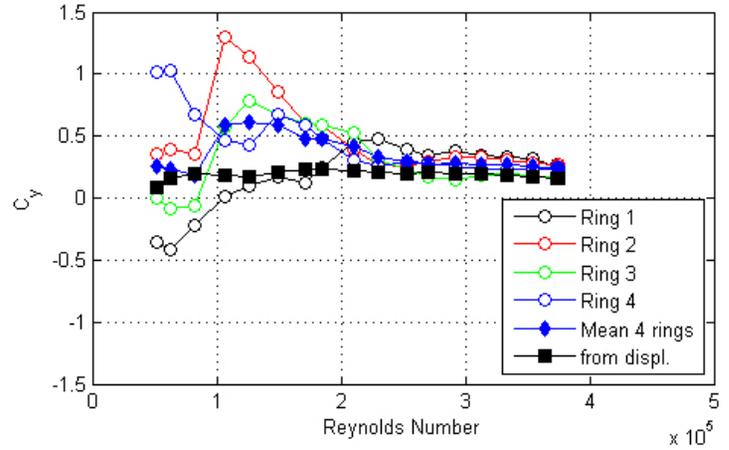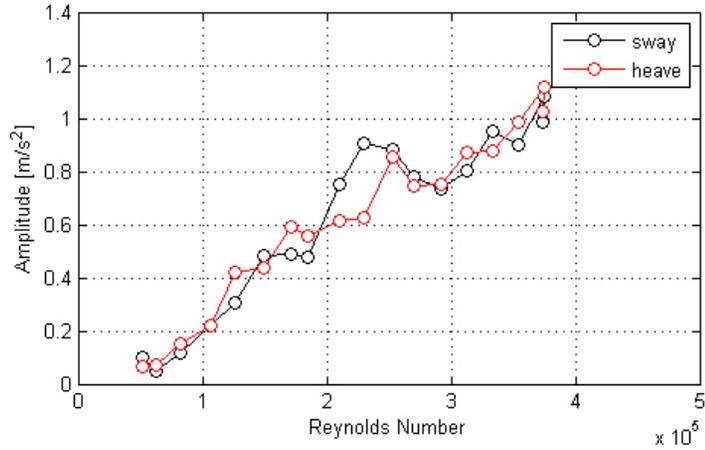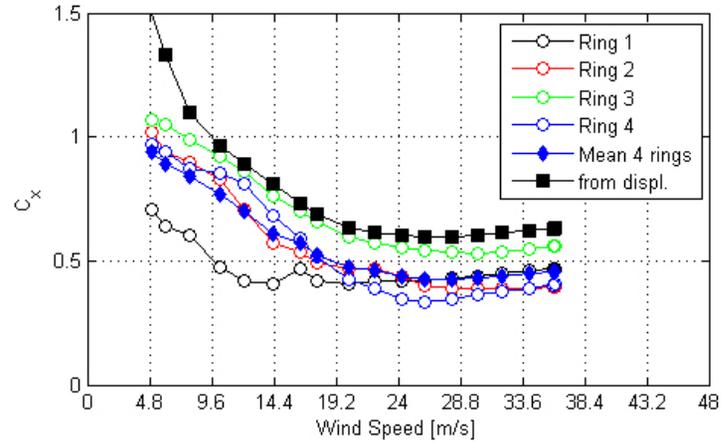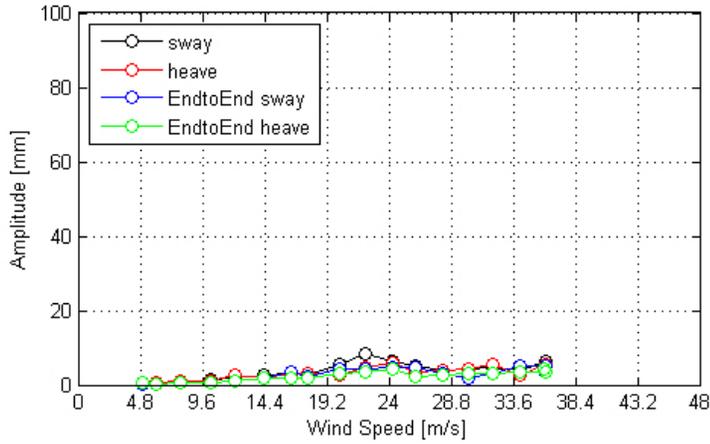
Figure 112. Graph. Response of the cable as a function of wind speed or Reynolds number as measured by the lasers, accelerometers, and surface pressures for run 131.
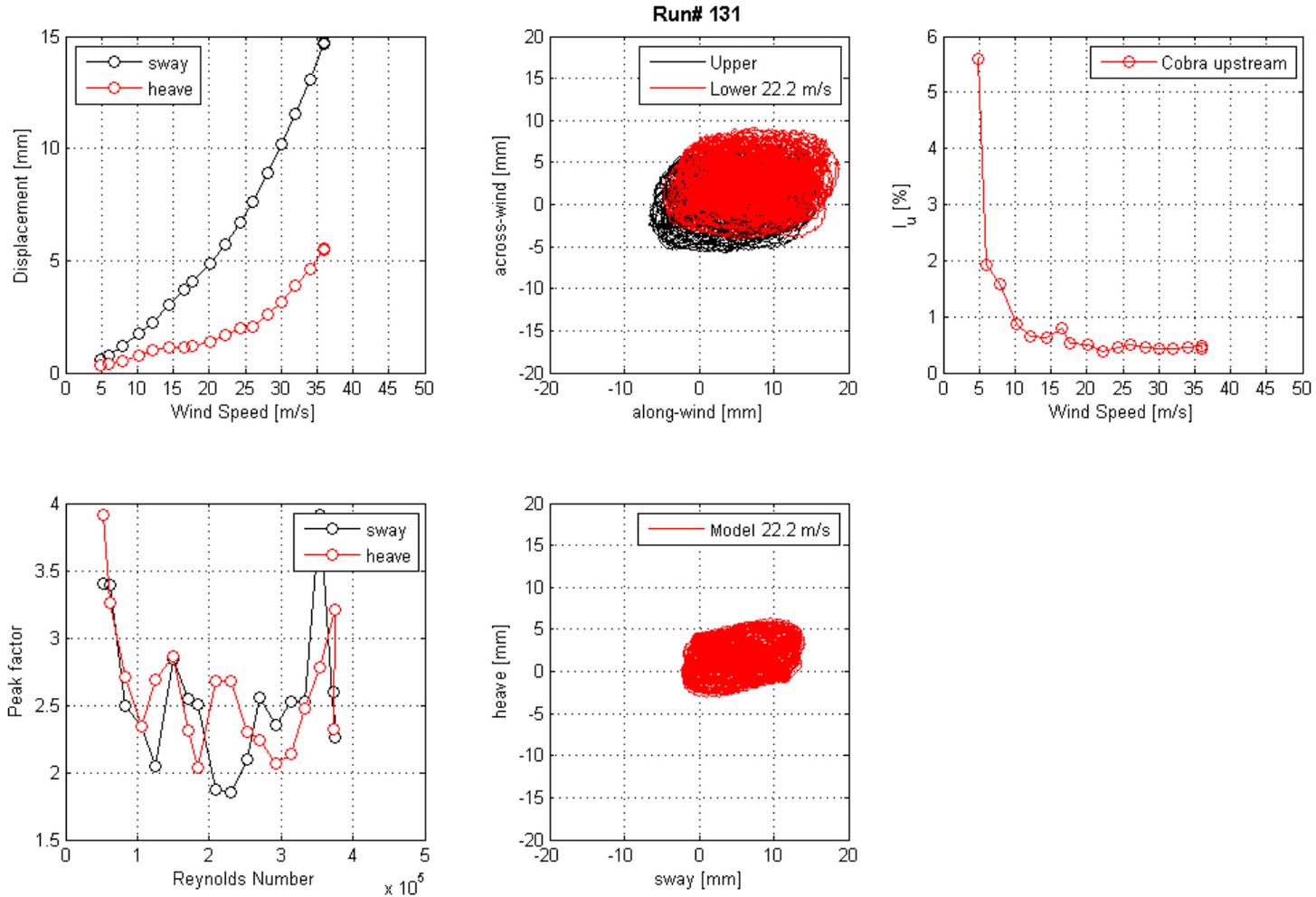
Figure 113. Graph. Mean displacement and peak factor from the laser, motion path at one wind speed, and intensity of turbulence measured at the entrance of the test section for run 131.
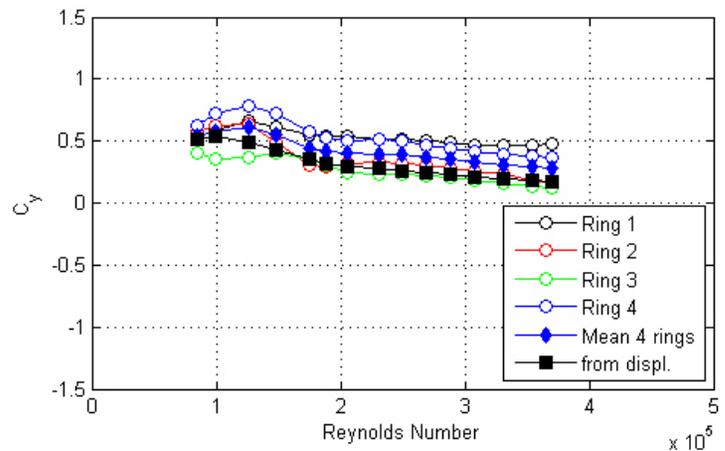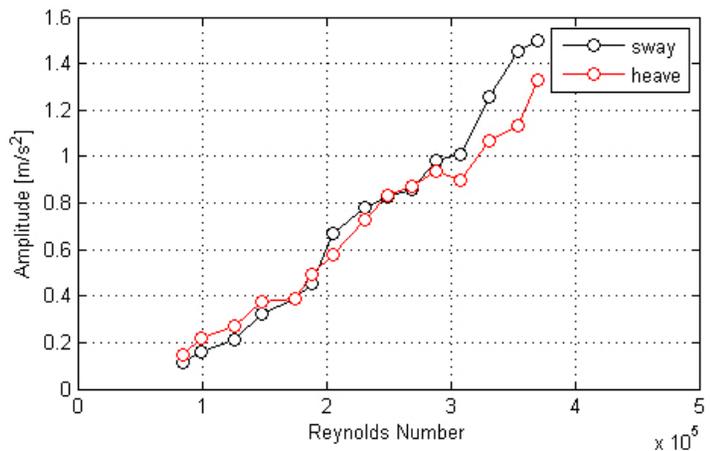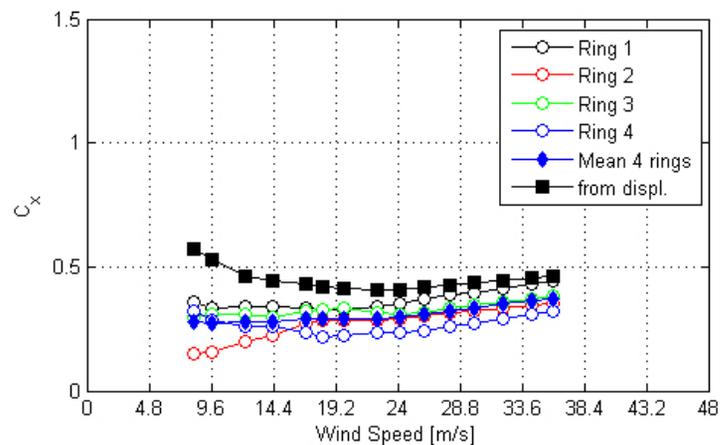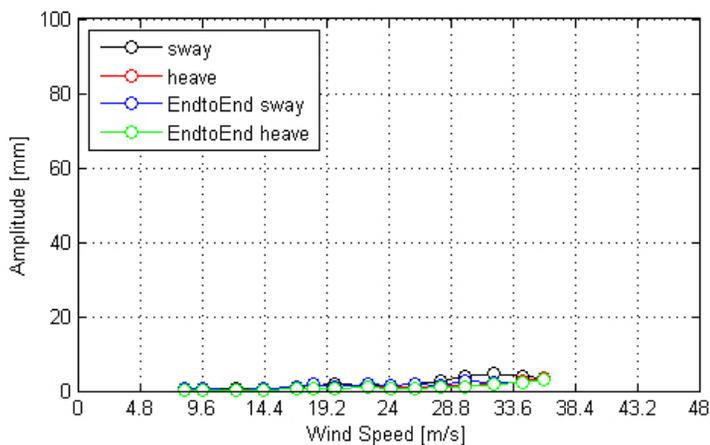
Figure 114. Graph. Response of the cable as a function of wind speed or Reynolds number as measured by the lasers, accelerometers, and surface pressures for run 136.
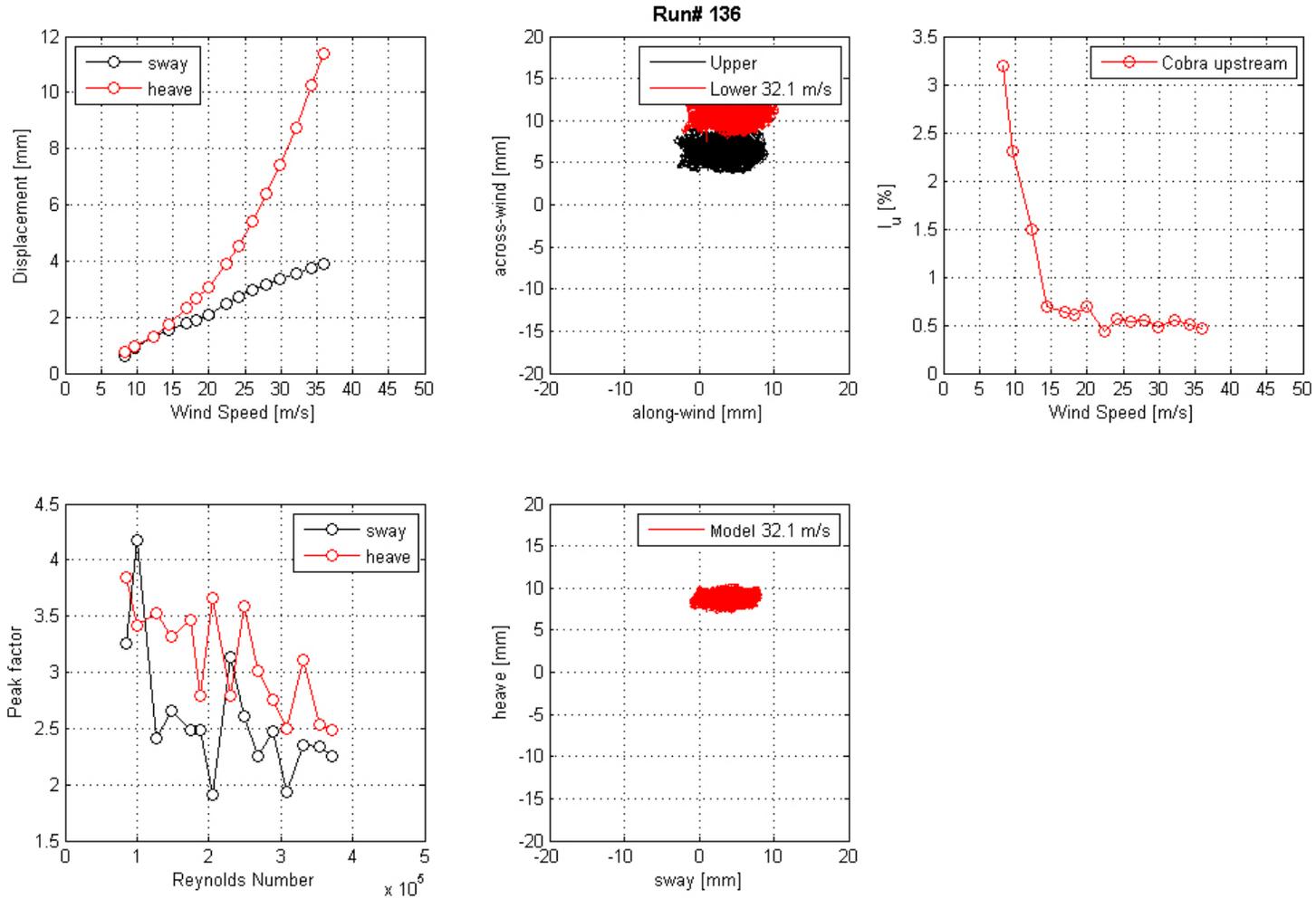
Figure 115. Graph. Mean displacement and peak factor from the laser, motion path at one wind speed, and intensity of turbulence measured at the entrance of the test section for run 136.
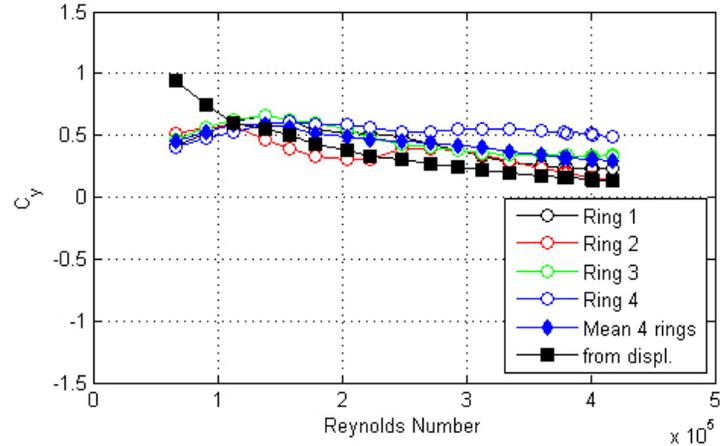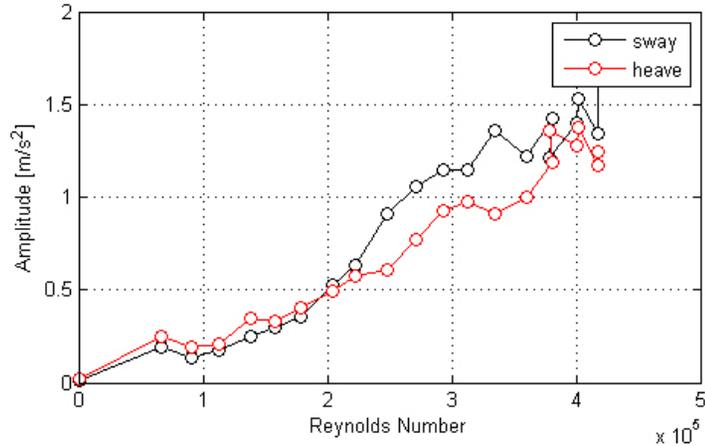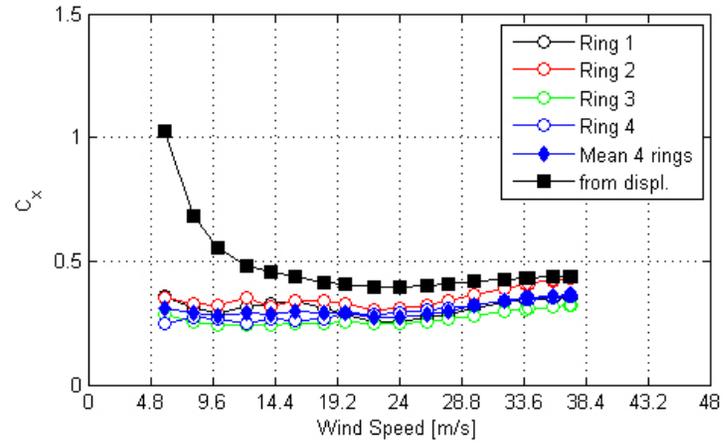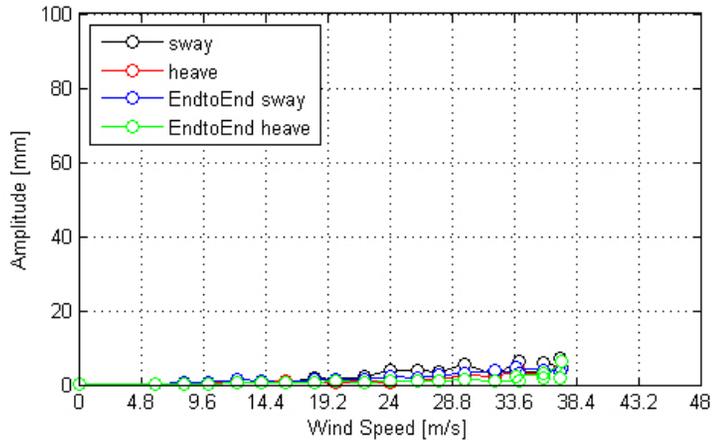
Figure 116. Graph. Response of the cable as a function of wind speed or Reynolds number as measured by the lasers, accelerometers, and surface pressures for run 137.
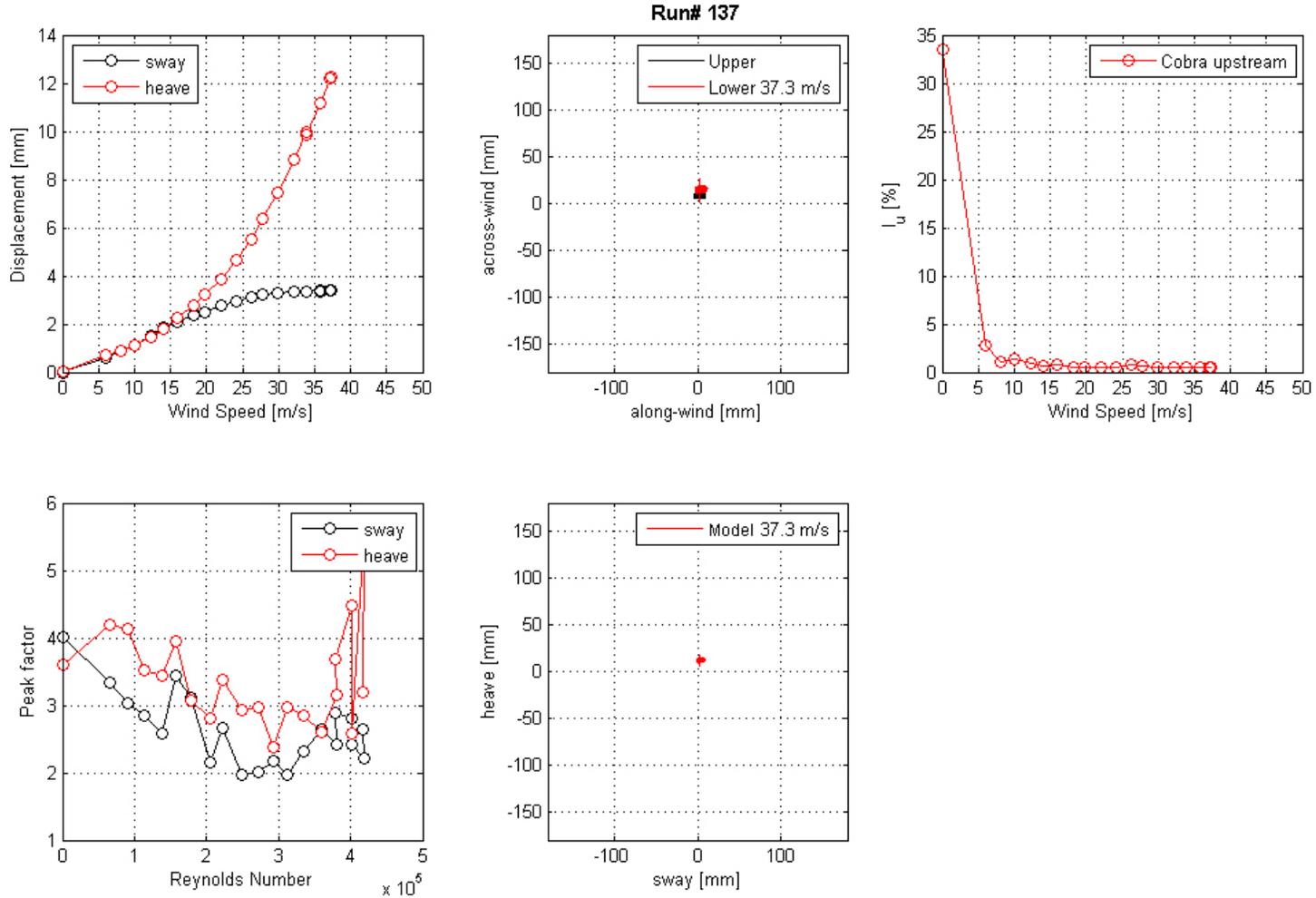
Figure 117. Graph. Mean displacement and peak factor from the laser, motion path at one wind speed, and intensity of turbulence measured at the entrance of the test section for run 137.
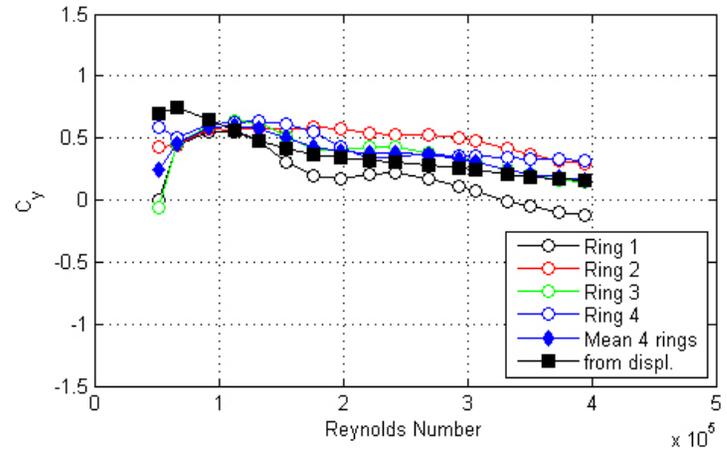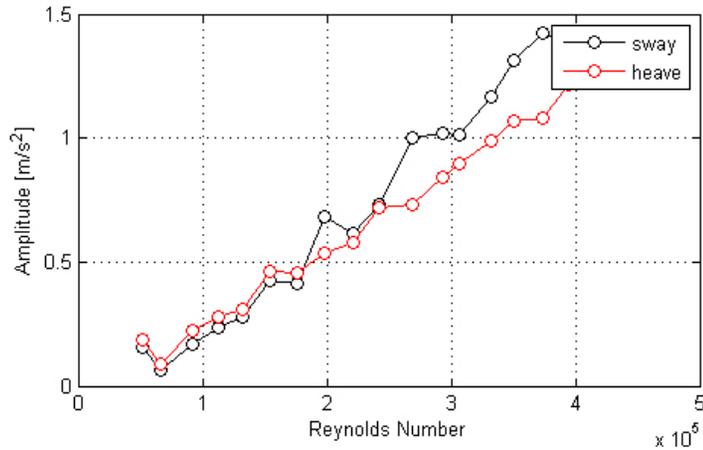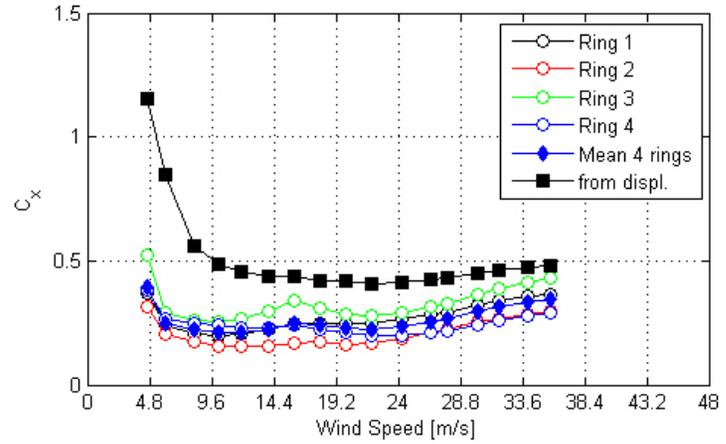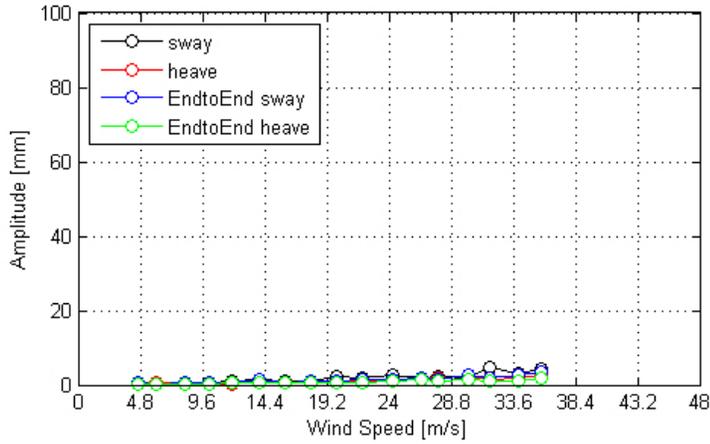
Figure 118. Graph. Response of the cable as a function of wind speed or Reynolds number as measured by the lasers, accelerometers, and surface pressures for run 140.
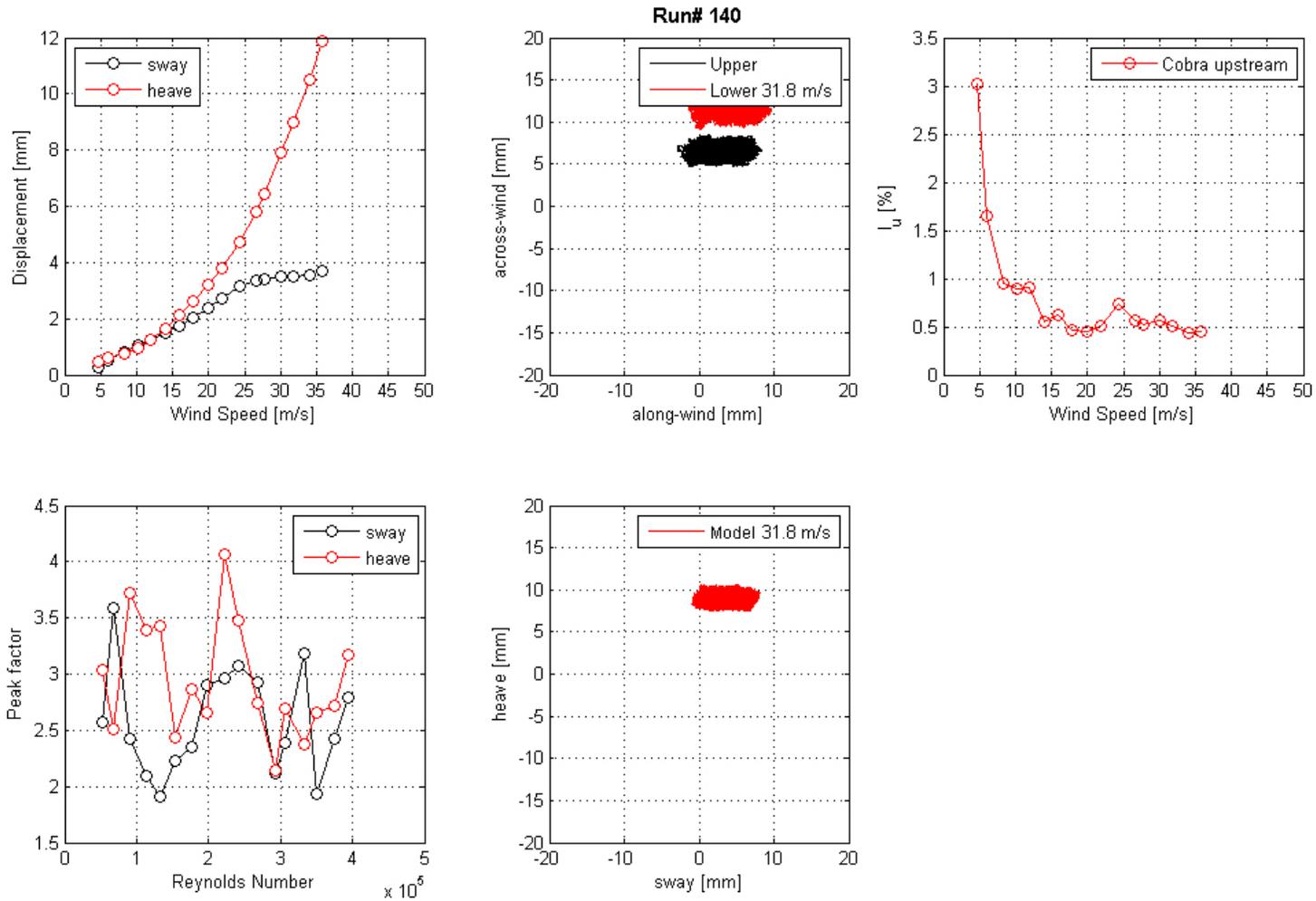
Figure 119. Graph. Mean displacement and peak factor from the laser, motion path at one wind speed, and intensity of turbulence measured at the entrance of the test section for run 140.
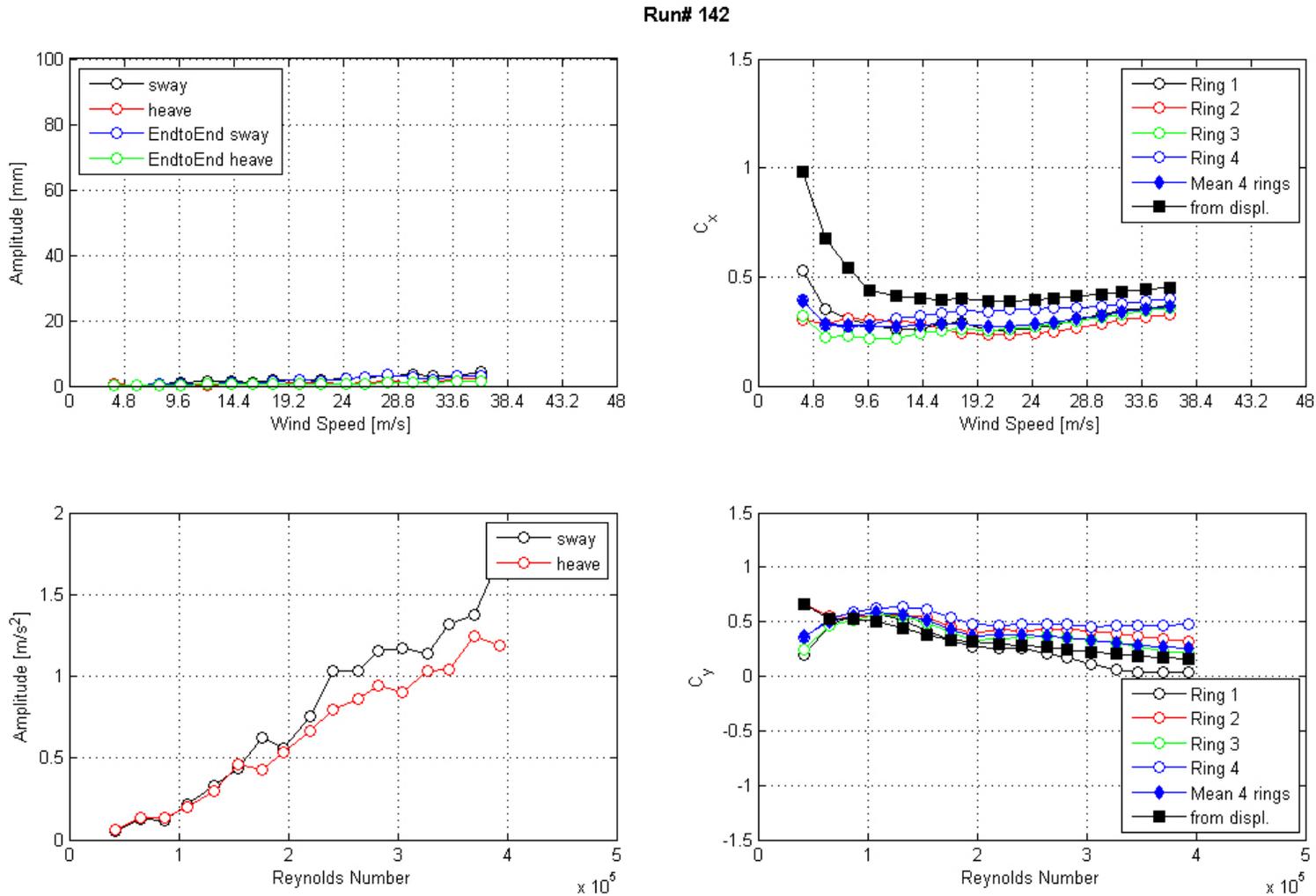
Run# 142

Figure 120. Graph. Response of the cable as a function of wind speed or Reynolds number as measured by the lasers, accelerometers, and surface pressures for run 142.
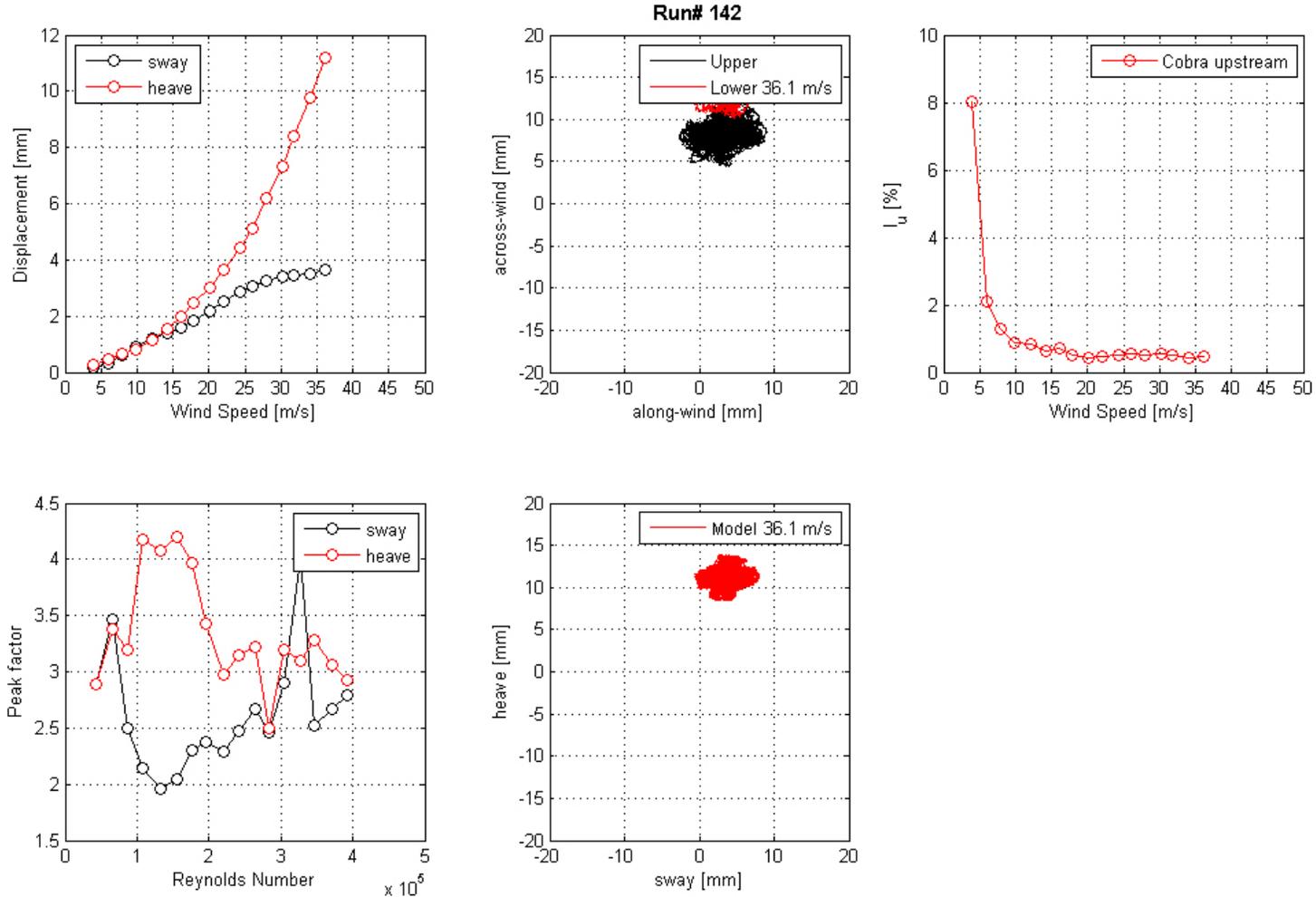
Figure 121. Graph. Mean displacement and peak factor from the laser, motion path at one wind speed, and intensity of turbulence measured at the entrance of the test section for run 142.

Run# 144
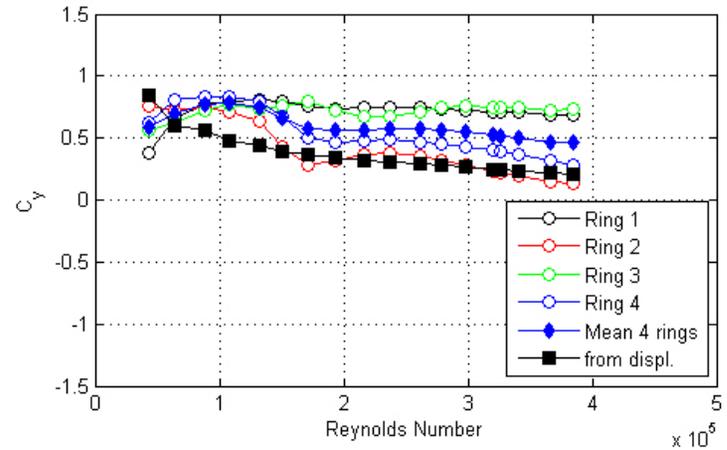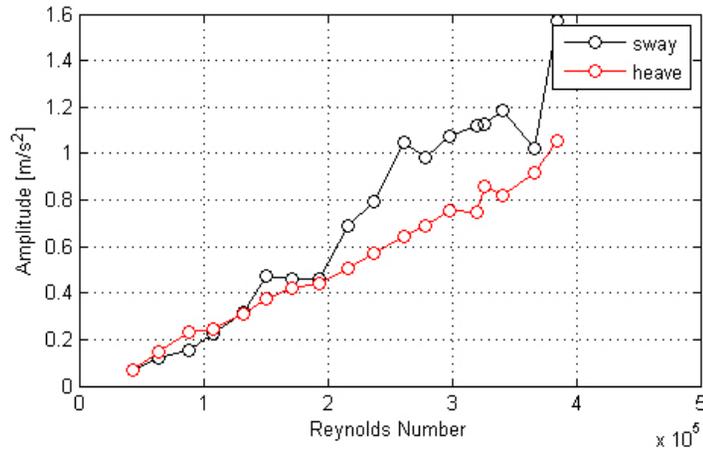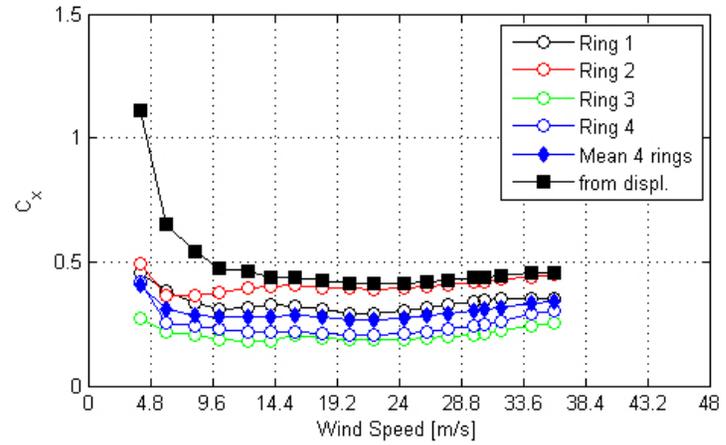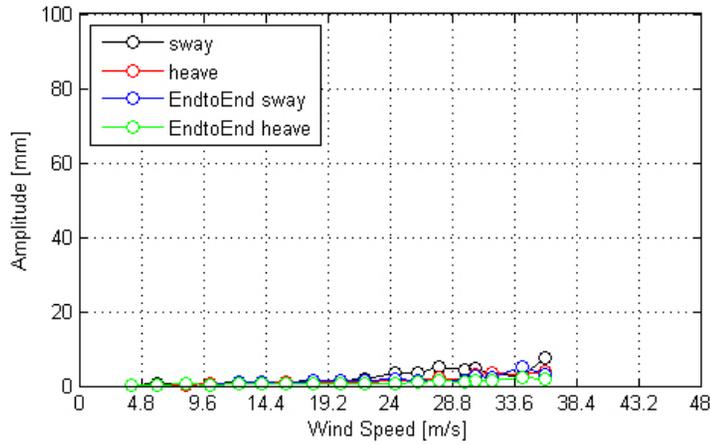
Figure 122. Graph. Response of the cable as a function of wind speed or Reynolds number as measured by the lasers, accelerometers, and surface pressures for run 144.
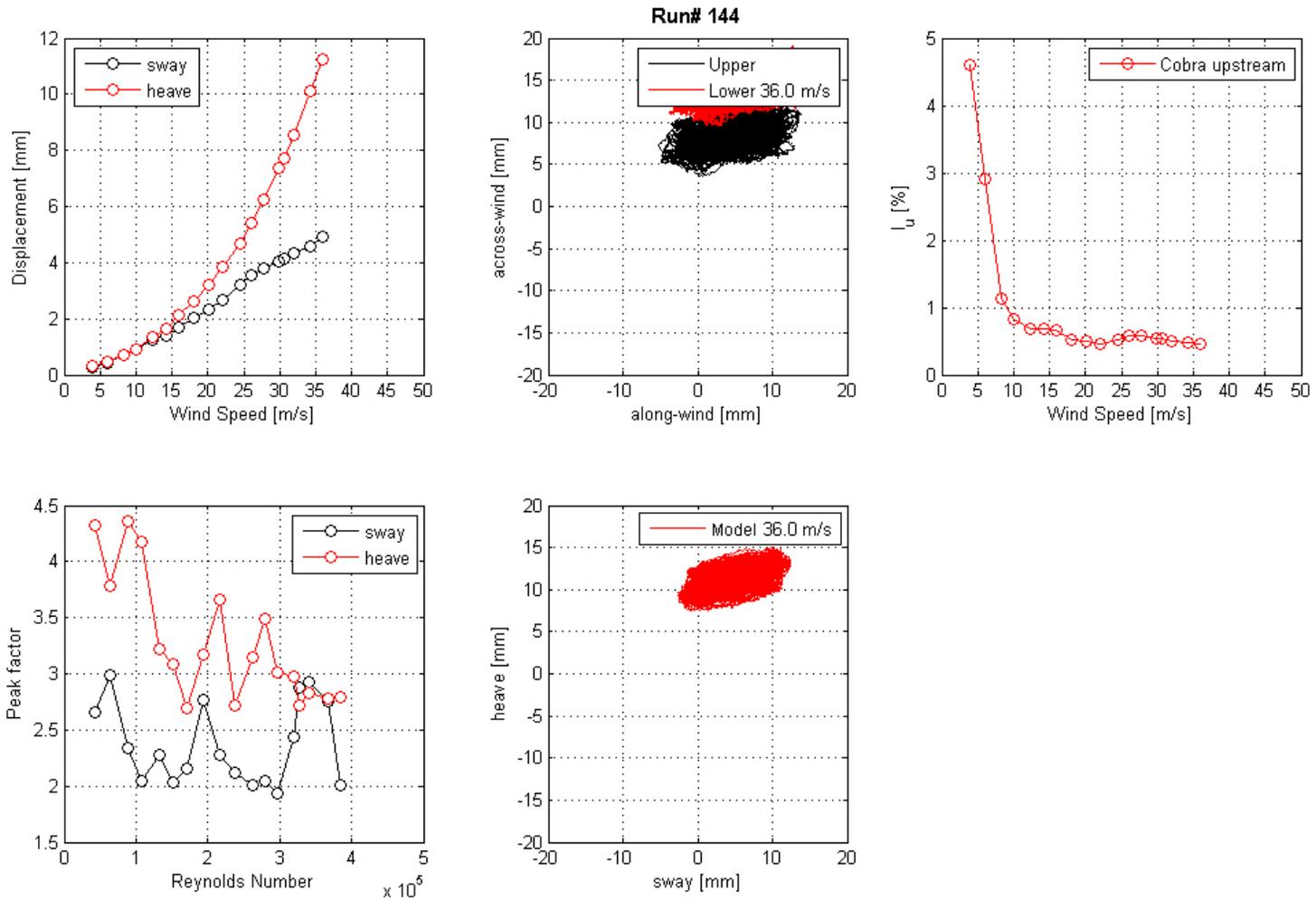
Figure 123. Graph. Mean displacement and peak factor from the laser, motion path at one wind speed, and intensity of turbulence measured at the entrance of the test section for run 144.
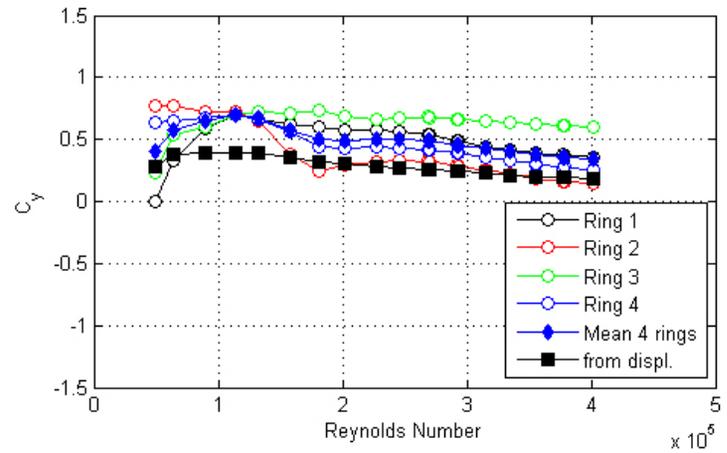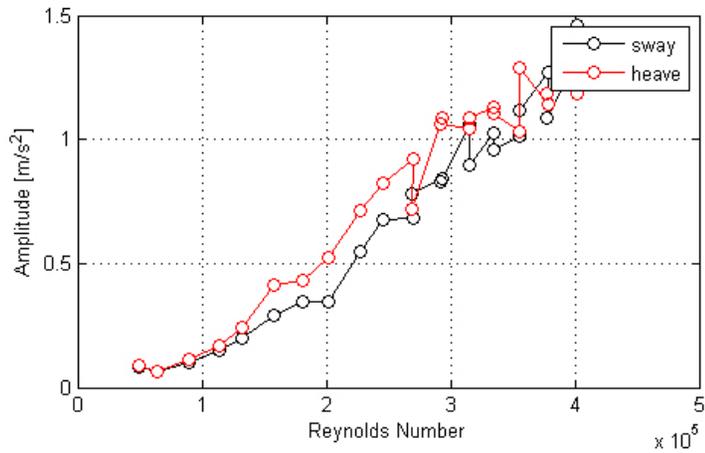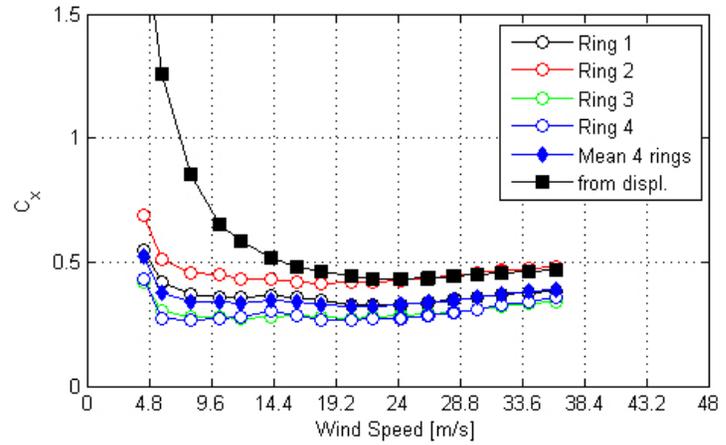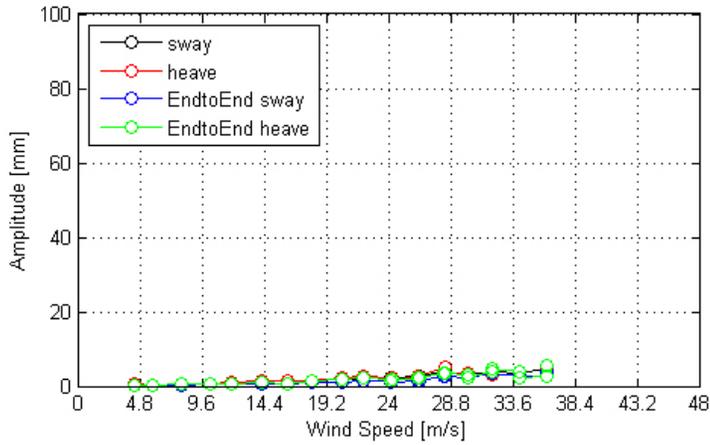
Figure 124. Graph. Response of the cable as a function of wind speed or Reynolds number as measured by the lasers, accelerometers, and surface pressures for run 149.
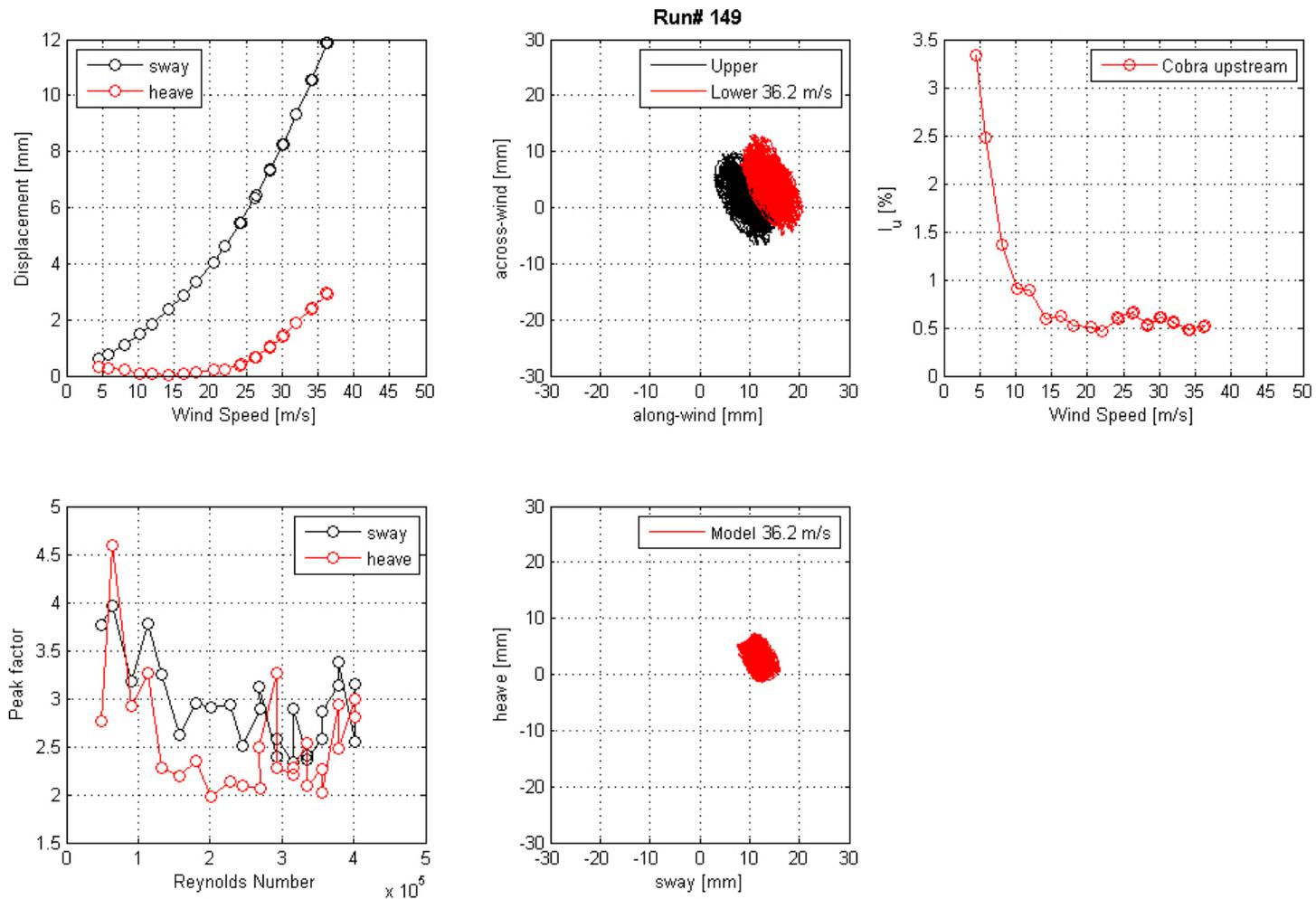
Figure 125. Graph. Mean displacement and peak factor from the laser, motion path at one wind speed, and intensity of turbulence measured at the entrance of the test section for run 149.
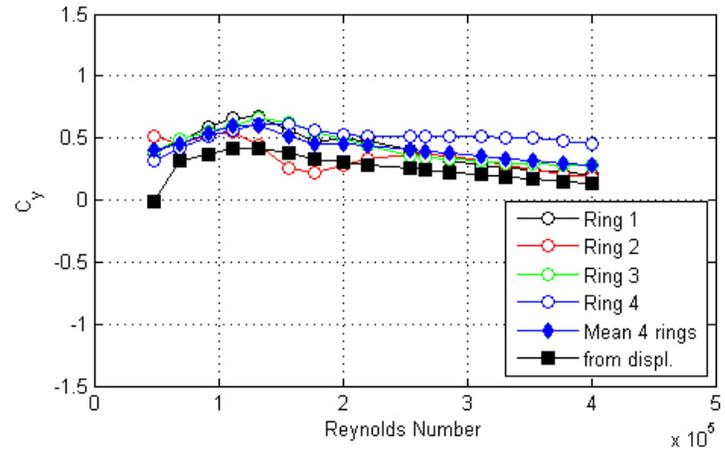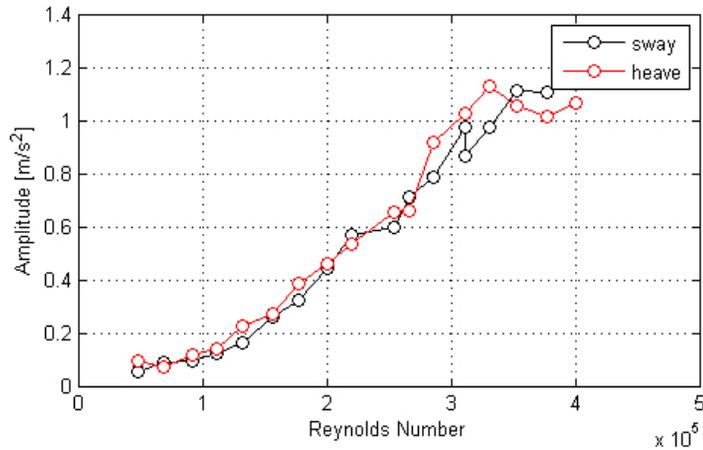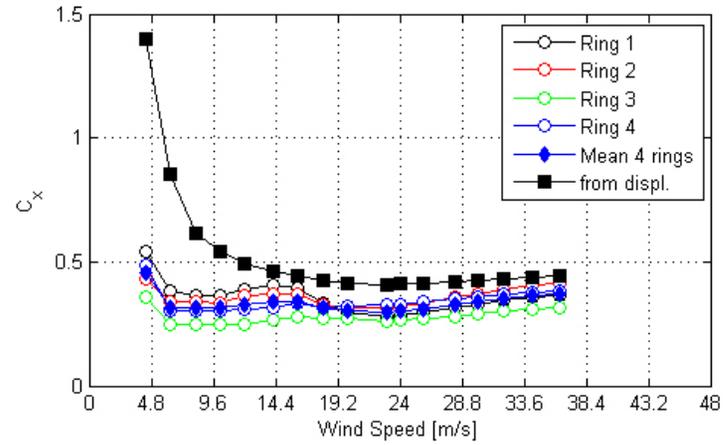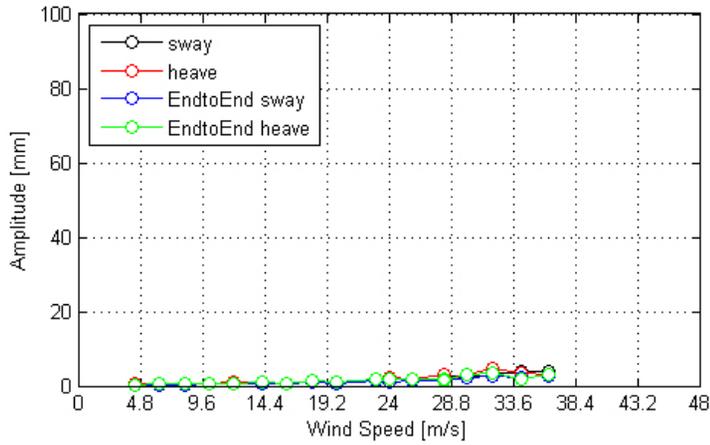
Figure 126. Graph. Response of the cable as a function of wind speed or Reynolds number as measured by the lasers, accelerometers, and surface pressures for run 152.
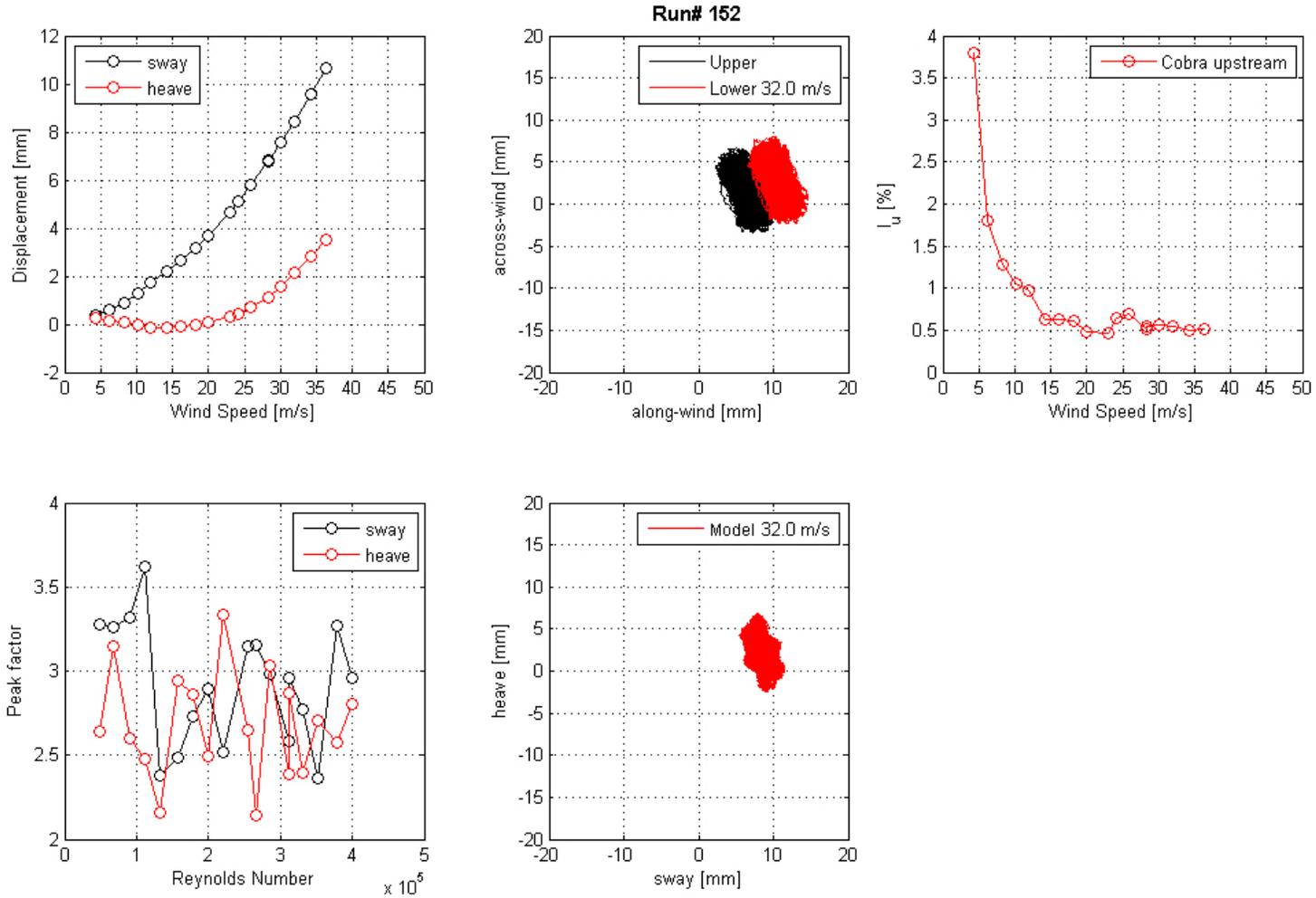
Figure 127. Graph. Mean displacement and peak factor from the laser, motion path at one wind speed, and intensity of turbulence measured at the entrance of the test section for run 152.
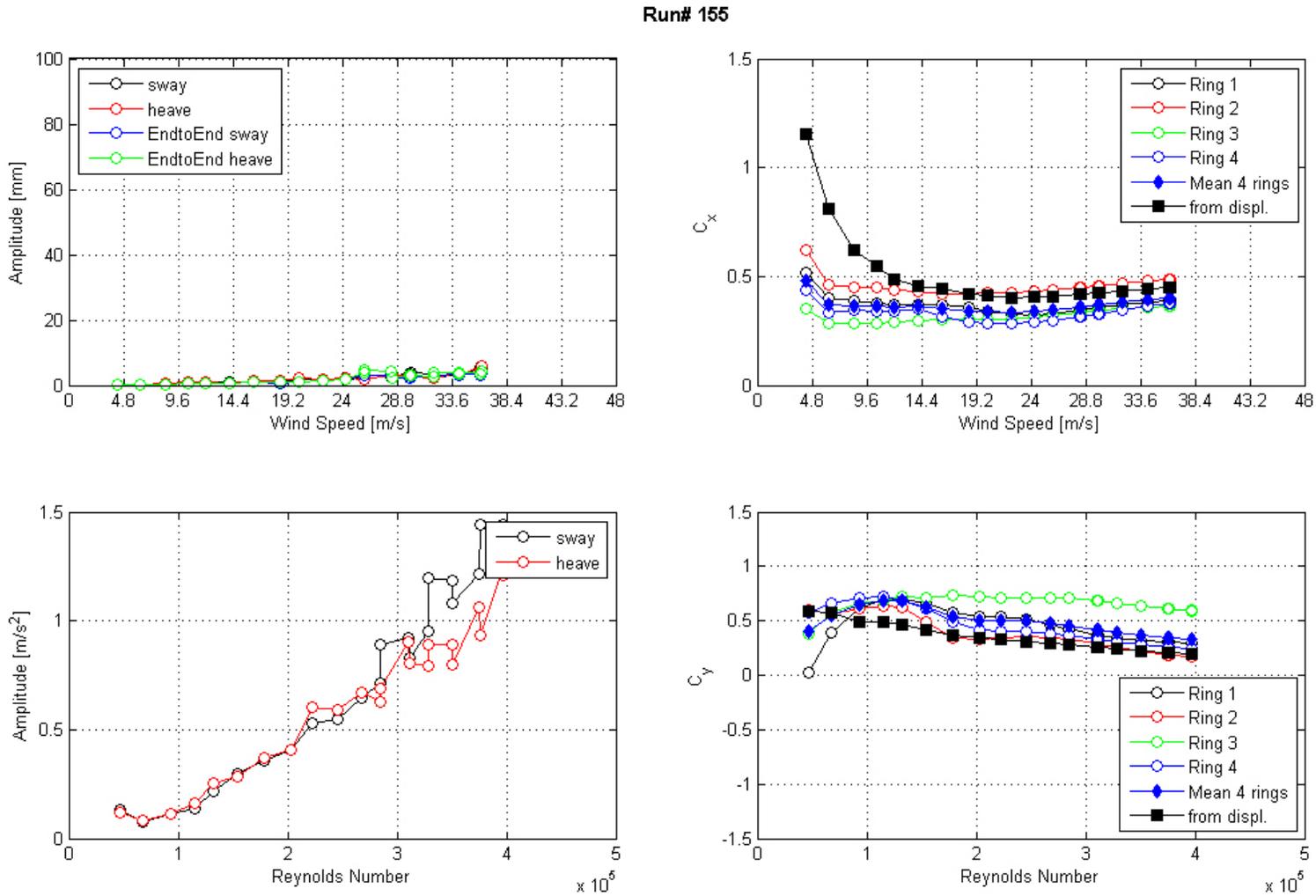
Figure 128. Graph. Response of the cable as a function of wind speed or Reynolds number as measured by the lasers, accelerometers, and surface pressures for run 155.
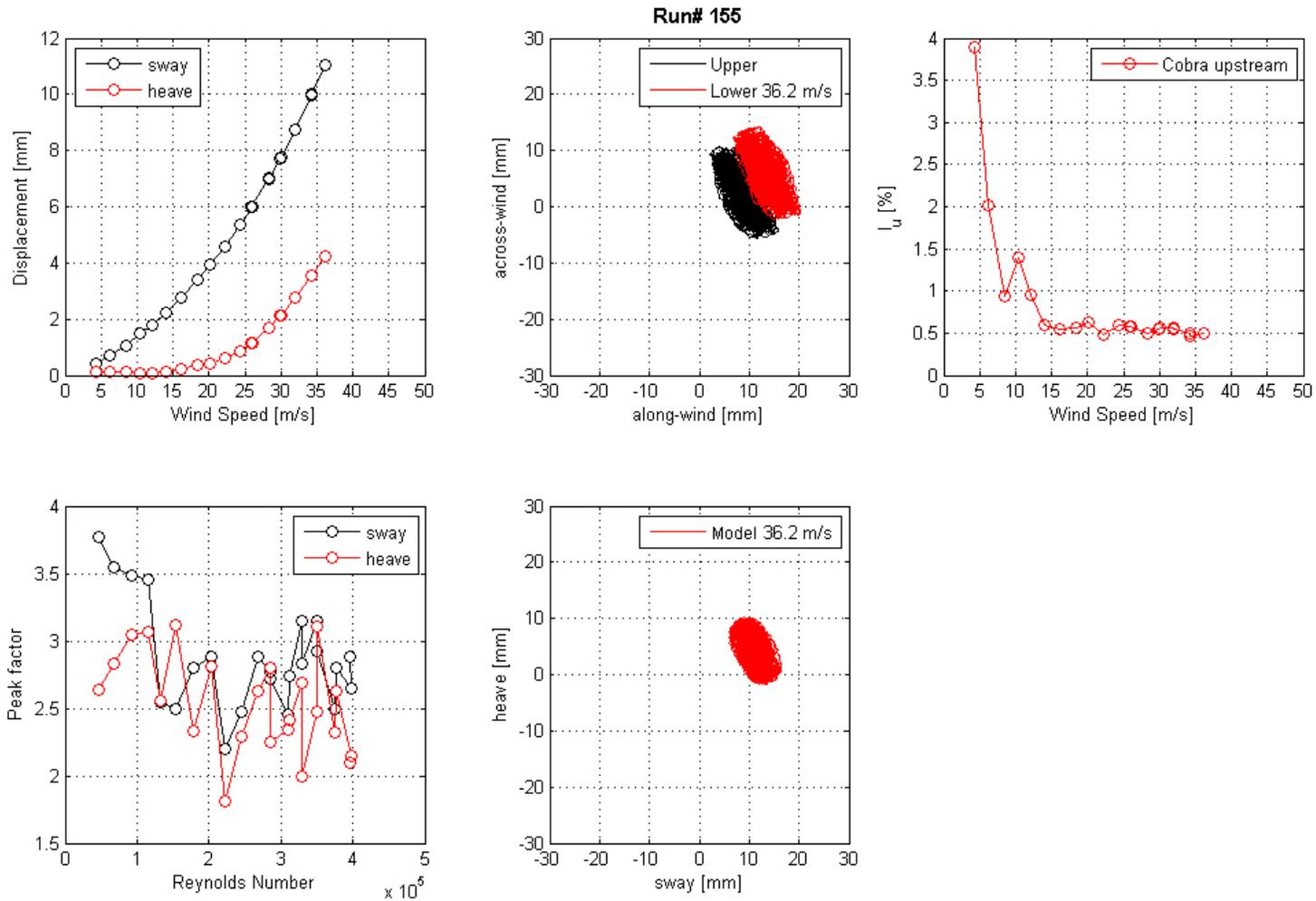
Figure 129. Graph. Mean displacement and peak factor from the laser, motion path at one wind speed, and intensity of turbulence measured at the entrance of the test section for run 155.
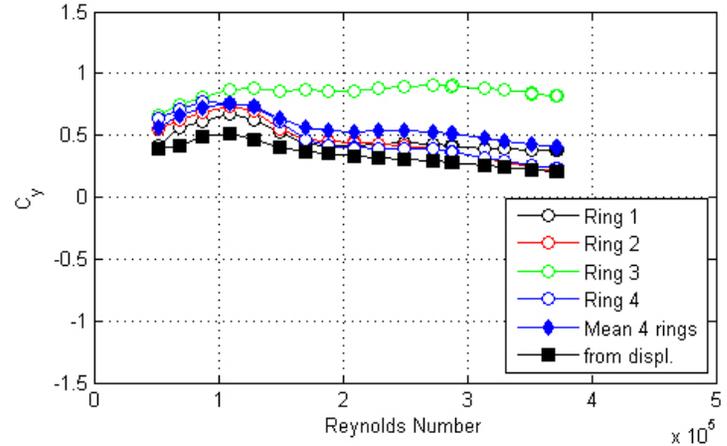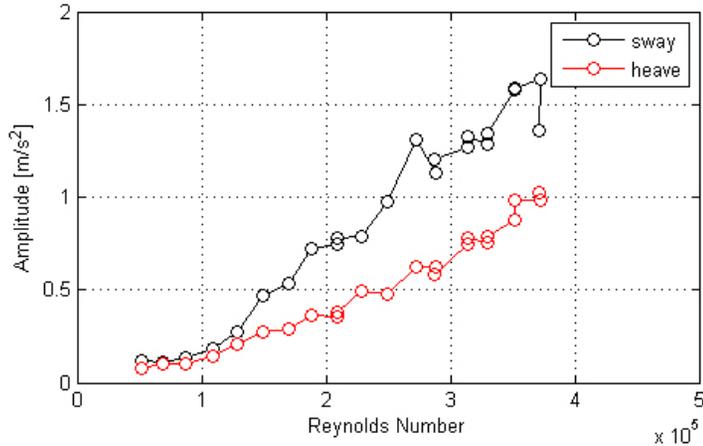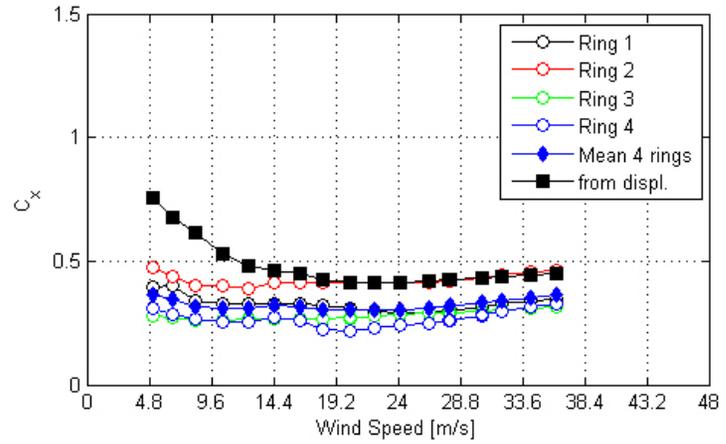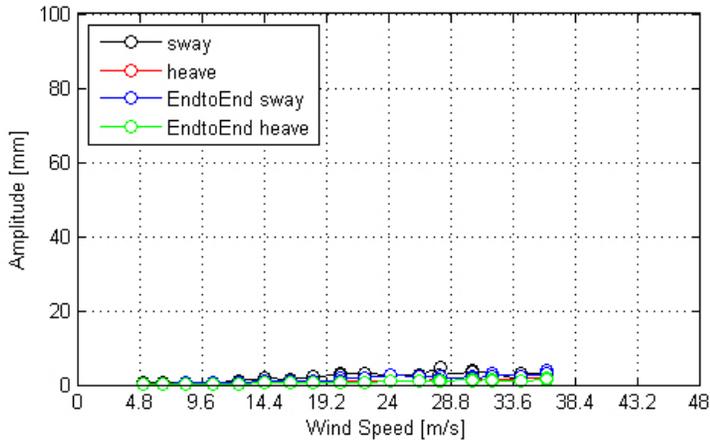
Figure 130. Graph. Response of the cable as a function of wind speed or Reynolds number as measured by the lasers, accelerometers, and surface pressures for run 159.
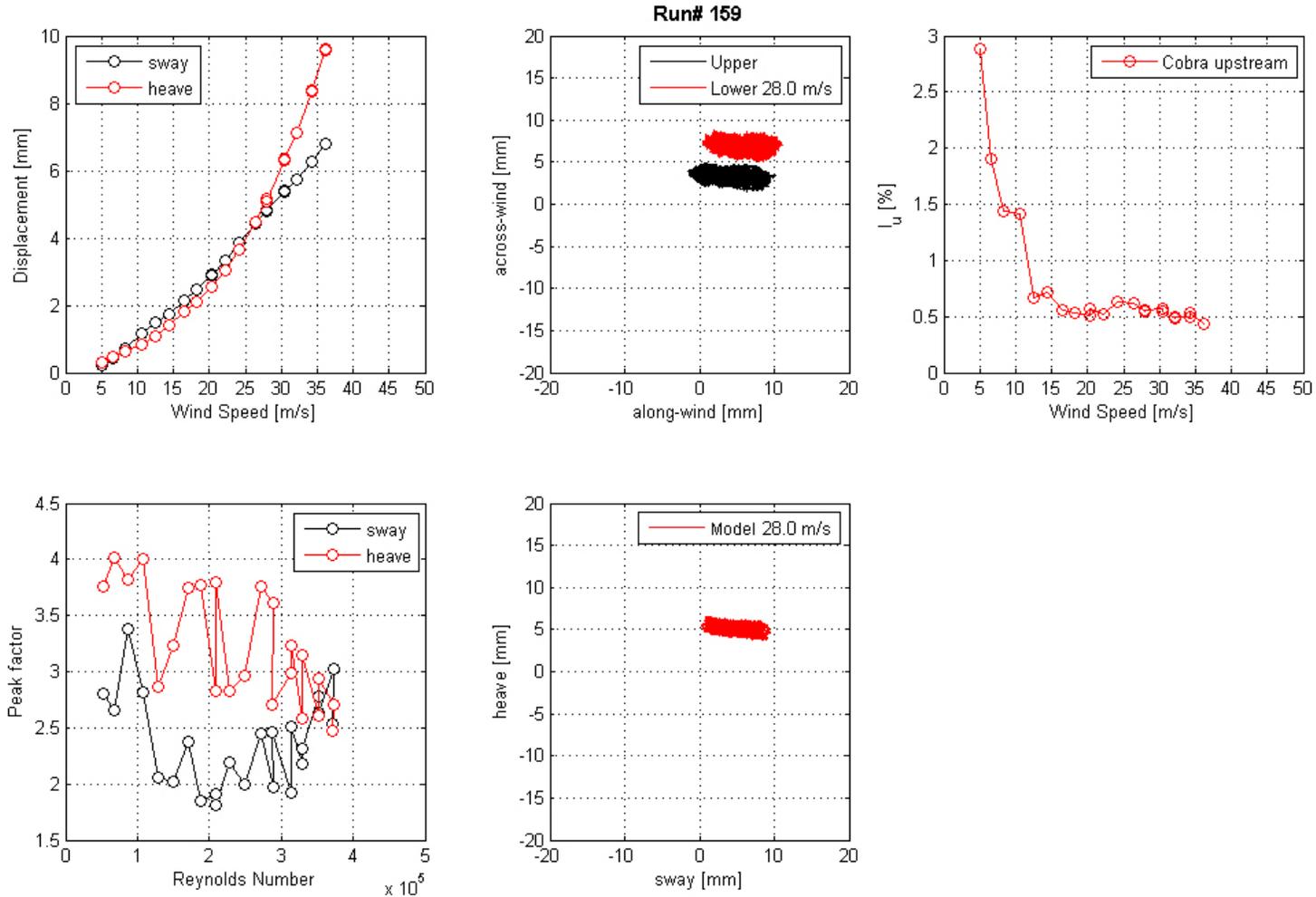
Figure 131. Graph. Mean displacement and peak factor from the laser, motion path at one wind speed, and intensity of turbulence measured at the entrance of the test section for run 159.
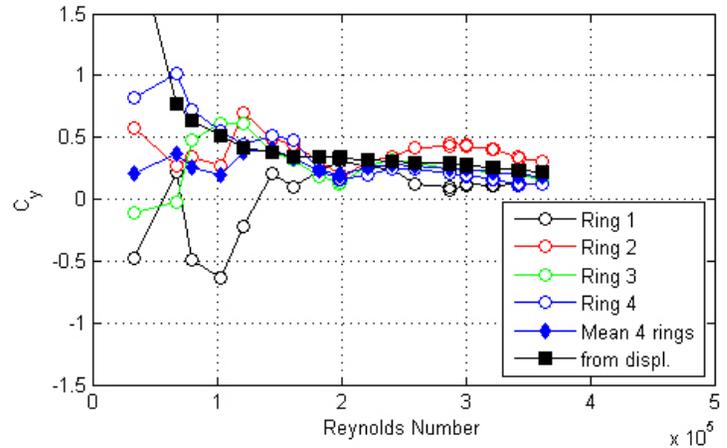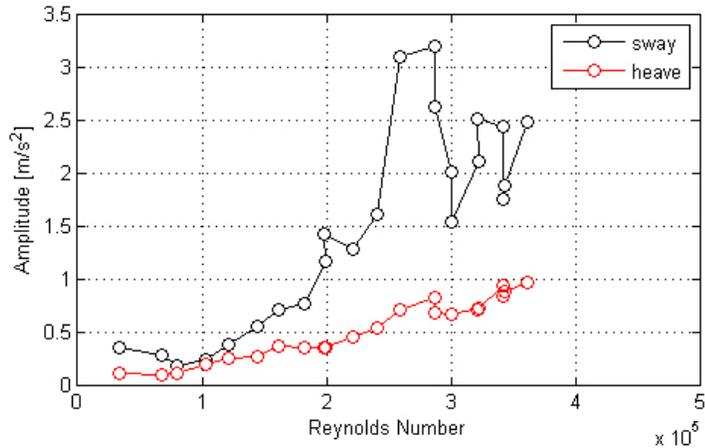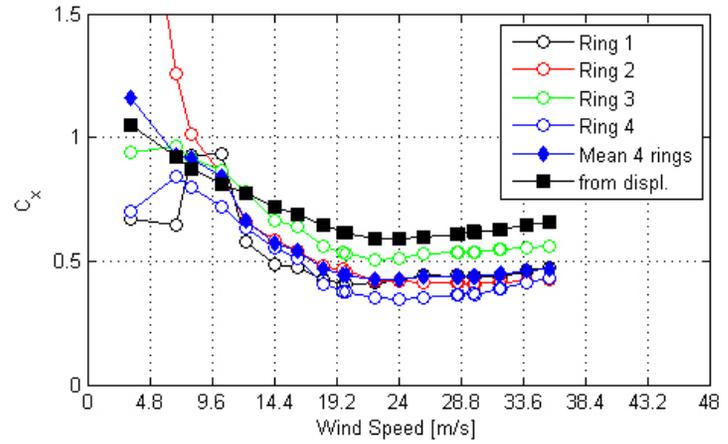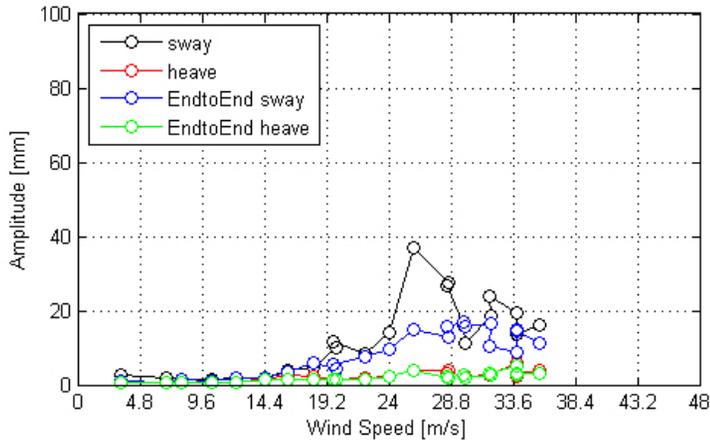
Figure 132. Graph. Response of the cable as a function of wind speed or Reynolds number as measured by the lasers, accelerometers, and surface pressures for run 163.
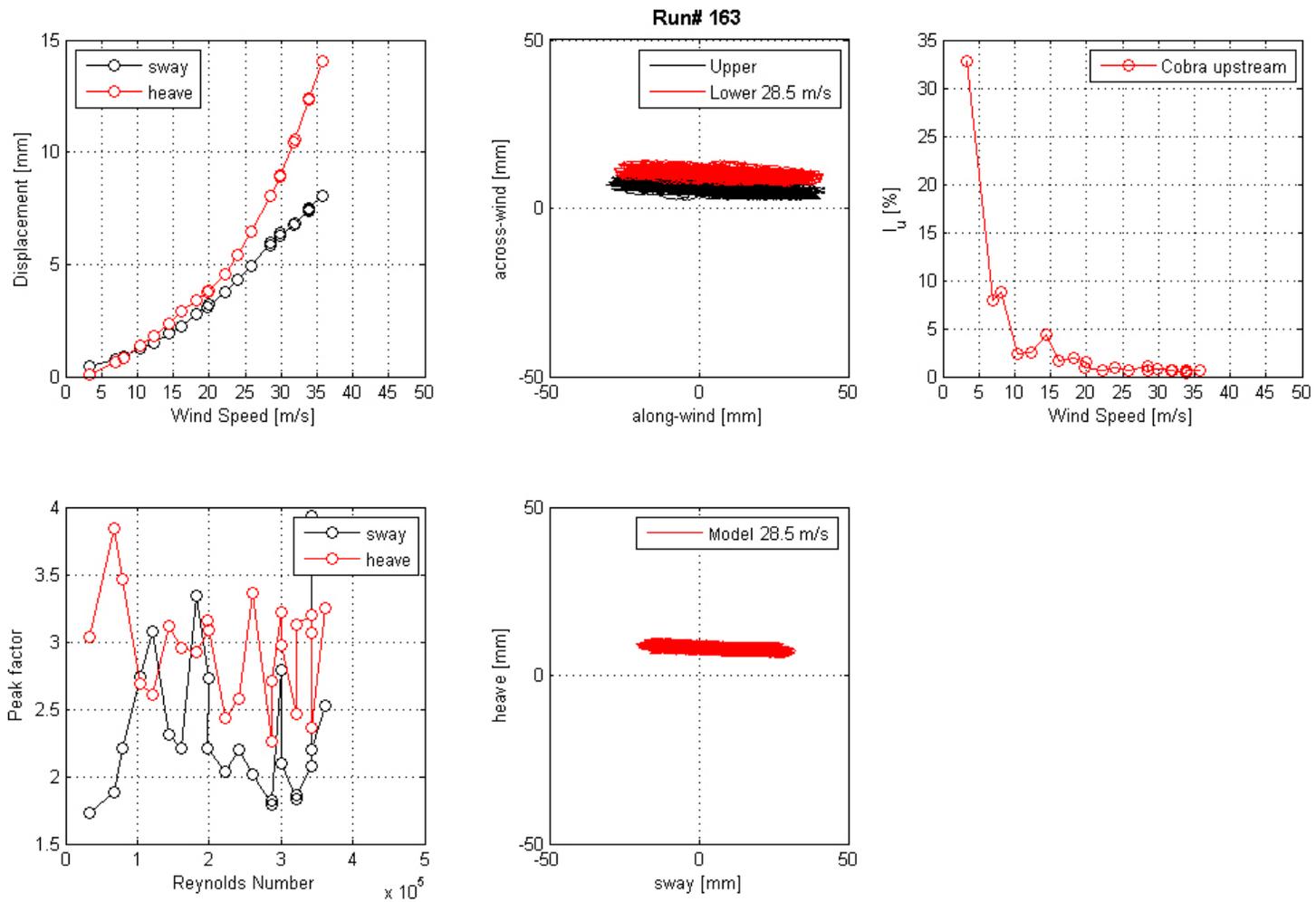
Figure 133. Graph. Mean displacement and peak factor from the laser, motion path at one wind speed, and intensity of turbulence measured at the entrance of the test section for run 163.
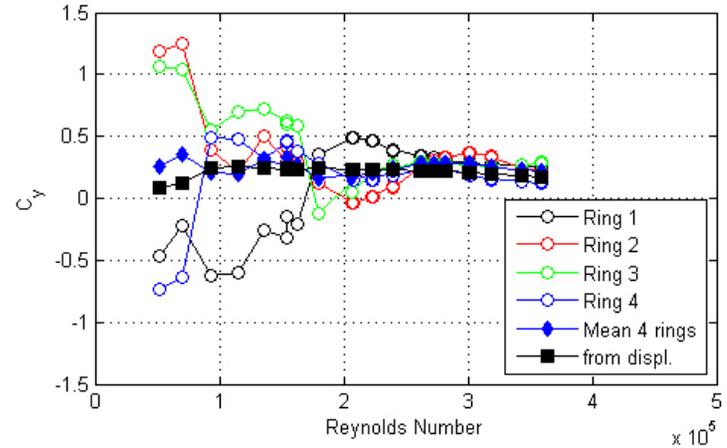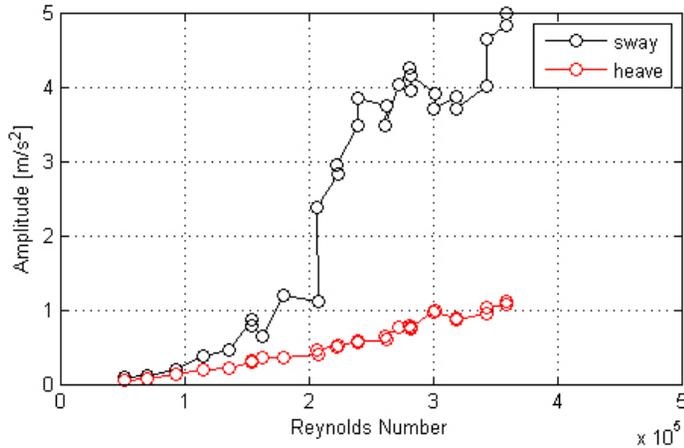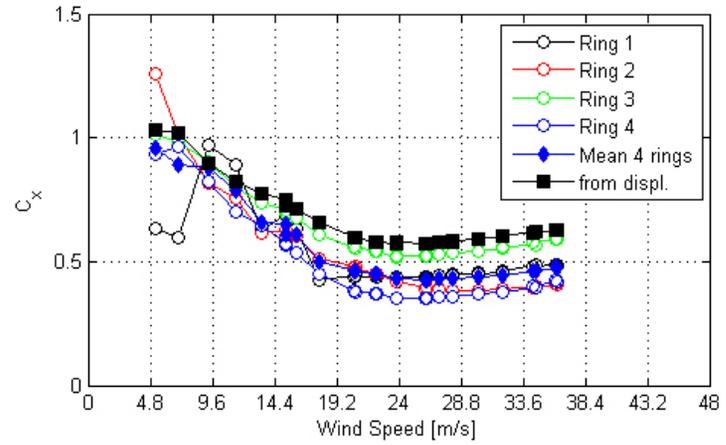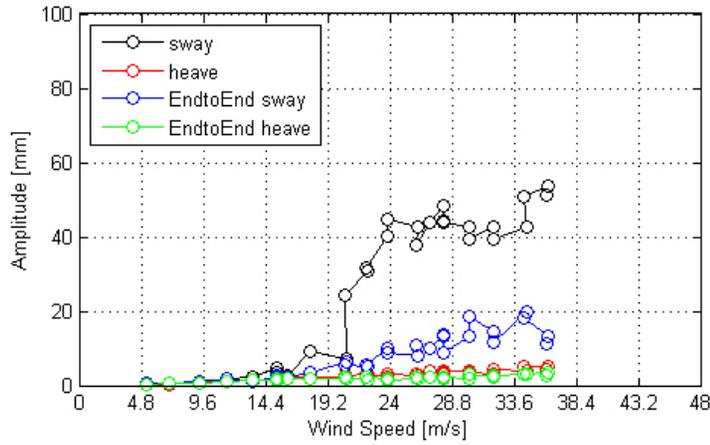
Figure 134. Graph. Response of the cable as a function of wind speed or Reynolds number as measured by the lasers, accelerometers, and surface pressures for run 167.
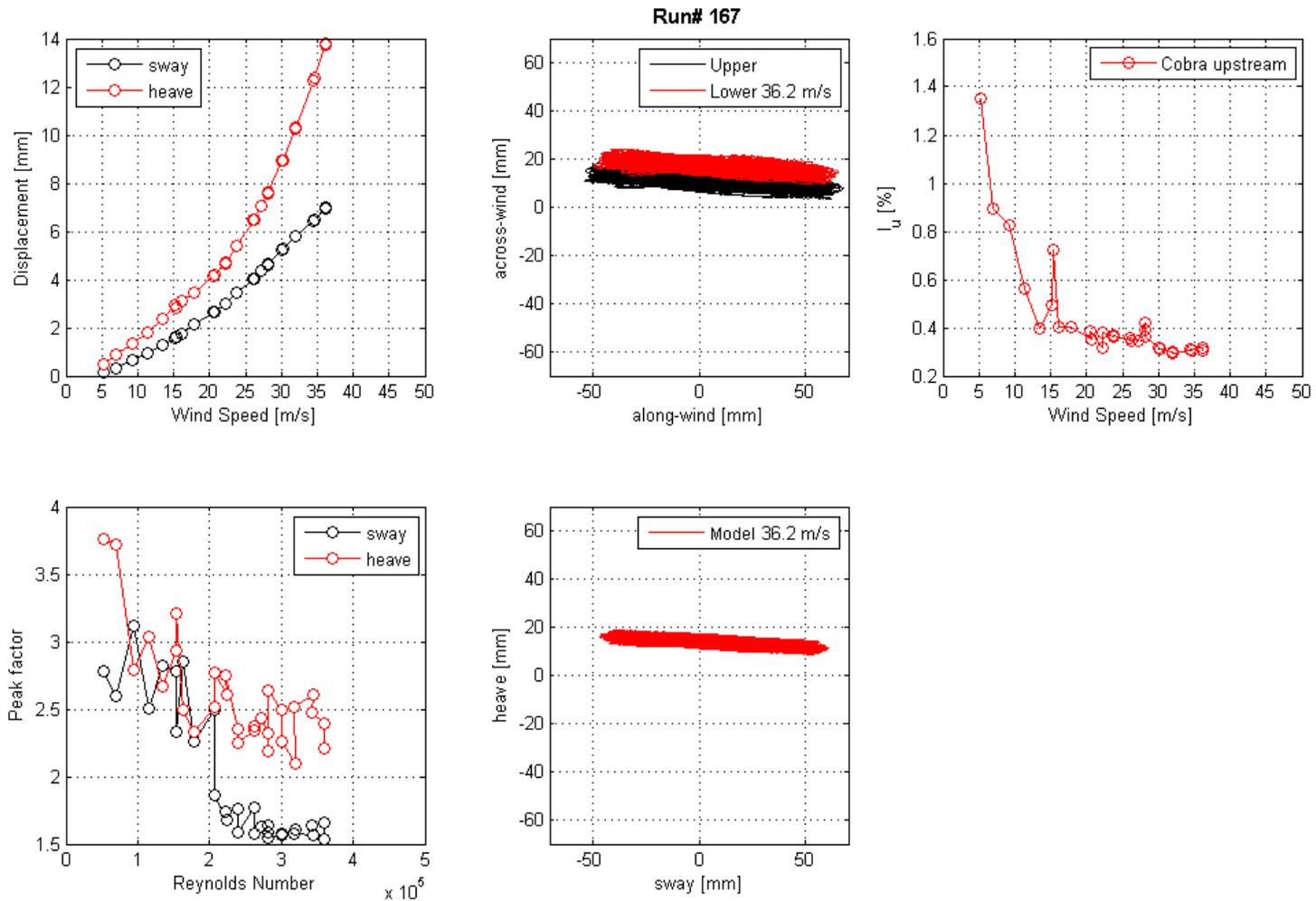
Figure 135. Graph. Mean displacement and peak factor from the laser, motion path at one wind speed, and intensity of turbulence measured at the entrance of the test section for run 167.
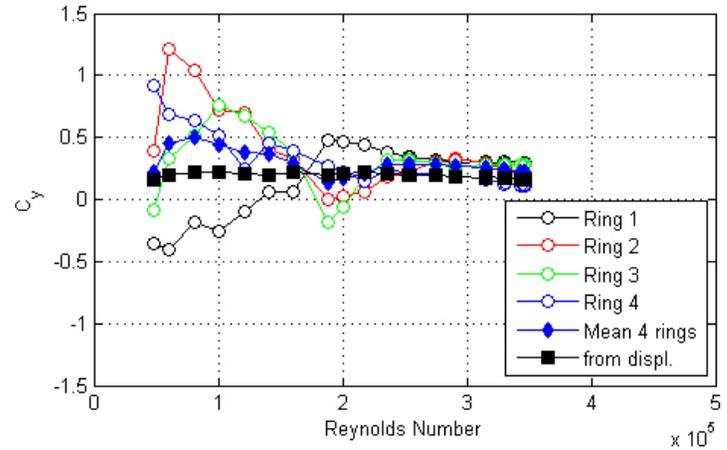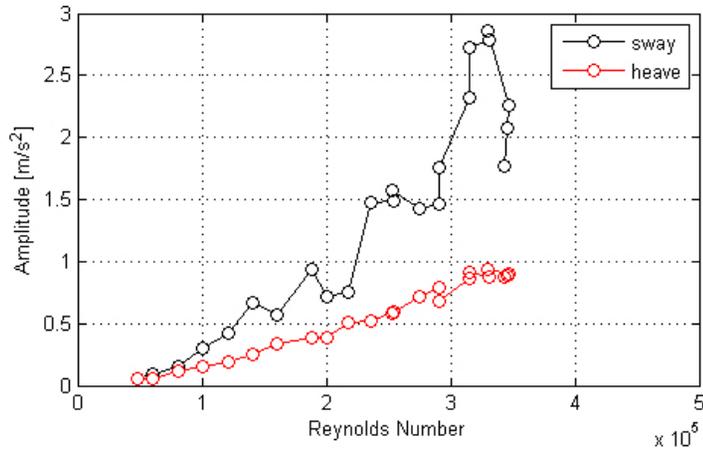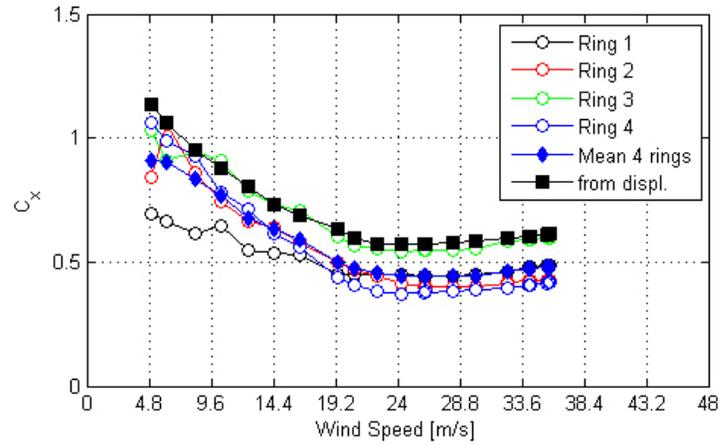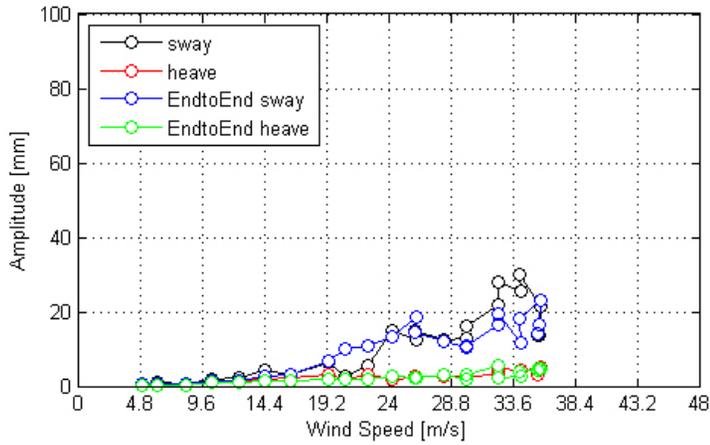
Figure 136. Graph. Response of the cable as a function of wind speed or Reynolds number as measured by the lasers, accelerometers, and surface pressures for run 176.
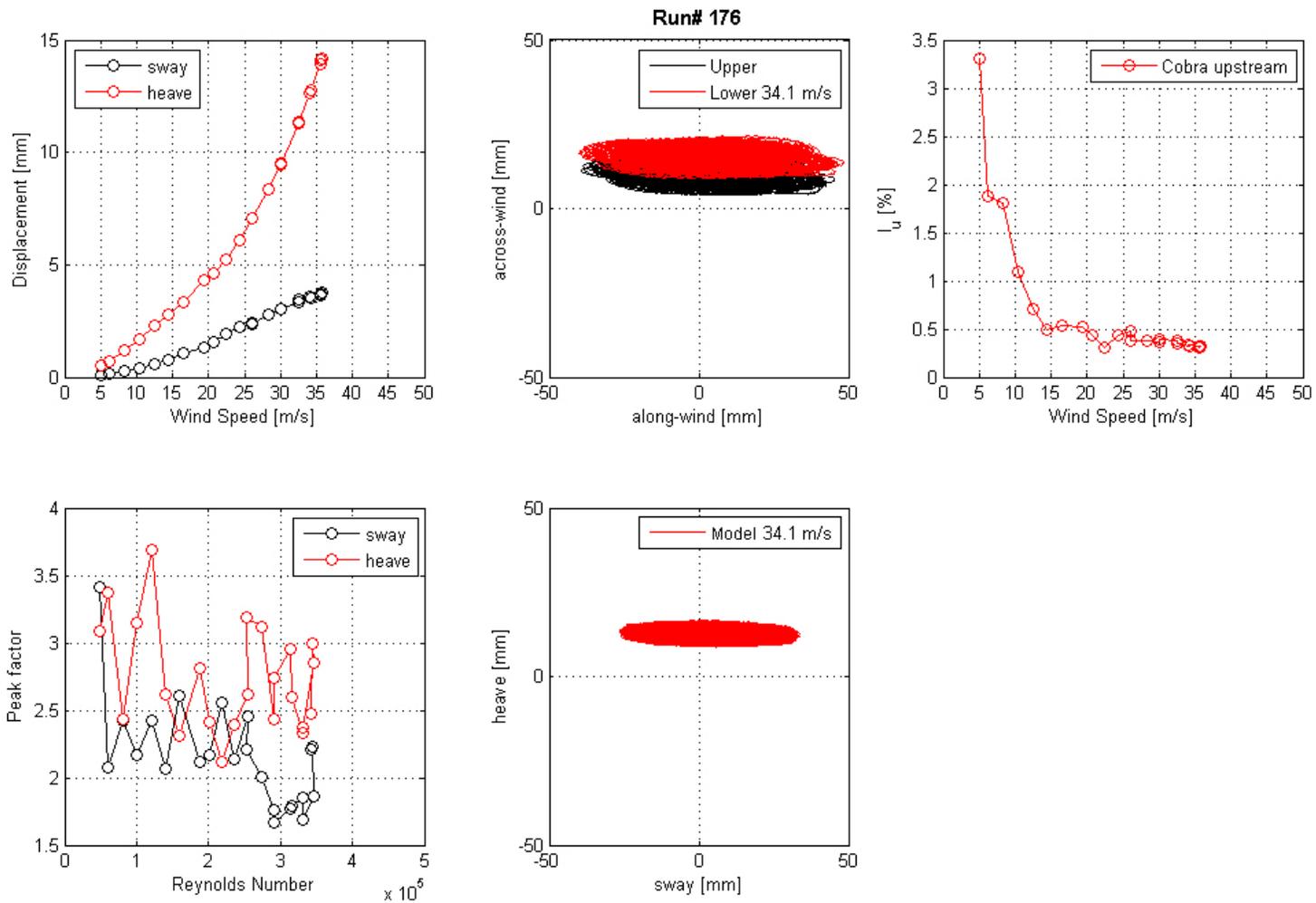
Figure 137. Graph. Mean displacement and peak factor from the laser, motion path at one wind speed, and intensity of turbulence measured at the entrance of the test section for run 176.
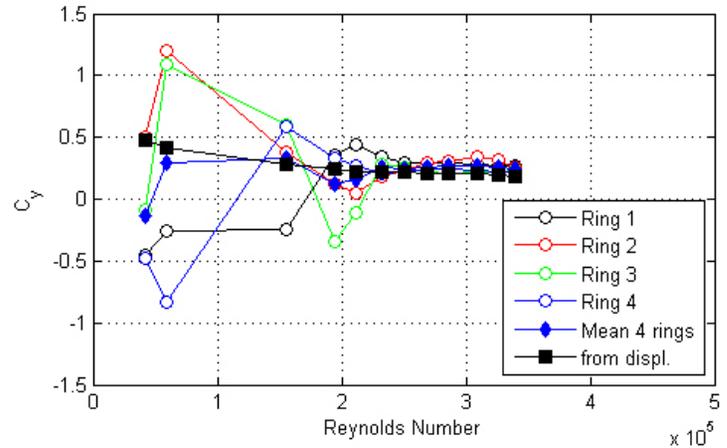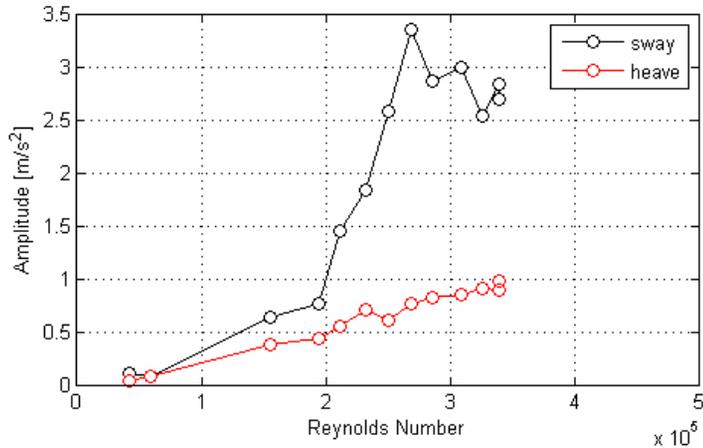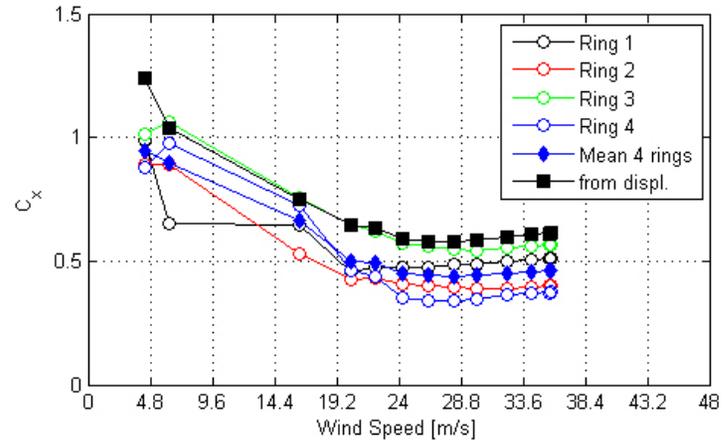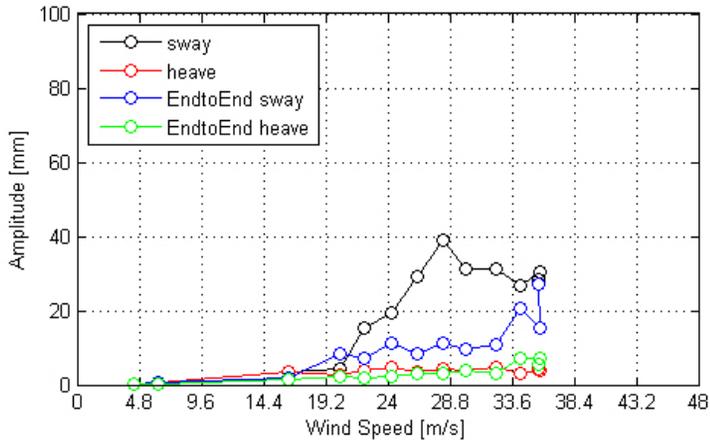
Figure 138. Graph. Response of the cable as a function of wind speed or Reynolds number as measured by the lasers, accelerometers, and surface pressures for run 178.
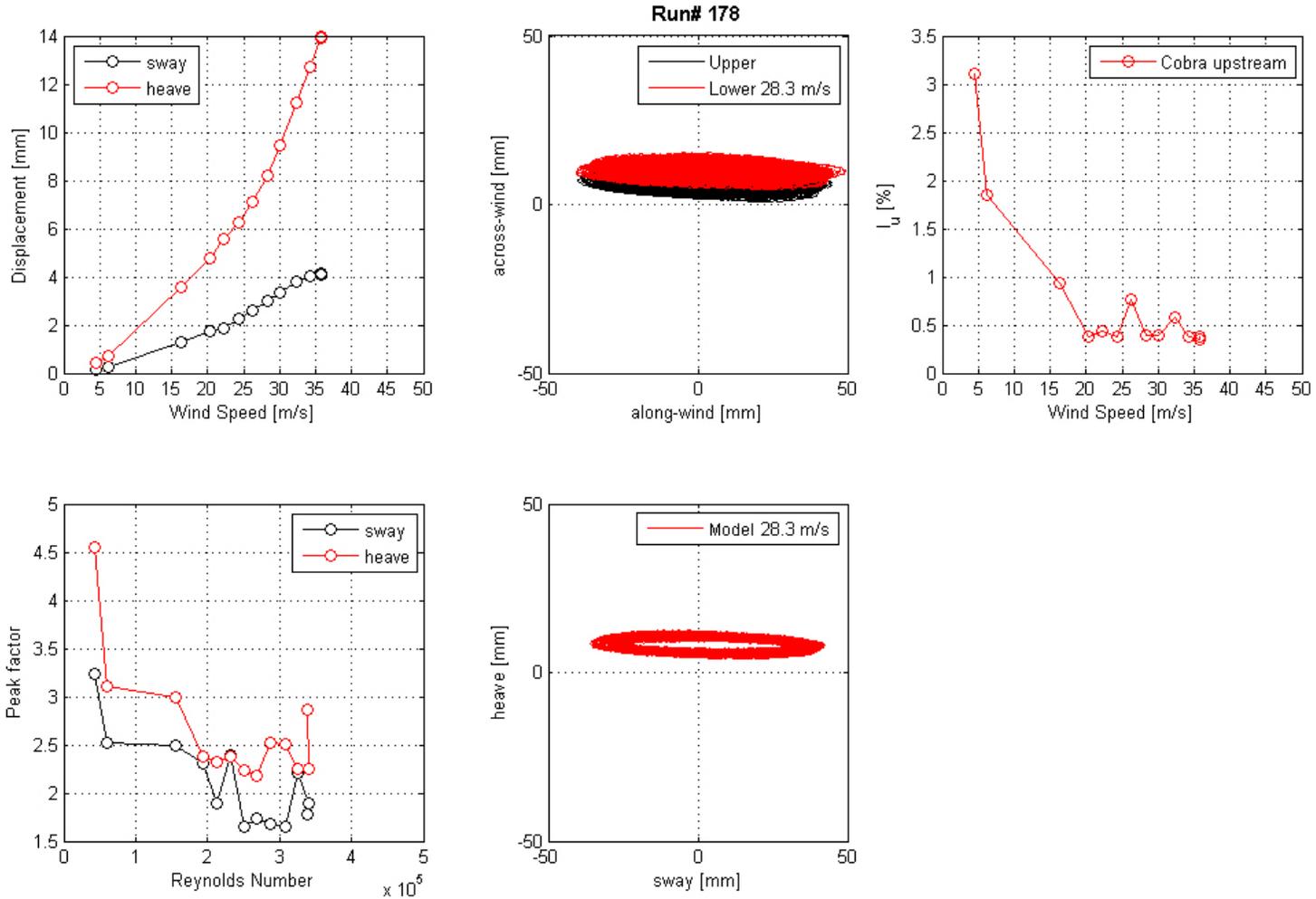
Figure 139. Graph. Mean displacement and peak factor from the laser, motion path at one wind speed, and intensity of turbulence measured at the entrance of the test section for run 178.
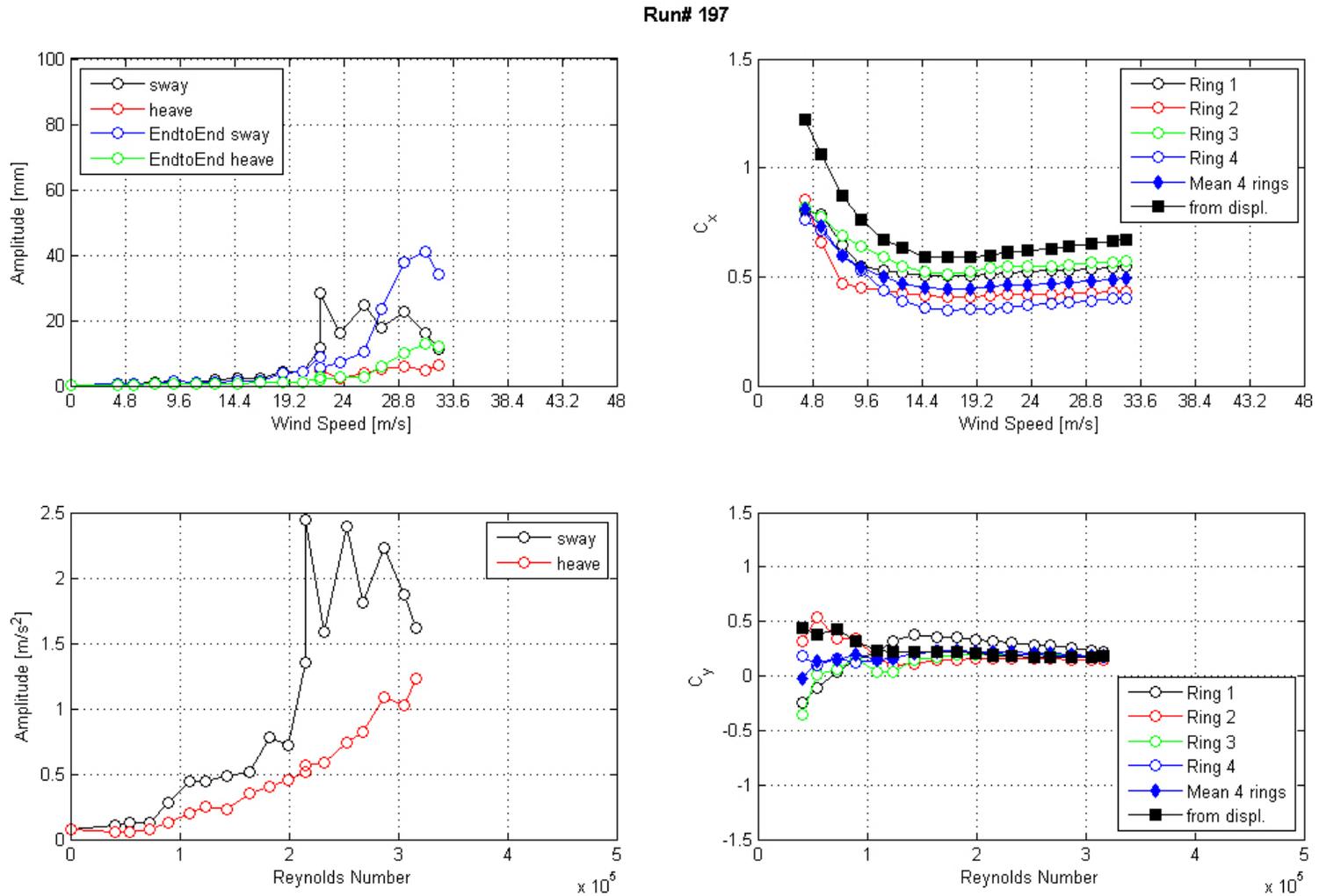
Figure 140. Graph. Response of the cable as a function of wind speed or Reynolds number as measured by the lasers, accelerometers, and surface pressures for run 197.
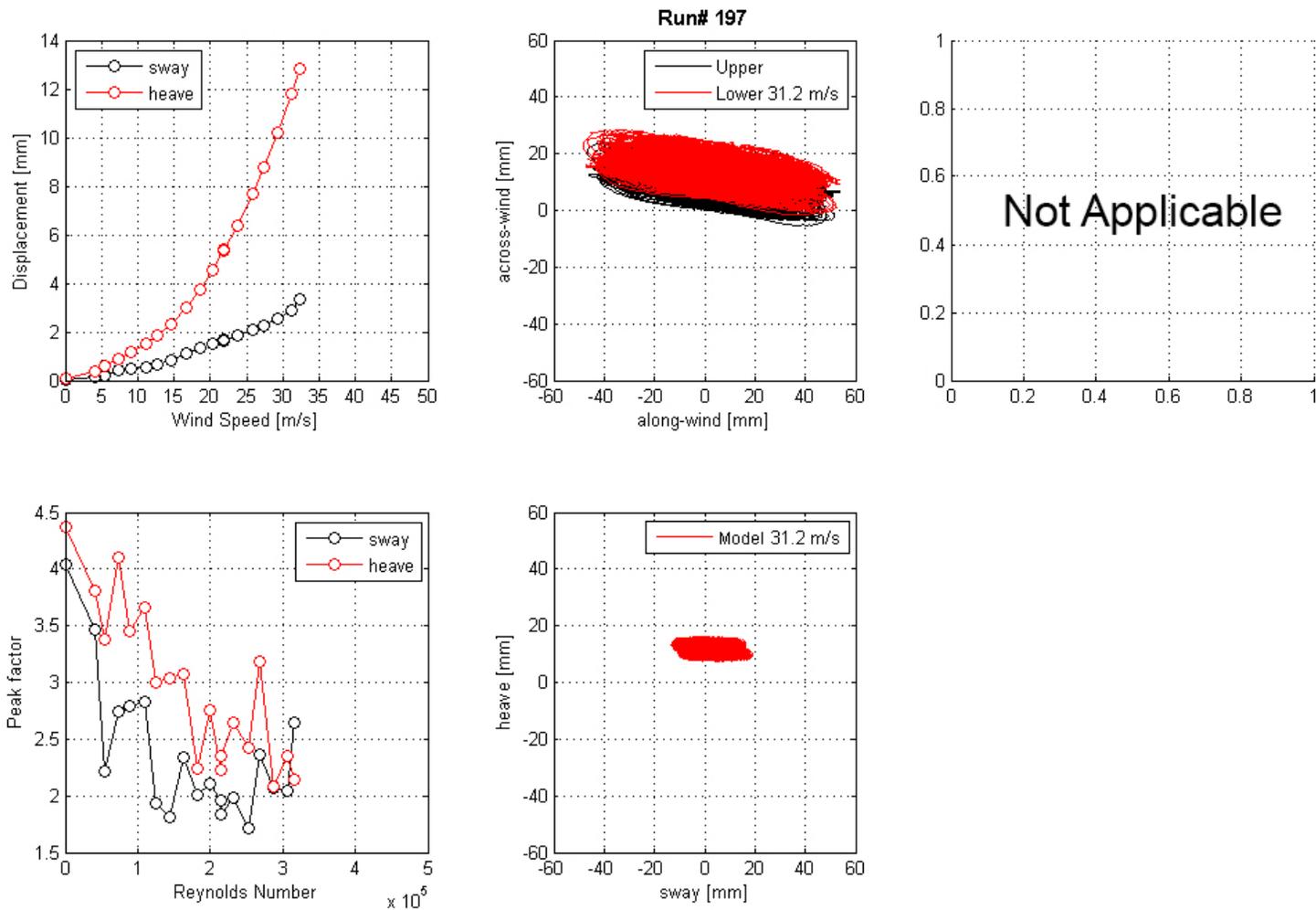
Figure 141. Graph. Mean displacement and peak factor from the laser, motion path at one wind speed, and intensity of turbulence measured at the entrance of the test section for run 197.
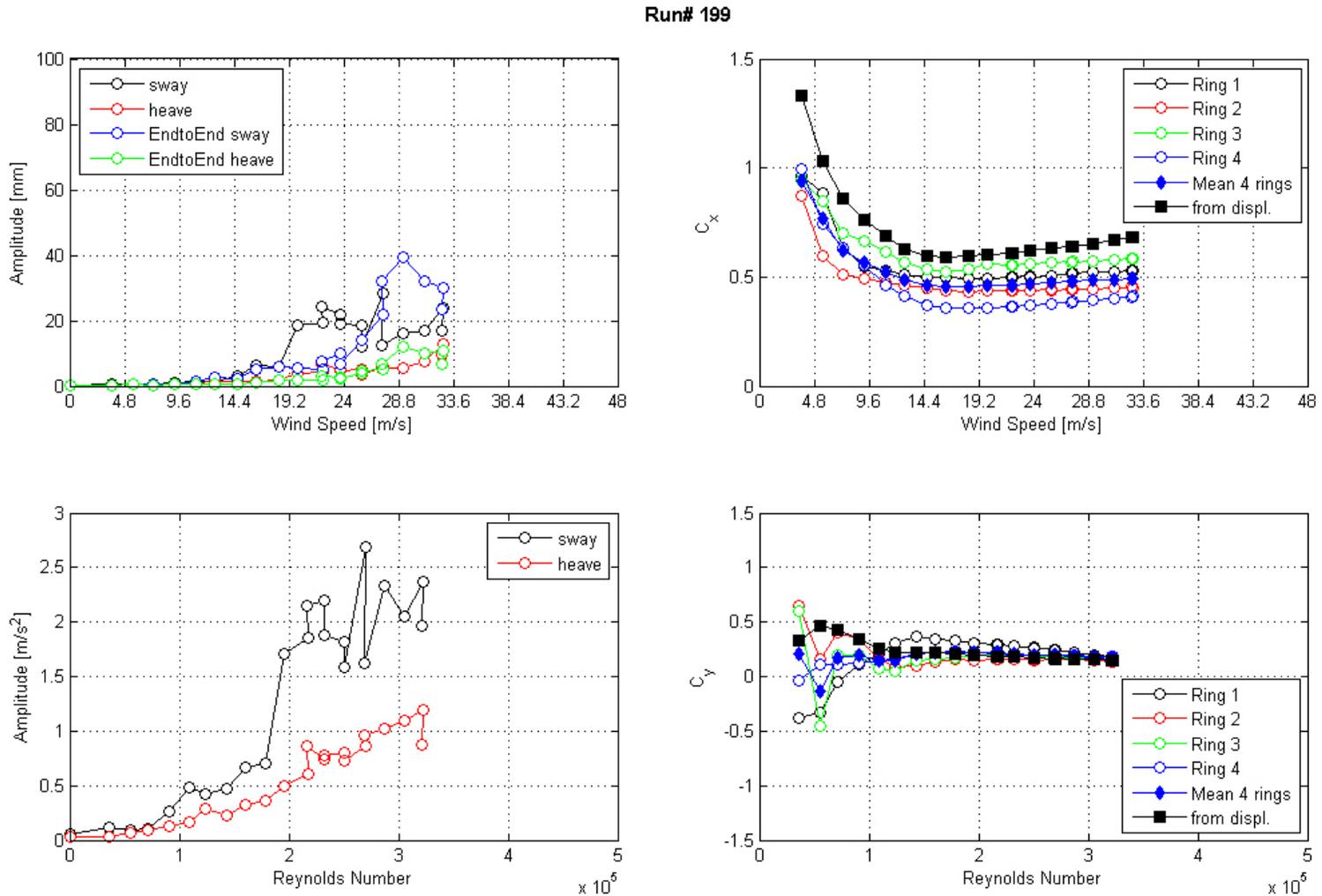
Figure 142. Graph. Response of the cable as a function of wind speed or Reynolds number as measured by the lasers, accelerometers, and surface pressures for run 199.
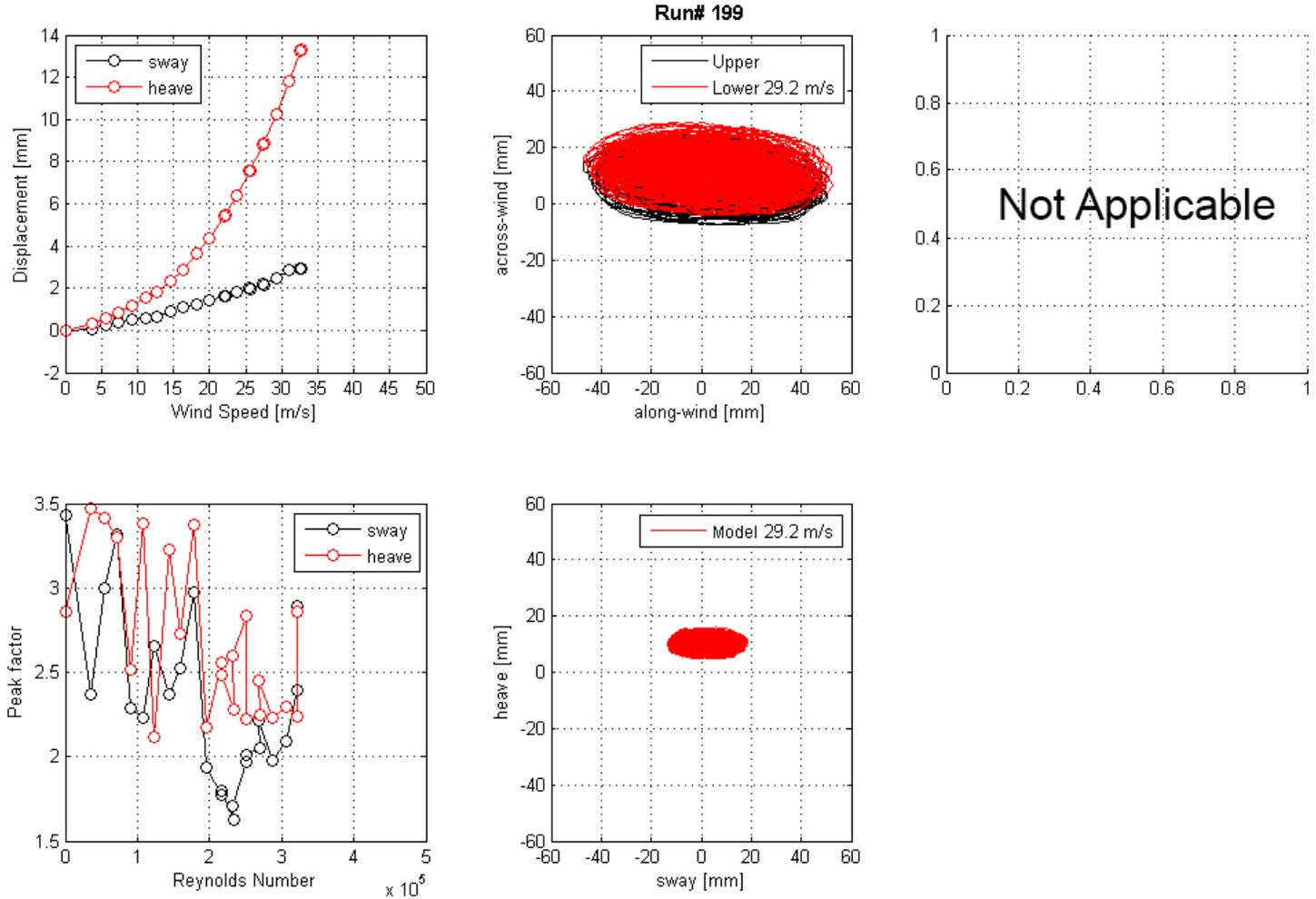
Figure 143. Graph. Mean displacement and peak factor from the laser, motion path at one wind speed, and intensity of turbulence measured at the entrance of the test section for run 199.
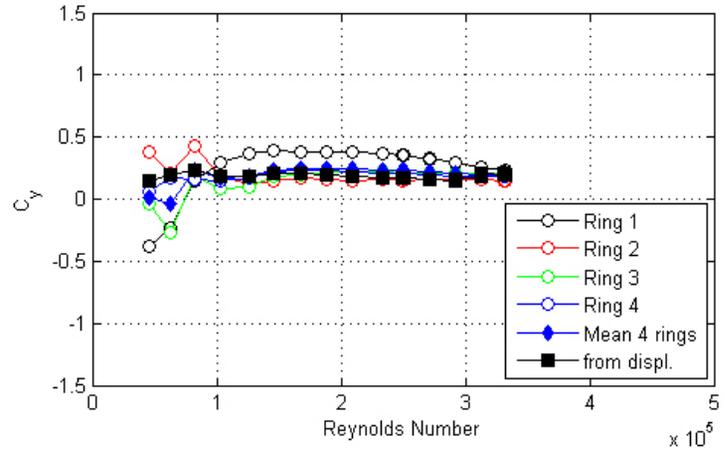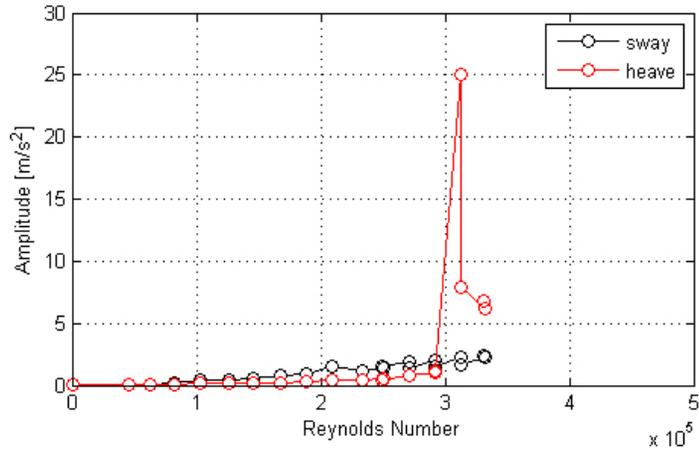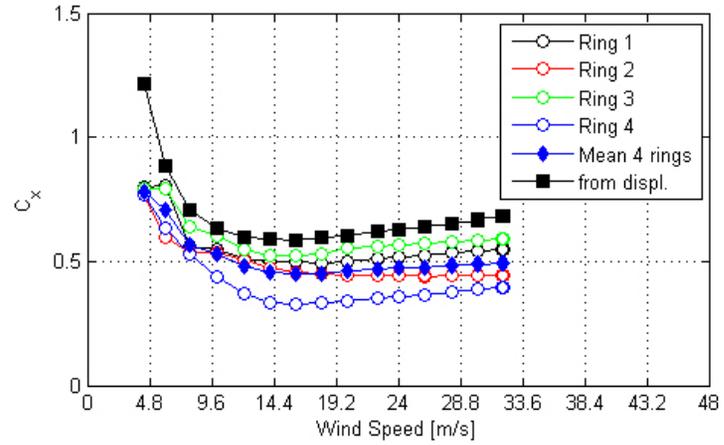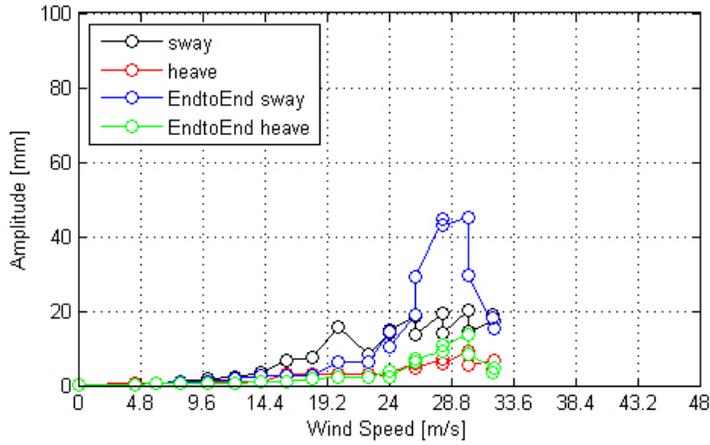
Figure 144. Graph. Response of the cable as a function of wind speed or Reynolds number as measured by the lasers, accelerometers, and surface pressures for run 203.
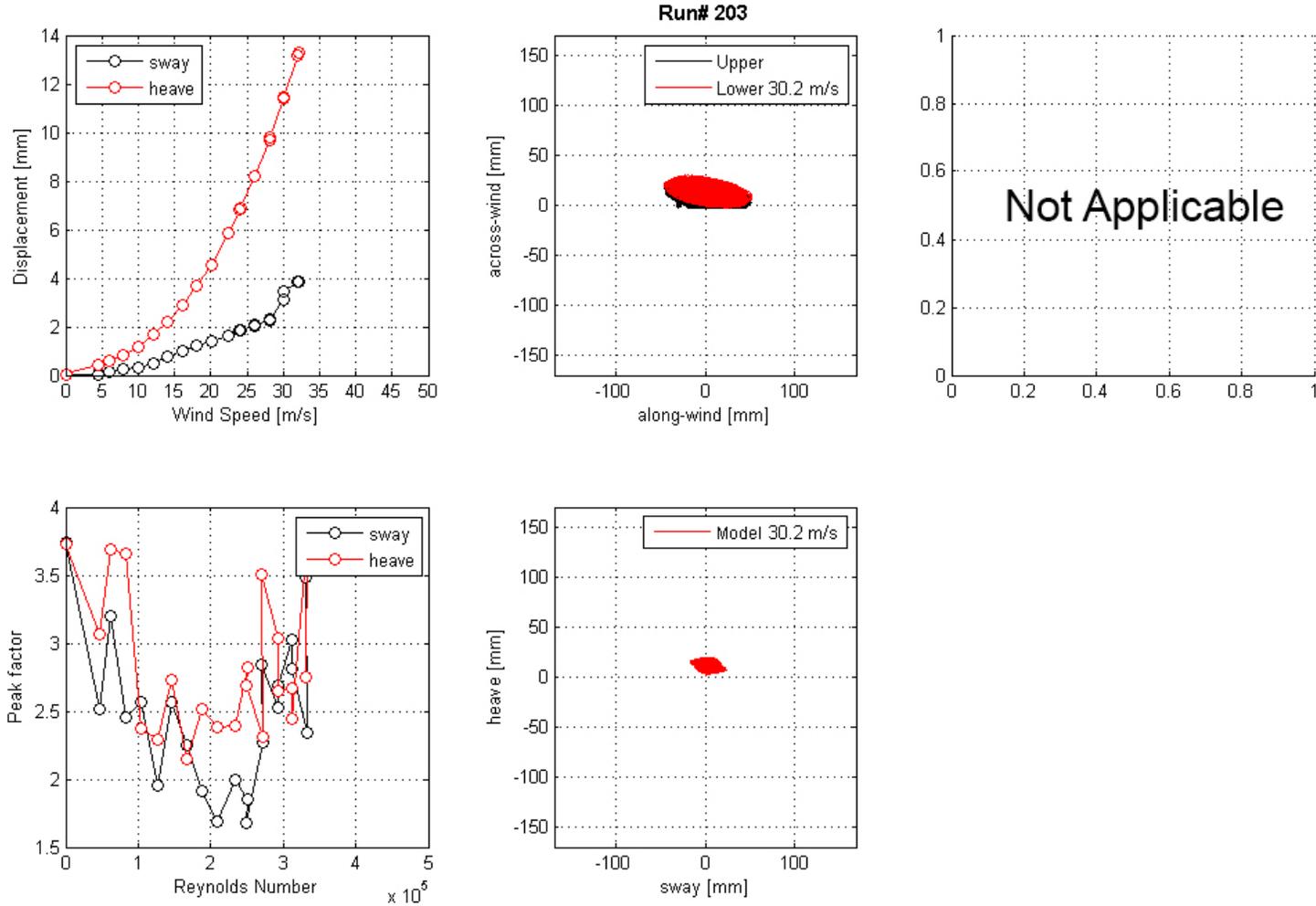
Figure 145. Graph. Mean displacement and peak factor from the laser, motion path at one wind speed, and intensity of turbulence measured at the entrance of the test section for run 203.
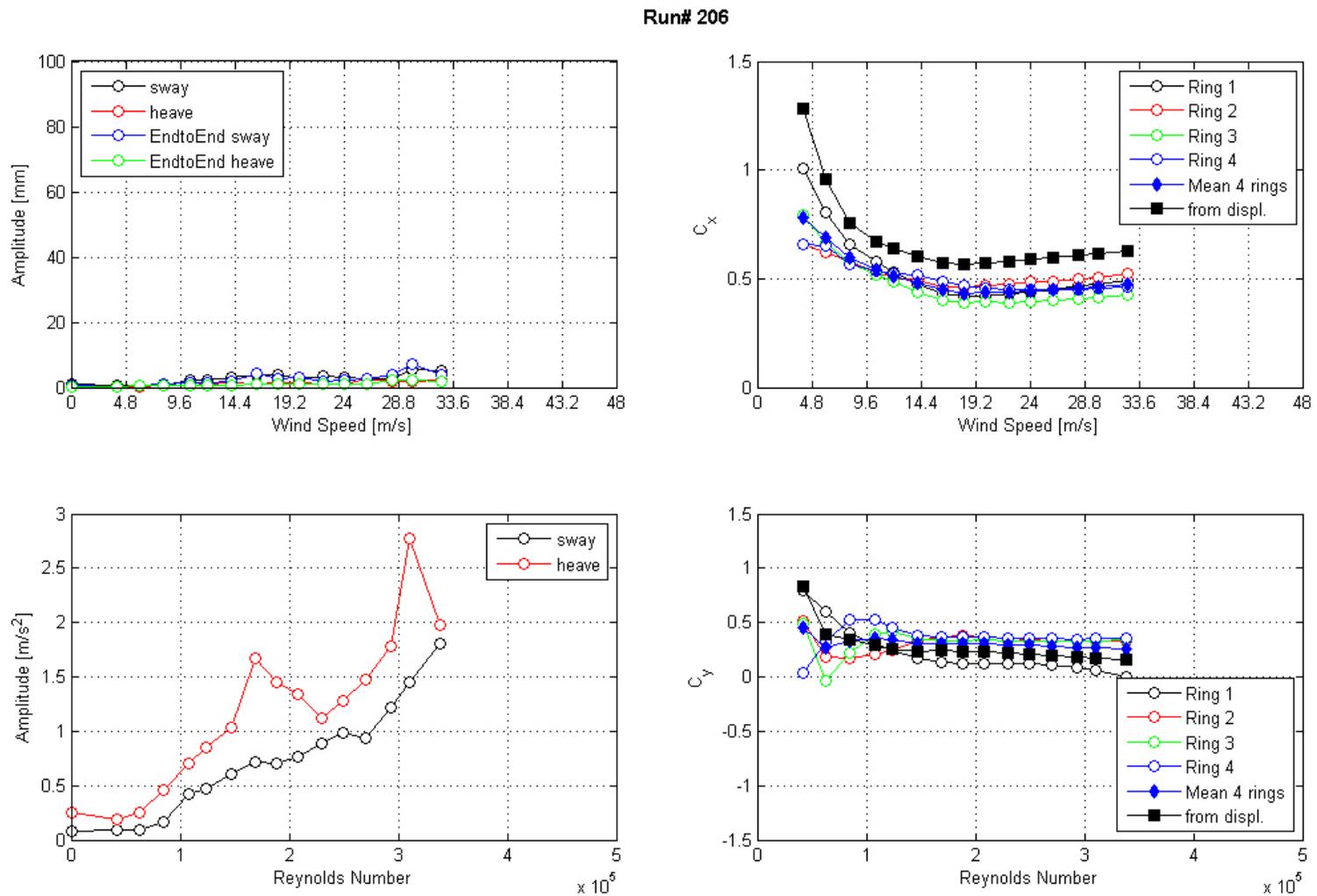
Figure 146. Graph. Response of the cable as a function of wind speed or Reynolds number as measured by the lasers, accelerometers, and surface pressures for run 206.
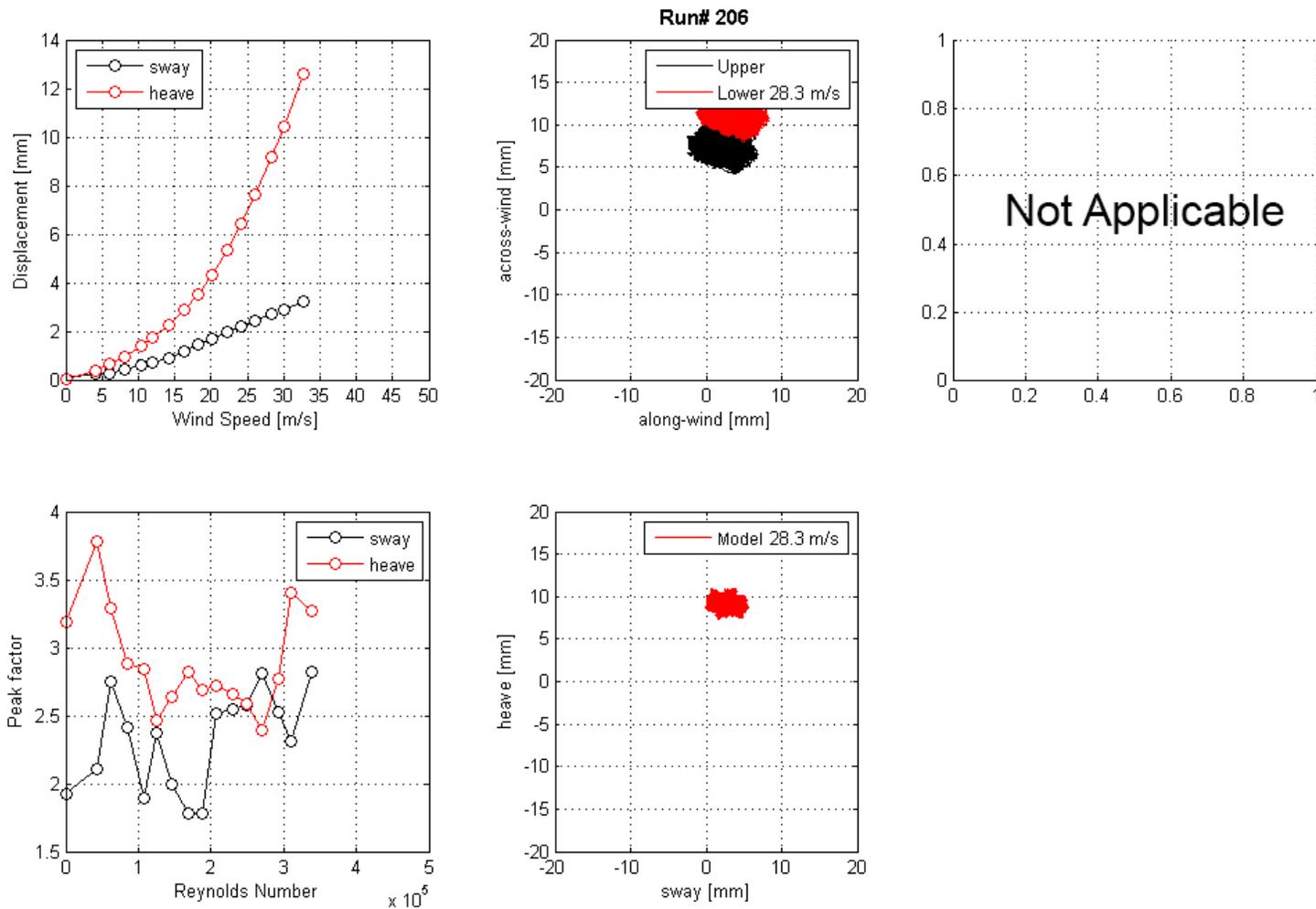
Figure 147. Graph. Mean displacement and peak factor from the laser, motion path at one wind speed, and intensity of turbulence measured at the entrance of the test section for run 206.
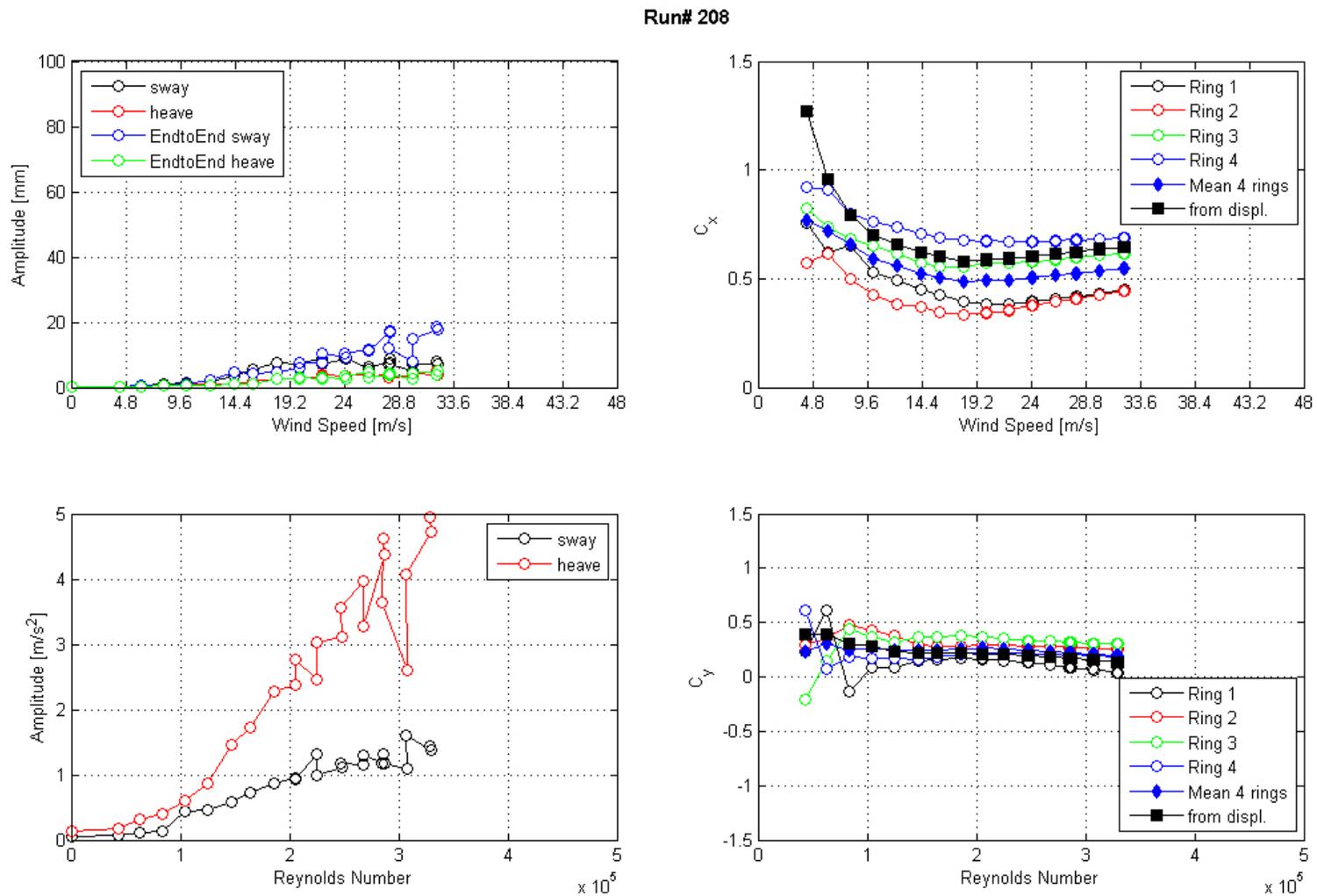
Figure 148. Graph. Response of the cable as a function of wind speed or Reynolds number as measured by the lasers, accelerometers, and surface pressures for run 208.
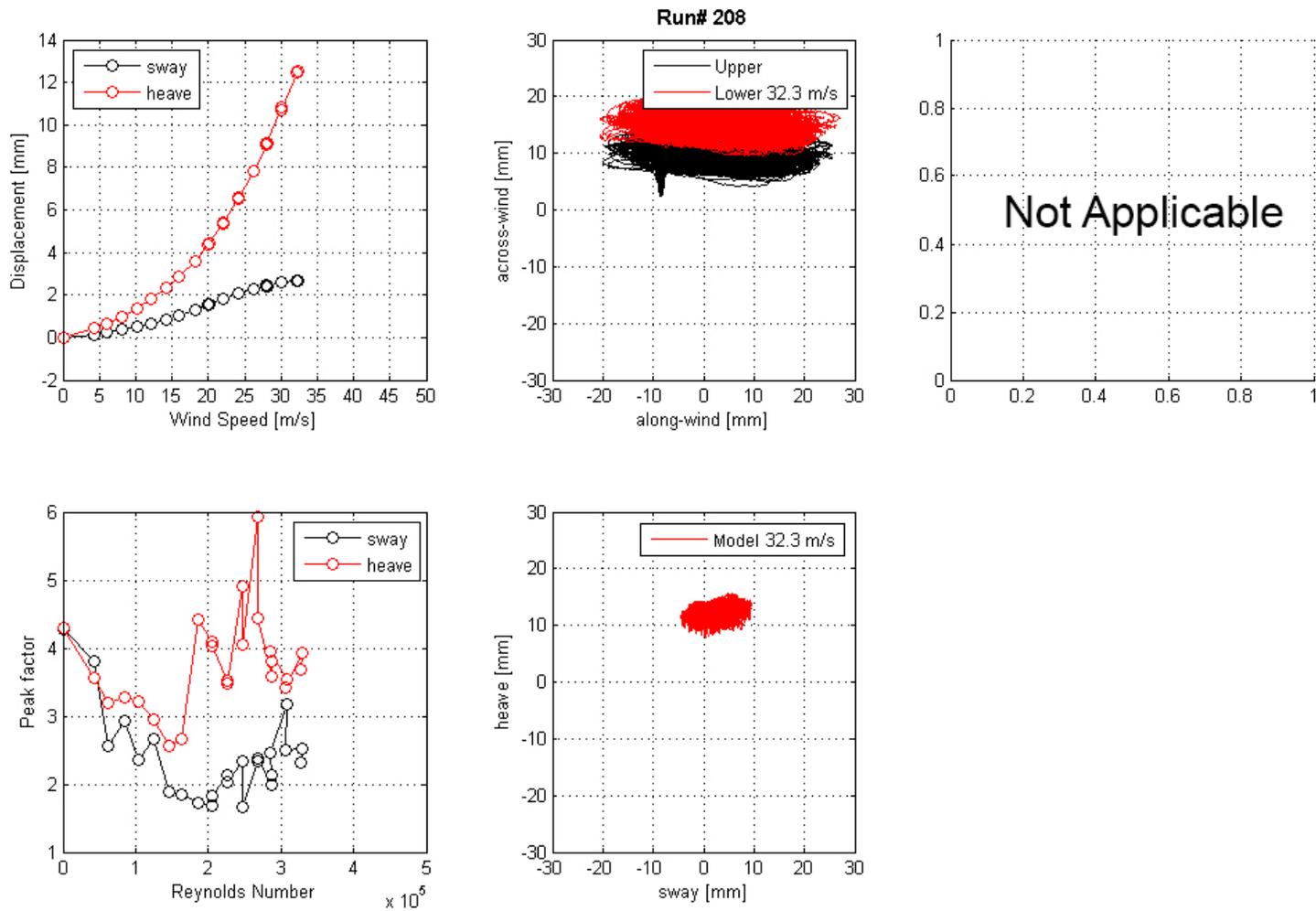
Figure 149. Graph. Mean displacement and peak factor from the laser, motion path at one wind speed, and intensity of turbulence measured at the entrance of the test section for run 208.
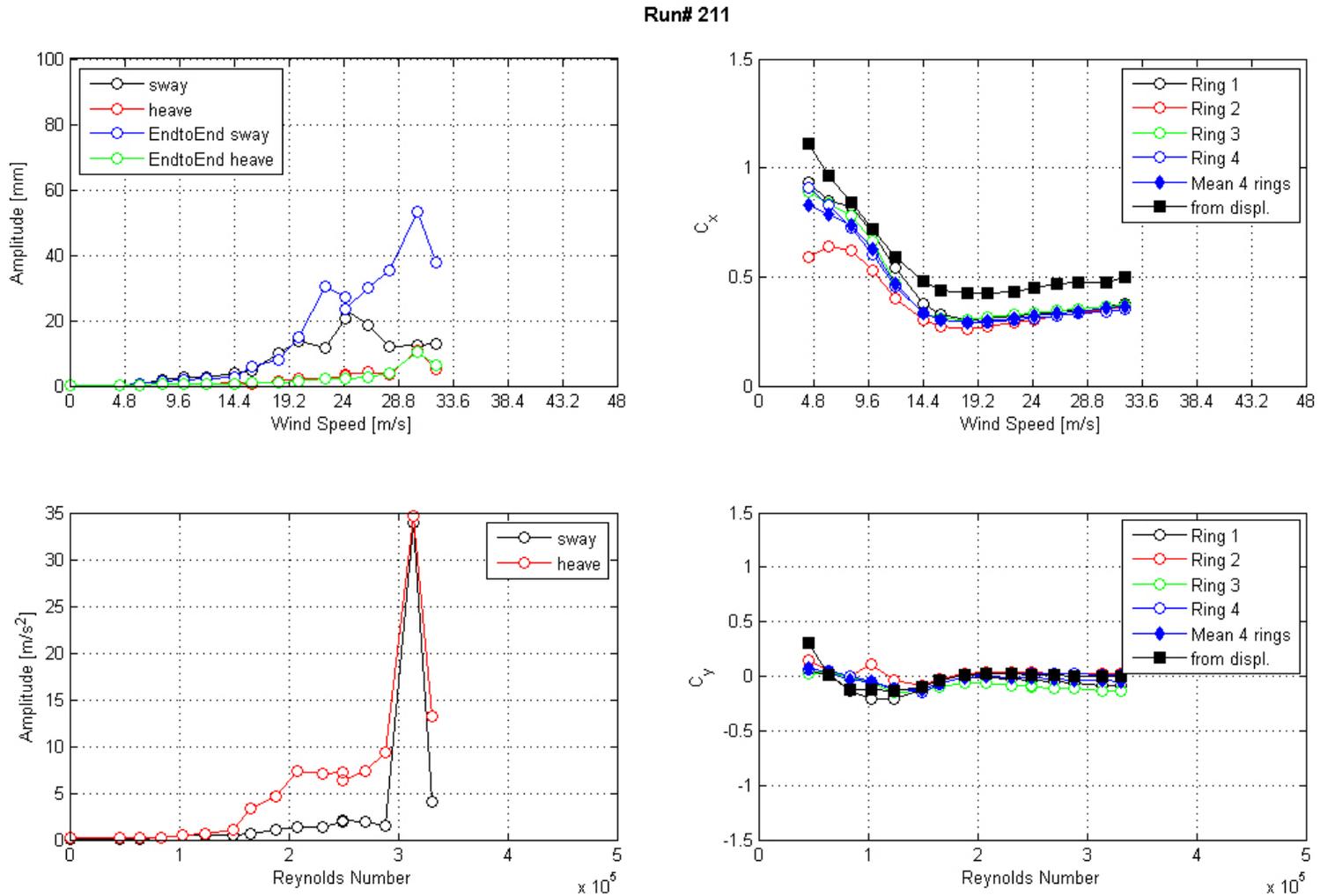
Run# 211

Figure 150. Graph. Response of the cable as a function of wind speed or Reynolds number as measured by the lasers, accelerometers, and surface pressures for run 211.
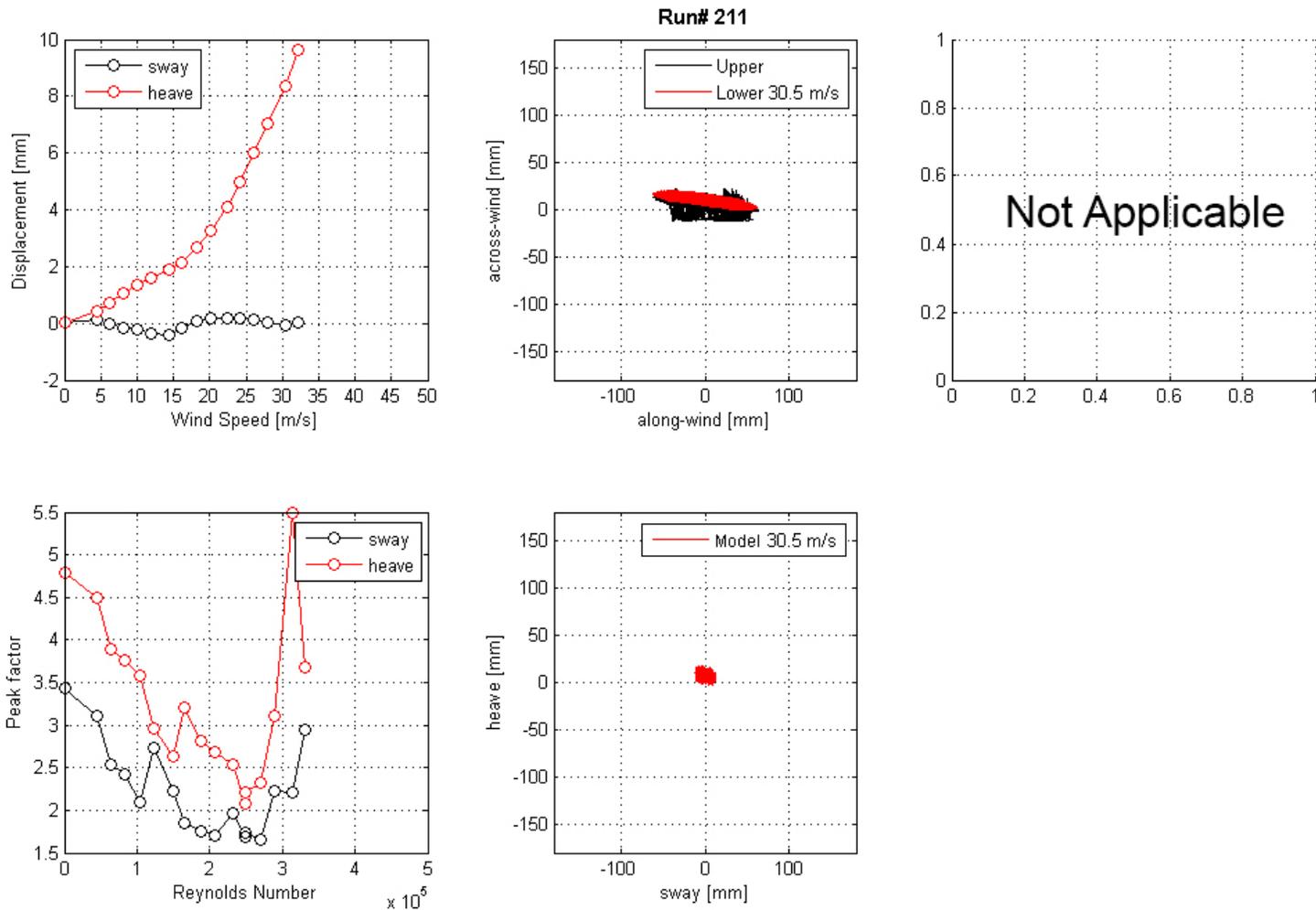
Figure 151. Graph. Mean displacement and peak factor from the laser, motion path at one wind speed, and intensity of turbulence measured at the entrance of the test section for run 211.
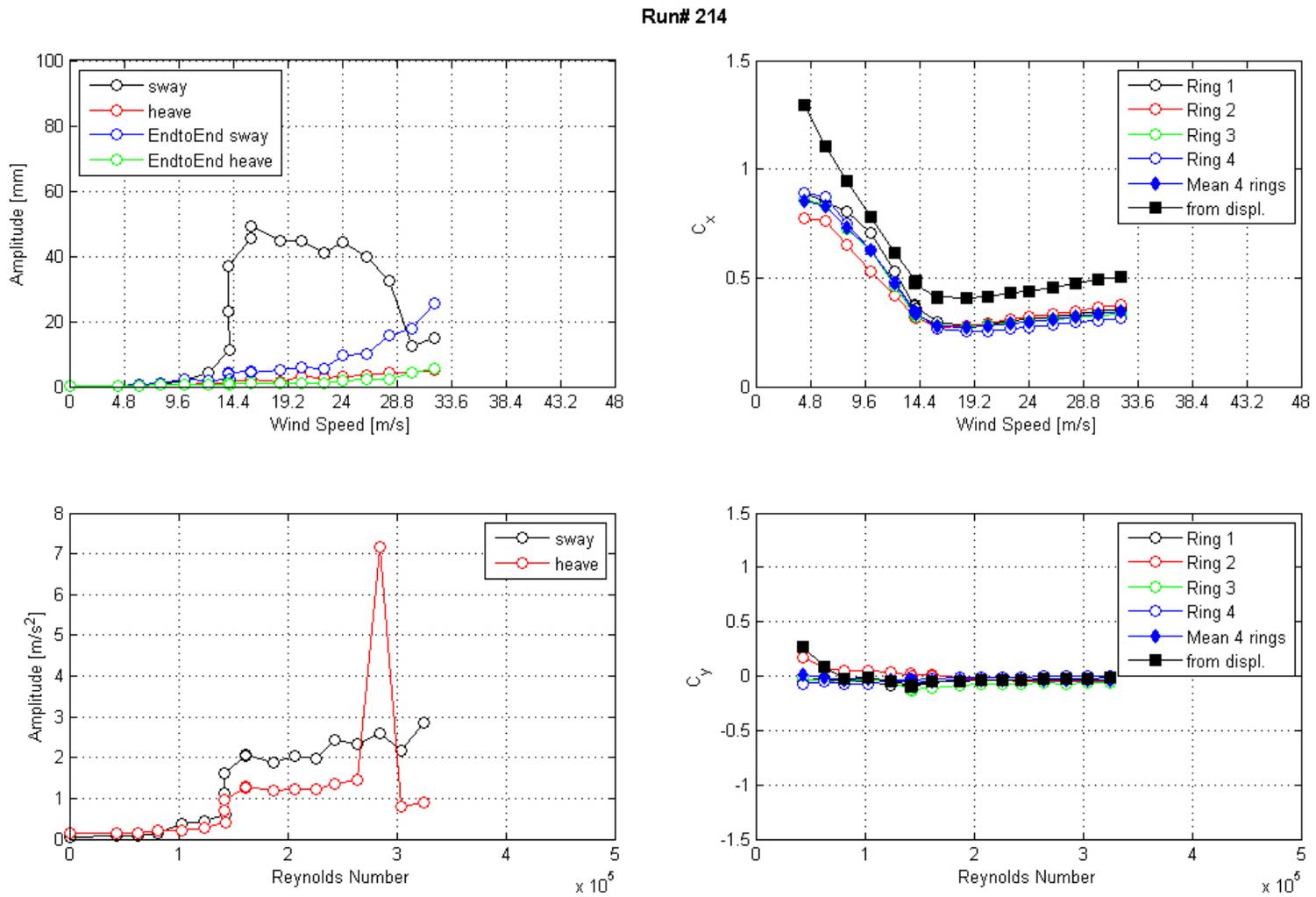
Figure 152. Graph. Response of the cable as a function of wind speed or Reynolds number as measured by the lasers, accelerometers, and surface pressures for run 214.
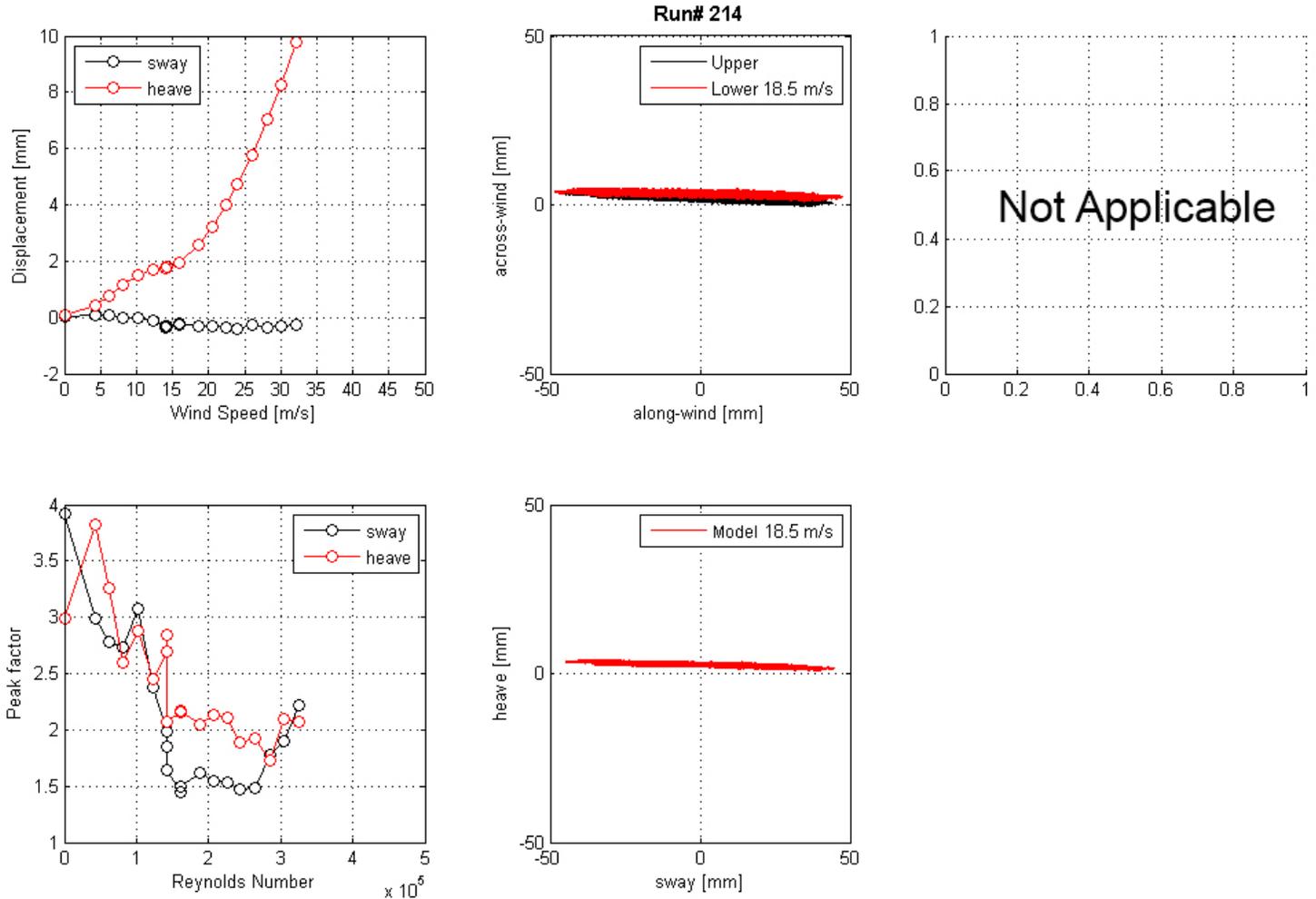
Figure 153. Graph. Mean displacement and peak factor from the laser, motion path at one wind speed, and intensity of turbulence measured at the entrance of the test section for run 214.
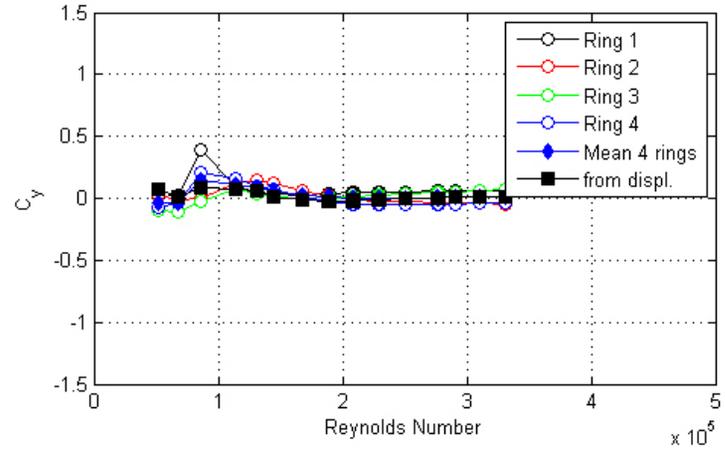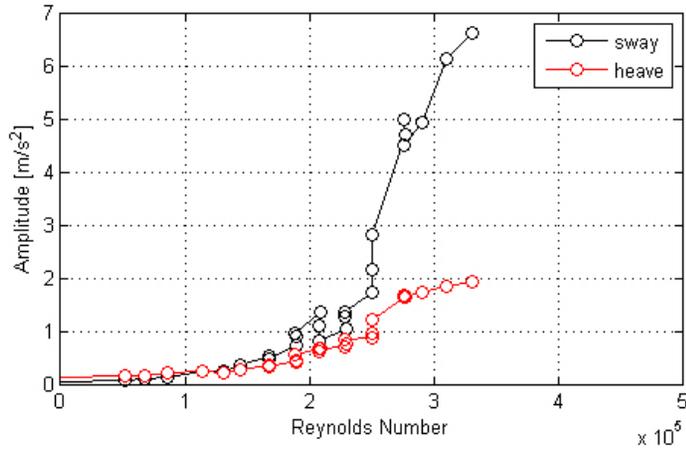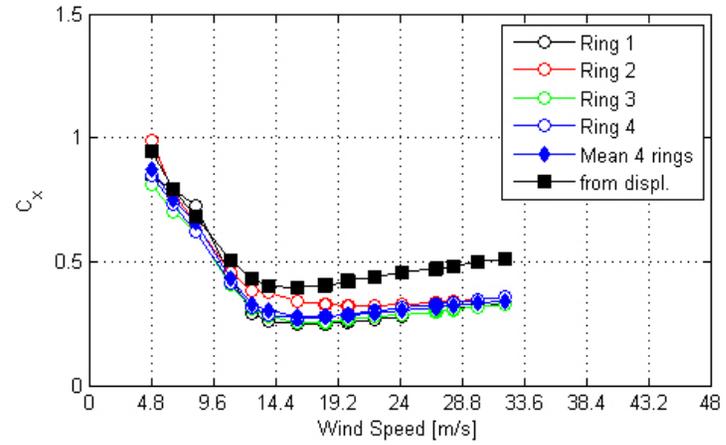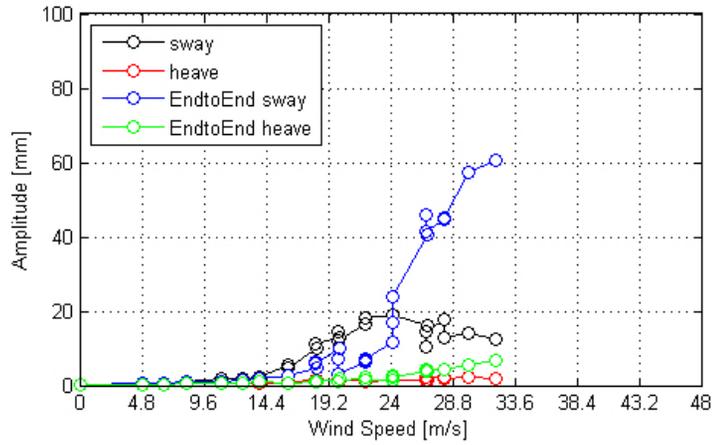
Figure 154. Graph. Response of the cable as a function of wind speed or Reynolds number as measured by the lasers, accelerometers, and surface pressures for run 216.
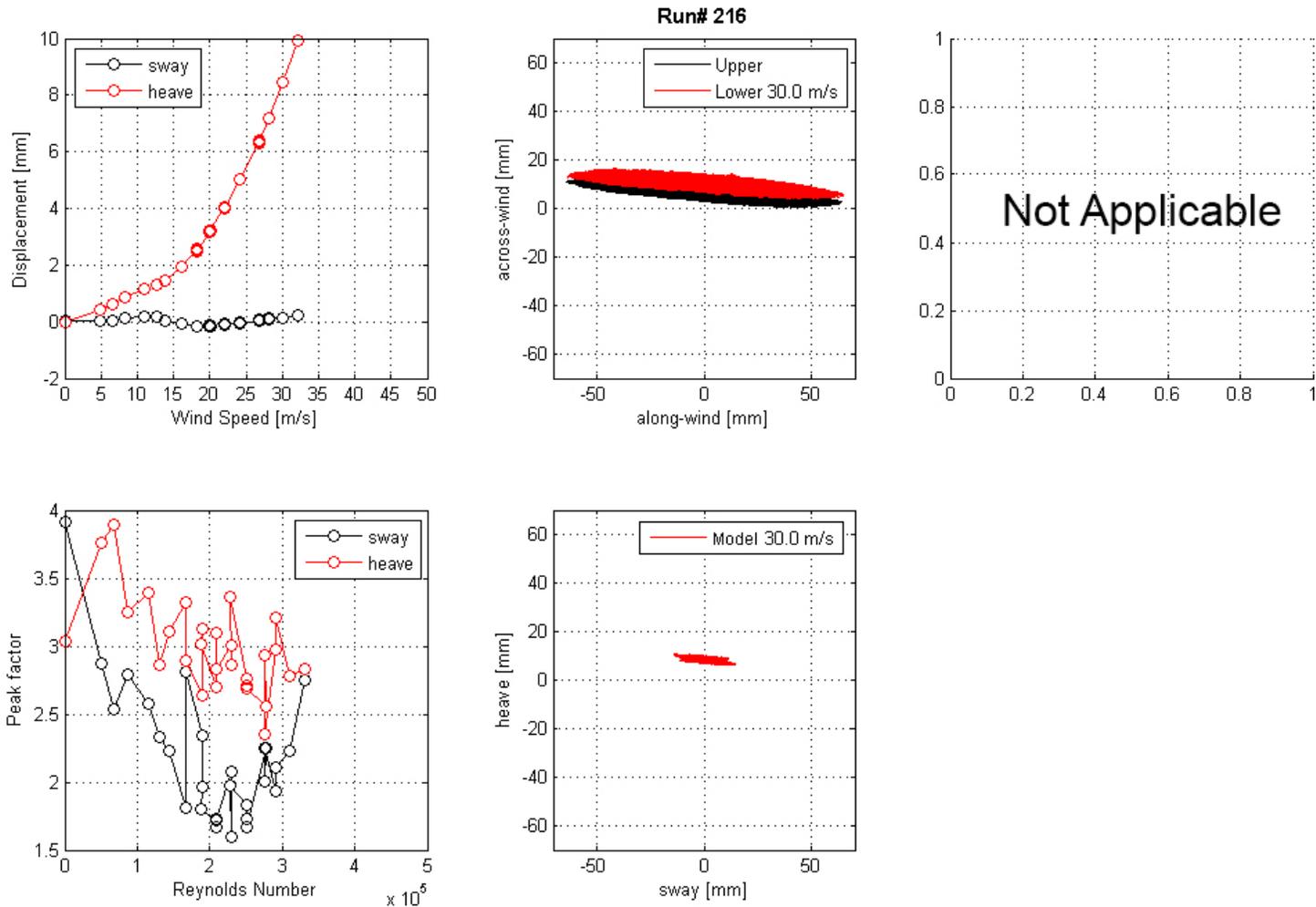
Figure 155. Graph. Mean displacement and peak factor from the laser, motion path at one wind speed, and intensity of turbulence measured at the entrance of the test section for run 216.
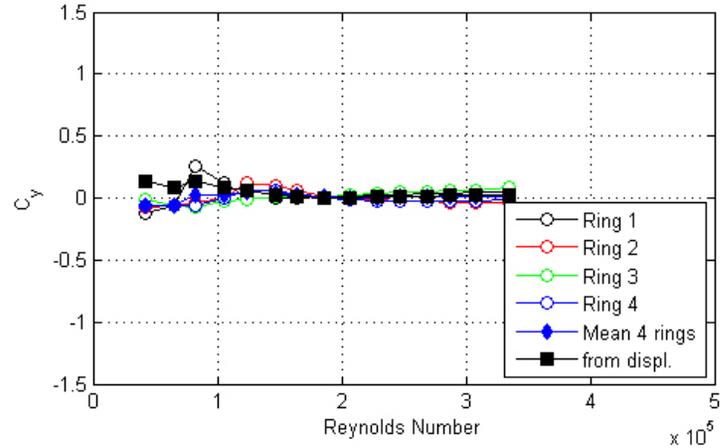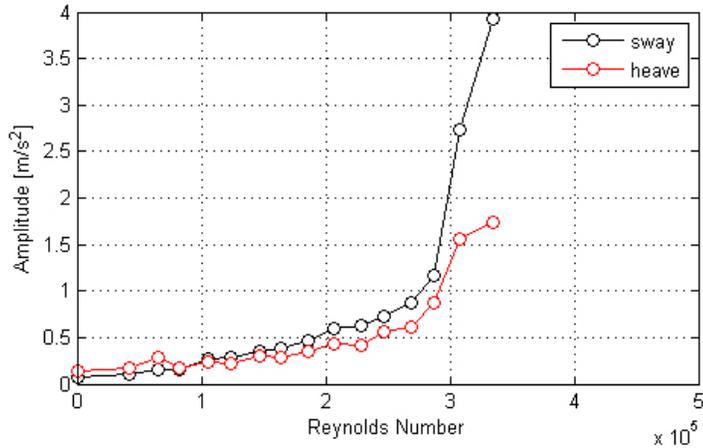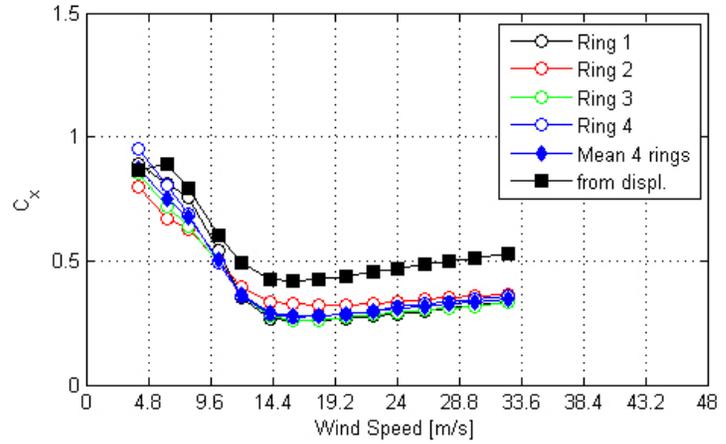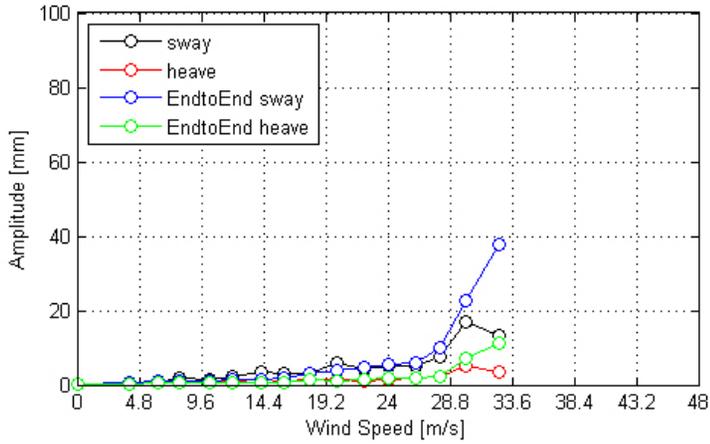
Figure 156. Graph. Response of the cable as a function of wind speed or Reynolds number as measured by the lasers, accelerometers, and surface pressures for run 219.
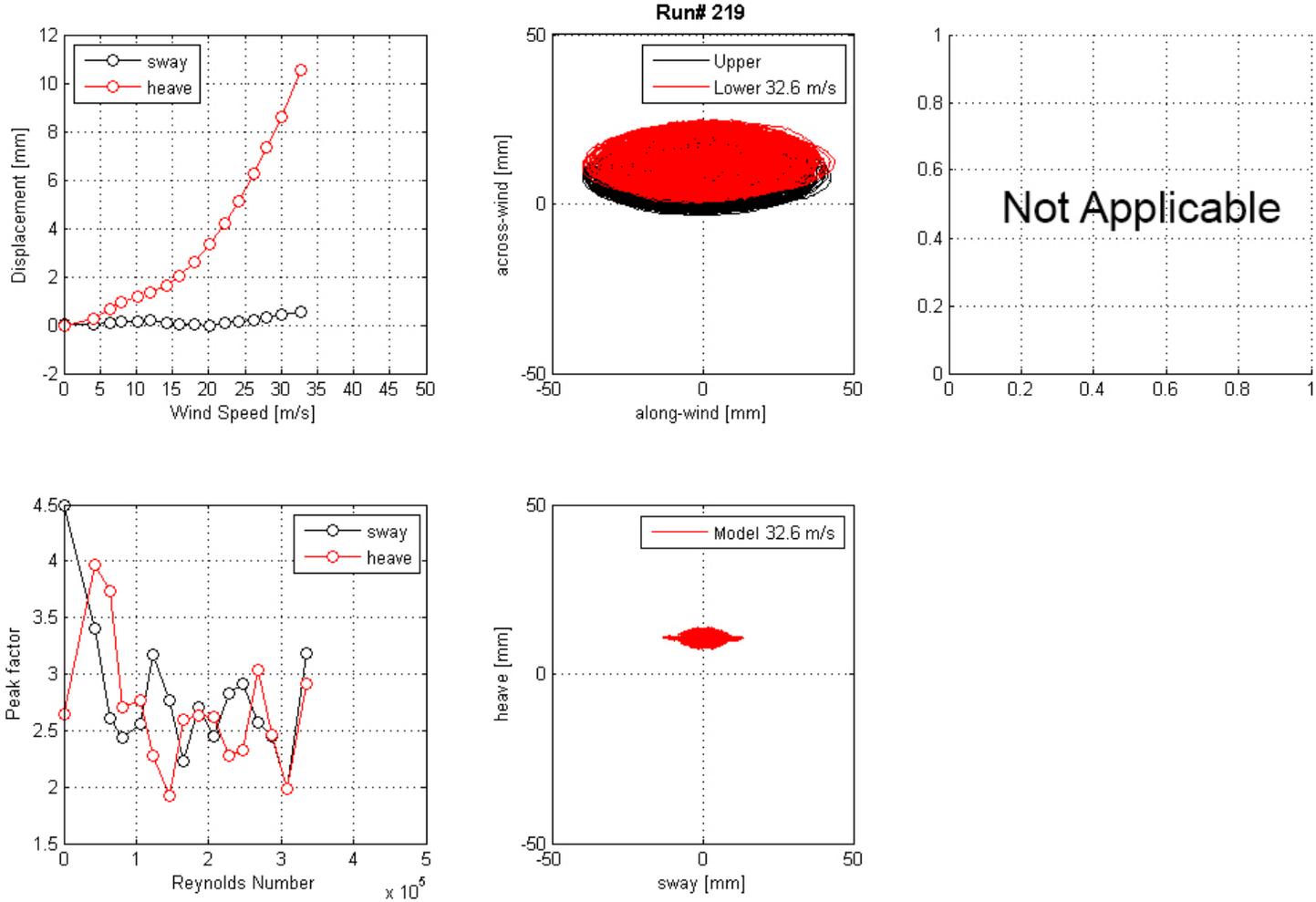
Figure 157. Graph. Mean displacement and peak factor from the laser, motion path at one wind speed, and intensity of turbulence measured at the entrance of the test section for run 219.

Run# 222
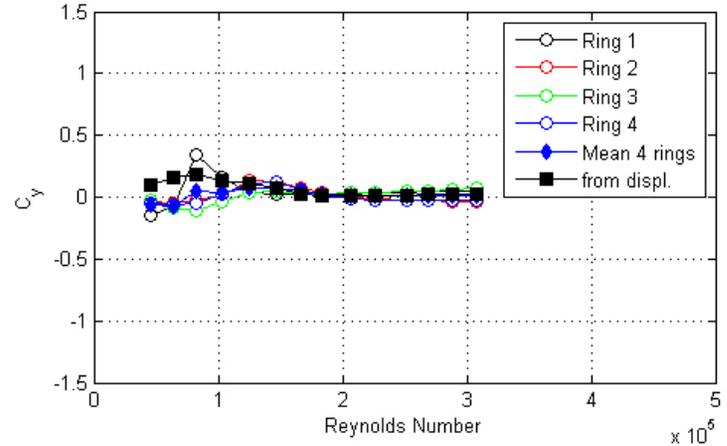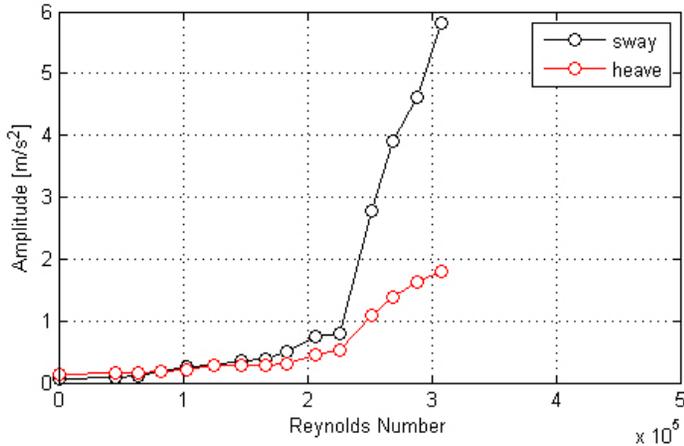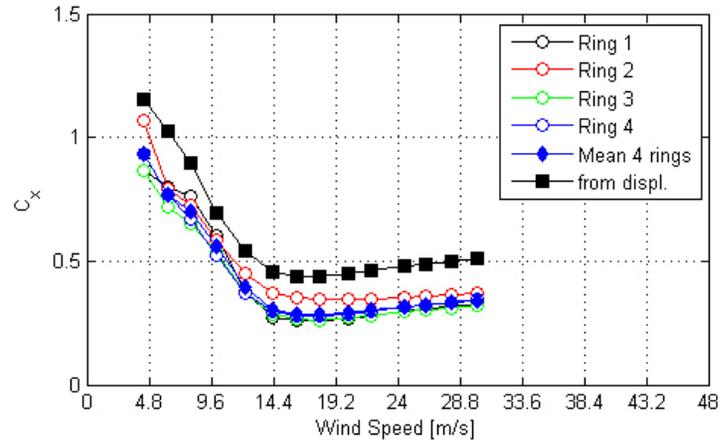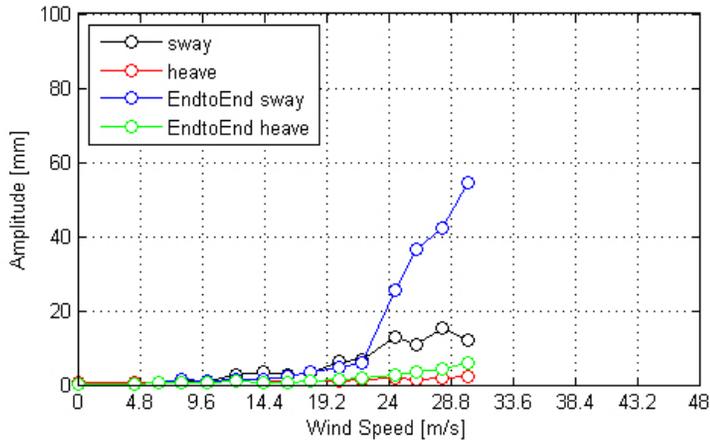
Figure 158. Graph. Response of the cable as a function of wind speed or Reynolds number as measured by the lasers, accelerometers, and surface pressures for run 222.
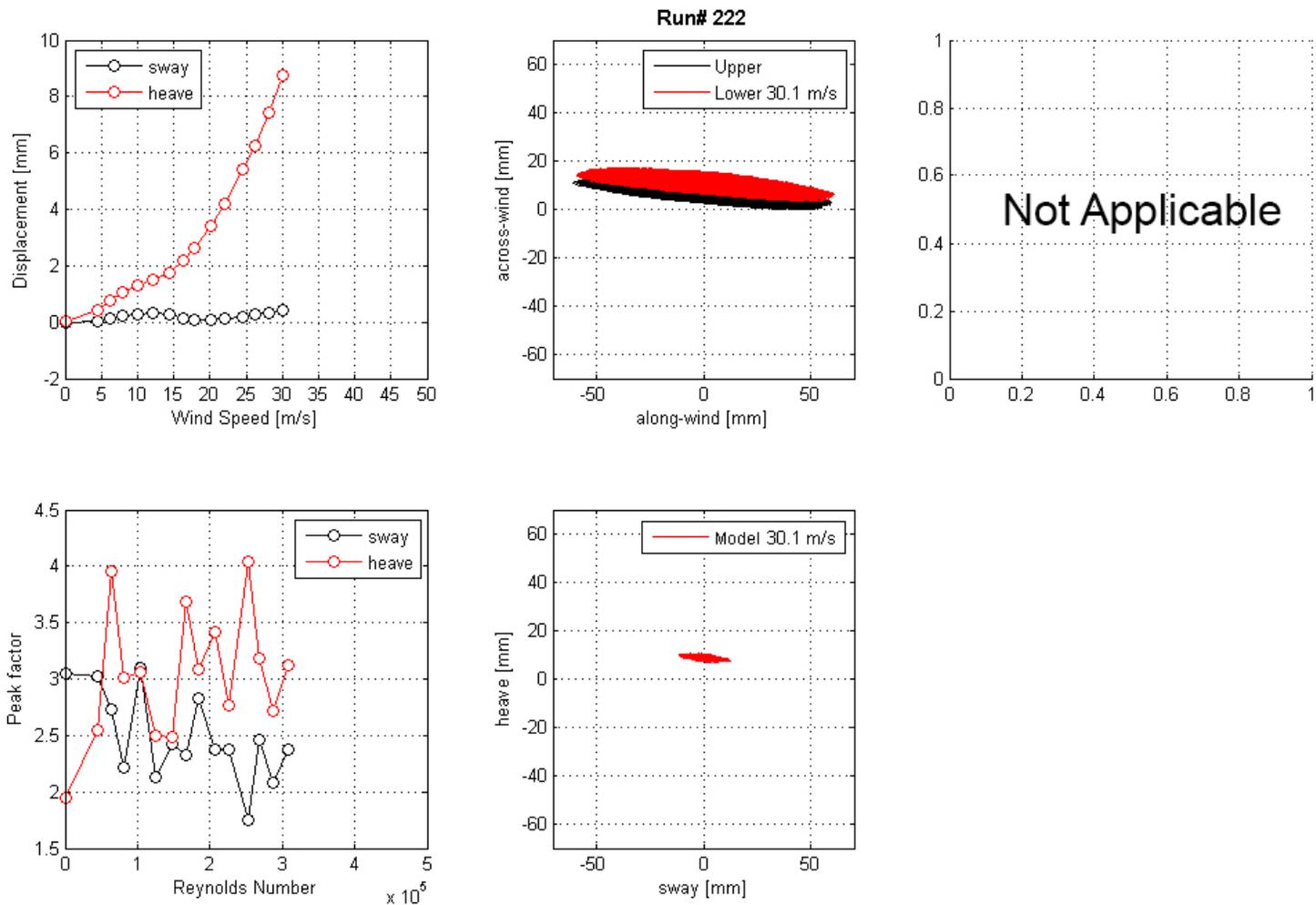
Figure 159. Graph. Mean displacement and peak factor from the laser, motion path at one wind speed, and intensity of turbulence measured at the entrance of the test section for run 222.
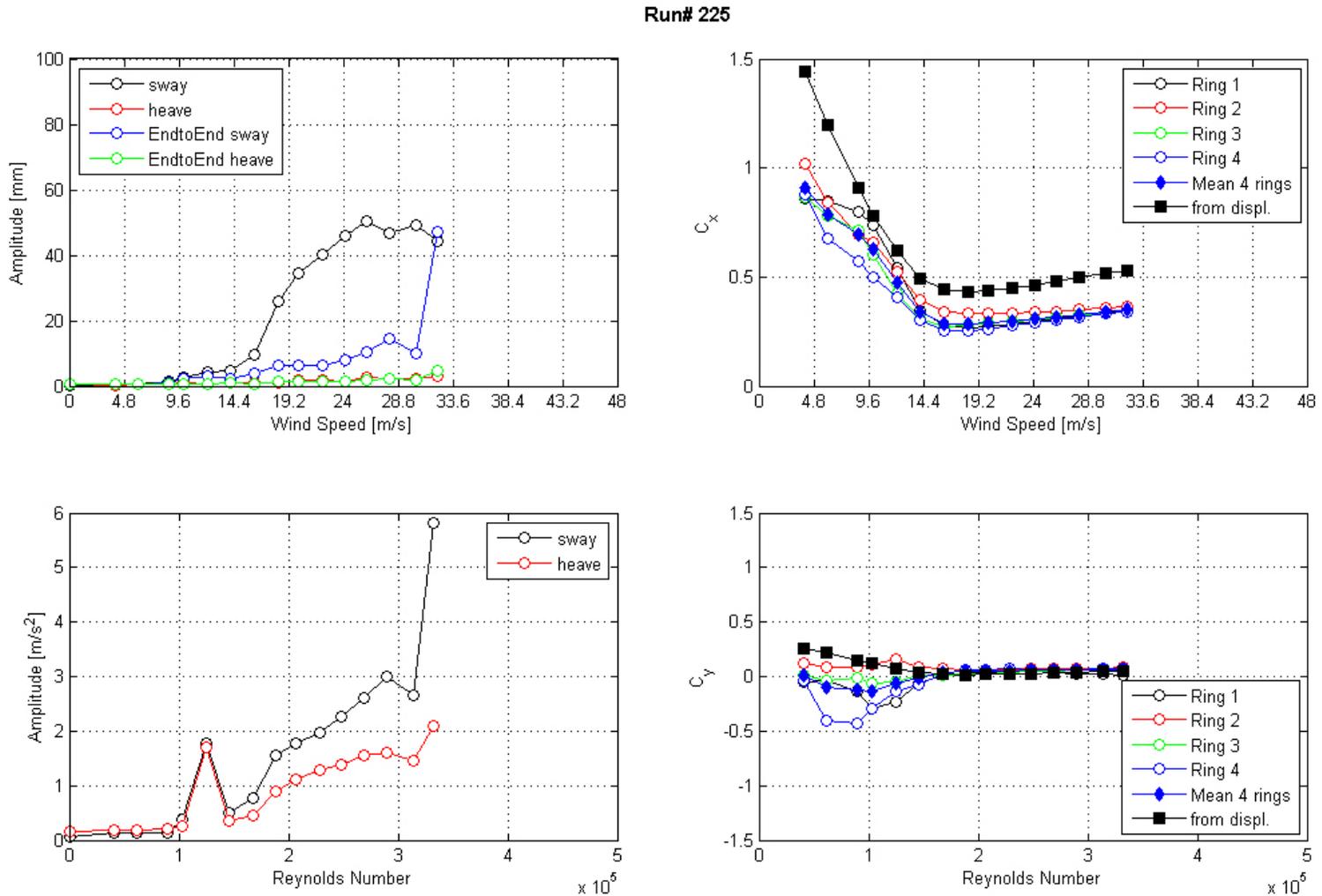
Figure 160. Graph. Response of the cable as a function of wind speed or Reynolds number as measured by the lasers, accelerometers, and surface pressures for run 225.
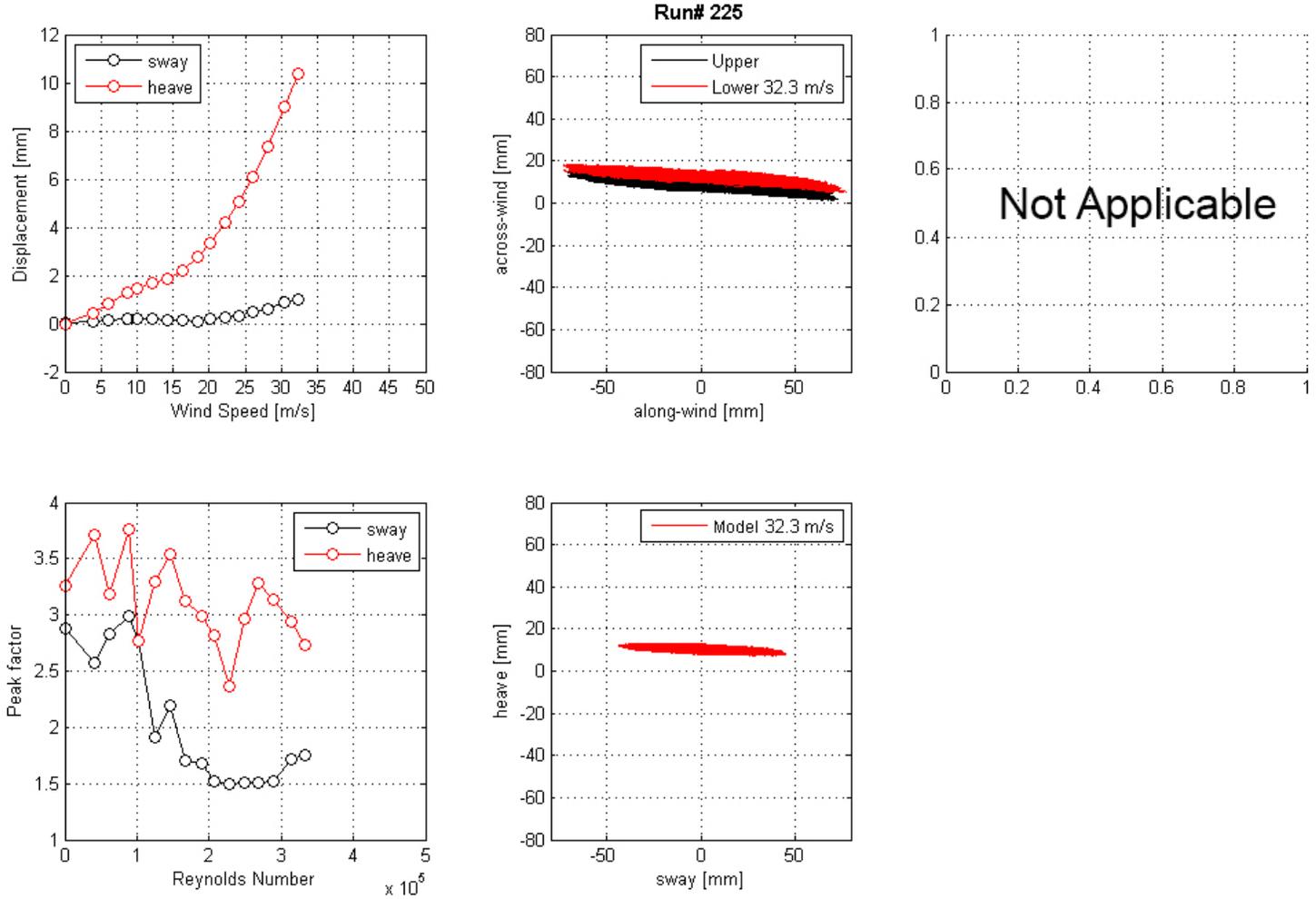
Figure 161. Graph. Mean displacement and peak factor from the laser, motion path at one wind speed, and intensity of turbulence measured at the entrance of the test section for run 225.
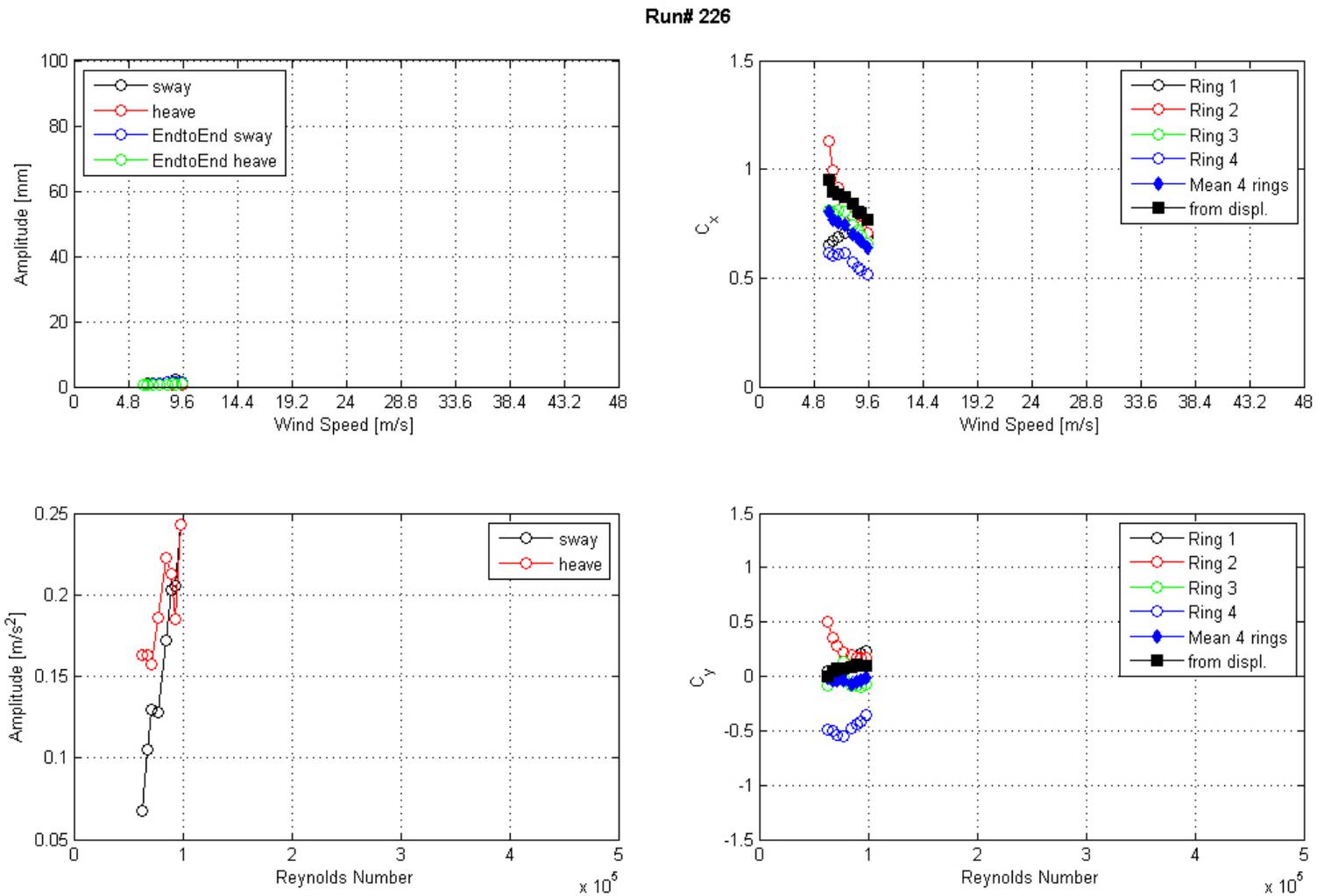
Figure 162. Graph. Response of the cable as a function of wind speed or Reynolds number as measured by the lasers, accelerometers, and surface pressures for run 226.
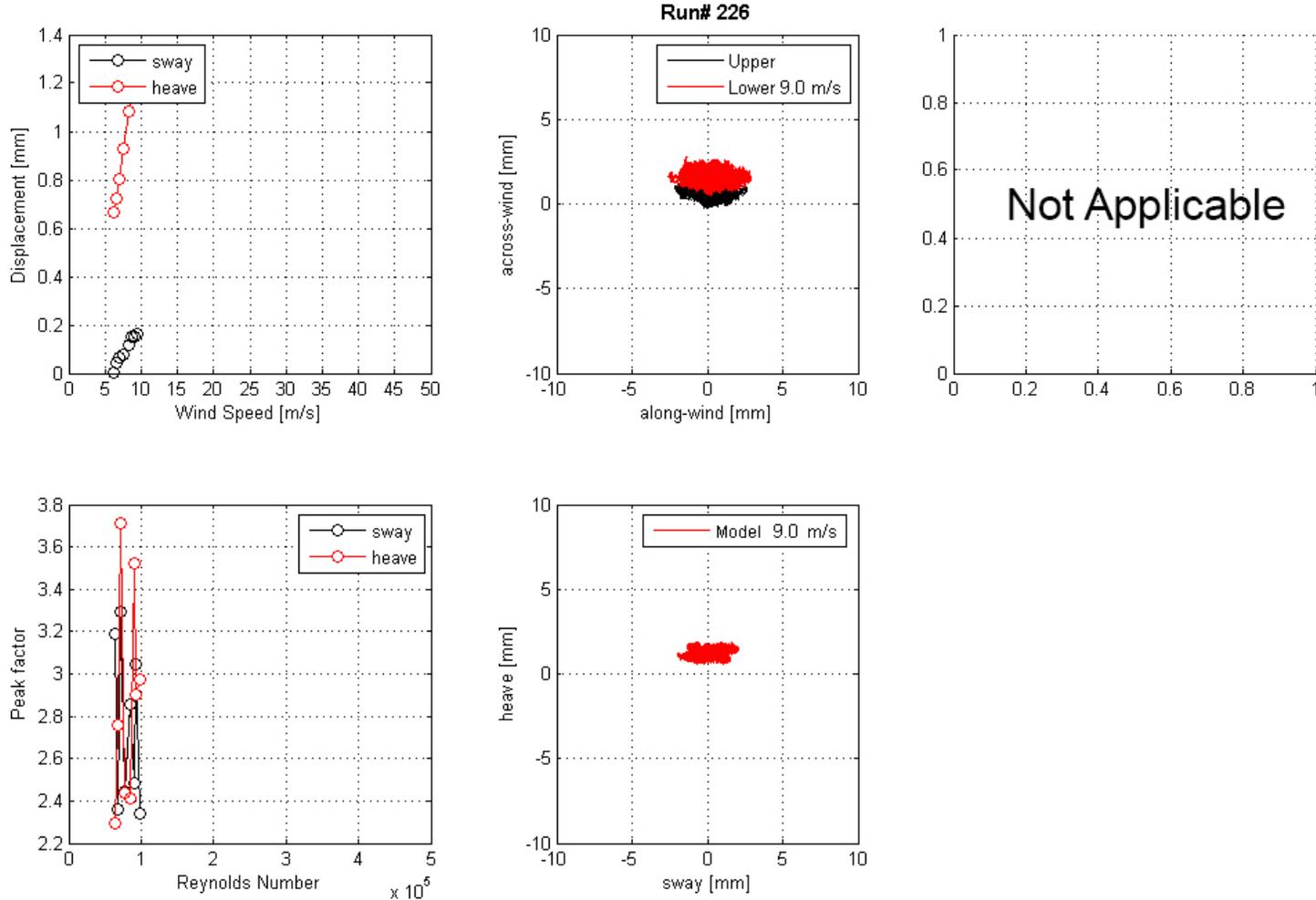
Figure 163. Graph. Mean displacement and peak factor from the laser, motion path at one wind speed, and intensity of turbulence measured at the entrance of the test section for run 226.
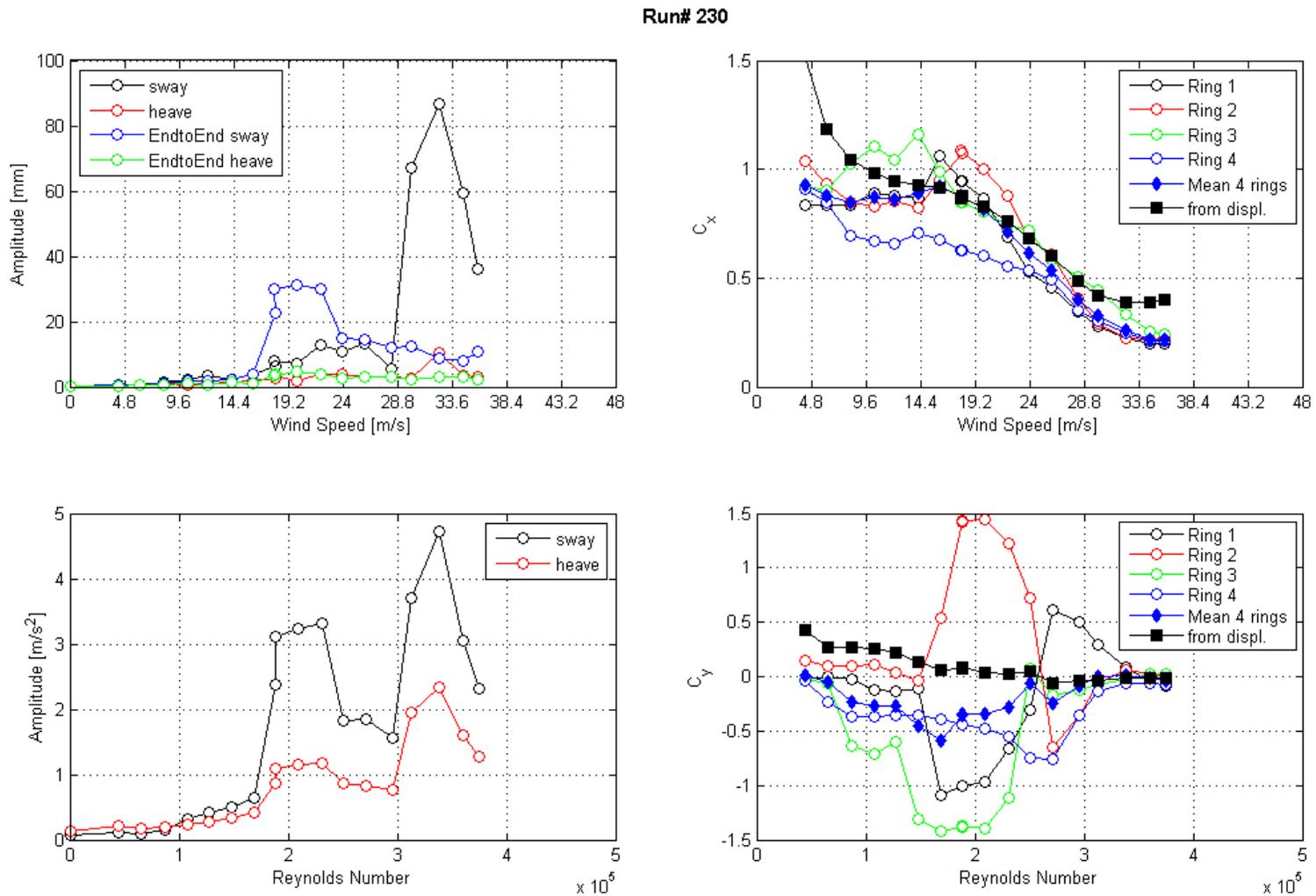
Figure 164. Graph. Response of the cable as a function of wind speed or Reynolds number as measured by the lasers, accelerometers, and surface pressures for run 230.
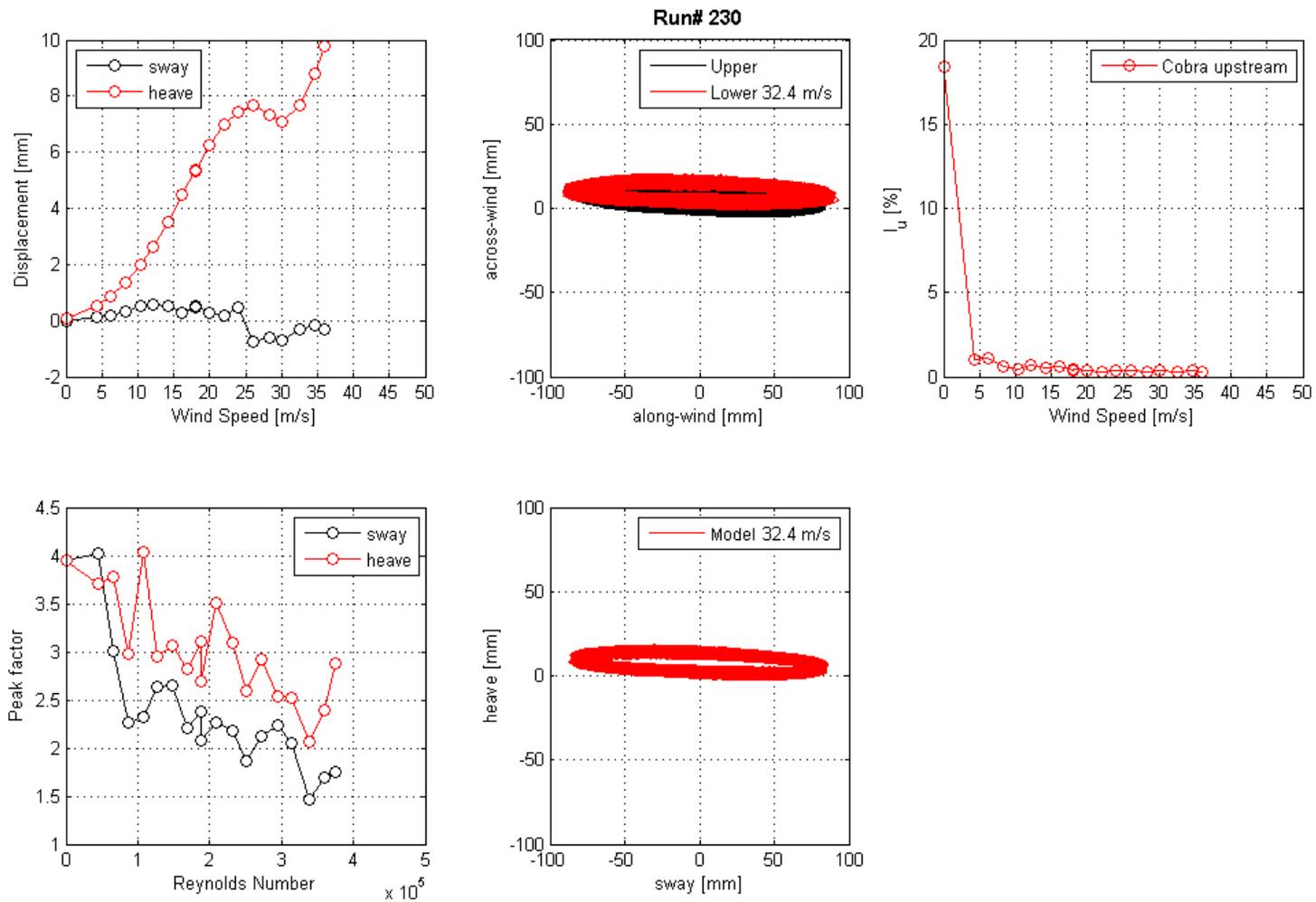
Figure 165. Graph. Mean displacement and peak factor from the laser, motion path at one wind speed, and intensity of turbulence measured at the entrance of the test section for run 230.
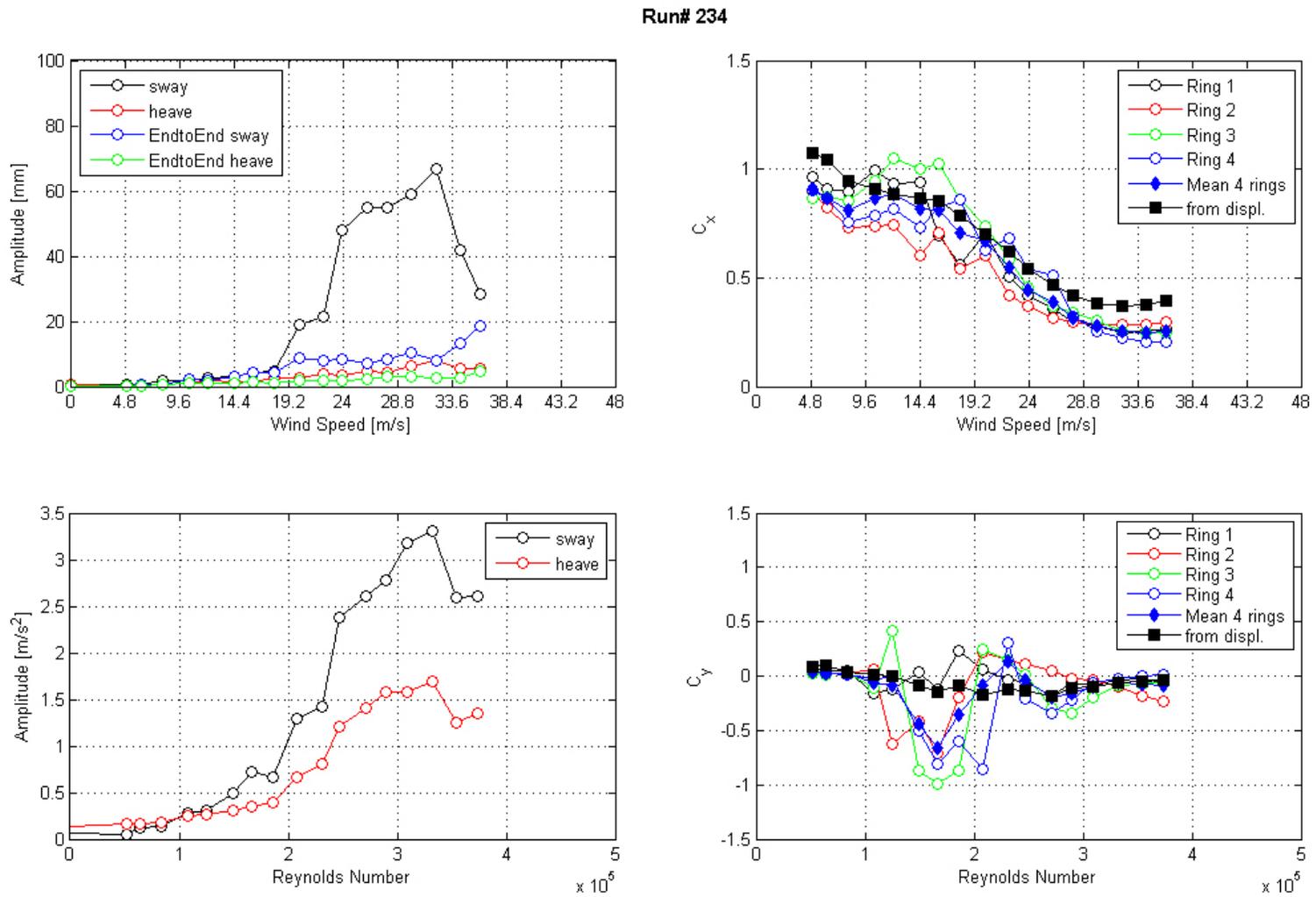
Figure 166. Graph. Response of the cable as a function of wind speed or Reynolds number as measured by the lasers, accelerometers, and surface pressures for run 234.
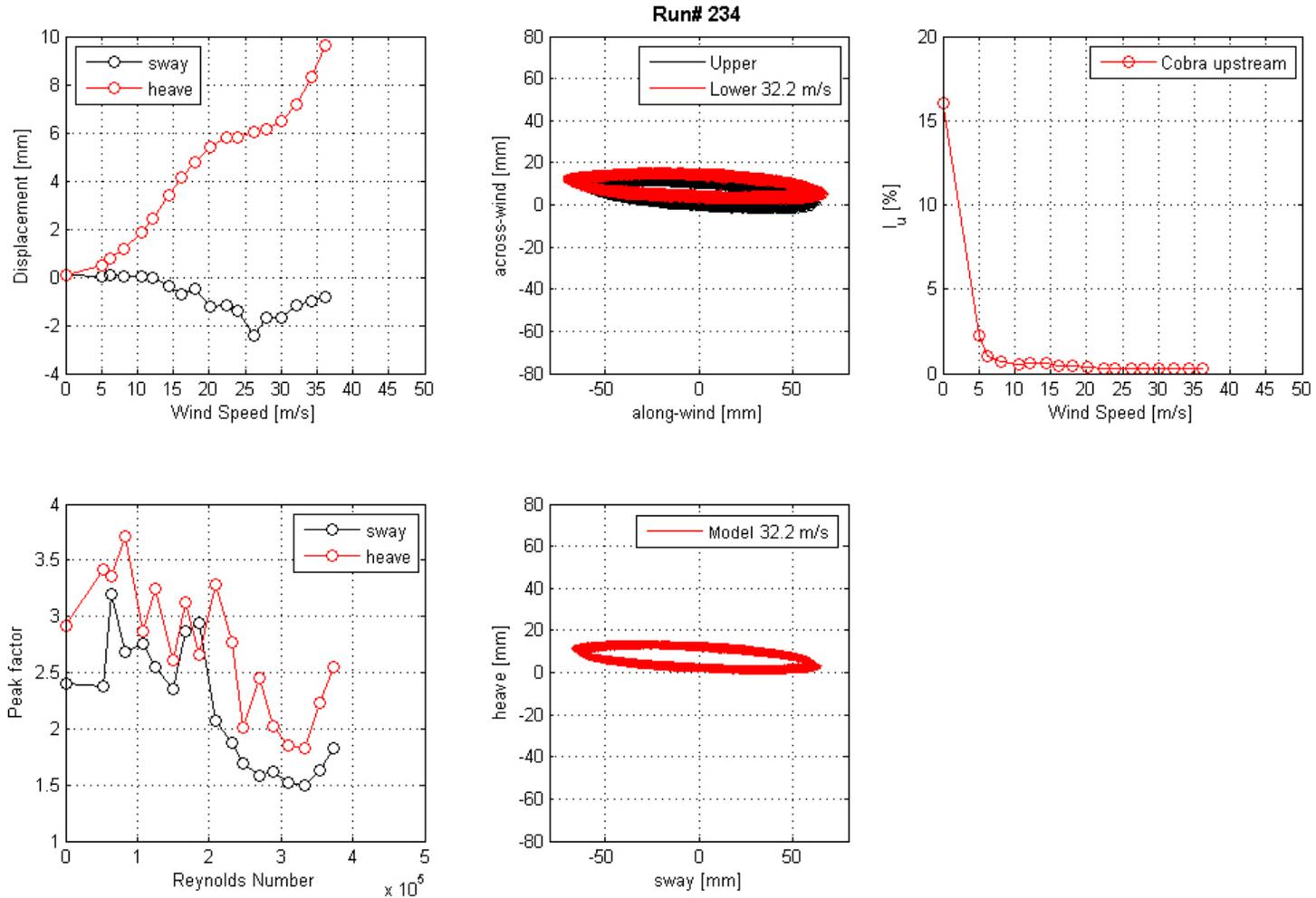
Figure 167. Graph. Mean displacement and peak factor from the laser, motion path at one wind speed, and intensity of turbulence measured at the entrance of the test section for run 234.
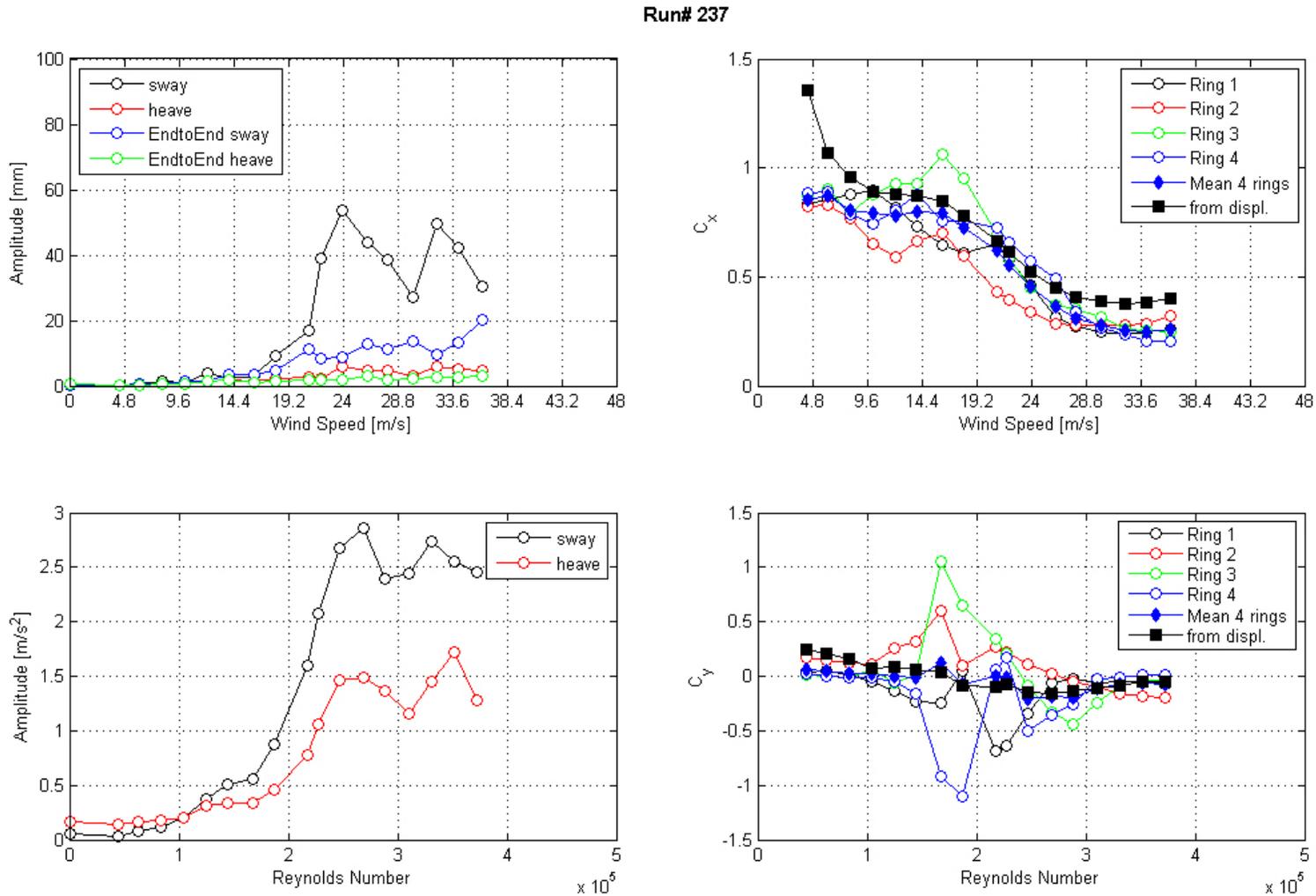
Figure 168. Graph. Response of the cable as a function of wind speed or Reynolds number as measured by the lasers, accelerometers, and surface pressures for run 237.
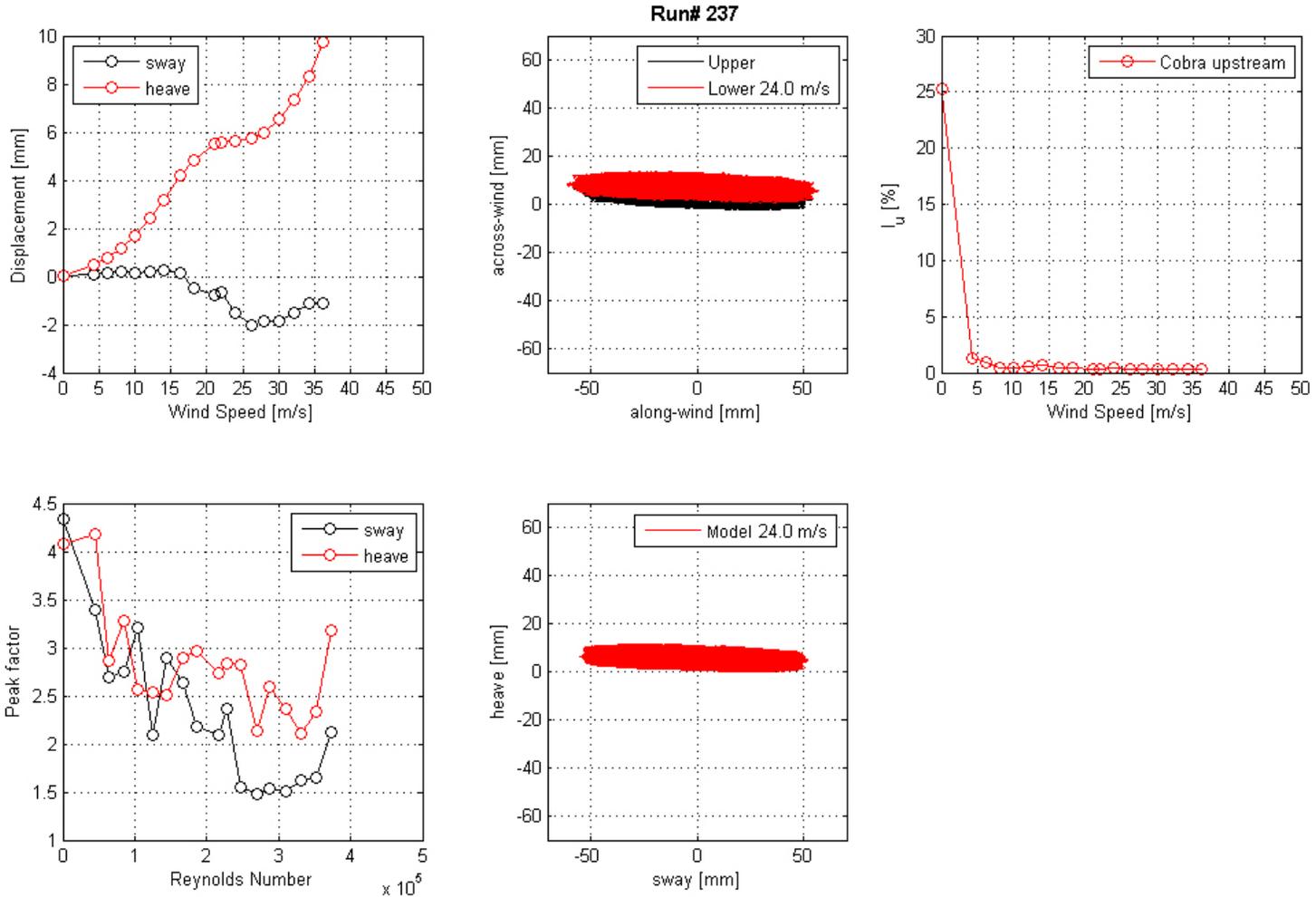
Figure 169. Graph. Mean displacement and peak factor from the laser, motion path at one wind speed, and intensity of turbulence measured at the entrance of the test section for run 237.
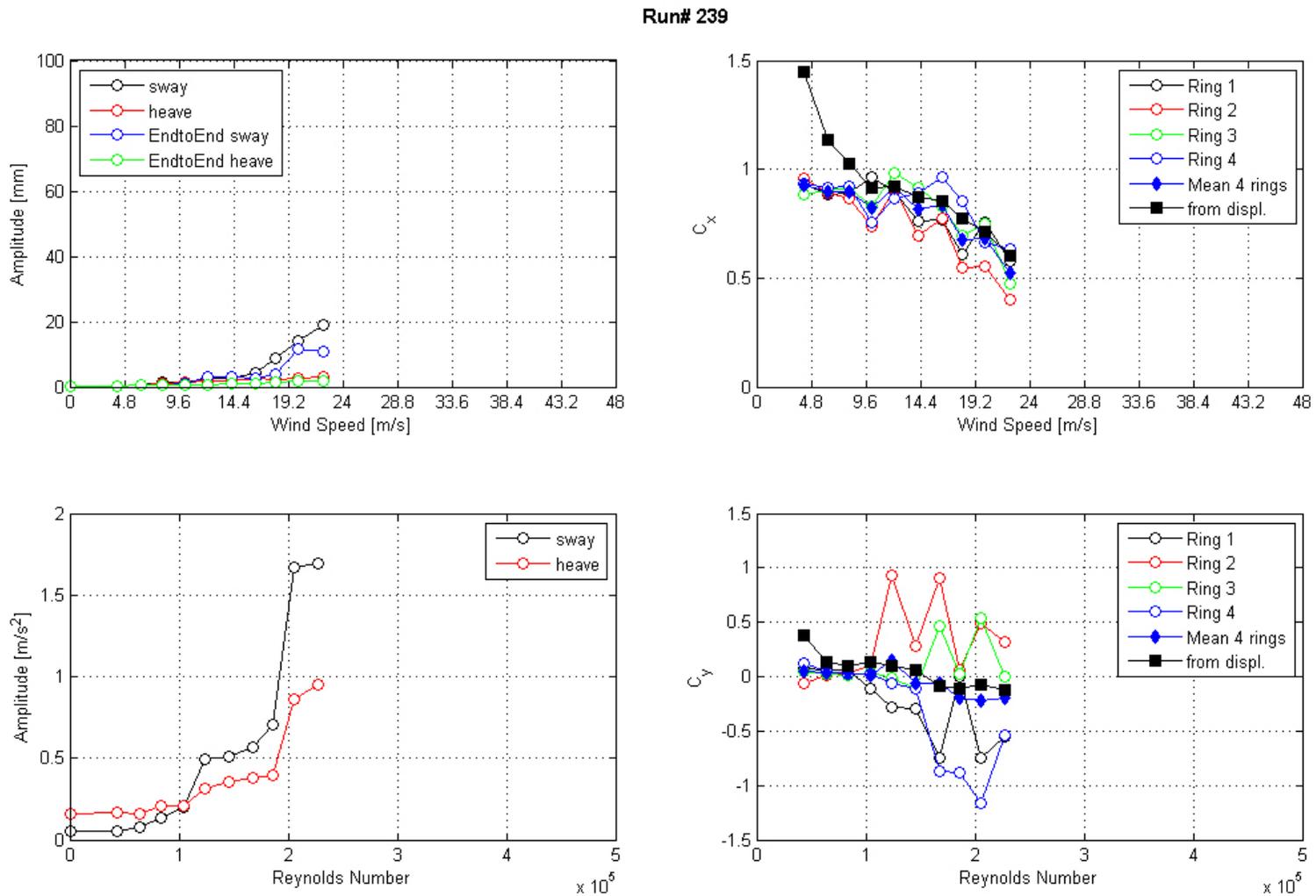
Figure 170. Graph. Response of the cable as a function of wind speed or Reynolds number as measured by the lasers, accelerometers, and surface pressures for run 239.
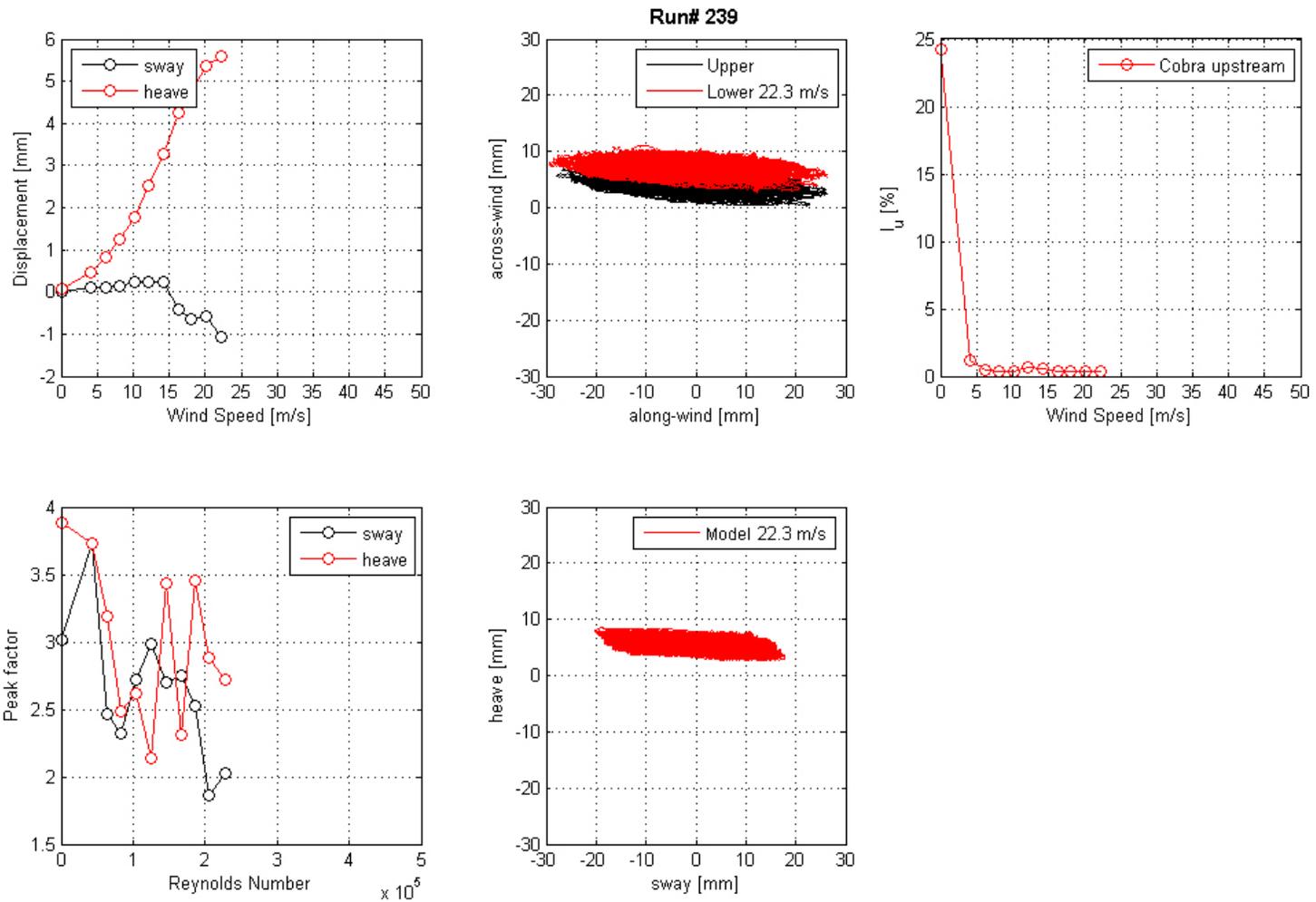
Figure 171. Graph. Mean displacement and peak factor from the laser, motion path at one wind speed, and intensity of turbulence measured at the entrance of the test section for run 239.

Run# 244
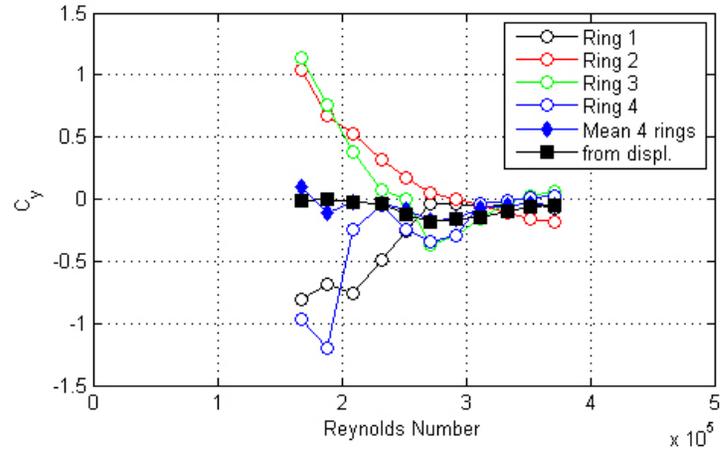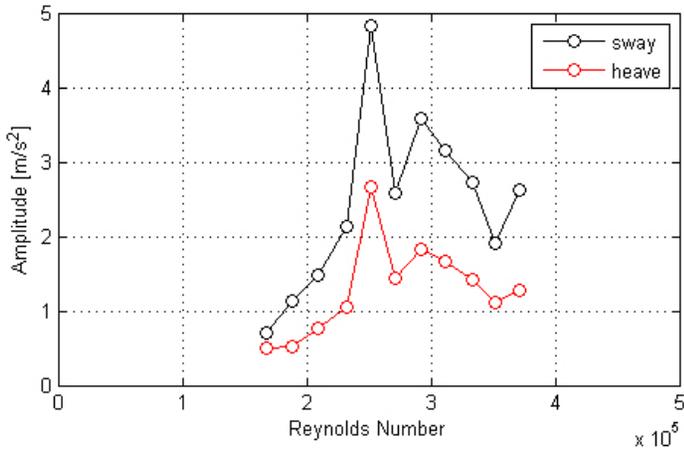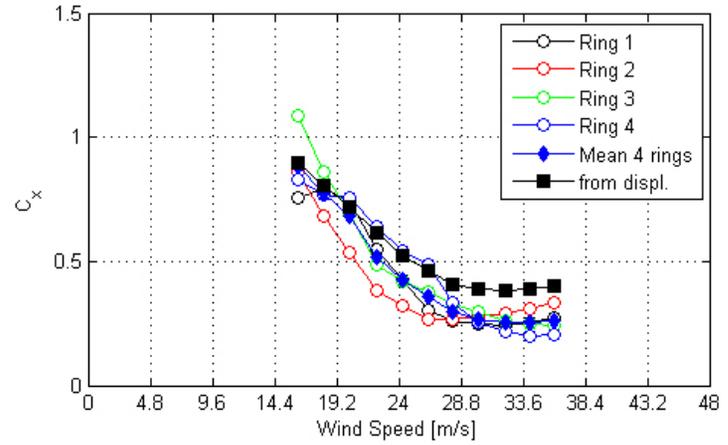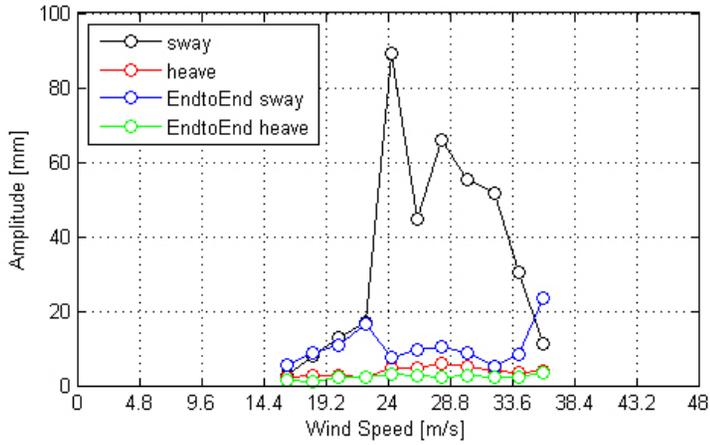
Figure 172. Graph. Response of the cable as a function of wind speed or Reynolds number as measured by the lasers, accelerometers, and surface pressures for run 244.
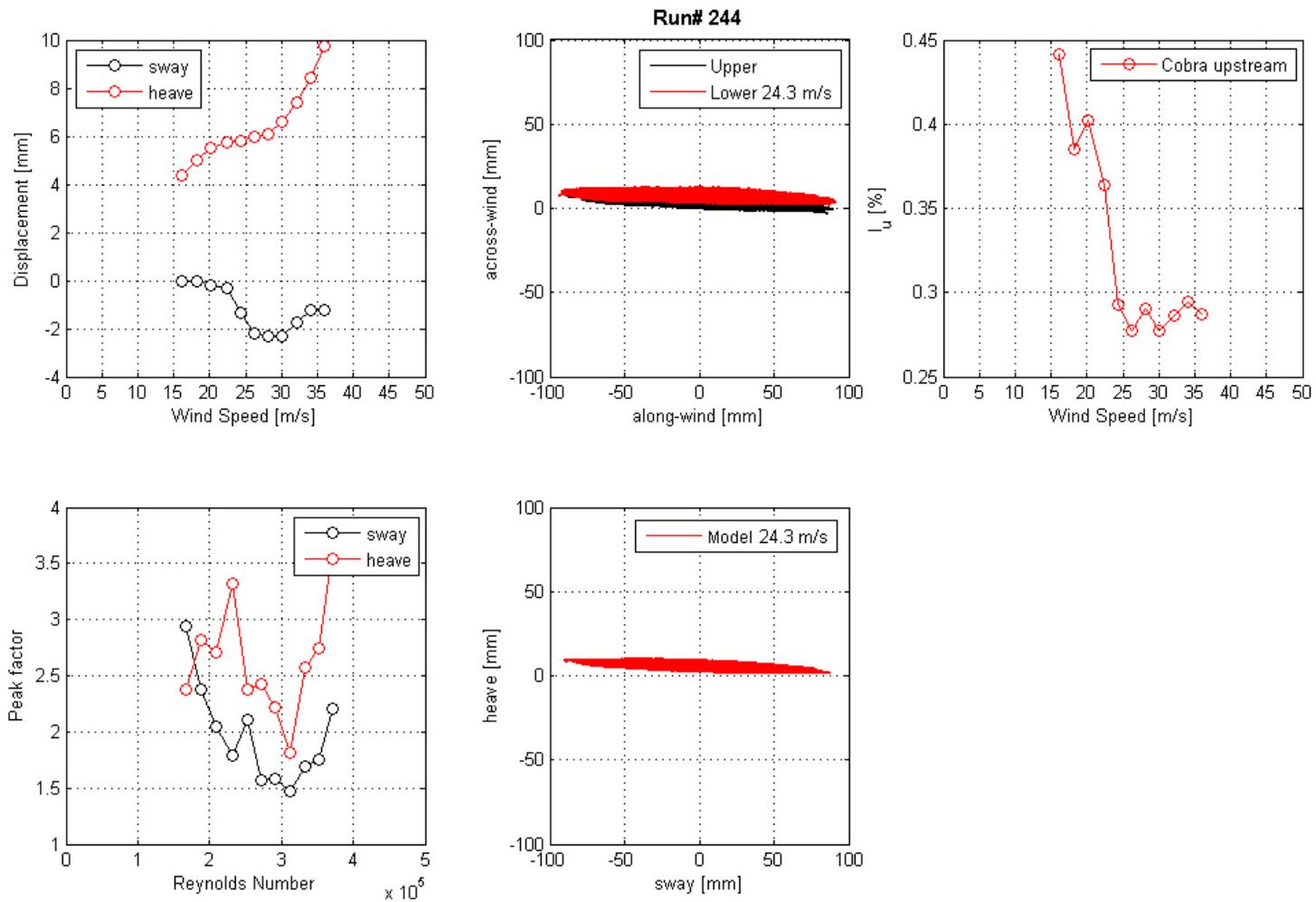
Figure 173. Graph. Mean displacement and peak factor from the laser, motion path at one wind speed, and intensity of turbulence measured at the entrance of the test section for run 244.
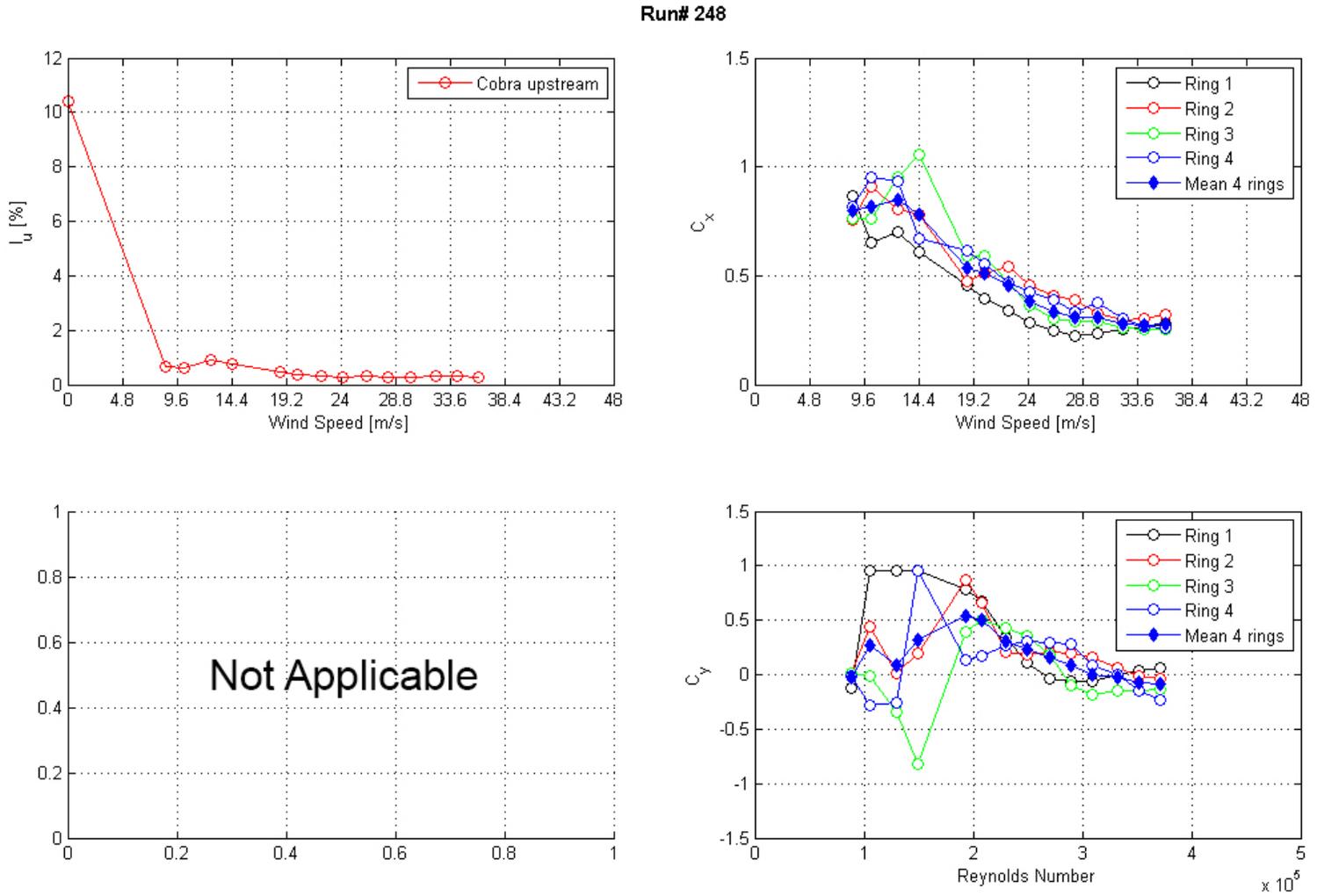
Run# 248

Figure 174. Graph. Intensity of turbulence measured at the entrance of the test section and *C_x* and *C_y* calculated from surface pressure measurements as a function of Reynolds number and wind speed for run 248.
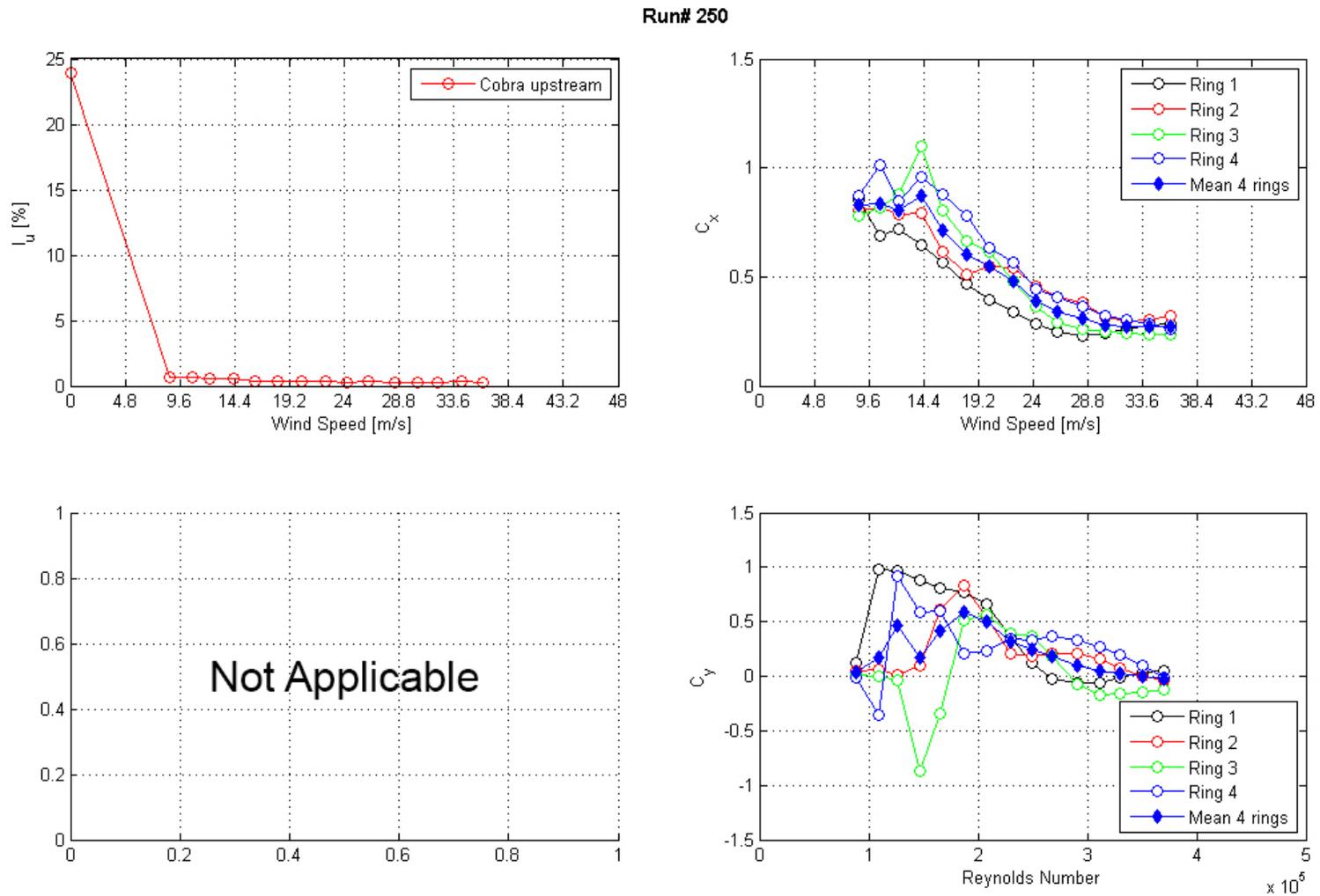
Figure 175. Graph. Intensity of turbulence measured at the entrance of the test section and C_x and C_y calculated from surface pressure measurements as a function of Reynolds number and wind speed for run 250.
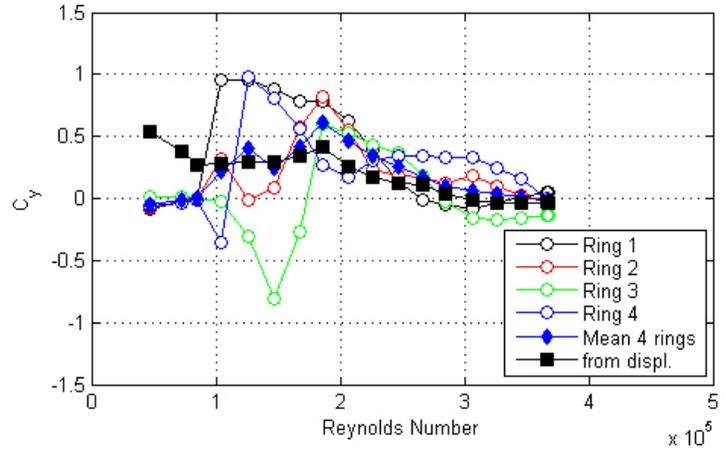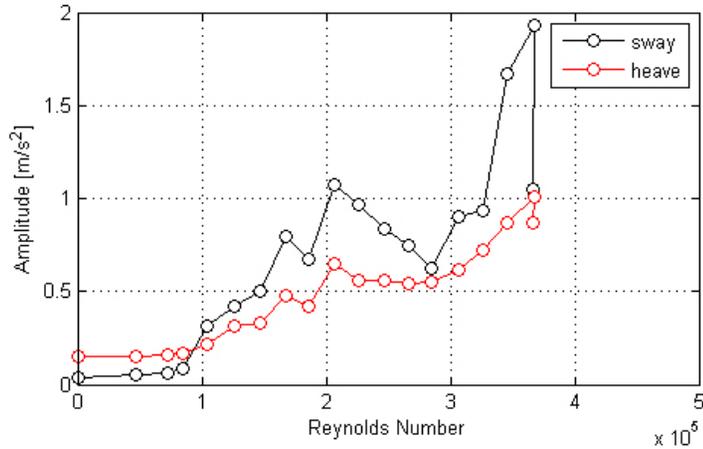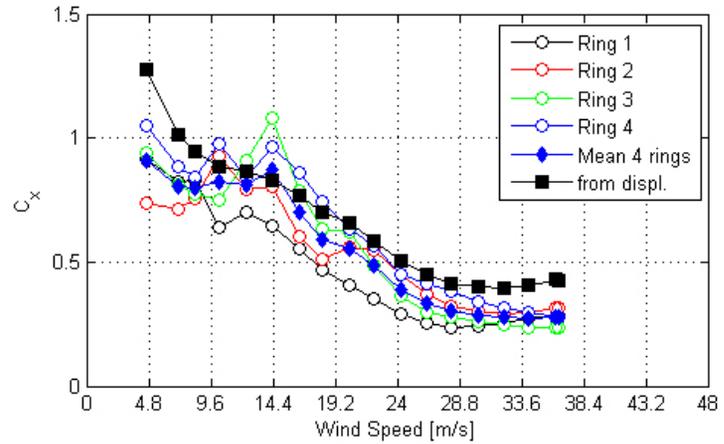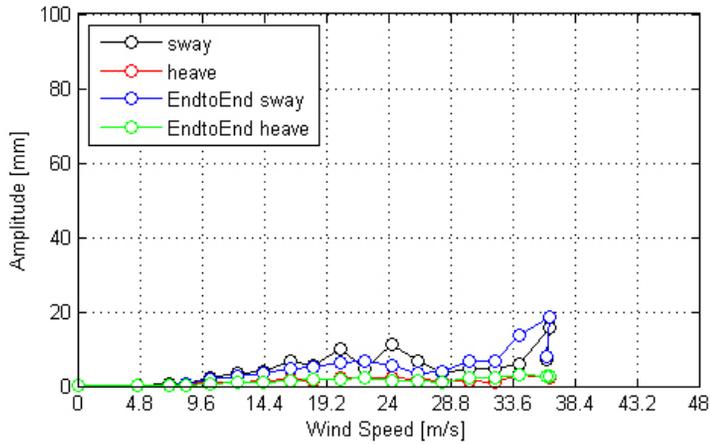
Figure 176. Graph. Response of the cable as a function of wind speed or Reynolds number as measured by the lasers, accelerometers, and surface pressures for run 253.
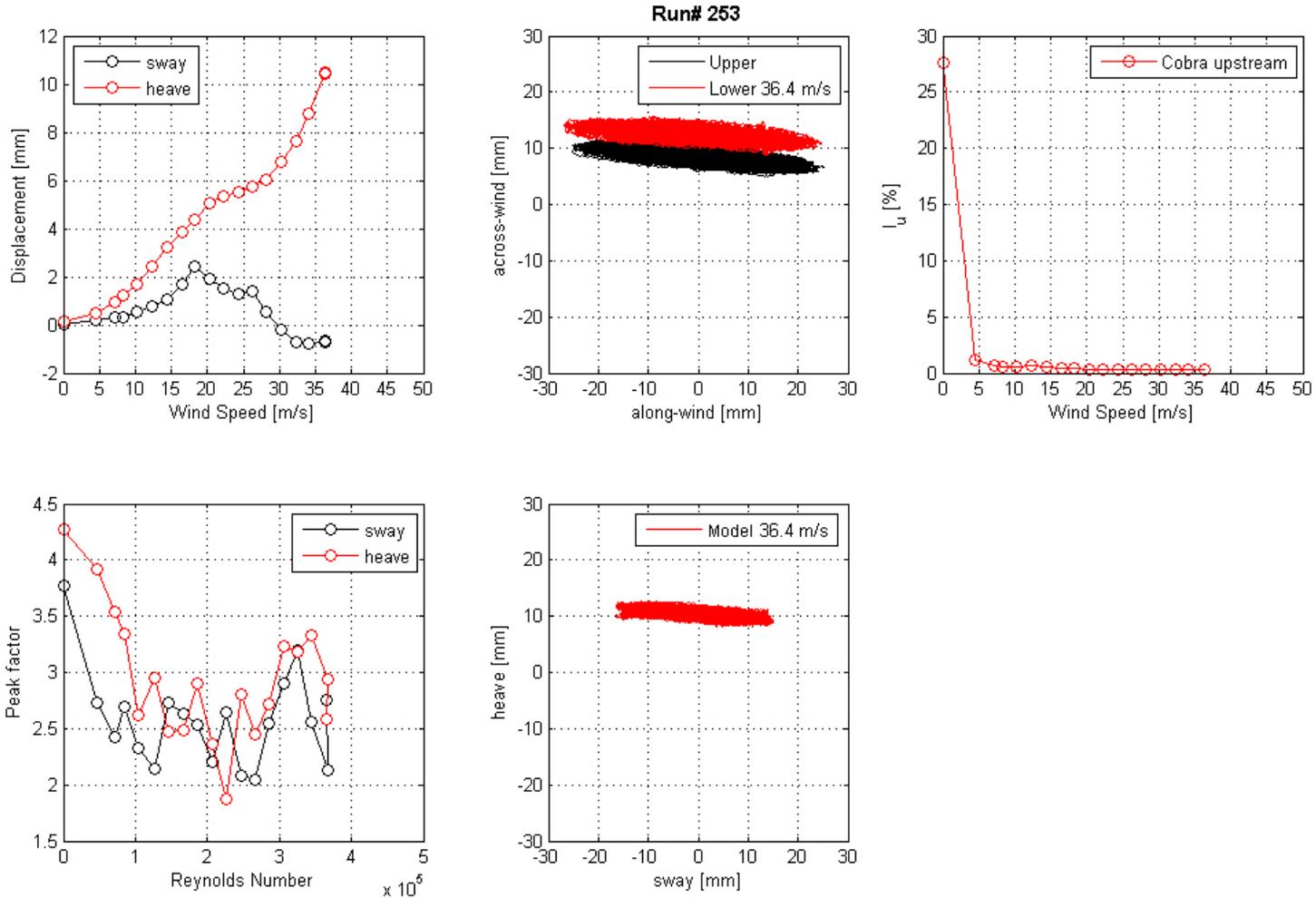
Figure 177. Graph. Mean displacement and peak factor from the laser, motion path at one wind speed, and intensity of turbulence measured at the entrance of the test section for run 253.
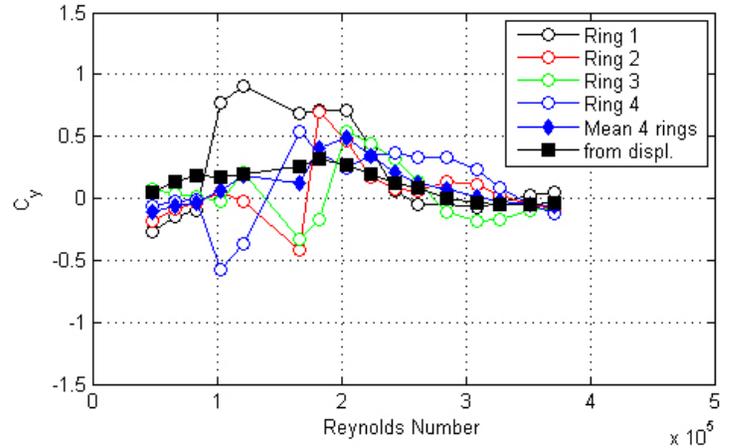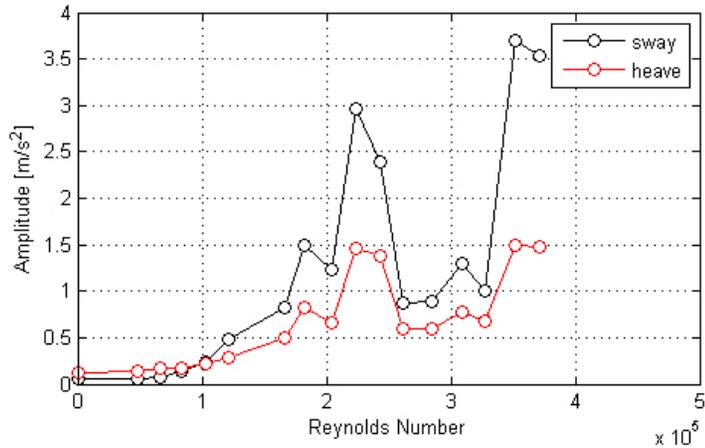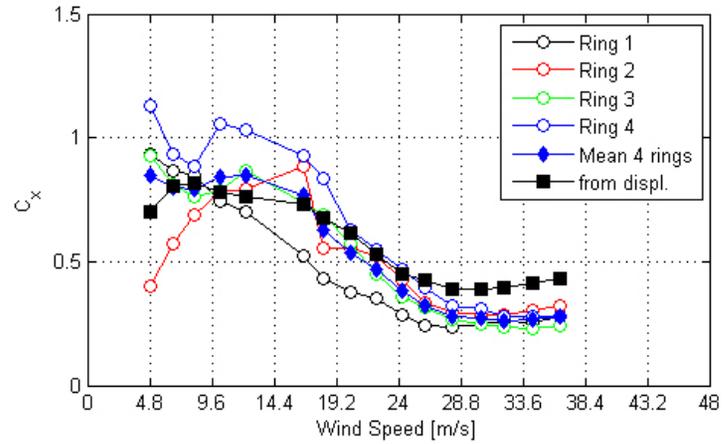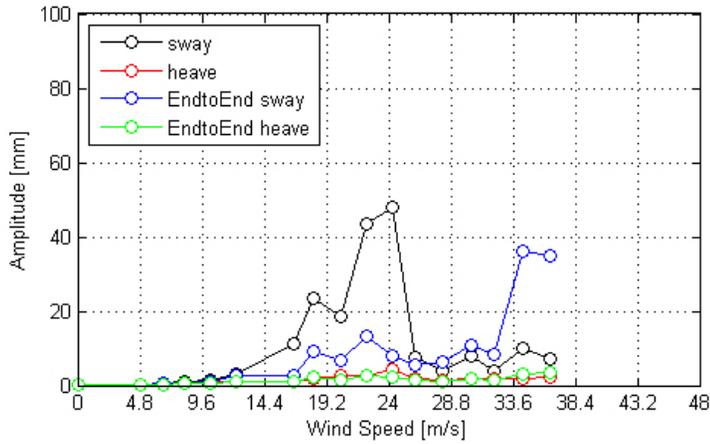
Figure 178. Graph. Response of the cable as a function of wind speed or Reynolds number as measured by the lasers, accelerometers, and surface pressures for run 255.
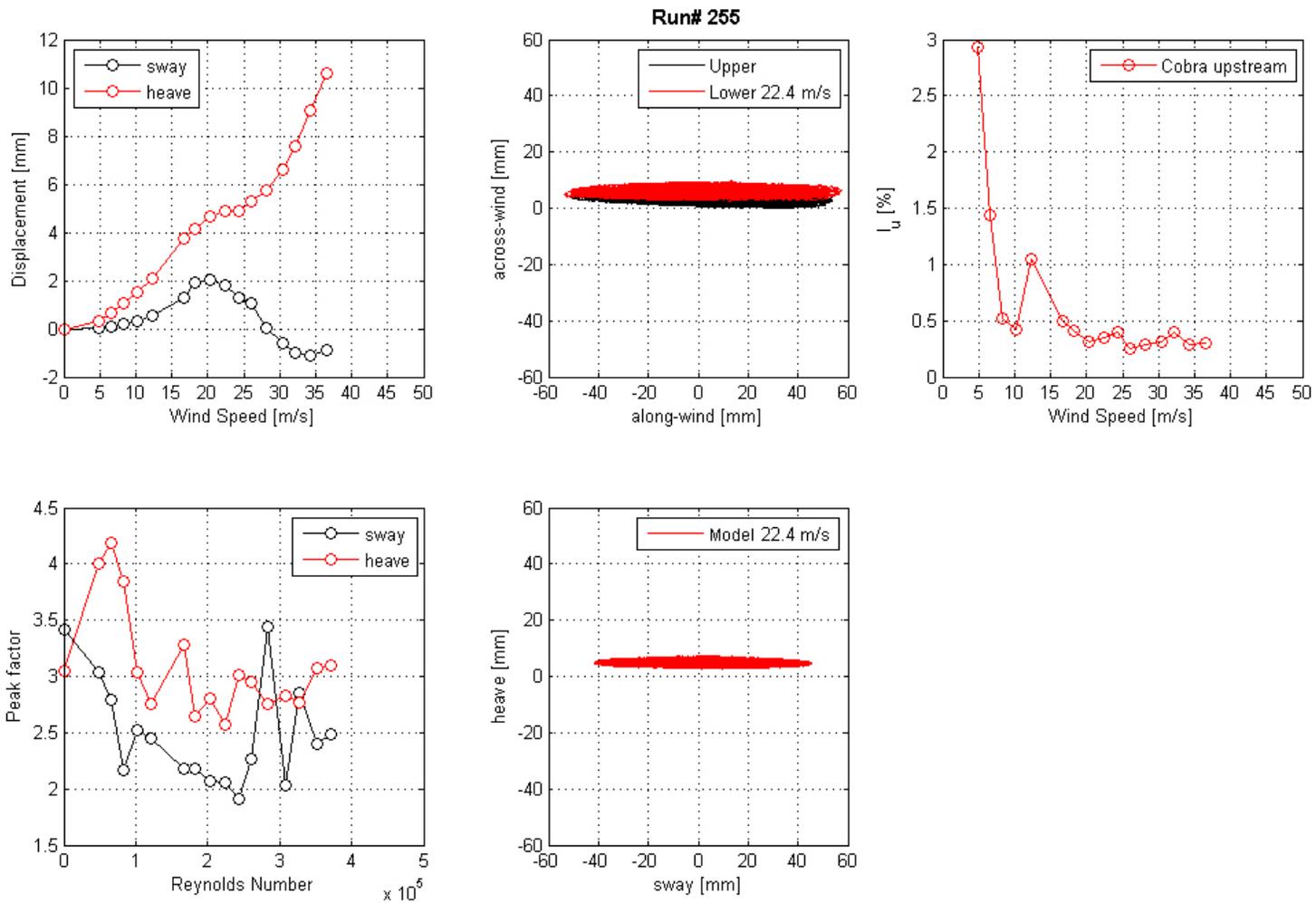
Figure 179. Graph. Mean displacement and peak factor from the laser, motion path at one wind speed, and intensity of turbulence measured at the entrance of the test section for run 255.
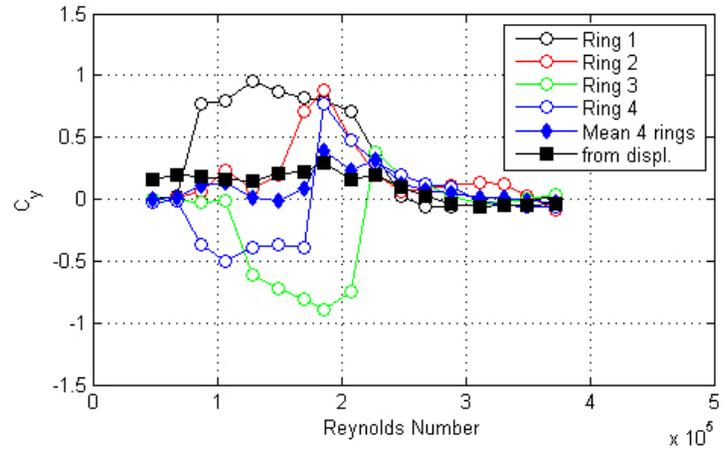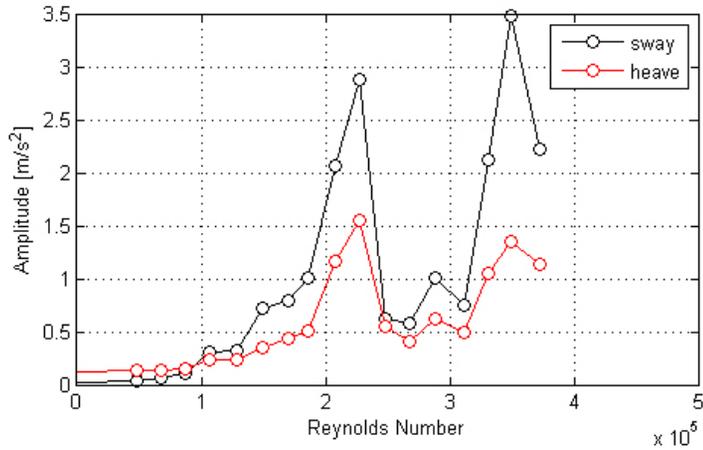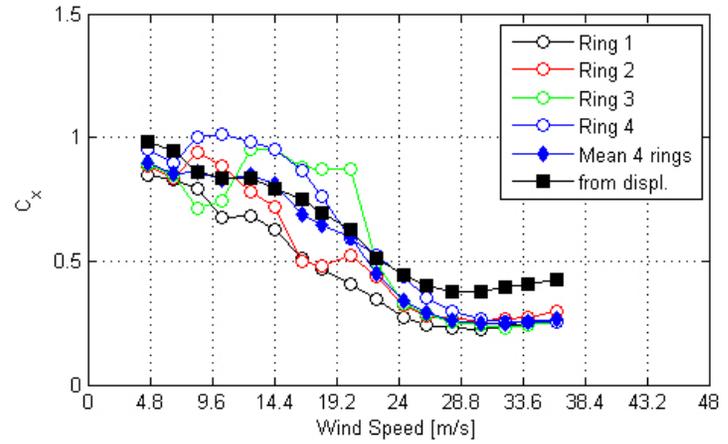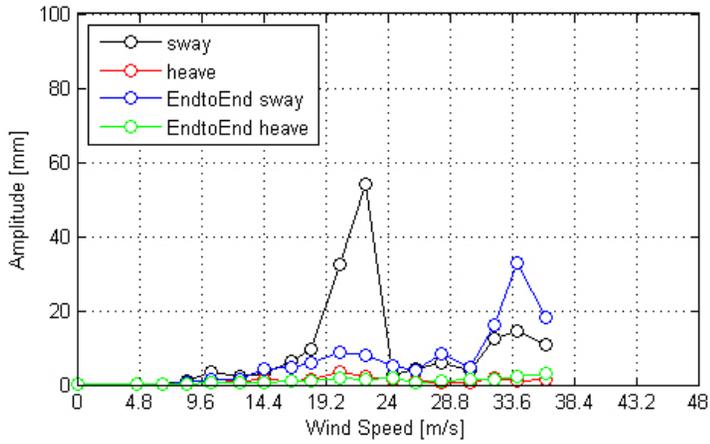
Figure 180. Graph. Response of the cable as a function of wind speed or Reynolds number as measured by the lasers, accelerometers, and surface pressures for run 257.
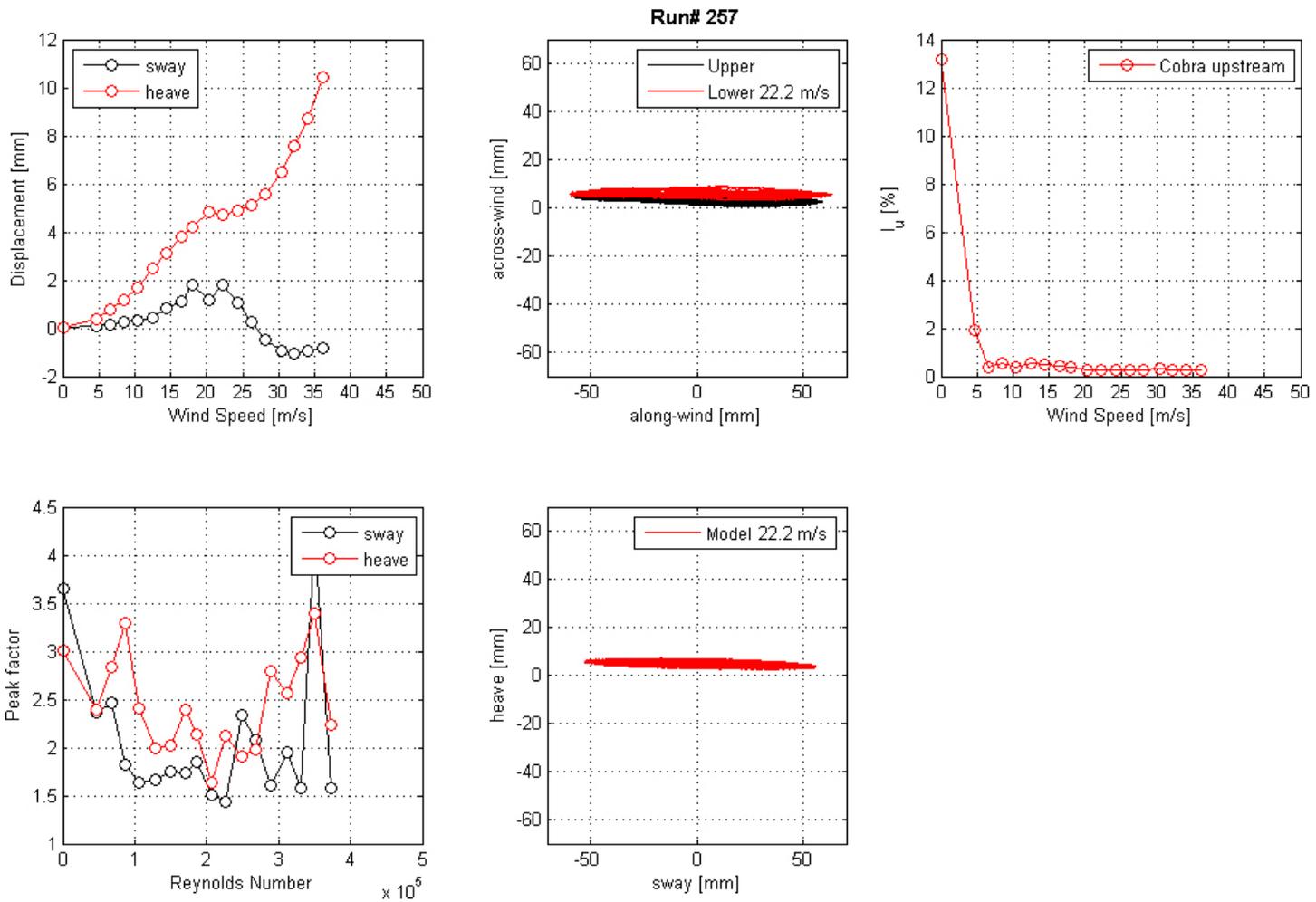
Figure 181. Graph. Mean displacement and peak factor from the laser, motion path at one wind speed, and intensity of turbulence measured at the entrance of the test section for run 257.
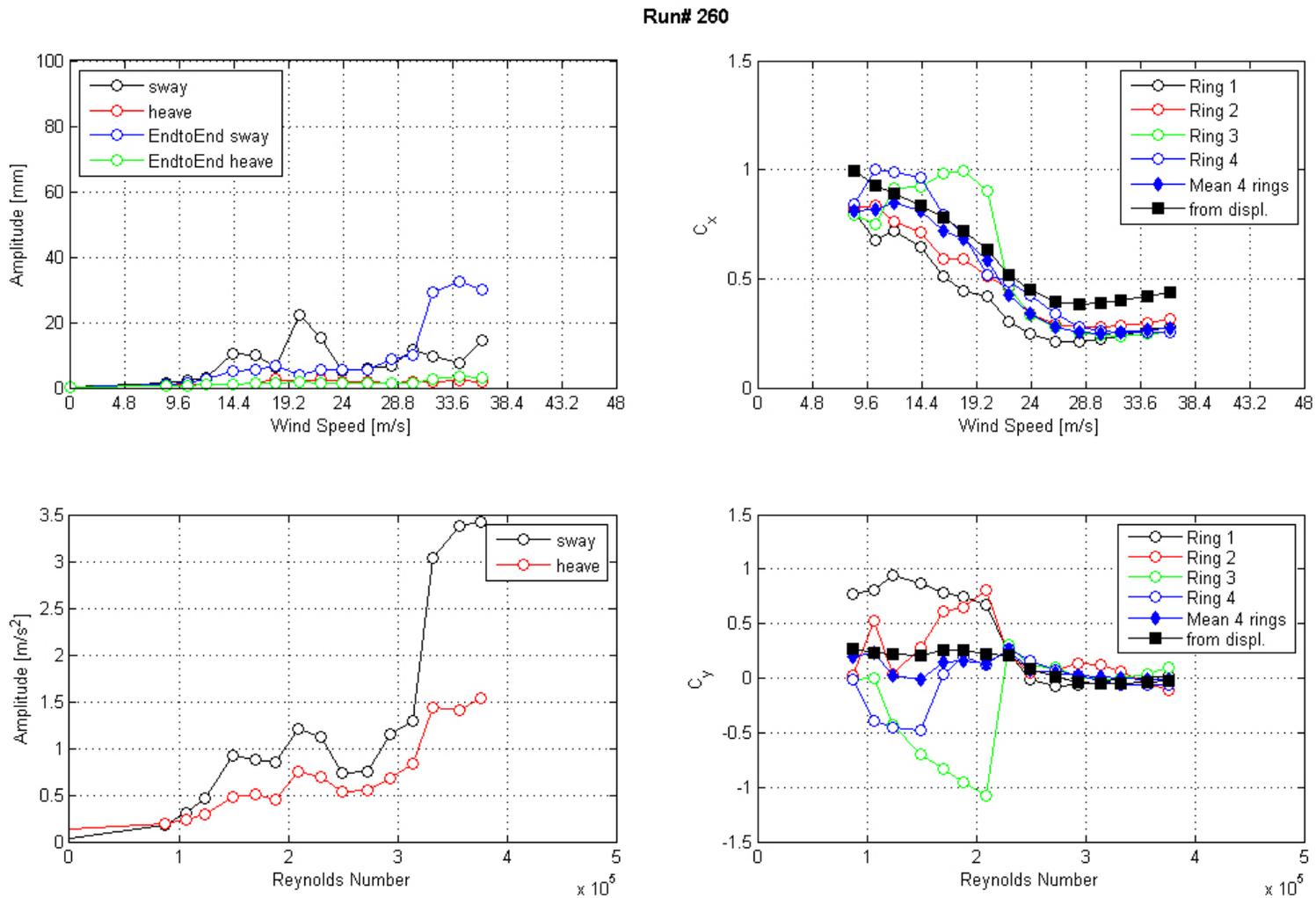
Figure 182. Graph. Response of the cable as a function of wind speed or Reynolds number as measured by the lasers, accelerometers, and surface pressures for run 260.
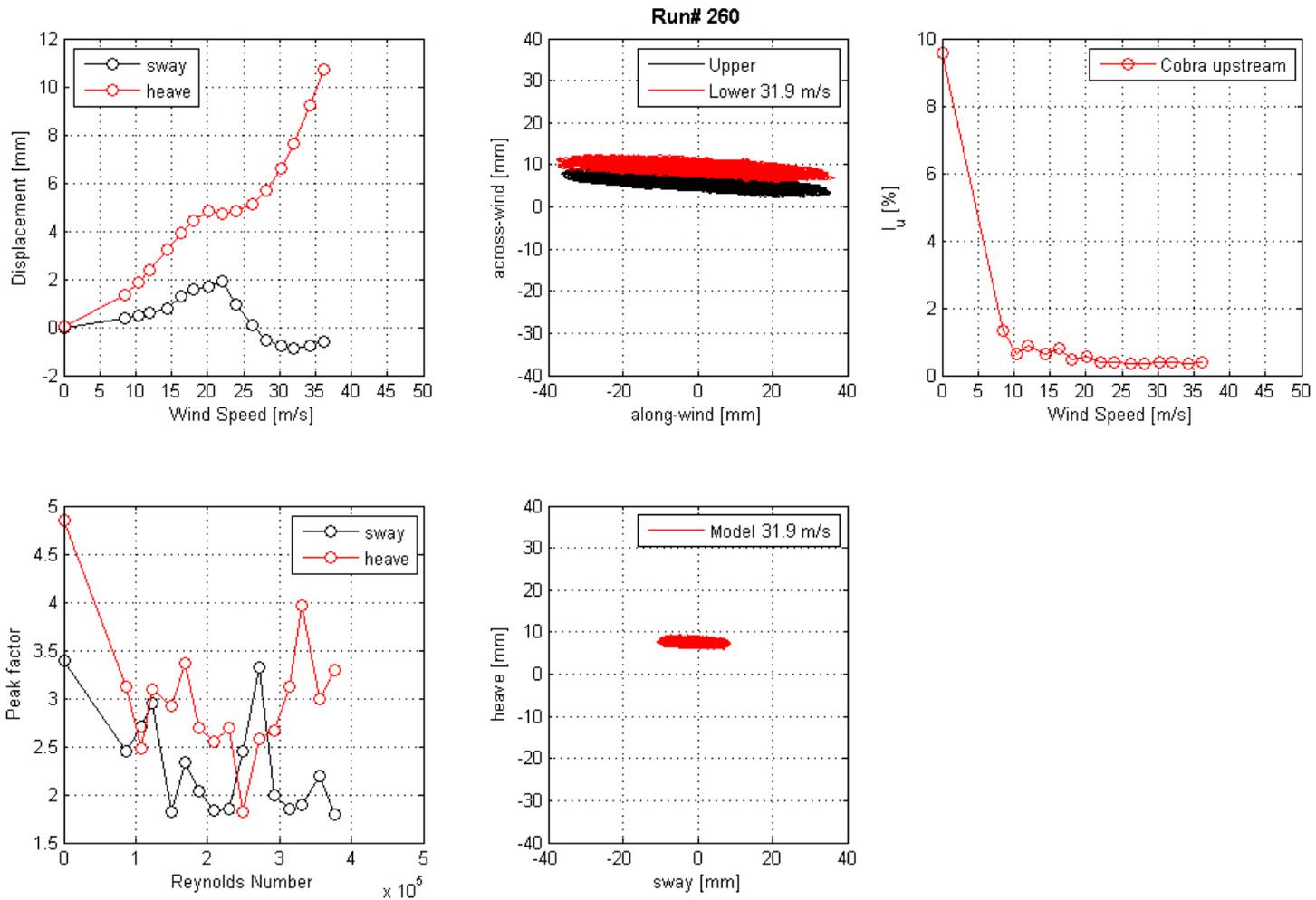
Figure 183. **Graph. Mean displacement and peak factor from the laser, motion path at one wind speed, and intensity of turbulence measured at the entrance of the test section for run 260.**
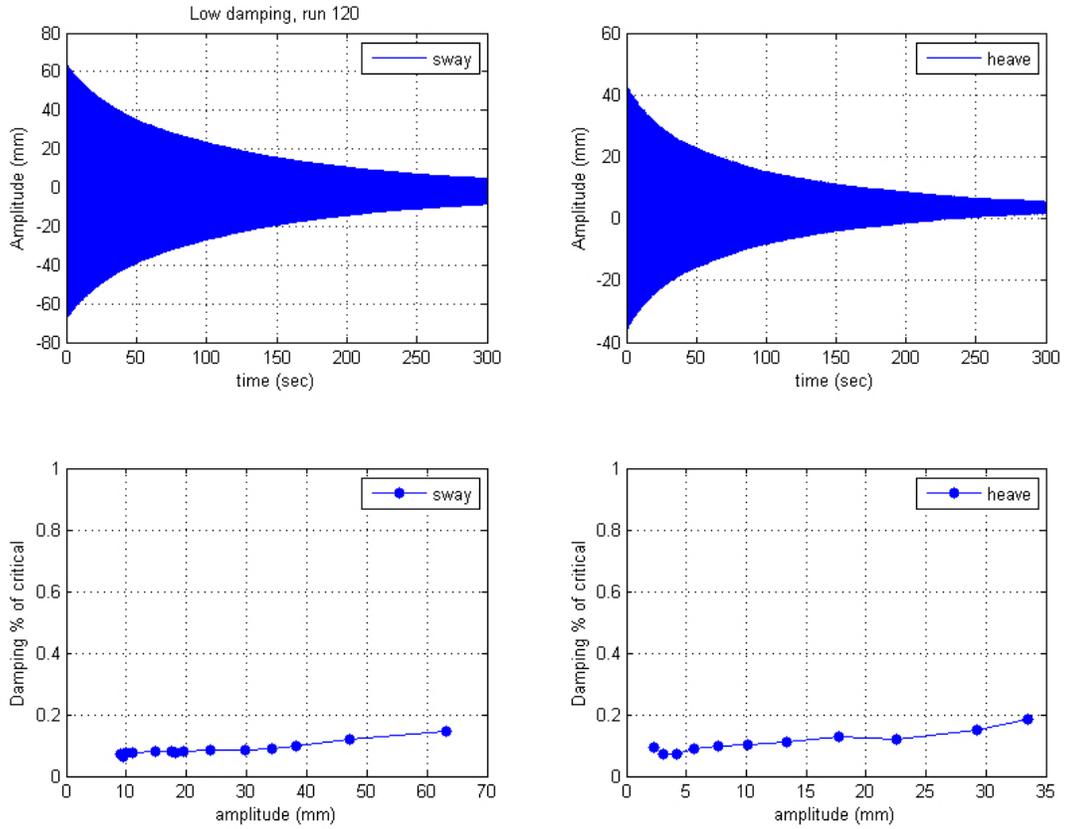
Figure 184. Graph. Damping traces and level for the sway and heave modes for the low damping level case.
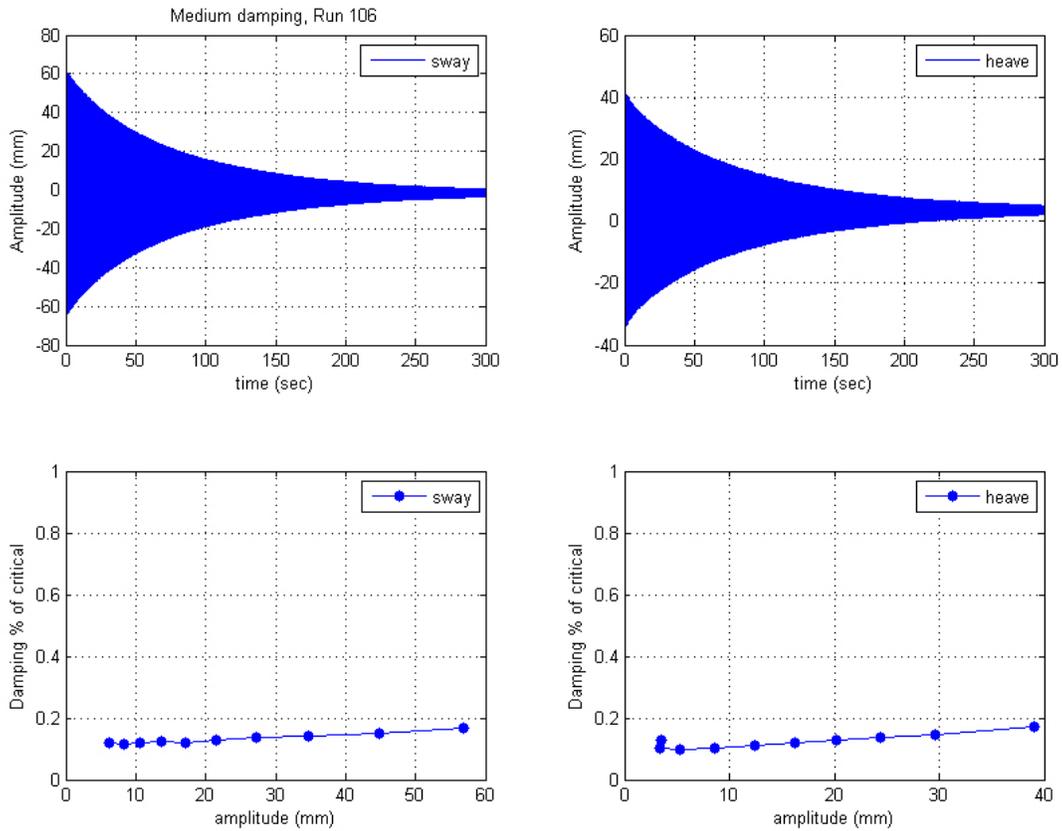
Figure 185. Graph. Damping traces and level for the sway and heave modes for the medium damping case.
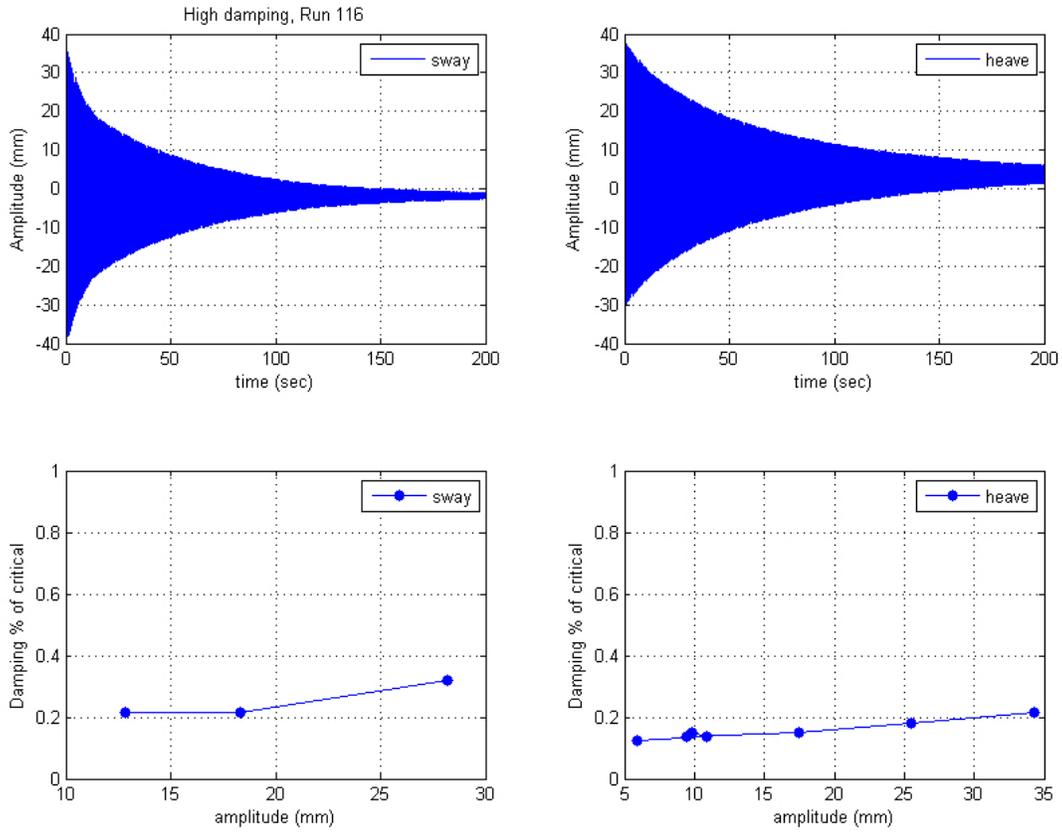
Figure 186. Graph. Damping traces and level for the sway and heave modes for the high damping level case.

ACKNOWLEDGEMENTS

REFERENCES

1. Post-Tensioning Institute. (2012). *Recommendations for Stay Cable Design, Testing, and Installation*, Sixth Edition, Post-Tensioning Institute, Farmington Hills, MI.

2. Flamand, O. and Gandemer, J. (1992). *Effet Combiné du Vent et de la Pluie Sur Les Haubans du Pont de Normandie*, No. EN-SC 92.31C, Centre Scientifique et Technique du Bâtiment, Nantes, France.

3. Larose, G. and Smitt, L. (1999). "Rain/Wind Induced Vibrations of the Parallel Stay Cables for the Oresund High Bridge," *Proceedings of the IABSE Conference, Cable-Stayed Bridges*, Malmö, Sweden.

4. Cheng, S., Larose, G., Savage, M., and Tanaka, H. (2003). "Aerodynamic Behaviour of an Inclined Circular Cylinder," J*ournal of Wind and Structures*, 6(3), 197–208.

5. Kumarasena, S., Jones, N., Irwin, P. and Taylor, P. (2007). *Wind-Induced Vibration of Stay Cables*, Report No. FHWA-HRT-05-083, Federal Highway Administration, McLean, VA.

6. Andersen, T., Jakobsen, J., Macdonald, J., Nikitas, N., Larose, G., Savage, M., and McAuliffe, B. (2009). "Drag-Crisis Response of an Elastic Cable-Model," *Proceedings of 8th International Symposium on Cable Dynamics*, 341–348, Paris, France.

7. Andersen, T. (2010). *Wind Load on Inclined Circular Cylinder in Drag Crisis*, Ph.D. Thesis, University of Stavanger, Stavanger, Norway.

8. Flamand, O. and Boujard, O. (2009). "A Comparison Between Dry Cable Galloping and Rain-Wind Induced Vibrations," *Proceedings of 5th European African Conference On Wind Engineering*, 485–488, Florence, Italy.

9. Cheng, S., Irwin, P., Jakobsen, J., Lankin, J., Larose, G., Savage, M., Tanaka, H., and Zurell, C. (2003). "Aerodynamic Behaviour of Cables Against Skew Wind," *Proceedings of 11th International Conference on Wind Engineering*, 301–308, Lubbock, TX.

10. Nikitas, N., Macdonald, J., Andersen, T., Jakobsen, J., Savage, M., and McAuliffe, B. (2009). "Wind Tunnel Testing of an Inclined Aeroelastic Cable Model—Pressure and Motion Characteristics, Part I," *Proceedings of 5th European African Conference On Wind Engineering*, Florence, Italy.

11. Jakobsen, J., Andersen, T., Macdonald, J., Nikitas, N., Savage, M., and McAuliffe, B. (2009). "Wind Tunnel Testing of an Inclined Aeroelastic Cable Model—Pressure and Motion Characteristics, Part II," *Proceedings of 5th European African Conference On Wind Engineering*, Florence, Italy.

12. Larose, G., Savage, M., and Jakobsen, J. (2003). "Wind Tunnel Experiments on an Inclined and Yawed Circular Cylinder in the Critical Reynolds Number Range," *Proceedings of 11th International Conference on Wind Engineering*, 1705–1712, Lubbock, TX.

13. Macdonald, J. and Larose, G. (2006). "A Unified Approach to Aerodynamic Damping and Drag/Lift Instabilities, and its Application to Dry Inclined Cable Galloping," *Journal of Fluids and Structures*, *22*(2), 229–252.